Technische Universität München
Lehrstuhl E15 für Experimentalphysik und Astroteilchenphysik

Signal processing and event classification for a background free neutrinoless double beta decay search with the GERDA experiment

Andrea Lazzaro

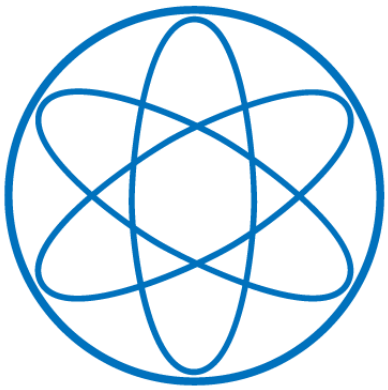

2019

Technische Universität München
Lehrstuhl E15 für Experimentalphysik und Astroteilchenphysik

Signal processing and event classification for a background free neutrinoless double beta decay search with the GERDA experiment

Andrea Lazzaro

Vollständiger Abdruck der von der Fakultät für Physik der Technischen Universität München
zur Erlangung des akademischen Grades eines
Doktors der Naturwissenschaften (Dr. rer. nat.) genehmigten Dissertation.

Vorsitzender: apl. Prof. Dr. Norbert Kaiser

Prüfender der Dissertation:

1. Prof. Dr. Stefan Schönert
2. Prof. Dr. Susanne Mertens

Die Dissertation wurde am 28/06/2019 bei der Technischen Universität München eingereicht

und durch die Fakultät für Physik am 19/07/2019 angenommen.

Abstract

The GERmanium Detector Array (GERDA) experiment searches for the rare neutrinoless double β decay ($0\nu\beta\beta$) of ^{76}Ge. In 2015, GERDA Phase II started taking data with 30 Broad Energy Germanium (BEGe) and 7 semi-coaxial detectors, 35.6 kg of enriched Ge in total. This phase features a new liquid Ar scintillation veto system and improved Pulse Shape Discrimination (PSD) techniques. While the first effectively reduces the γ count rate, the key role of the PSD is to reject the decays on the surfaces of the detectors. This dissertation concerns the recognition and discrimination of signals that could mimic the $0\nu\beta\beta$ decay events. In particular, it addresses the rejection of signals from α decays on the read-out contact of semi-coaxial detectors, β decays of ^{42}K on the surface of BEGe detectors, and unphysical events triggered by micro-discharges along the high voltage lines. A novel PSD method was developed to identify the fast signals produced near the α-sensitive surfaces of the semi-coaxial detectors. The discrimination is based on a rise time parameter and has a signal acceptance of $0.843 \pm 0.004(\text{stat}) \pm 0.01(\text{syst})$. Its combination with the other PSD techniques removes $96.1\% \pm 0.6$ of the counts with energy $E > 3$ MeV, where the α component dominates the spectrum. A five-fold reduction of the expected number of counts in the region of interests (background index) was obtained after the introduction of the Rise Time PSD. The PSD for BEGe detectors was originally developed to reject multiple site events produced by γ-rays. The same classifier (A/E) can discriminate also the events induced by decays occurring on the surface. The effect of the A/E analysis on the ^{42}K component of the BEGe spectrum is investigated with measurements of β-emitters and Monte Carlo simulations. This study shows that the combination of PSD, liquid Ar scintillation veto and mechanical barriers against the collection of ^{42}K ions can reduce the ^{42}K count rate by three orders of magnitude, and bring it to an acceptable level for GERDA Phase II and also for its successor experiment, LEGEND-200. A significant fraction of the GERDA Phase II data is produced by a high rate of micro-discharges (~ 10 mHz). To reject these events, the Phase I waveform-based data selection was improved to consider the whole set of ~ 40 waveforms recorded for each trigger. The data selection retained 99.918% of the physical signals while completely removing hundreds of thousands of spurious events. The PSD of surface events lowered the background indices of both BEGe and semi-coaxial datasets to $0.6^{+0.4}_{-0.3} \cdot 10^{-3}$ cts/(keV $\cdot$ kg $\cdot$ yr). With the application of methods developed within this dissertation, in 2018 the GERDA Phase II median sensitivity reached $T^{0\nu}_{1/2} > 1.1 \cdot 10^{26}$ yr (90% C.L.). Since no signal was found, new limits have been set on $T^{0\nu}_{1/2} > 0.9 \cdot 10^{26}$ yr (90% C.L.) and on $m_{\beta\beta} < 0.11 - 0.25$ eV (90% C.L.).

Zusamenfassung

GERmanium Detector Array (GERDA) ist auf der Suche nach dem neutrinolosen doppelten Betazerfall ($0\nu\beta\beta$) von ^{76}Ge. Im Jahr 2015 wurde mit der Datennahme im Rahmen von Phase II begonnen. Seit Phase II werden 30 sogenannte Broad-Energy-Germanium- (BEGE) und 7 Semi-Koaxial-Detektoren mit einer Gesamtmasse von 35.6 kg an angereichertem Germanium verwendet. Besonderheiten in Phase II sind die Untergrundunterdrückung mittels eines neuen Flüssigargonszintillationsvetos sowie eine verbesserte Pulsformdiskriminierung (PSD). Erstere erlaubt es, γ-Untergrund stark zu reduzieren, während PSD eine Schlüsselfunktion in der Unterdrückung von Oberflächenereignissen einnimmt. Diese Dissertation beschäftigt sich mit der Erkennung und Diskrimierung von Untergrundereignissen, welche $0\nu\beta\beta$-Signale nachahmen können - im genaueren: Ereignissen aufgrund von α-Zerfällen an der Auslese-Elektrode der Semi-Koaxial-Detektoren, β-Ereignissen durch ^{42}K an der Oberfläche der BEGE-Detektoren, und Signalen durch Mikro-Entladungen an den HV-Kabeln. Eine neue Methode zur Identifikation von schnellen Signalen, hervorgerufen durch Ereignisse nahe der α-empfindlichen Oberfläche der Semi-Koaxial-Detektoren, wurde entwickelt. Diese Methode basiert auf dem Parameter Rise-Time und erreicht eine Akzeptanz für Signal-Ereignisse von $0.843 \pm 0.004(\text{stat}) \pm 0.01(\text{syst})$. In Kombination mit weiteren PSD-Methoden werden $96.1\% \pm 0.6$ der Ereignisse mit Energie $E > 3$ MeV entfernt. Dieser Teil des Spektrums ist durch α-Zerfälle dominiert. Die Anzahl der erwarteten Ereignisse im Signalbereich des neutrinolosen doppelten β-Zerfalls von ^{76}Ge wird durch die Rise-Time-PSD um den Faktor 5 reduziert. Eigentlich dafür entwickelt, γ-Ereignisse zu unterdrücken, kann die PSD-Methode der BEGE-Detektoren auch Oberflächenereignisse unterdrücken. Die Leistungsfähigkeit der A/E-Analyse zur Reduzierung von ^{42}K-Oberflächenereignissen im BEGE-Spektrum wurde mittels spezieller Messungen und Monte-Carlo-Simulationen studiert. Die Studien zeigen, dass die Kombination aus PSD, Flüssigargonveto und einer mechanischen Barriere, welche ein Ansammeln von ^{42}K-Ionen unterdrückt, diesen Untergrund um 3 Größenordnungen unterdrücken kann. Ein Großteil der während der Datennahme von GERDA Phase II aufgezeichneten Daten sind ungewünschte Mikro-Entladungen. Die Rate liegt bei etwa ~ 10 mHz. Zur Unterdrückung dieser Ereignisse wurde die in Phase I verwendete Datenselektion, die auf einzelnen Signalen beruhte, auf eine Datenselektion erweitert, die alle ~ 40 Signale berücksichtigt. Durch diese Methoden können Tausende dieser Störereignisse entfernt werden, während die Signalakzeptanz bei 99.918% bleibt. Nicht zuletzt durch die Möglichkeit, Untergrundereignisse durch PSD stark zu unterdrücken, konnte die Untergrundrate sowohl in BEGE- als auch Semi-Koaxial-Detektoren auf $0.6^{+0.4}_{-0.3} \cdot 10^{-3}$ cts/(keV $\cdot$ kg $\cdot$ yr) reduziert werden. Durch Anwendung der Methoden, welche im Rahmen dieser Dissertation entwickelt wurden, konnte GERDA Phase II 2018 eine mittlere Sensitivität von $T^{0\nu}_{1/2} > 1.1 \cdot 10^{26}$ yr (90% C.L.) für den $0\nu\beta\beta$ von ^{76}Ge erreichen. Es wurde kein Signal gefunden. Die dadurch abgeleitete Untergrenze für $T^{0\nu}_{1/2}$ beträgt $> 0.9 \cdot 10^{26}$ yr (90% C.L.), die entsprechende Untergrenze für $m_{\beta\beta}$ liegt bei $< 0.11 - 0.25$ eV (90% C.L.).

Contents

Chapter 1

Neutrinoless double beta decay

The neutrinoless double beta decay ($0\nu\beta\beta$) is a hypothetical process in which a nucleus X(A, Z) decays on Y(A, $Z \pm 2$) emitting two electrons or two positrons. If observed, it would be the first known process to alter, by two units, the difference between the numbers of particles and anti-particles. The observation of $0\nu\beta\beta$ would imply that neutrinos are their own anti-particles (Majorana particles) and could be the key to understanding the asymmetry between matter and anti-matter in the universe. This chapter introduces the history and the current state of neutrino physics (Section 1.1), its connection to the $0\nu\beta\beta$ decay (Section 1.2) and the on-going experimental efforts for the discovery of this process (Section 1.3).

1.1 Neutrino physics: from discovery to oscillations

Neutrinos are neutral fundamental light particles with spin 1/2 and the most abundant known massive particles in the universe. Their existence was postulated in 1930 by W. Pauli as a solution to the problem of energy and momentum conservation in β decays [1]. The first neutrino interaction was observed in 1956 when Frederick Reines and Clyde L. Cowan detected anti-neutrinos produced by a nuclear reactor [2]. Due to the extremely small cross-sections, the detection of neutrinos requires big fluxes, large detectors, and low backgrounds.

Fermi included the neutrino in his theory of β decay [3] which was later expanded by the Standard Model of particle physics (SM) developed by Glashow, Salam and Weinberg in 1961 [4]. In the SM, neutrinos are massless fermions with left-handed helicity, while anti-neutrinos are right-handed. Each of the three types of neutrinos (and anti-neutrinos) observed so far, is always produced by charged current interactions of the corresponding charged fundamental lepton. The fundamental leptons form therefore three singlets of right-handed leptons and three doublets of left-handed leptons:

$$(e)_R, \quad (\mu)_R, \quad (\tau)_R,$$
$$\begin{pmatrix} e \\ \nu_e \end{pmatrix}_L, \begin{pmatrix} \mu \\ \nu_\nu \end{pmatrix}_L, \begin{pmatrix} \tau \\ \nu_\tau \end{pmatrix}_L.$$

Some extensions of the SM proposed the existence of one or more sterile neutrinos that do not interact through the weak force but may contribute to a neutrino mass term. The neutrino mass is indeed required to explain neutrino oscillations. The idea of neutrino oscillation was introduced by Pontecorvo in 1958 [5]. Since at the time only one flavour of neutrino was known, he considered the possible oscillation of massive neutrinos into anti-neutrinos. This hypothesis required neutrinos (and anti-neutrinos) to be symmetrical (and anti-symmetrical) combinations of two neutral Majorana particles (ν_1 and ν_2).

In 1962, the Brookhaven experiment discovered that neutrinos produced by the decay of $\pi^\pm$ are different from the ones produced in $\beta^\pm$ decays [6]. At the same time Maki, Nakagawa, and

Sakata were discussing the idea of flavour mixing in the neutrino sector [7]. They proposed that the *true neutrinos* (ν_1 and ν_2) were a mixture of the two flavour eigenstates (ν_e and ν_μ):

$$\nu_1 = +\nu_e \ \cos\theta + \nu_\mu \ \sin\theta, \qquad \nu_2 = -\nu_e \ \sin\theta + \nu_\mu \ \cos\theta. \tag{1.1}$$

In a second paper on neutrino oscillation, Pontecorvo discussed the possibilities of $\nu_e \leftrightarrows \nu_\mu$ and $\nu \leftrightarrows \bar{\nu}$ oscillations [8]. Before the detection of solar neutrinos, he suggested to test the flavour oscillation hypothesis comparing the flux of solar ν_e on Earth with the expectations for solar ν_e production. He pointed out that in the case of oscillations between the two neutrino flavours the ν_e flux would be half of the one expected.

The same year Davis, Harmer, and Hoffman published the results of their experiment in the Homestake mine in South Dakota [9]. The upper limit set for the solar neutrino rate was not compatible with the solar-model calculations for the flux of ^{8}B electron neutrinos. Later the same experiment found that the flux of solar ν_e is equal to about one third of the one predicted by the solar-models [10].

The first Homestake results were discussed by Gribov and Pontecorvo in 1969 [11] under the assumption of neutrino flavour oscillation in vacuum with two active left-handed neutrinos and two active right-handed neutrinos (and no sterile neutrinos). The basic assumption for neutrino flavour oscillation is that the weak flavour eigenvectors are not identical to the mass eigenvectors. Moreover, the oscillation probability depends on the difference between the mass eigenstates. In the current framework with three ν flavours, at least two of the mass eigenstates must differ from zero to allow all the observed oscillations. More details on the history of the oscillation models can be found in [12].

The existence of a third neutrino flavour (ν_τ) was postulated after the discovery of the third charged lepton τ in 1975 [13]. The SM required for each neutrino to be associated with a charged lepton but gave no indication about the number of flavours, with some theories considering the possibility of thousands of lepton families. In 1989, the measurements of the visible cross-section of the e^-e^+ annihilation around the Z resonance in electron-positron colliders (LEP and SLC) showed that indeed the Z boson decays in three light neutrino species [14], thus establishing the existence of only three lepton families. The ν_τ was later detected for the first time in the year 2000 by the DONUT experiment at Fermilab [15].

The Pontecorvo-Maki-Nakagawa-Sakata (PMNS) matrix that connects the flavour base (ν_f) and the mass base (ν_m) had to be extended into a 3×3 matrix U:

$$|\nu_f\rangle = \sum_m U^*_{fm} |\nu_m\rangle, \ \text{with} \tag{1.2}$$

$$U = \begin{pmatrix} c_{12}c_{13} & s_{12}c_{13} & s_{13}e^{-i\phi} \\ -s_{12}c_{23} - c_{12}s_{23}s_{13}e^{i\phi} & c_{12}c_{23} - s_{12}s_{23}s_{13}e^{i\phi} & s_{23}c_{13} \\ s_{12}s_{23} - c_{12}c_{23}s_{13}e^{i\phi} & -c_{12}s_{23} - s_{12}c_{23}s_{13}e^{i\phi} & c_{23}c_{13} \end{pmatrix} \begin{pmatrix} 1 & 0 & 0 \\ 0 & e^{i\alpha} & 0 \\ 0 & 0 & e^{i(\beta+\phi)} \end{pmatrix}, \tag{1.3}$$

where s_{ij} and c_{ij} are the sine and cosine of the three mixing angles θ_{ij}, ϕ is the Dirac CP-violating phase, and α and β are the two Majorana CP-violating phases which have physical meaning only for Majorana neutrinos. The three neutrinos system can, therefore, be parametrised by 3 neutrino masses (m_1, m_2, m_3), 3 mixing angles $(\theta_{12}, \theta_{23}, \theta_{13})$ and 3 phases (ϕ, α, β). The flavour oscillations, however, are independent of the phases. Moreover, the oscillations in vacuum are also independent of the absolute scale of the masses as their probability is related only to the squared mass differences (Δm^2_{12}, Δm^2_{23}).

Neutrinos always interact with the mediators of the weak force in their flavour eigenstates; therefore, every neutrino is produced (and can be detected) in one of these three states. After being produced they propagate in their mass eigenstates, according to the probability assigned by the PMNS matrix. Each mass eigenstate is a superposition of flavour neutrinos and will collapse onto one of these states when interacting, again according to the probability assigned by the

conjugate transposed PMNS matrix. Thus, the probability to detect a flavour eigenstate ν_η that was produced as ν_ρ is given by

$$P_{\rho\to\eta} = \delta_{\rho\eta} - 4\sum_{i>j} \mathrm{Re}\left(U^*_{\rho i}U_{\eta i}U_{\rho j}U^*_{\eta j}\right)\sin^2\left(\frac{\Delta m^2_{ij}L}{4E}\right) + 2\sum_{i>j} \mathrm{Im}\left(U^*_{\rho i}U_{\eta i}U_{\rho j}U^*_{\eta j}\right)\ \sin\left(\frac{\Delta m^2_{ij}L}{2E}\right), \tag{1.4}$$

where $\delta_{\rho\eta}$ is the Dirac delta function, the mass squared difference is $\Delta m^2_{ij} = m^2_j - m^2_i$, E is the neutrino energy and L is the distance between the two interactions (production and detection). The oscillation wavelength depends on L, E, and Δm^2_{ij} while the maximum probability at the distance

$$L = \frac{\pi E}{\Delta m^2_{ij}} \tag{1.5}$$

depends only on the mixing angles.

If the neutrino propagates through matter (e.g. in the Sun or through the Earth), the probability of oscillations is altered by the Mikheyev Smirnov Wolfenstein (MSW) effect [16]. This is the alteration of the transition probability caused by the coherent forward scattering of neutrinos on the particles they encounter along their path. The precise measurement of the MSW effect allows the determination of the sign of Δm^2_{ij}.

The long-standing solar neutrino problem, created by the discrepancy between the low rate measured by the Homestake experiment and the solar-model prediction, was finally solved at the turn of the millennium when the neutrino oscillations were confirmed by several experimental results. The complementary measurements of the solar neutrino flux performed during the nineties by GALLEX [17] and SAGE [18] (low energy, pp-neutrinos) and KAMIOKANDE [19] (^{7}Be neutrinos) left no room for different solutions to the problem. In 1998, the SUPER-KAMIOKANDE experiment measured the disappearance of atmospheric ν_μ and $\bar{\nu}_\mu$ showing the dependence on the zenith angle thanks to the possibility to detect the direction of the incoming neutrinos [20]. Using neutral current interaction, the SNO experiment measured in 2002 the total solar neutrino flux and found evidence for flavour conversion of ν_e [21]. The KAMLAND experiment confirmed in 2003 the oscillation of $\bar{\nu}_e$ emitted by nuclear reactors [22]. The disappearance of ν_μ and $\bar{\nu}_\mu$ was further confirmed by $\nu_\mu - \bar{\nu}_\mu$ beam experiments, in 2006 by K2K [23] and in 2009 by MINOS [24]. Finally, in 2012 three short baseline (L$\sim$ 1 km) reactor experiments (DayaBay [25], RENO [26] and DoubleChooz [27]) published their results on $\bar{\nu}_e$ disappearance.

The results of the oscillation experiments can be used to constrain the value of most of the 9 parameters from Equation 1.3. In particular, the disappearance of ν_e and $\bar{\nu}_e$ in solar and long-baseline reactor experiments provide a good measurement of θ_{12} and Δm^2_{12}. The sign of the squared mass difference has been determined by measuring the MSW effect on solar neutrinos. The disappearance of $\bar{\nu}_e$ a few hundreds of metres away from the production is connected with the amplitude of θ_{13}, the smallest of the three angles. The disappearance of ν_μ generated by cosmic rays or accelerator beams provides information on θ_{23} and $\left|\Delta m^2_{23}\right|$. The difference between these two masses is much larger than Δm^2_{12} but its sign is still unknown, thus the lightest known mass eigenstate could be either m_1 or m_3. The solution with m_1 as the lightest neutrino is usually called normal ordering, while the inverted ordering is $m_3 < m_1 < m_2$. The latest global fit of the neutrino oscillations data favours the normal ordering over the inverted one [28]. The parameters that do not influence the transition probability (Equation 1.4) are not constrained by any of these measurements. The absolute values of m_1, m_2, m_3 and the three phases (ϕ, α, β) are therefore unknown. Figure 1.1 shows the flavour composition and the mass splittings of the three mass eigenstates as derived from the measured transition probabilities.

Figure 1.1: Summary of the neutrino parameters derived from oscillation experiments. The scenario on the left is for the normal ordering and the inverted ordering is shown on the right side. The colours represent the flavour composition of the three mass eigenstates. Figure from [35].

The three mass parameters of the PMNS matrix cannot be measured directly. However, the precise measurement of the β spectrum end-point can reveal the value of

$$m_\beta = \sqrt{\sum_{i=1} |U_{ei}^2|\, m_i^2}. \tag{1.6}$$

This method, called direct kinematic search, provides a model-independent test of the neutrino masses. The current limits $m_\beta < 2.2$ keV (95% C.L.) have been set by the Mainz [29] and Troitzk [30] experiments studying the β spectrum of tritium near the 18.5 keV end-point with MAC-E filters. The next generation of kinematic searches will increase the sensitivity to the point of being able to set a limit at the level of $m_\beta < 0.2$ keV (90% C.L.) in a few years [31, 32, 33].

Cosmological observations give the strongest limit to the sum of the three neutrino mass eigenstates:

$$\Sigma = \sum m_i. \tag{1.7}$$

The limit, however, depends on the combination of different datasets and on models with several cosmological parameters. In 2018, assuming the standard spacially-flat 6-parameters ΛCDM cosmology framework, the Planck collaboration set a limit of $\sum m_i < 0.12$ eV (95% C.L.) [34].

1.2 Neutrinos and neutrinoless double beta decay

The lepton number is an accidental global symmetry of the SM, in which there is no theoretical justification for this conservation law. If observed, however, the $0\nu\beta\beta$ would be the first known process to alter the net number of leptons in the universe. A positive measurement of $0\nu\beta\beta$ would also provide a path to the explanation of the dominance of matter over anti-matter, as it would be the first known process to change the difference of the numbers of matter particles and anti-matter particles [37].

Many possible diagrams of the process have been proposed to describe the $0\nu\beta\beta$ process. The standard mechanism is the exchange of a light neutrino between two $W_L - e^-$ vertices. The list of other proposed mechanisms includes the exchange of heavy neutrinos (left- or right-handed), and supersymmetric models with the exchange of gluino and neutrino-squark interactions [38]. In the standard scenario of light neutrino exchange, the half-life of the $0\nu\beta\beta$ is related to the square of the $m_{\beta\beta}$:

$$\left(T_{1/2}^{0\nu}\right)^{-1} = G_{0\nu}|\mathcal{M}_{0\nu}|^2 m_{\beta\beta}^2, \tag{1.8}$$

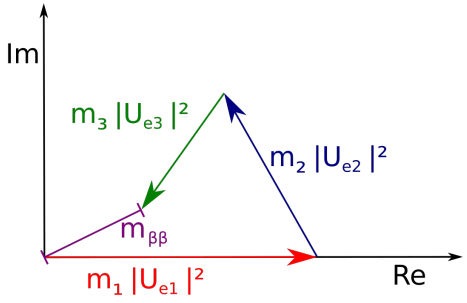

Figure 1.2: Illustration of the definition of $m_{\beta\beta}$ as a coherent sum of the mass eigenstates on the complex plane (Equation 1.9).

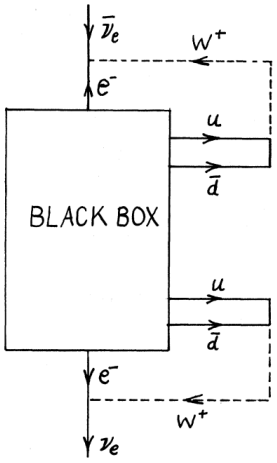

Figure 1.3: The Schechter–Valle theorem states that any realization of $0\nu\beta\beta$ could be inserted in the black box and would allow for the transformation of a ν_e into an $\bar{\nu}_e$. Figure from [36].

where $G_{0\nu}$ is the phase factor and $\mathcal{M}_{0\nu}$ is the nuclear matrix element (NME). The quantity $m_{\beta\beta}$, effective Majorana mass, is the module of the coherent sum of the electron neutrino mass components and is expressed in the parametrisation of the PMNS (Equation 1.3) as:

$$m_{\beta\beta} = \left| m_1 \cdot cos^2\theta_{12} \cdot cos^2\theta_{13} + m_2 \cdot sin^2\theta_{12} \cdot cos^2\theta_{13} \cdot e^{i2\alpha} + m_3 \cdot sin^2\theta_{13} \cdot e^{i2\beta} \right|, \tag{1.9}$$

where θ_{12}, θ_{23}, θ_{13} are the three mixing angles, and α and β are the two Majorana phases (Figure 1.2). The largest component of the electron neutrino is m_1 which in the case of normal ordering is the smallest mass eigenstate. In this case, the combination of the phases may reduce $m_{\beta\beta}$ down to zero. In the inverted ordering scenario, m_1 would be one of the two heavy neutrinos and its contribution to $m_{\beta\beta}$ would be larger than the combined contributions of m_2 and m_3. In other words, if neutrinos have only three mass eigenstates and m_1 is the smallest, for certain combinations of m_1, θ_{12}, θ_{23}, and θ_{13} the allowed space for the half-life of $0\nu\beta\beta$ has no upper bound.

Most of the other mechanisms proposed involve the exchange of heavier propagators with a shorter range. Many mechanisms can contribute to the process, in this case, Equation 1.8 must be modified to include the coherent sum of all contributions:

$$\left(T^{0\nu}_{1/2}\right)^{-1} = G_{0\nu} \left| \sum_i \mathcal{M}_i \eta_i \right|^2, \tag{1.10}$$

where i indexes the list of contributing mechanisms, $\mathcal{M}_i$ are the specific NMEs and η_i are the lepton number violating parameters, e.g. $m_{\beta\beta}$ for the light neutrino exchange. Some of the different mechanisms could in principle interfere with each other in the coherent sum (e.g. the light neutrino and the gluino exchange), in a constructive way decreasing the half-life of the process or in a destructive way increasing it.

The contributions of the different mechanisms cannot be deduced from the measurement of the $T^{0\nu}_{1/2}$ on a single isotope. However, with multiple measurements of $T^{0\nu}_{1/2}$ for different isotopes and a good knowledge of the $\mathcal{M}_i$ involved, it would be possible to constrain the dominant contributions. For example, if the decay is induced only by two non-interfering mechanisms their contributions could be derived from the half-lives of two isotopes, while three are needed if the two mechanisms

are interfering [38]. Moreover, the existence and properties of the short-range propagators can be studied with different experimental approaches, e.g. at the Large Hadron Collider [39, 40].

The $0\nu\beta\beta$ also implies the existence of a Majorana mass term for neutrinos which would then be the only known fundamental massive Majorana particles. This is true regardless of the light Majorana neutrino exchange contribution to Equation 1.10. The Schechter–Valle theorem, illustrated in Figure 1.3, shows how the existence of a process that converts two neutrons into protons with the emission of two electrons would allow the conversion of a neutrino into an anti-neutrino [36]. However, if the $0\nu\beta\beta$ is not dominated by the exchange of the light neutrino the Majorana mass term induced by the black box theorem may be so small that its contribution to the total neutrino mass would be negligible [41].

1.3 Experimental searches for neutrinoless double beta decay

Since the two electrons carry almost the totality of the energy emitted by $0\nu\beta\beta$ and the detectors employed for its discovery can measure the electrons kinematic energies, the expected signals are therefore mono-energetic peaks at the Q-value of the $0\nu\beta\beta$ ($Q_{\beta\beta}$). The theoretical uncertainties on the peak position are smaller than the precision of the calorimetric measurements, therefore the width of the Region of Interest (ROI) depends on the energy resolution of the detector. Some experiments also have the possibility to extract additional information about the event topology, e.g. the position of the event, its extension in space or even the individual tracks of two e^-.

Many experiments integrate the target mass in the detector medium. This can be obtained by choosing a medium that intrinsically contains the decaying isotope (e.g. ^{76}Ge in Ge semiconductor detectors or ^{136}Xe in time projection chambers) or by dissolving the target mass in the detector (e.g. in liquid scintillators). Since the path lengths of the two e^- is typically much shorter than the dimensions of the detector, this approach leads to the optimal detection efficiency. If the source is instead external to the detector, part of the energy can be degraded by self-absorption of the source or one of the two e^- can even escape detection. The main advantage of the external sources is the superior tracking capability and the possibility to easily test different isotopes. This approach can bring important contributions beyond the mere discovery of the process in the study of the $0\nu\beta\beta$ properties.

The expected number of signal counts ($N_{0\nu}$) depends on the half-life of the process ($T^{0\nu}_{1/2}$), on the target mass (M) and on the measurement time (t):

$$N_{0\nu} = \frac{a\,N_A}{W}\ln(2)\;\varepsilon\;\cdot\;\frac{M\cdot t}{T^{0\nu}_{1/2}}, \tag{1.11}$$

where ε is the detection efficiency of the experiment, N_A is Avogadro's number, W is the molar mass of the target material, and a is the isotopic abundance of the decaying isotope. The product $M\cdot t$, usually referred to as exposure ($\mathcal{E}$), indicates the amount of data collected. Given the current limits on the half-life of the process (10^{24-26} yr) and the size of the detectors in operation or in construction (10–1000 kg), only a few counts per year are expected from the signal.

The sensitivity of every experiment strongly depends on the expected number of counts in the ROI from the continuum background distribution (N_{bkg}). If $N_{bkg} \ll 1$, the experiment can be considered background free because every count in the ROI will be interpreted as a $0\nu\beta\beta$ decay. In this case, the sensitivity for the half-life scales linearly with the expected number of signal counts $N_{0\nu} \propto \mathcal{E} \propto t$. In a regime of Gaussian background ($N_{bkg} > 10$), the minimal number of signal counts that can be distinguished from the background is approximately $\sqrt{N_{bkg}}$. Since the $N_{bkg} \propto \mathcal{E}$, in this case, the sensitivity scales as the square root of the exposure

$$T^{0\nu}_{1/2} \propto a\cdot\varepsilon\cdot\sqrt{\frac{M\cdot t}{\Delta E\cdot \mathrm{B.I.}}}, \tag{1.12}$$

where ΔE is the width of the ROI and the background index (B.I.) is the expected number of background counts per unit of exposure and energy, usually expressed in $\mathrm{cts}/(\mathrm{keV}\cdot\mathrm{kg}\cdot\mathrm{yr})$. Computing the exact value of the sensitivity is a more complicated issue [42], but any experiment should aim to be as close as possible to the background free regime to increase its sensitivity faster.

Historically, the main sources of background have been: natural radioactivity of the detector material and from the surroundings, radioactivity induced by cosmic rays, and neutrino accompanied double β ($2\nu\beta\beta$) decays of the target isotope. The natural radioactivity is the dominant one and it is mainly constituted of contaminations from isotopes of the decay chains of ^{238}U and ^{232}Th. These contaminations are present at some level in every material and on any surface. The main strategies to reduce this background usually involve material selection, purification and screening, shielding the detector from external radioactivity with concentric layers of material of increasing radio-purity, and the selection of events from an inner fiducial volume with lower background rate. The cosmic rays can directly produce counts in the detector or indirectly through secondary particles or cosmogenically activated isotopes. Cosmic rays are the reason why all $0\nu\beta\beta$ experiments take place in deep underground laboratories where only a fraction of the muon flux can reach the detector, and the residual component is often vetoed with dedicated muon detection systems. The $2\nu\beta\beta$ background is irreducible because every candidate isotope for $0\nu\beta\beta$ can also undergo $2\nu\beta\beta$ decay with half-lives of about 10^{19-22} yr. The $2\nu\beta\beta$ emits two electrons and two neutrinos, which escape the detector. The events, therefore, have the same topology of $0\nu\beta\beta$ events. This process produces a continuum spectrum with end-point at $\mathrm{Q}_{\beta\beta}$. The only way to lessen the impact of this background is to improve the detector resolution, thus reducing the portion of continuum double β spectrum falling inside the ROI. In fact, the ratio of $0\nu\beta\beta$ to $2\nu\beta\beta$ signals in the ROI is approximately [43]:

$$\frac{S}{B} \propto \left(\frac{Q_{\beta\beta}}{\Delta E}\right)^6 \frac{T_{1/2}^{2\nu}}{T_{1/2}^{0\nu}}. \tag{1.13}$$

The search for $0\nu\beta\beta$ is concentrated on a handful of isotopes for which the single β decay is either energetically forbidden or strongly suppressed. While these conditions are not strictly necessary for the $0\nu\beta\beta$ to occur, it would be impossible to detect the rare event in a target mass which is quickly decaying via single β. Most of the available candidate isotopes are even-even nuclei (A, Z) with bigger binding energy than their even-odd neighbours (A, Z+1) but smaller than the even-even produced by a double β decay (A, Z+1).

The ideal isotope should also be available in large quantities and with high natural isotopic abundance. Given the amount of target mass required for the current and the next generation of experiments, the cost of the material and its isotopical enrichment can be a limiting factor in the sensitivity of the experiment. Another desired feature is a high value of $\mathrm{Q}_{\beta\beta}$ because the $0\nu\beta\beta$ rate is proportional to the phase factor $G_{0\nu}$ which scales as the fifth power of $\mathrm{Q}_{\beta\beta}$. Moreover, since the 2.6 MeV γ-line of ^{208}Tl is one of the main γ emissions of the primordial radio-isotopes, the γ background is drastically lower above this energy.

Different detection methods can be used in the search for $0\nu\beta\beta$. For calorimetric experiments, in which the source is integral to the detector medium, the main channels of detection are phonons, charge, and scintillation light. The ability to simultaneously read more than one channel can be useful to identify the primary particle (α, β, or γ) and thus discriminate between signal and background events. The detector medium can be in solid, liquid or gaseous form. Solid state detectors are compact, modular and can achieve higher intrinsic purity. Liquid and gaseous media can be scaled to larger sizes and are less exposed to surface contaminations. The main detector technologies involved in the $0\nu\beta\beta$ field are the high purity semiconductor detectors (e.g. GERDA, MAJORANA[44] and LEGEND[45]), scintillating bolometers (e.g. AMORE [46], LUCIFER [47]), and time projection chambers (e.g. EXO [48] and NEXT [49]). In general, large volume detectors can achieve a lower specific background rate ($\mathrm{cts}/(\mathrm{keV}\cdot\mathrm{kg}\cdot\mathrm{yr})$) thanks to the lower surface to volume ratio and to the detector self-shielding from external radiation combined with the possibility of hard fiducial volume cuts. The larger distance between the decays and the instrumentation limits the energy resolution which for such experiments can be at the level of 1% or worse. For modular solid detectors, the relatively larger surface per kg of target mass increases the impact of

α and β contaminations. However, modular solid detectors can reach energy resolutions of the level of 0.1% in the ROI. Since the size of the ROI is reduced by the higher energy resolution, despite the higher specific background, the number of expected background events in the ROI can be lower than for large volume detectors. This is a great advantage since, as already discussed, the growth of the sensitivity over time depends on the number of expected background counts, i.e. the sensitivity grows linearly with time only if every count in the ROI can be attributed to the $0\nu\beta\beta$ signal. Moreover, the observation of a few signal counts would make a more compelling argument in case of discovery if the ROI were background free. In this case, the measurement of the signal strength would not depend on the accuracy of the background model.

The many different experimental approaches offer several options to discriminate the background events on the basis of their topology. Time projection chambers with low-density gas medium (such as NEXT) can in principle track the paths of the two electrons emitted by $0\nu\beta\beta$, this could allow for a rejection of all backgrounds but for the irreducible $2\nu\beta\beta$ which presents the same topology features. In denser media, such as liquid scintillators, the electrons deposit their energy in the span of a few millimetres and it is typically not possible to record their paths. It is often possible, however, to recognize compact energy depositions associated with charged primary particles and distinguish them from the one produced by γ rays, which are likely to scatter and deposit energy in several locations within the detector. The compact energy depositions are usually referred to as single site events (SSE) while the others are called multiple site events (MSE). Several different techniques can distinguish SSE and MSE, such as the time coincidence of energy depositions in different detector modules or the analysis of the signals pulse shape.

Many $0\nu\beta\beta$ programmes are currently ongoing. Table 1.1 provides a selection of the latest results for the most relevant investigated isotopes. The half-lives of different isotopes cannot be directly compared but are nevertheless indicative of the challenge of the task. A direct comparison between experiments using different isotopes must rely on the comparison of $m_{\beta\beta}$ constraints. This, however, requires the assumption that the process is mediated by light Majorana neutrinos and depends on the value of the nuclear matrix element ($\mathcal{M}_{0\nu}$). Many of the current and proposed experiments are compared in Figure 1.4. For each experiment, the level of background in the ROI is expressed in a uniform way and plotted against the foreseen exposure.

Table 1.1: Summary of the most stringent limits (90% C.L.) for $T^{0\nu}_{1/2}$ and $m_{\beta\beta}$ for the most promising $\beta\beta$ decaying isotopes.

Isotope	Limit		Median Sensitivity		Experiment	
	$T^{0\nu}_{1/2}$ [10^{25} yr]	$m_{\beta\beta}$ [eV]	$T^{0\nu}_{1/2}$ [10^{25} yr]	$m_{\beta\beta}$ [eV]		
^{48}Ca	> 0.0058	$< 3.5 - 22$	> 0.0018	$< 6.3 - 40$	ELEGANT-IV	[50]
^{76}Ge	> 9.0	$< 0.11 - 0.25$	> 11	$< 0.10 - 0.23$	GERDA	[51]
^{76}Ge	> 2.7	$< 0.20 - 0.43$	> 4.7	$< 0.16 - 0.35$	MAJORANA	[52]
^{82}Se	> 0.24	$< 0.38 - 0.77$	> 0.23	$< 0.39 - 0.81$	CUPID-0	[53]
^{100}Mo	> 0.11	$< 0.33 - 0.62$	> 0.10	$< 0.35 - 0.65$	NEMO-3	[54]
^{130}Te	> 1.5	$< 0.11 - 0.52$	> 0.7	$< 0.16 - 0.76$	CUORE	[55]
^{136}Xe	> 10.7	$< 0.06 - 0.16$	> 5.6	$< 0.08 - 0.23$	KAMLAND-ZEN	[56]
^{136}Xe	> 1.8	$< 0.15 - 0.40$	> 3.7	$< 0.09 - 0.29$	EXO-200	[57]

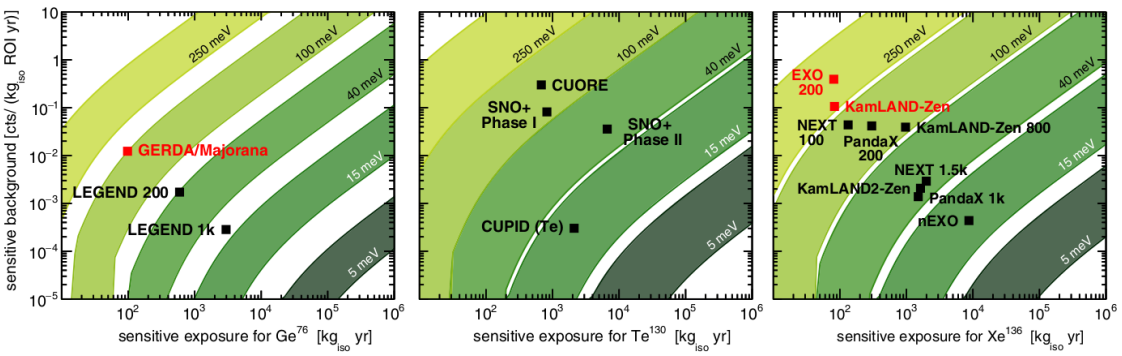

Figure 1.4: Discovery sensitivity of current, running and proposed experiments for $2\nu\beta\beta$ of ^{76}Ge ^{130}Te, and ^{136}Xe [58]. The contours for the values of $m_{\beta\beta}$ depend on the range of values considered for $\mathcal{M}_{0\nu}$. The levels of background in the ROI and the exposures are expressed in a uniform way (sensitive background and sensitive exposure) to allow for the comparison of experiments with different analyses. For future experiments (in black), five years of live time are considered, while the red points refer to already published results of running experiments. More details on the method used for the comparison can be found in [58].

Chapter 2

Overview of the GERDA experiment

The GERmanium Detector Array (GERDA) experiment searches for the neutrinoless double β decay of ^{76}Ge. High purity germanium detectors (HPGe) are immersed in liquified argon, which serves both as a coolant and shield against the α, β, and γ radiation from decays occurring in the near or far materials. The experiment is located in the Gran Sasso National Laboratories (LNGS) at a depth of 3500 m water equivalent below the highest mountain of the Italian peninsula. In its first configuration (Phase I) the experiment ran from 2011 until 2013. It accumulated 21.6 kg·yr of exposure and set a limit on the $0\nu\beta\beta$ half-life $> 2.1 \cdot 10^{25}$ yr (90% C.L.). After the upgrade of the set-up (Phase II), it has been taking data since December 2015 with an increased target mass and a reduced background level. Section 2.1 introduces the technology of the HPGe detectors and, in particular, discusses the features of the GERDA detectors: Broad Energy Germanium (BEGE) and semi-coaxial. The experimental concept and its development through the different phases of the experiment are discussed next.

2.1 HPGe detectors for the search of ^{76}Ge $0\nu\beta\beta$

For several decades the germanium detectors have been among the double beta experiment with the leading sensitivities. The first ^{76}Ge limit on $0\nu\beta\beta$, $T^{0\nu}_{1/2} > 3.0 \cdot 10^{20}$ yr, was set in 1967 by E. Fiorini, A. Pullia et al. [59] with a Ge(Li) detector. The same group improved their result in 1973 [60] by more than one order of magnitude, $T^{0\nu}_{1/2} > 5.0 \cdot 10^{21}$ yr, measuring in a laboratory situated in the Mont Blanc tunnel. New limits, $T^{0\nu}_{1/2} > 2 \cdot 10^{24}$ yr, were provided in 1990 by UCSB/LBL [61] the first experiment to operate multiple Ge detectors and ITEP/YePI [62] the first experiment to operate detectors fabricated of enriched material, 85% of ^{76}Ge compared with a natural abundance of 7.8%. The next leap in sensitivity was performed by the two experiments HEIDELBERG-MOSCOW [63] and IGEX [64] which provide limits at the level of 10^{25} yr, $T^{0\nu}_{1/2} > 3 \cdot 10^{25}$ yr (68% C.L.). The sensitivities of experiments running multiple HPGe detectors in underground laboratories was limited by background radiation external to the crystals. In order to reduce the background level, the Majorana collaboration improved the purity vacuum cryostat material by electro-forming underground copper with an unprecedented level of radio-purity [44]. The GERDA collaboration adopted a novel design concept operating bare detectors in high purity LAr. While cooling the detectors to the operational temperature, the LAr shields the detectors from external radiation and thanks to its UV scintillation allows the active veto of background events that release part of their energy outside the HPGe detectors. Moreover, the background levels can be further reduced by the analysis of the topology of the recorded events which is possible thanks to new pulse shape discrimination (PSD) techniques and novel detector designs. After more than 50 years, ^{76}Ge is still one of the most promising isotopes in the search for $0\nu\beta\beta$ decay.

Germanium is a semiconductor metal, this means that the energy gap between the valence and the conductive bands of its crystal lattice is of the same scale as the electrons' thermal kinetic energy. Above a characteristic critical temperature, the electrons have enough energy to populate

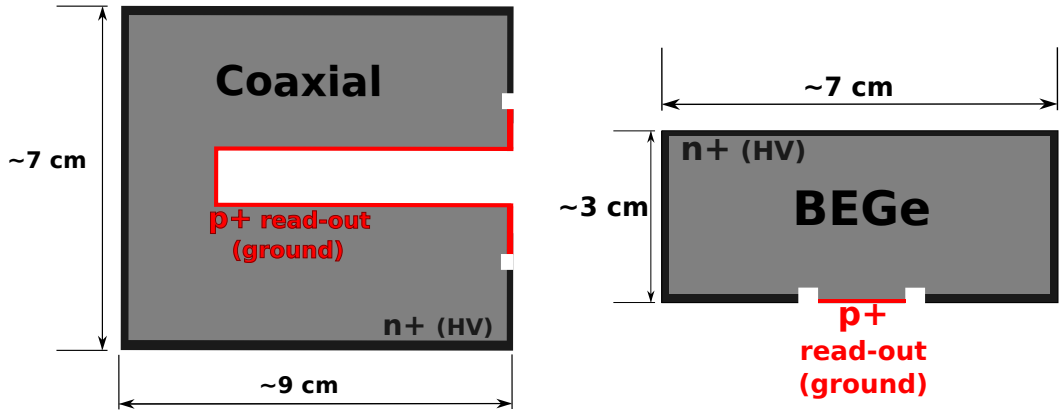

Figure 2.1: Schematic cross-section of the GERDA detectors: semi-coaxial on the left and BEGE on the right. The dimension varies for each detector and some show a bevel around the face opposite to the cathode.

the conductive band while at colder temperatures the material is not conductive. The principle of semiconductor radiation detectors is that the ionising radiation can provide to some electrons enough energy to leave the valence band even below the critical temperature. The number of charge carriers produced is proportional to the amount of energy released by the ionising particle (ions, α, β, or γ). In a reverse biased diode build out of semiconductor material, it is possible to collect all the free charge carriers from a volume next to the p-n junction. The charge carriers produced by an energy deposition in this volume will then induce on the electrodes a current proportional to their number and therefore to the energy released.

The main feature of Ge detectors with respect to other semiconductor detectors (e.g. Si) is the small band gap of 0.7 eV. In order to operate a Ge detector the crystal has to be cooled to cryogenic temperature, typically using liquid nitrogen, at 77–100 K. The second consequence of the small Ge band gap is that even soft ionising radiations will produce thousands of charge carriers, reducing the statistical uncertainty of the measure. The Ge detectors are therefore among the radiation detectors with the best energy resolution, in the order of FWHM$=0.1\%$ in the energy interval $\sim 0.1 - 10$ MeV.

A HPGe detector is a germanium diode whose contacts are realized by doping two thin layers of its surface, usually infusing lithium for the n+ and implanting boron for the p+. According to the net impurity concentration in the germanium crystal, HPGe detectors can be divided into p-type and n-type. In the first case when the reverse bias voltage is applied, the junction forms next to the n+ doped electrode and from there the depleted volume expands, ramping up the High Voltage (HV), until it reaches the p+ doped layer. Once the non-doped bulk material is depleted of charge carriers, no more current flows through the diodes. Further increase of the HV above the depletion voltage will not change the configuration of the electric field or the properties of the detectors. A more detailed description of the germanium detectors principles can be found in [65].

In GERDA only p-type crystals are operated, hence this Section will focus on this case. The best performances are achieved when the p-type detectors signals are acquired from the p+ contact. Thus the detectors are biased with positive HV applied to the n+ electrode while the readout contact is grounded through the preamplifier. Two detector designs have been used in the two phases of GERDA: semi-coaxial detectors and custom Broad Energy Ge (BEGE) detectors (see Figure 2.1).

From the location of the interaction, holes and the electrons move along the electric field lines to the corresponding electrode. A charge moving in the detector induces a mirror charge on the two electrodes. In particular, the mirror charge induced in the readout electrode forms the signal which is then amplified by the preamplifier. The amount of signal charge (Q) produced by a charge

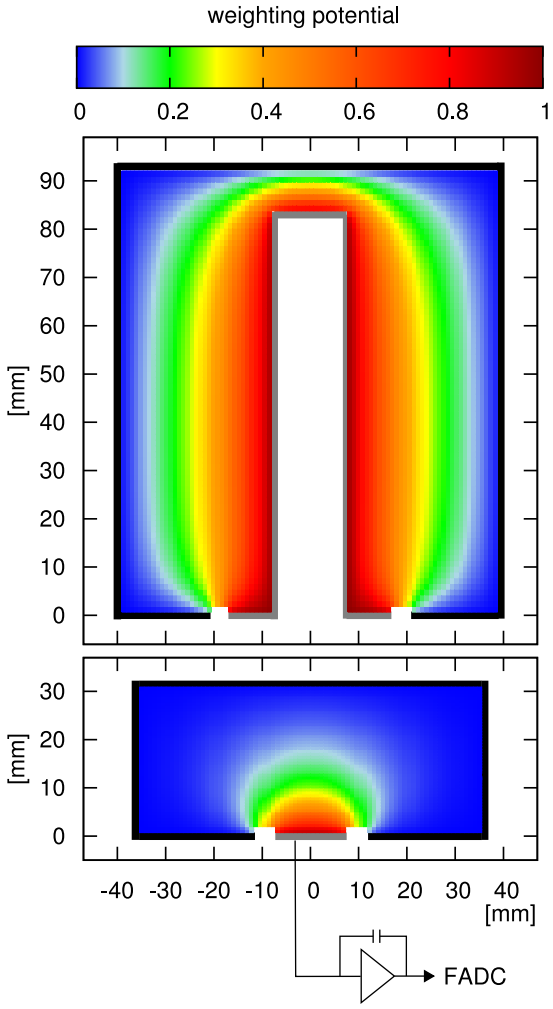

Figure 2.2: Weighting potentials for a generic semi-coaxial detector and for a generic BEGe detector. The weighting potential is equivalent to the electric potential generated by the electrode with a unitary potential difference. Figure from [67].

(q) moving in the detector depends on its position ($\vec{r}$) and it is described by the Shockley-Ramo theorem [66]:

$$Q\left(\vec{r}\right) = -q \cdot \phi_w\left(\vec{r}\right), \tag{2.1}$$

where $\phi_w(\vec{r})$ is the weighting potential which provides the amount of charge induced on the readout contact by a unitary moving charge located in $\vec{r}$. The weighting potential is the electric potential that would be produced in vacuum (i.e. removing all stationary charges) by setting the read-out electrode at a unit potential and the other electrode at zero potential. Figure 2.2 shows the weighting potentials for generic semi-coaxial and BEGe detectors.

The design of the detector defines its capacitance, the configuration of the electric field and of the weighting potential. It impacts therefore on the energy resolution, detection efficiency and pulse shape discrimination performance. The geometry of the diodes together with its net-impurity concentration also determines the bias voltage needed to deplete the active volume.

The dimensions of the crystals then have a direct impact on the background levels of the experiment. Smaller detectors have a higher surface to volume ratio and are therefore more prone to surface contaminations. The contribution of external β backgrounds depends on the thickness of the n+ dead layers, which range between ~ 0.5 mm and ~ 2 mm, a thicker doped layer can mitigate

these components while reducing the active Ge mass. Since the α particles cannot penetrate the n+ contact, the impact of the external α contamination depends on the extension of the p+ electrode and of other open surfaces that separate the two electrodes. To allocate the same target mass with smaller detectors, more channels are needed. This implies the use of additional materials for holders, cables and readout; potentially increasing the γ background.

The semi-coaxial detectors are large cylindrical crystals (1-2 kg) with a cylindrical cavity along a part of the axis (bore-hole). The inner surfaces of the bore-hole are implanted with boron ions to create the p+ electrode. The outer surfaces of the cylinder (one base, the side, and part of the bore-hole's base) are doped with Li. Thus the maximum distance between the two electrodes is less than the crystal radius (3-4 cm). Hence the detectors can be fully depleted with 3-4 kV of bias voltage with a good charge collection from the whole volumes. In the middle of the crystal, the field lines are almost radial, going from the the bore-hole to the external surface. The relative contribution of holes and electrons to the signal generally depends on the distance of the interaction from the two electrodes. More information about the enriched semi-coaxial detectors of GERDA can be found in [68] and a discussion of their signal shapes in Chapter 5.

The BEGE detectors are smaller crystals ($\sim$ 0.67 kg) with the p+ electrode at the centre of one of the bases. The radius of the p+ electrode of the GERDA detectors is about 1 cm. BEGE detectors are a commercial product of Canberra Semiconductor [69], in this work the term BEGE always refers to the custom version produced for the GERDA experiment. In the custom BEGE detectors, the outer surface is uniformly doped with Li with the only exception being the centre of one base. In the commercial product, the n+ contact is thinner on the face opposite to the cathode, thus creating a thin entrance window for low energy X-rays. This feature is not desirable for GERDA since the n+ dead layer is an important shield against external α and β contamination. The smaller cathode reduces the readout capacitance and therefore the level of electronic noise compared to the semi-coaxial detectors. This is of paramount importance since in GERDA the preamplifiers are located far from the crystals (about 50 cm away) to reduce the background. The electronic noise (and the cross-talk) picked up by the signal cables between the detectors and the preamplifier, can be a limiting factor for the performance of GERDA in terms of data quality, energy resolution and pulse shape discrimination. The features of the BEGE signals and their pulse shape analyses are discussed in Chapter 4.

In all the GERDA detectors the two electrodes are separated by a groove, a small circular ditch a few millimetres deep and wide. For some detectors, the surface of the groove is passivated with silicon oxide. The non-active layer on the groove and on the p+ electrode has a thickness of the order of 100 nm. Groove and p+ contact are the only regions where the detectors are sensitive to external α particles.

2.2 Experimental setup and main results of Gerda Phase I

The idea of operating bare HPGe detectors immersed in liquid nitrogen and held by minimal solid structure to reduce the background was first proposed in 1995 by Gerd Heusser [70]. This idea was adopted for the first experimental concept (GENIUS) in 1998 [71]. Yu G. Zdesenko and collaborators developed the concept further including the cryostat into a water tank for the GEM project [72]. The GERDA design builds on these previous works. A vacuum insulated cryostat, filled with liquid argon (LAr), is inserted in a water tank that is used as a neutron shield and as muon Cherenkov veto. LAr was preferred to liquid N because, being denser, it provides a more compact shield against external radiations. However, the main advantage of LAr is that it is an excellent scintillator. When ionised, the LAr produces tens of thousands of 128 nm photons per MeV of electron-gamma energy deposited [73]. The GERDA experiment was proposed in 2004 [74] and realized in the LNGS underground laboratories. In Nov. 2011 GERDA Phase I started to take physics data [75].

The core of the experiment is an array of enriched HPGe detectors suspended in strings inside a cryostat filled with 64 m^3 of LAr. The cryostat is a steel vessel with a copper lining to absorb the γ radiation of the steel. The cryostat is placed in a larger water tank which shields it from radiation

Figure 2.3: Artistic view of the GERDA experiment. The germanium detector array (not to scale) (1), inside the LAr steel cryostat (2) with its internal copper shield (3) and the surrounding water tank (4). The clean room is located above the water tank (5) around the cryostat neck (6).

coming from the laboratory hall, such as neutrons, as well as providing a sensitive medium for a Cherenkov muon veto system. The neck of the cryostat is accessible from a clean room placed on top of the water tank. The detector array is assembled in a glove-box inside the clean room. The Phase I lock system consisted of two independent arms: one connected to a set of three strings and the other connected to the fourth string. An additional muon veto system, based on plastic scintillators, is placed on top of the clean room to cover the neck of the cryostat, which is a blind spot for the Cherenkov system. A representation of the GERDA design is shown in Figure 2.3.

In order to calibrate the detectors within the LAr cryostat, three ^{228}Th sources can be moved along the array. This is achieved by three vacuum sealed mechanical systems that are mounted on top of the cryostat flange. The three sources can be lowered independently to reduce the coincidence rate.

The charge sensitive amplifiers (CC2) [76] for the readout of the detectors are located in the LAr cryostat in a copper box about 30 cm above each string. The data are digitised and recorded by commercial FADC (100 MHz, 14 bit) of type SIS 3301 by Struck [77].

For Phase I, all eight detectors from the former HDM [63] and IGEX [64, 78] experiments were refurbished and redeployed. These are standard closed-end coaxial p-type HPGe detectors originally produced by ORTEC and then refurbished by Canberra [69]. They have a "wrap around" n+ conductive lithium layer ($\sim$ 1 mm) that is separated from the boron implanted p+electrode by a groove. The enriched semi-coaxial detectors have a total weight of 17.7 kg and an active volume of 87%.

In July 2012 five enriched BEGE detectors were introduced in the GERDA cryostat. Besides contributing to the Phase I results, the operation of these five detectors for almost one year represented an important opportunity to test the detectors before Phase II. The enriched BEGE detectors have a total weight of 3.7 kg and an active volume of 92%.

Two of the eight semi-coaxial detectors (ANG1 and RG3) started to draw leakage current soon after their deployment and one of the five BEGE detectors showed an unstable behaviour. Three of the 12 enriched detectors deployed in Phase I were therefore not considered in the analysis. The exposure collected in Phase I between November 2011 and May 2013 was 21.6 kg·yr [79].

Since the signals from $0\nu\beta\beta$ are most likely to be generated by the energy deposited in a single location by the two e^-, it is possible to reduce the background rate by rejecting events in coincidence with other Ge detectors or with the muon veto system. Moreover, pulse shape discrimination techniques [67] were applied to both semi-coaxial and BEGE detectors to reject

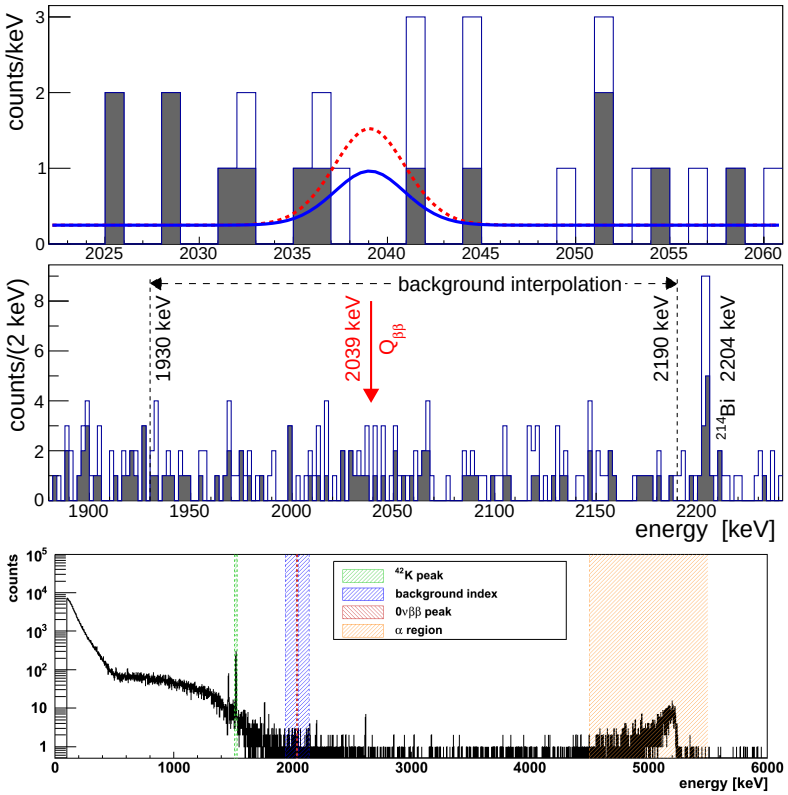

Figure 2.4: GERDA Phase I spectrum. The top panel shows the counts in the region of interest, the middle one shows the side-bands where the background index is computed, and the bottom panel shows the full spectrum. The empty (grey) histograms in the top panels report the counts rejected (accepted) by pulse shape analysis. The blue line on the top panel shows the limit on $0\nu\beta\beta$ signal ($T_{1/2} = 2.1 \cdot 10^{25}$ yr 90% C.L.) and the dashed red line shows the expected distribution of counts in the hypothesis of $T_{1/2} = 1.19 \cdot 10^{25}$ yr. This was the half-life previously measured by an analysis of the HDM experiment [82].

events with energy deposition in multiple locations of the Ge crystals (multiple site events). The BEGE detectors' PSD also allows to reject events generated on the surface of the detectors where the background rate is higher, due to α and β external decays [80, 81].

The background level in the $Q_{\beta\beta}$ region is computed in the interval 1930–2190 keV. According to the background model described in [83], a flat energy distribution is expected in this region, with the exception of two γ lines (2104 keV, 2119 keV) excluded from the computation. The overall background index of Phase I is about 0.01 cts/(keV · kg · yr), with the semi-coaxial dataset at $11^{+2}_{-2} \cdot 10^{-3}$ cts/(keV · kg · yr) and the BEGE dataset at $5^{+4}_{-5} \cdot 10^{-3}$ cts/(keV · kg · yr) [79].

GERDA Phase I was the first $0\nu\beta\beta$ experiment to perform a blind analysis. Events with energies within $Q_{\beta\beta} \pm 5$ keV were not immediately processed and were not available until after all the details of the analysis (e.g. background model, pulse shape discrimination, Bayesian and frequentist statistical analyses) had been frozen.

Figure 2.4 shows the recorded spectrum. Three counts were found in the blinding window, all in the semi-coaxial detectors and none in the interval $Q_{\beta\beta} \pm \sigma$. Both frequentist and Bayesian analyses result in a best fit of zero signal counts and limits for the $T^{0\nu}_{1/2}$ of $> 2.1 \cdot 10^{25}$ yr (90% C.L.) and $> 1.9 \cdot 10^{25}$ yr (90% C.I.) respectively [79].

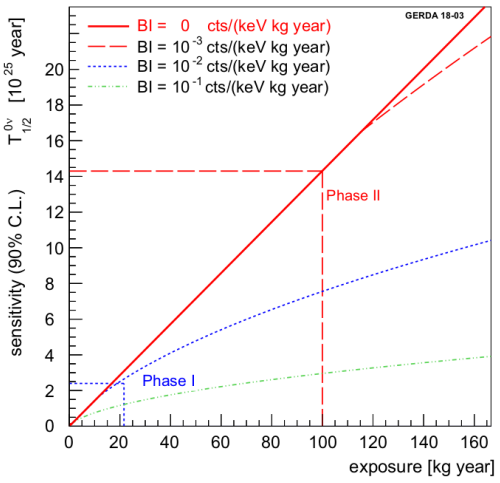

Figure 2.5: Frequentist model of the sensitivity for limit setting. The different lines represent different background levels, in particular the blue and red dashed lines correspond respectively to the Phase I and Phase II scenarios under the assumption of 60% detection efficiency. Figure from [84].

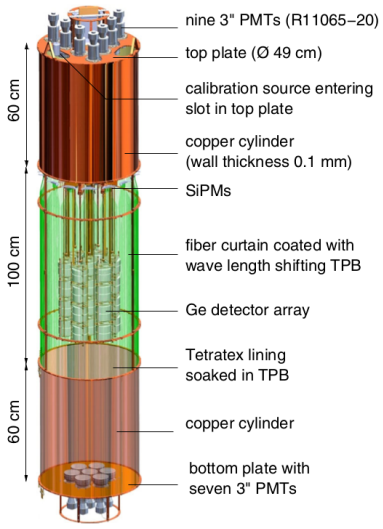

Figure 2.6: Rendering of the LAr veto system surrounding the detector array. Figure from [84]. The LAr veto structure is connected to the same chain that holds the Ge detectors array. The three sections are assembled in the lock and immersed in the cryostat with the array.

2.3 Key innovations for Gerda Phase II

Figure 2.5 shows the sensitivity of GERDA as a function of the collected exposure for different background levels. As discussed in Chapter 1, the sensitivity scales linearly for background free experiments. It only scales as the square root of the exposure if the distribution of the expected number of background events is Gaussian, see Equation 1.12. In other words, to improve upon the results of previous experiment is always necessary to reduce the background level to move closer to the background free regime.

Since most of the Phase I background events were induced by radioactive decays in the solid material surrounding the detectors, the array has been redesigned to reduce the amount of material per kg of active mass and improve its radio-purity. The Phase II detector holders consist of 3 thin copper rods connected to high purity mono-crystalline silicon plates. In order to reduce the copper mass and the mechanical stress of the holder, the spring contacts of Phase I have been substituted by wire bonds on aluminium pads evaporated on the detector surfaces [85]. For each contact (signals and HV) three Al wire are bonded to a 600 nm thin Al pad. The wires connect the detector to the end of the flat cables fixated on the silicon plate. The detectors are mounted on their holder and bonded to the cables before the array is assembled in the lock. The modular design allows the placement of up to eight BEGE detectors (or 3 semi-coaxial detectors) in a single vertical string.

The second phase of the GERDA experiment aimed to reach a sensitivity of 10^{26} yr for the $0\nu\beta\beta$ half-life in about 3 years of data-taking. The target mass has been increased to about 40 kg with the goal of reducing the background level below 0.001 cts/(keV $\cdot$ kg $\cdot$ yr) in the signal region. The additional mass is constituted by newly produced custom BEGE detectors, bringing their number to 30.

Several technical upgrades of the system have been realised to operate the new detector array with a lower background target [84]. The $0\nu\beta\beta$ are expected to deposit energy in a single confined location (a few mm^3) inside the germanium crystal. The background radiations can scatter in

several locations inside the detector or in the surrounding LAr (external γ), or deposit energy on the detector surfaces (β and α). With the deployment of light detectors around the array it is possible in GERDA Phase II to veto most of the background events that produce scintillation light in the LAr.

The liquid argon veto system (LAr veto) is constituted by 3 cylindrical sections that can be deployed together with the HPGe detectors array through the cryostat lock, see Figure 2.6.

The top and bottom copper sections are lined internally with a wavelength shifter reflector and host on the top and bottom panel respectively nine and seven 3" photomultiplier tubes (PMTs). In the middle section, a curtain of wavelength shifting fibres coupled to silicon photomultipliers (SiPMs) is held in place by a thin copper frame that does not obstruct the detection of light produced in the LAr surrounding the curtain. The three sections have a diameter of about 50 cm and a combined length of $\sim$2.6 m.

The twin lock system from Phase I has been replaced with a larger one ($\varnothing = 550$ mm) which is able to host the full array to be deployed together with the LAr veto instrumentation.

2.4 Legend: the approach to ^{76}Ge tonne-scale experiment

Whether GERDA Phase II finds a $0\nu\beta\beta$ signal or not, further progress in the sensitivity will be needed to push the limit further or confirm the signal with a better measurement of the process' half-life.

Since the beginning, the GERDA collaboration has been planning to cooperate with its American counterpart working on the Majorana demonstrator [44]. This is the other prominent ^{76}Ge $0\nu\beta\beta$ experiment, which operates about 40 kg of HPGe detectors in two vacuum cryostat built with radio-pure copper, which was electroformed underground to reduce contaminations and cosmogenic activation. A new collaboration has been formed in 2017 to prepare a single tonne-scale ^{76}Ge experiment: LEGEND [86].

The LEGEND experiment aims to reach the discovery potential for a half-life beyond 10^{28} yr. This target will be approached in two stages. The first phase, LEGEND-200, will exploit once more the GERDA cryostat at LNGS where an array with 200 kg of detectors will collect about 1 T·yr of exposure to bring the sensitivity above 10^{27} yr. To reach this goal, a further reduction of the background level to the order of 10^{-4} cts/(keV $\cdot$ kg $\cdot$ yr) is necessary. The preparation for this first stage is already ongoing and will be realized shortly after the conclusion of the GERDA experiment and is expected to start data-taking in 2021.

A new infrastructure will be built for the following stages to gradually increase the target mass up to 1 t of enriched Ge. To reach the sensitivity for 10^{28} yr half-life, about 10 t·yr of data have to be acquired with a 10-fold reduction in the background level compared to the current technology.

Chapter 3

Data processing and reduction

This chapter describes the processing and selection of the GERDA data. Section 3.1 delineates the series of the digital filters that are applied to the waveforms of HPGe detectors in Phase II. A first selection of the recorded events is performed through a series of quality cuts described in Section 3.2. The selection of the physical events is of paramount importance due to the high rate ($\sim$ 10 mHz) of triggers induced by electric micro-discharges along the HV lines of the detectors. The quality cuts remove the majority of the recorded events with a reconstructed energy above 1.5 MeV. The estimation of the quality cuts efficiency is reported in Section 3.3. The GERDA Phase II energy spectrum of the selected physical events is shown and discussed in Section 3.5.

3.1 Data processing

When ionising radiation deposits energy in the germanium detectors it creates electron-hole pairs which induce a signal while drifting towards the electrodes. The charge signals of the HPGe detectors are composed of: the baseline recorded before the particle interaction; the transient where the signals rises from the baseline level to the peak amplitude in ~ 1 μs; and an exponential tail ($\tau \sim 150$ μs) associated with the RC preamplifier feedback. The signals are digitised at 100 Mhz by 14-bit flash-ADCs (FADC) [77]. Current pulses causing a sudden increase of the charge signal are detected by an on–line digital filter and trigger the data acquisition. When the data acquisition (DAQ), is triggered two traces are written on disk for each HPGe channel . All recorded traces are centred around the trigger position. The high-frequency (HF) trace, sampled at 100 MHz, is 10 μs long. The low-frequency (LF) trace, sampled at 25 Mhz, is 160 μs long. An example of the two HPGe traces is reported in Figure 3.1. For every HPGe trigger, 160 µs traces are recorder from the liquid argon scintillation light detectors (PMTs and SiPMs). The muon-veto system detectors (Cherenkov light PMT's and plastic scintillators) have a similar but independent data acquisition [87]. The timestamps of the muon-veto triggers are later used (off-line) to reject HPGe events in coincidence with the passage of cosmic muons.

The raw data files are automatically closed, backed up and processed every 3 hours. The new files are processed in the GELATIO framework described in [88]. The digital signal processing is based on modules, which handle a precise and self-consistent task. The output of each module can be a set of scalar parameters (e.g. the amplitude, the rise time or the trigger time) or a shaped trace, which can be used as input for other modules. The two germanium traces are processed along different chains of GELATIO modules.

The LF trace is processed by the following modules:

- `GEMDBaseline` analyses the first 70 µs of the trace. It computes the average value, the root-mean-square deviation (RMS) and the linear slope before the leading edge. The module also performs the baseline restoration – a subtraction of the average baseline value to the trace – and provides to the other modules the new signal with the baseline centred at zero. Additional portions of the trace are analysed to evaluate the general shape of the waveforms:

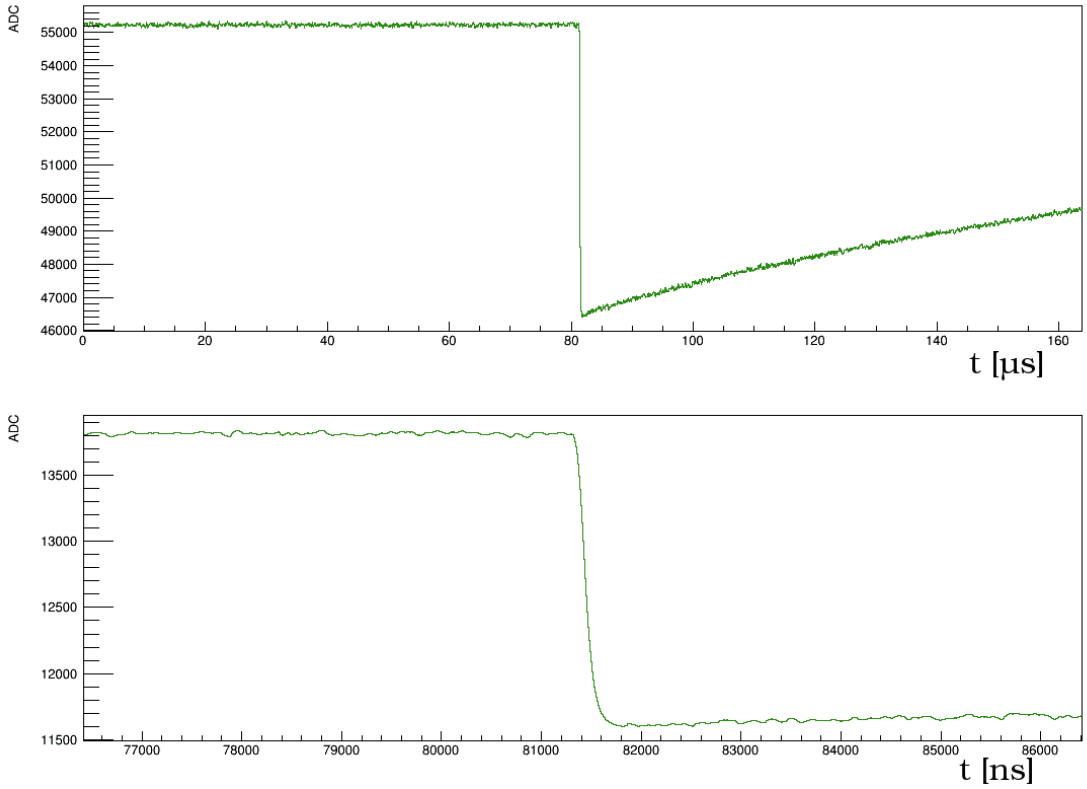

Figure 3.1: Example of two traces recorded for a HPGe detector. The top panel contains the 160 µs long LF trace sample at 25 MHz. The bottom panel contains the 10 µs long HF trace sample at 100 MHz. All the waveforms in this chapter are shown in accordance with the same colour scheme: the ones accepted by the quality cuts are green (signals) or blue (baselines), the waveforms rejected are red and the one of OFF channels excluded by the analysis are black.

the last 70 µs, the first and the last 5 µs. This intervals, called auxiliary baselines, are then used for pile-up rejection in the calibration data and in the quality cuts for waveforms with no energy depositions.

- `GEMDFTTrigger`, a fast trapezoidal filter which identifies events with multiple pulses occurring within the same trace. This module applies a deconvolution of the preamplifier decay tail, a 2.5 µs moving window differentiation, and a 2 µs moving average for noise reduction. The resulting trace has a peak for each sharp variation of the signal (such as the leading edge of a pulse). The peak width is similar to the size of the moving differentiation and was chosen to maximise the pile-up identification efficiency and to avoid the misidentification of highly multiple site events. The number and the position of the peaks are estimated by applying a leading-edge discriminator, whose threshold is 5 times the RMS of the baseline. After this condition is met, the signal has to remain above the threshold for at least 2 µs.

- `GEMDTrigger`, this module is used to identify the beginning of the pulse leading edge (trigger position). It implements a leading-edge discriminator with a threshold defined dynamically as two times the RMS of the signal baseline. After the trigger, the signal has to remain above threshold for at least 40 µs, otherwise the trigger is rejected.

- `GEMDZACShaping`, measures the amplitude of the signals with a Zero-Area finite-length Cusp filter with a central flat top (ZAC). The details and the performances of this filter are described in Ref. [89]. The parameter of these energy filters are tuned after each calibration

run to optimise the energy resolution of each detector. This filter provides the best energy resolution and it is the standard energy reconstruction method adopted by the GERDA collaboration.

- `GEMDEnergyGauss` reconstructs the event energy using an approximate Gaussian filter [90, 91]. The pulse is differentiated by a moving differentiation filter and then integrated 13 times by a moving average filter (MWA) with 10 μs width to achieve an approximated Gaussian shape. The energy information is eventually stored in the maximum amplitude of the quasi-Gaussian pulse. This energy filter provides lower energy resolution than the standard ZAC filter and is not optimised for each channel and for variation of the noise. It is used for data quality monitoring and for pulse shape analyses (PSA).

- `GEMDEnergyGast`, this module measures the signal amplitude according to the Gast Moving Window Deconvolution [92]. The moving window deconvolution is equivalent to a differentiation with 10 μs width and a deconvolution with an exponential function. The pulse is then de-noised with a moving window average of 8 μs. The result is a trapezoidal waveform with the same amplitude as the original waveform. The value of the amplitude is read from the middle of the flat top, found in relation to the trigger position computed by the `GEMDTrigger`.

- `GEMDMinMaxFinder`, a simple module which records the maximum and the minimum values of the waveform. A short interval around the trigger position, from 75 μs to 82 μs, is excluded due to the occurrence of spikes induced by cross-talk among neighbour channels. This module is used to assert the quality of pure baseline waveforms where no energy deposition occurred.

- `GEMDDecayTailFit`, this module fits the exponential decay tail of the waveform, from 20 μs to 60 μs after the trigger position.

- `GEMDRiseTimeLF`, computes the 10-90% rise time of the low frequency trace. The maximum amplitude is computed as the difference between the maximum of the pulse and the average baseline value. Then, the first samples below the 10% and 90% of the amplitude are found by moving backwards from the position of the maximum.

The HF trace is processed by the following modules:

- `GEMDRiseTimeHF`, computes the rise time 10-90% of the high frequency trace. The algorithm is the same as the one used for the `GEMDRiseTimeLF`.

- `GEMDRiseTimeHD_1090` computes the rise time 10-90% of the high frequency trace after a 30 ns MWA and a 10 fold interpolation to 1 ns sampling. Similar modules compute the rise time 2-60% and 5-60%.

- `GEMDCurrentPSA`, which computes the current signal as the derivative of the charge signal and then extracts the basic features of the current pulse, like amplitude (A), width and area. The current pulse is computed with a moving window differentiation of 10 ns width, after 3 MWA of 50 ns. The current pulse is also interpolated to 1 ns sampling, to improve the precision of the extracted parameters.

The data processing and the tools used are a direct derivation of the ones developed for GERDA Phase `I` described in [93].

During the physics data-taking a new file is produced and processed every 3 hours. Hence it is possible to monitor the parameters of interest almost in real-time.

3.2 Data reduction

All recorded waveforms are processed by the aforementioned GELATIO modules. The output of the modules are stored on disk. Most of the analyses of the GERDA data (e.g. BEGE's PSA,

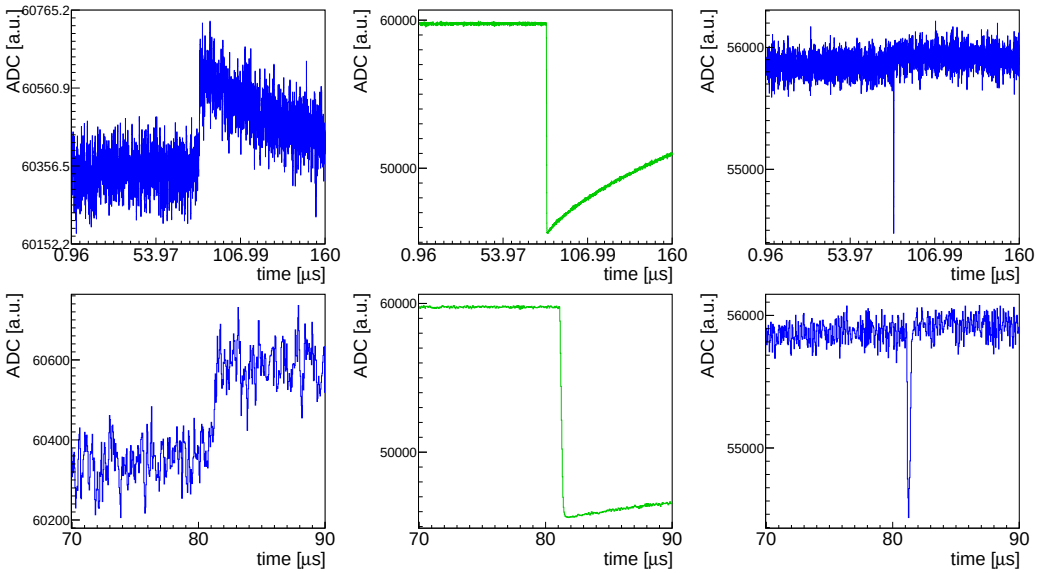

Figure 3.2: Example of cross talk among HPGe channels. Each bottom panel shows the central 20 µs of the LF trace displayed on the top panel. The green signal in the centre produced cross-talk pulses in two neighbouring detector. The cross talk induced by an event in channel 38 (centre) on the channel 23 (left) is a current with inverse polarity. The cross-talk on channel 39 (right) is a short spike with the same polarity of the physical signals. This event was recorded on June 18, 2017 and the reconstructed energy for channel 39 is 2.598 MeV.

background model and $0\nu\beta\beta$) are based on these output files. It is necessary to tag any events for which the computed parameters do not have the proper physical meaning. These can be non-physical events not related to an energy deposition (i.e. micro-discharges or cross-talk) or signals with a different shape than the one for which the digital filter were implemented (i.e. pile-up events or signals that exceed the dynamic range). This section illustrates the different classes of signals and the sets of quality cuts implemented to tag them.

3.2.1 Classes of spurious signals

This section presents a list of possible classes of signals that differ from the ones associated with a standard physical energy deposition shown in Figure 3.1.

Test pulser Every 20 seconds of data-taking, a pulse is injected into the preamplifier of each channel. This pulse resembles a physical pulse, with a slightly faster rise time and equivalent energy around 3 MeV. For these events an additional waveform with the injected pulse is recorded to monitor the stability of the pulse generator. The test pulser is used to measure the duty cycle and the live-time of each channel, to monitor the stability of the preamplifiers between calibrations and to estimate the efficiency of the quality cuts.

Baseline events From March 2016 (run 60) an external trigger was injected in the FADC every 47 s (changed to 40 s in November 2016). The waveforms recorded are typically 160 µs of baseline of each channel. These events are tagged by the FADC firmware as externally triggered. The baseline waveforms are used to study the noise frequency spectrum, the rate of random coincidences (with the veto systems) and the efficiency of the quality cuts.

Saturated waveforms If the signal exceeds the FADC dynamic range the waveform is tagged as saturated. This can happen for high energy pulses, typically above 6-7 MeV, or fluctuations

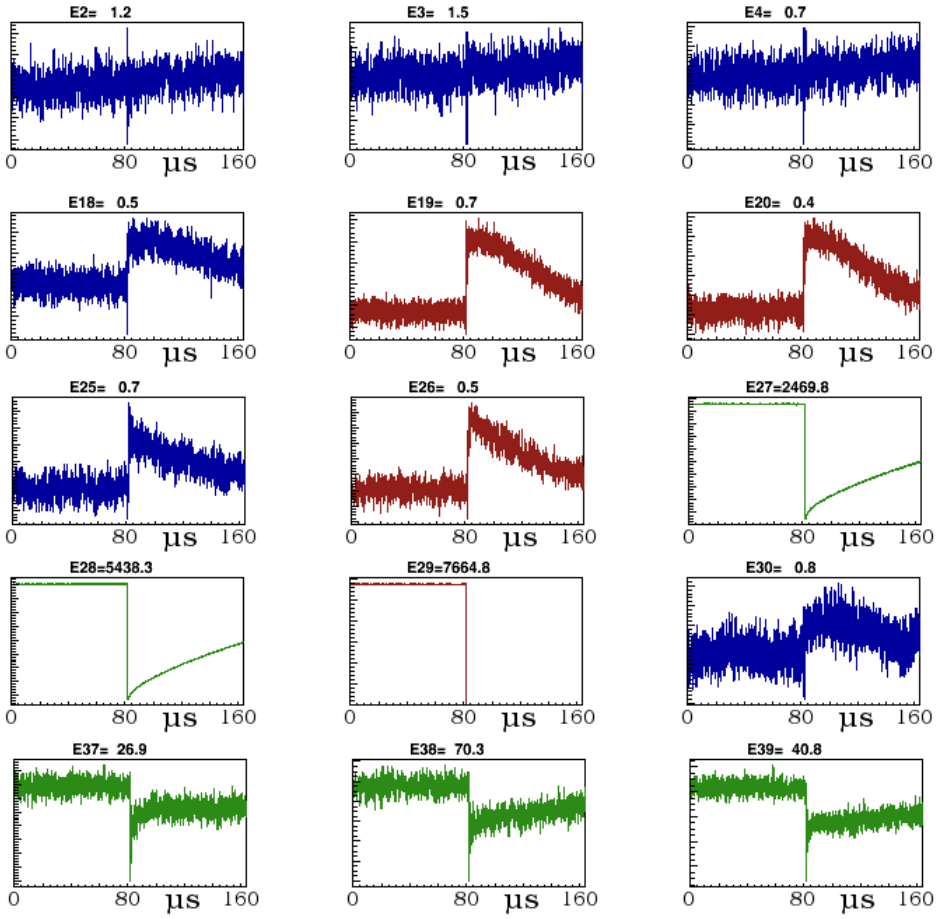

Figure 3.3: Example of strong cross-talk among the HPGe channels due to the interaction of a cosmic muon with six detectors (channels 27, 28, 29, 37, 38, 39). In this case no influence from the SiPMs is visible. The channels with no energy deposition show pulses with inverse polarity and oscillations at the time of the interactions. The channels with low energy signals, probably due to secondary γ, show a deformation of the pulses due to the influence of the cross-talk.

of the baseline level below the low limit of the range. In the first case, the pulse is physical but the energy cannot be properly reconstructed. Since the calibration of the energy scale relies on the fit of the 2.6 MeV line of ^{208}Tl, this energy is within the dynamic range during the whole data-taking. The saturated waveforms have energies well above the ones of the region of interest (ROI) and its side-bands, and can be excluded from the $0\nu\beta\beta$ analysis. They may nevertheless be relevant for the analysis of the high energy part of the data, especially above the α Po peak. If on the other hand, the baseline lies out of the dynamic range, the waveform must be discarded because aside from the uncertainty about the energy reconstruction there is no information about the baseline and the quality of the event cannot be assessed. This can occur when the leakage current of a channel decreases shifting the baseline position close to the edge of the dynamic range. In these cases, the detectors are excluded from the analyses until the following calibration. In the meantime, a manual intervention is needed to change the off-set of its FADC channel.

Cross-talk A strong pulse in a channel usually brings a fluctuation in the signals of the neighbouring channels. This effect is well known, and the effect of the distortion on the energy reconstruction for coincidence events have been quantified [94]. It is important that waveforms

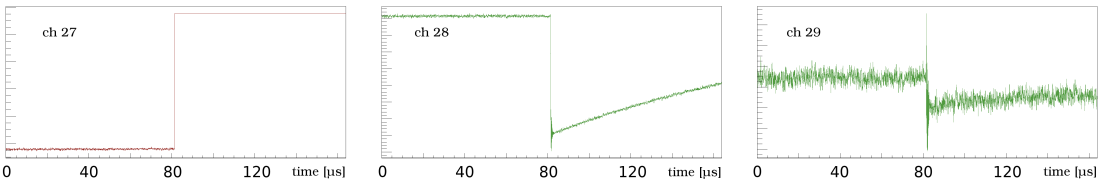

Figure 3.4: The left panel shows the discharge trace in channel 27 that induced a cross-talk signal in the two neighbouring channels, 28 (middle) and 29 (left).

distorted by the cross-talk of another HPGe channel are not rejected by the quality cuts. This would for example reduce the efficiency of the granularity background rejection (events with energy deposits in more than one HPGe are unlikely to be associated with $0\nu\beta\beta$). Figure 3.2 shows an example of the cross-talk induced on two channels by a 2.6 MeV signal; Figure 3.3 shows a more complex event produced by a cosmic muon with high energy interactions in several HPGe detectors.

Muons induced cross-talk Muons crossing the GERDA apparatus are efficiently tagged by the muon-veto. When the mouns interact with one or more germanium detectors they also release several MeV in the liquid argon thus producing scintillation light. The LAr veto is designed to trigger on a single photon to veto energy deposition of $\mathcal{O}(100$ keV) and the large amount of scintillation light of a high energy muon produces a very strong signal in most of the channels. Since the SiPMs are located rather close to the HPGe preamplifiers, such a strong signal can produce cross-talk between the devices. It follows that for a significant fraction of the muon induced events it is not possible to apply the normal signal processing (e.g. estimate the energy and the multiplicity of the event) due to the cross-talk distortion of the signals. All the events in coincidence with the muon-veto system are removed from most of the physics analyses, like the spectral fit for the background model and the $0\nu\beta\beta$ limit setting.

Pile-Up The low event rate of GERDA reduces the probability of random coincidence in the same detector to a negligible level. During the calibrations the rate is much higher and a significant fraction of the signals sit on the tail of the previous pulse. Most of these events could be recovered with standard filters widely used in γ spectroscopy. Nevertheless, in GERDA these are removed from the spectrum to avoid bias of the energy calibration and PSD techniques, which are then applied to pile-up-free physics data.

Micro-Discharges A high rate (5–10 mHz) of triggers induced by micro-discharges have been registered since the beginning of the Phase II data-taking. These micro-discharges occur along the high voltage (HV) lines, and it has not been possible to pinpoint the origin of the problem. Possible sources may be the HV cables, or sparks in the liquid Ar along the cables or the bonding wires. A discharge produces in one or more channels a strong and very fast jump in the charge signal with inverse polarity with respect to a physical event. These waveforms do not trigger the DAQ, exceed the dynamic range and can be easily rejected due to polarity. The other channels, and the neighbouring ones in particular, can show cross-talk pulses. Since the cross-talk is generally of opposite direction of the original pulse, the cross-talk of HV micro-discharges generates waveforms with the polarity of a physical signal and may trigger the DAQ. These waveforms have a well behaving baseline and the correct trigger position. Thus it is not possible to efficiently identify them as non-physical with a set of quality cuts based on the single waveform, like the one applied in GERDA Phase I. Figure 3.4 shows an example of three waveforms from a discharge event: the trace of channel 27 is obviously not physical because of the large amplitude with wrong polarity but the neighbouring channels show almost well behaving pulses with ringing induced by oscillations of the preamplifier due to the fast rise time of the leading edge.

3.2.2 Quality cuts

The increased rate of micro-discharges of Phase II required a novel design of the automatic check on the quality of the waveforms. In Phase I a series of quality cuts was applied to each waveform to select the ones with a physical energy deposition. For events with multiplicity 1, i.e. with energy deposition in only one detector of the array, the waveform of the fired channel would be accepted by the quality cuts while the ones of all the other channels would be rejected. In Phase II some of the waveforms induced by the cross-talk of the a micro-discharge can mimic a proper physical signal, but in every discharge event at least one channel registers a strong pulse with the wrong polarity. A good efficiency in the rejection of the micro-discharges can be achieved by moving from a waveform based set of quality cut to an event based system. This means that all the waveforms of the event must be considered to assess its quality. Every event with at least one waveform rejected by the quality cuts would then be discarded. This approach requires new sets of quality cuts in order to classify not only the waveform associated with a particle interaction but also the "empty" waveforms of the other channels. Moreover, any problematic channel must be removed from the analysis or it would potentially reject every event of the dataset. This is done by manually setting every non-working detector as "OFF" so that its waveform is not taken into account by the quality cuts. The reasons for which detectors have been marked "OFF" are: problems with the preamplifiers, low values of the bias voltage, or shifts of the baseline position at the edge of the dynamic range.

Some basic requirements must be satisfied by all the good waveforms of every class. The waveform must be correctly processed by the FADC and by each module of the GELATIO chain. Since the trigger position is set in the centre of the traces, the first half of each LF trace from 0 µs to 70 µs must be flat. This is verified through an exponential fit of the baseline, which identifies the signals sitting on the tail of a previous event. All the waveforms with a pulse with inverted polarity are rejected as micro-discharges. This is verified by running the `GEMDEnergyGauss` on the inverted trace and requiring an amplitude compatible with the noise level of the baseline.

Baseline waveforms (isBaseline) Baseline waveforms contain no signal. A well behaving baseline must therefore be flat and featureless. Since the electronic noise level can change over time and among detectors, for each waveform the RMS of the first 70 µs is computed and used as a reference to measure acceptable deviations. The position and RMS of four intervals are compared to verify the coherence of different parts of the waveform:

A. (0–70 µs), the reference;

B. (0–10 µs), the start;

C. (90-160 µs), post-trigger;

D. (150–160 µs), the end.

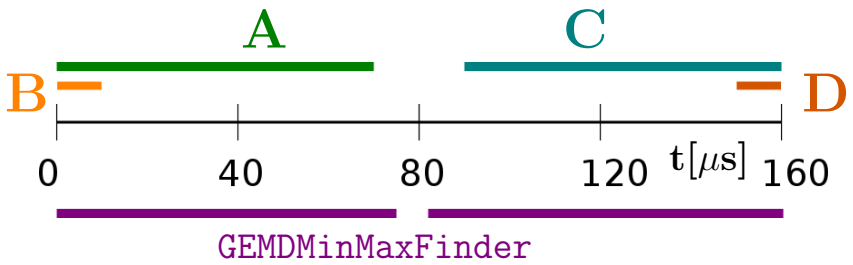

Figure 3.5: The scheme shows the four intervals (A, B, C, D) of the LF waveform on which the baseline parameters are computed. The `GEMDMinMaxFinder` searches for the minimum and maximum values around the trigger position.

In a baseline waveform, the difference between the average value of each interval and the reference one must be small in relation to the reference RMS. Moreover, no interval can have a RMS much bigger than the others. The maximum and minimum sample values of the waveforms are also compared with the RMS. Finally, the `GEMDEnergyGauss` filter running on the waveform with both polarities should reconstruct an energy value compatible with the noise level.

The classification of baseline waveforms can be complicated by the HPGe channels cross-talk. The quality cuts must accept distortions induced by neighbouring channels onto the baseline waveforms. In particular, these distortions can be significant in coincidence at the position of the trigger, in the centre of the trace. The central part of the trace (from 75 µs to 82 µs) is therefore excluded from the checks. The `GEMDMinMaxFinder` module registers the highest and the lowest amplitudes outside of the central interval. Figure 3.5 shows the intervals of the waveform that are analysed by `GEMDBaseline` and `GEMDMinMaxFinder`, to set the isBaseline flag.

The accepted thresholds for the baseline quality cuts have been set using two special calibration runs in which all channels were recorded; in normal calibration mode only the channels that trigger the DAQ are stored to save disk space. The values chosen provide a close to 100% acceptance of the 2.6 MeV peak from ^{208}Tl.

One BEGe channel (#23, crystal 79C) is connected to the same preamplifier of three enriched semi-coaxial detectors. Thus it shows much higher levels of cross-talk due to the difference in capacity between BEGe and semi-coaxial detectors. The requirements on the baseline quality cuts for this detector have been loosened to account for the higher cross-talk.

$0\nu\beta\beta$ analysis (isPhysical) The physical events which are shown in any GERDA spectrum must have one, and only one, pulse in the waveform and all parameters must be computed properly. Hence only one trigger can be found by the `GEMDFTTrigger` module and this must be at centre of the waveform (77 µs $< t.p. <$ 84 µs). The energy reconstructed by the `GEMDEnergyGauss` filter must be related to the amplitude of the waveform at the trigger position. The 10-90% rise time of the leading edge must be no faster than 70 ns, and no slower than 5 µs. Since the `GEMDRiseTimeLF` it is not reliable at extremely low energy, this requirement is dropped for signals with amplitudes similar to the baseline RMS (E$<<$ 100 keV).

Saturated waveforms (isSaturated) For waveforms which saturate the dynamic range, the requirements are relaxed. The waveforms are tagged as saturated by the FADC and some of the GELATIO modules may fail. The minimum 10-90% rise time is lower then 40 ns because only part of the leading edge is available, hence it is not possible to compute the time when the signal reaches 90% of the amplitude. The position of the maximum of the `GEMDEnergyGauss` can be delayed by the lack of the decay tail in the saturated portion of the waveform.

Calibration (is0vbbFromCal) In order to better suppress pile-up events in calibration, stronger requirements are applied to the first 70 µs of the baseline. In particular, the requirement on the exponential fit of the baseline is 5 times stronger than for the isPhysical flag. Moreover, the RMS of the baseline is compared with the value computed on the first 10 µs to reject waveforms with small pre-trigger energy deposition.

3.3 Efficiency

Due to the high rate of HV micro-discharge, the quality cuts remove a significant fraction of the recorded data. This brings two obvious risks: non-physical events could be accepted (false-positive) and pollute the spectrum; or good events could be rejected (false-negative) reducing the overall efficiency for $0\nu\beta\beta$.

There is no evidence of contamination of non-physical events in the analysis datasets. All the features of the spectrum are understood and can be reproduced by the background model fit of all components above $\sim$ 500 keV [95]. All events (about 2000) with energy above 1.6 MeV recorded

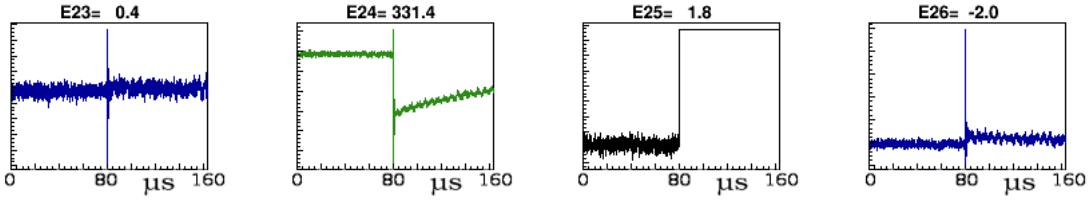

Figure 3.6: Discharge induced events passing the quality cut. The event was recorded on June 25, 2016 at 4:11:36 (Time-Stamp: 1469419896).

in the first six months of data-taking, until the first unblinding of June 2016 have been visually inspected to guarantee that none appears to be non-physical. For the data acquired between June 12, 2016 and December 18, 2017, the waveforms of the events with energy between 1.6 MeV and 3 MeV (about 2000 events) have been visually inspected; no clear spurious event was found.

Only one discharge induced event not removed by the quality cut was found. It was induced by a discharge occurring in a channel tagged as "OFF", thus not considered by the quality cuts. The channel was set "OFF" for a short time (June 21-27, 2016) because the position of the baseline drifted too close to the edge of the dynamic range. A discharge along the HV line of this channel induced a cross-talk signal in the adjacent channel, see Figure 3.6. The reconstructed energy of the cross-talk signal is ~ 300 keV.

Test Pulsers (TP) and Baseline (BL) events are used to estimate the rate of false-negative, i.e. physical events discarded by quality cuts. The rate of rejected TP corresponds to the probability of failure of the flag isPhysical. It also includes the rate of random coincidences.

The probability of failure of the isBaseline flag is extracted from the rate of rejected baseline events. The events tagged by the FADC as "not wrapped" are not taken into account because these are induced by the coincidence with another trigger from the TP or a physics events. The rate of random coincidences with physics events is already accounted for the TP efficiency and the rate of coincidence between the TP and the BL is not relevant for the signal acceptance.

The first two runs of Phase `II` have been particularly unstable with many detectors excluded from the analysis. The data taken until January 29, 2016 have therefore been excluded from the TP and BL efficiencies. Moreover, every detector marked as OFF and therefore not considered by the quality cuts was also excluded.

The dataset contains about 2 million TP events with 93 million TP waveforms and about 1 million baseline events with about 40 million recorded waveforms. A $0\nu\beta\beta$ event would be composed of 1 waveform with a physical signal relative to the fired detector and baselines in all other channels. The probability of accepting a $0\nu\beta\beta$ event is therefore the combination of the efficiency for a single TP waveform combined with the efficiency for BL events. Of over 93 million recorded TP waveforms, 12 thousand were rejected, this corresponds to a waveform efficiency $P_{TP} = 99.987(1)\%$. Of over 1 million recorded BL events (with ~ 40 waveforms), 734 were rejected corresponding to an event efficiency $P_{BL} = 99.930(3)\%$. The acceptance for $0\nu\beta\beta$ events therefore is:

$$P_{0\nu\beta\beta} = P_{TP} \cdot P_{BL} = 99.918(3)\%. \tag{3.1}$$

This is negligible in comparison to the total signal efficiency of GERDA which varies from 48% (semi-coaxial) and 60% (BEGE) [51].

3.4 Micro-discharges

The recorded micro-discharge events can be identified by the presence of a signal with inverted polarity in at least one channel. Figure 3.7 shows the time distribution of such events. In the first part of the data-taking their rate varied between 5 mHz and 10 mHz. In October 2017 the trigger threshold was lowered by almost 90%, from ~ 150 keV to ~ 16 keV; since then the rate

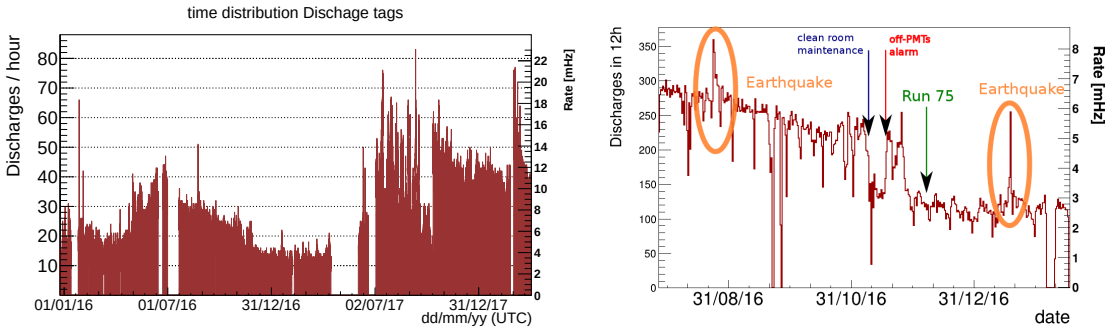

Figure 3.7: Rate of recorded micro-discharge events. The plot on the left shows the rate (events per hour) over a 2 year period 2016-2017. The plot on the right side shows the peaks in the rate corresponding to the days of the strongest earthquakes.

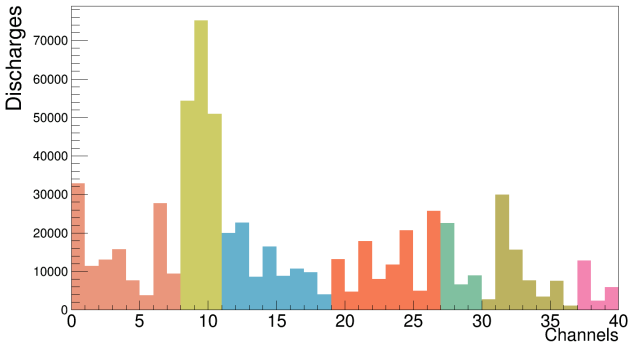

Figure 3.8: Channel distribution of the inverted polarity signals for micro-discharge events.

of discharges that trigger the DAQ was consequently increased (about 26 times). The rate often increases after the bias voltage value of one or more detectors is modified. It slowly decreases when the system operates smoothly without interferences, as can be seen in the period between summer 2016 and summer 2017. In this period some earthquakes hit the Gran Sasso region. Increase rates of micro-discharges can be observed in the days of two of the strongest quakes (August 24, 2016 and January 18, 2017), see the left plot in Figure 3.7.

It can be assumed that the micro-discharges happened on the HV-lines of the channels that show strong inverted signals. Figure 3.8 shows the distribution of these channels for the recorded events. It must be considered that only the events that trigger the data acquisition are recorded; any micro-discharge that does not induce a strong cross-talk pulse in the other channels is not. This could explain the relative high count rates in the second string (channels 8,9,10) that contains semi-coaxial detectors with stronger cross-talk; however, the other two semi-coaxial (channels 17,18,19, and 37,38,39) strings do not show high count rates. Overall, all strings and channels seem to be affected by the issue, no channel is immune.

3.5 Physics data

After every three hours of data-taking, a file is closed and processed. The output of the digital signal processing described in Section 3.1 is saved in a secondary file (tier2). The third file produced (tier3) contains the quality cuts flags, LAr and muon veto flags, and calibrated energy, Once the data have been processed, a series of automatic scripts produces a set of monitoring plots that are checked daily. These plots provide basic information on the status of each detector (HPGe, SiPM and PMT); such as position and RMS deviation of the baselines, and trigger rates. One of these

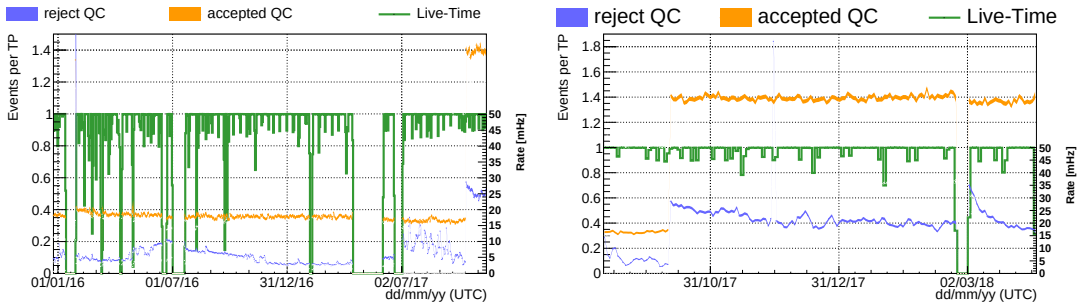

Figure 3.9: Quality cuts monitoring plot. Plots like these are produced daily to monitor the data-taking. The green graph provides the live-time fraction and is computed as the ratio of recorded versus the expected test pulser events. The orange band reports the count rate of the (physical) events accepted by the quality cuts, this is normalised on the number of recorded TP and assuming a live-time close to 100%, it can be converted into rate per second (y-scale on the right). The blue band corresponds to the rejected events rate, mostly due to micro-discharges.

plots, shown in Figure 3.9 for the first 2 years of Phase II, reports the rate of different classes of events according to the quality cut flags. In the plot the live time is computed as the ratio of the accepted over expected TP events. The rates of accepted and rejected events are also shown in relation to the number of expected TP, set at 50 mHz (1/20 s). The rate of rejected events is one of the main diagnostic tools to identify issues with the data-taking. Its value is mostly driven by the rate of micro-discharges that constitutes the majority of the rejected events. The rate of physical events accepted by the quality cuts depends on the number of active detectors and the background level. In the first year, a slight decrease can be observed, from $\sim$ 20 mHz to $\sim$ 18 mHz. During the first run in January 2016 one detector was OFF due to high leakage current values and it can be seen in the plot how the rate of physical events increases (from $\sim$ 19 mHz to $\sim$ 20 mHz) once this was recovered. A similar small drop in the rate can be observed after the summer of 2017, since during some operations on the system, one HPGe channel was lost due to a burned JFET. In the last part of the plot both rates increase due to the lowering of the trigger energy threshold.

The rate of physical events can also be analysed considering the energy of the events. The plots in Figure 3.10 show the count rates for different energy intervals. Already before any PSD or LAr veto, the rate around the ROI is on the level of $2.5 \cdot 10^{-2}$ cts/(keV $\cdot$ kg $\cdot$ yr) even considering a wider interval than the one where the official GERDA B.I. is computed. This interval, from 1.55 MeV to 3.0 MeV, includes a larger contribution from the $2\nu\beta\beta$ spectrum and also some weak γ-lines which are excluded from the B.I. computation. The last plot shows the rate of high energy events, mostly connected to α decay on the detector surfaces. It is clear that this rate is decreasing over time indicating that most the α contamination is due to ^{210}Po on the α-sensitive surfaces. A fit of the time distributions of the counts in the range (3.5, 5.25) MeV, shows that the behaviour is well described by the 138 days decay time of ^{210}Po and that an additional component with about 1 cts/day is present in each dataset (enriched BEGE, enriched semi-coaxial and natural detectors)[96]. The constant component of the α background is mostly attributed to ^{210}Po supported by ^{210}Pb on the detector surfaces and impurities of the LAr.

Figure 3.11 shows the energy spectrum resulting from the application of the quality cuts. The grey spectrum shows the reconstructed energies of the un-physical events rejected by the quality cuts. Since these events are mostly connected with cross-talk of micro-discharges, the value of the reconstructed energy is not a well defined quantity and varies according to the energy reconstruction method applied. The most evident structures are several bumps above 6 MeV where the saturated events of the different channels are reconstructed. The blue spectrum shows the energy spectrum of the events accepted by the quality cuts before PSD and LAr veto. The structures at low energies (E<300 keV) are due to the non-uniform energy threshold in time and among the 40 channels. The first physical structure at low energy is the β-spectrum of the ^{39}Ar decays in the proximity of the detectors. The ^{39}Ar β-decay has a Q-value of 565 keV and part of the energy is lost in the

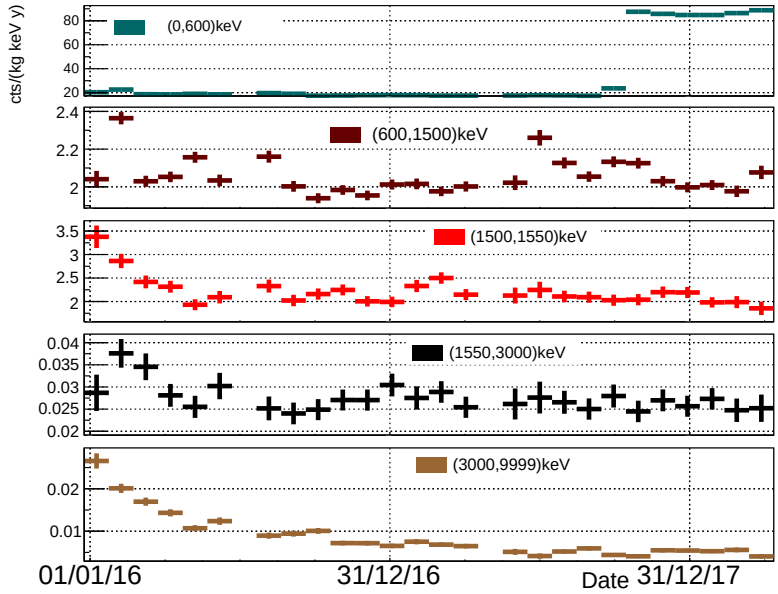

Figure 3.10: Event rate for different energy intervals. This plot is produced automatically by the monitoring tools. The top panel shows the low-energy (E<600 keV) rate, these counts mostly come from the ^{39}Ar β-spectrum. The increase of the rate at the end of 2016 corresponds to the shift of energy thresholds to about 10% of the previous values. The second panel shows the count rate in the interval (600,1500) keVdominated by the $2\nu\beta\beta$ spectrum. The middle panel shows the count rate of a narrow 50 keV interval containing the two main γ-lines of the spectrum, from ^{40}K and ^{42}K. The fourth panel displays the raw count-rate in the region containing the ROI, it shows that prior to any active background rejection, the count rate is at the level of 10^{-2} cts/(keV $\cdot$ kg $\cdot$ yr). The last panel shows the count rate from high energy events (E>3 MeV) due α decay on the detector surfaces; note that the y-axis starts at about $5 \cdot 10^{-2}$ cts/(keV $\cdot$ kg $\cdot$ yr).

thick n+ layer, therefore the end-point is below 500 keV. At higher energies the $2\nu\beta\beta$ is the main component and the shape of its spectrum defines the global spectrum between 500 keV and 2 MeV. The two strongest γ-lines are from ^{40}K at 1.46 MeV and from ^{42}K at 1.52 MeV, their Compton shoulders and Compton continuum are visible above the $2\nu\beta\beta$ spectrum in the region between 500 keV and 1.3 MeV. Between 1.5 MeV and 2.6 MeV a few weak γ-lines are visible, most notably 1.76 MeV from ^{214}Bi and 2.614 MeV from ^{208}Tl. The ROI is included in the blinding window, marked yellow on the plot. Above this energy the spectrum is dominated by the α decay on the detector surfaces.

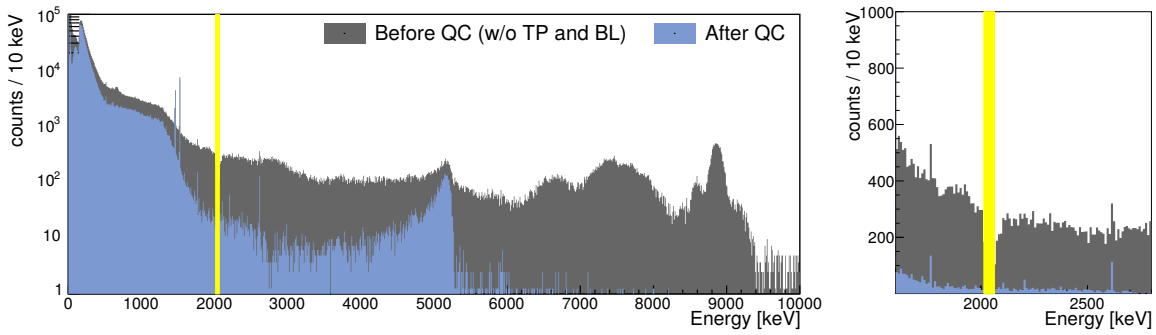

Figure 3.11: GERDA Phase II spectrum. The blue histogram is the energy spectrum of the events accepted by the quality cuts, before PSD and LAr veto. The grey spectrum shows the energy attributed to the rejected events by the energy reconstruction algorithm.The yellow region is the blinding window around the ROI.

Chapter 4

Pulse shape discrimination for BEGe detectors

The core of the GERDA experiment is the array of high purity germanium detectors. While the semi-coaxial detectors represent the key-stone of Phase I, the results of GERDA Phase II are largely driven by the Broad Energy Ge (BEGe) detectors. This is mostly due to their superior pulse shape analysis (PSA) potential for background discrimination. While the general principles of HPGe detectors and their signal formation are discussed in Chapter 2, this chapter focuses on the pulse shape analysis of BEGe detectors. Section 4.1 illustrates the signal formation and the GERDA PSA technique for BEGe detectors. The calibration process for the A/E analysis is described in Section 4.2. This section also reports on the performances of the first BEGe detectors deployed in Phase I. The discrimination of background induced by external β decays is addressed in Section 4.3. The response to this class of events has been studied with measurements and Monte Carlo simulations of detectors in vacuum cryostats and in liquid argon, also by enhancing the ^{42}K count rate with argon enriched in ^{42}Ar. This chapter summaries the development of the A/E analysis performed by many GERDA collaborators, such as D. Budjáš [97], M. Agostini [81], B. Lehnert [98], and V. Wagner [99] along with my original contributions in particular on the calibration of the PSD for GERDA Phase I (Section 4.2), ande the estimation of the potential surface event rejection (Section 4.3 and Section 4.4).

4.1 The A/E parameter

As discussed in Section 2.1, the detectors produced by the GERDA collaboration are custom designed BEGe detectors. This particular design was chosen after the first tests with prototype detectors showed the possibility of rejecting Multiple Site Events (MSE) with a mono-parametric analysis, the A/E Pulse Shape Discrimination (PSD) [100, 101]. The study of the signal formation for these detectors [102] showed that they present a peculiar weighting potential (Figure 4.1) with values close to zero in most of the active volume, i.e. about 90–95%. For interactions occurring in this weak weighting potential volume, the electron contribution to the induced signal is negligible. Most of the charge is therefore induced by the hole cluster once it reaches the proximity of the small p+ electrode.

The effective electric field of a generic BEGe detector is shown in Figure 4.3. In an important fraction of the crystal volume, the field produced by the net impurities concentration is stronger than the field of the electrodes. Holes produced in the periphery of the detector are pulled towards its centre by the distribution of negatively ionised acceptors. Without the contribution of the impurities, the electric field would be too weak to collect the charges before their recombination. Once the holes reach the centre of the crystal, they are pulled by the field of the cathode which here is stronger than (and opposite to) the one of the impurities. The fact that the holes approach the cathode from the centre of the detector implies that they cross the volume where the weighting

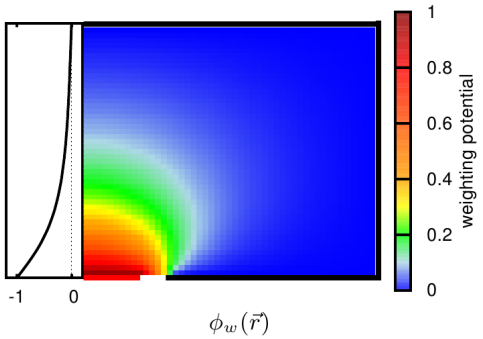

Figure 4.1: Weighting potential of a BEGe detector. Figure from [102].

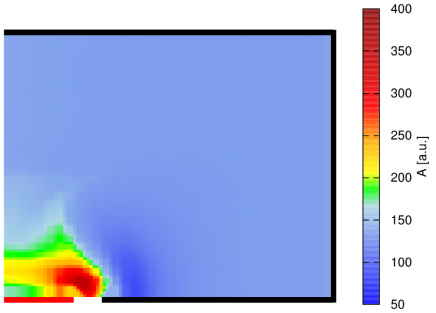

Figure 4.2: Map of the amplitude of the current signal (A) for events of given energy. Figure from [102].

potential is significant, moving almost vertically. Since the electrons' contribution is negligible and the holes approach the cathode with similar trajectories, all interactions occurring far from the p+ electrode induce signals with similar shapes.

The GERDA experiment searches for $0\nu\beta\beta$ events inside the germanium crystals. Only two electrons are emitted by the process and they share the 2039 keV of available kinetic energy. Due to the short range of 1–2 MeV electrons in Ge (about 1 mm) and to the low probability of bremsstrahlung emission ($< 10\%$), the two e^- typically release their energy in a single location in the crystal (within a radius of 1–2 mm). The $0\nu\beta\beta$ events are therefore mostly single site events (SSE) and in BEGe detectors all the $0\nu\beta\beta$ decays that happen far enough from the electrodes produce the same signal shape.

The events induced by γ rays are likely to interact in several locations at once, producing MSE. There are three processes through which photons interact with matter: photoelectric effect, Compton scattering and pair production. The cross-section of the photoelectric effect is small for high energy photons (> 1 MeV). After a Compton scattering, the γ may interact in a new location within the same crystal producing a MSE, it may be detected by another detector (HPGe or LAr veto) producing a coincidence, or it can escape detection carrying away part of the primary photon energy. The pair production can only occur for energies above the 1022 keV threshold. In this case, the γ is fully absorbed by the interaction and the kinetic energy of the electron-positron pair is typically released within a few millimetres. The positron then undergoes annihilation and emits two 511 keV photons that can travel for centimetres inside the crystal and release more charge carriers in one or two sites apart from the original pair production location. In the case that both 511 keV photons escape the crystal, the event would be a SSE with energy equal to the incoming γ energy minus 1022 keV. These events are referred to as Double Escape Peak (DEP) events and can be used as a control sample of SSE to calibrate and test pulse shape discrimination techniques. It must be noted that the DEP are not uniformly distributed in the crystal, the 511 keV photons are emitted back to back hence the probability of a DEP is higher near the edges of the crystal. The small height of the BEGe, ~ 3 cm, mitigates this issue with respect to bigger semi-coaxial detectors. In a Single Escape Peak event (SEP), one of the two annihilation γ escapes the detector carrying away all its energy and the other is fully absorbed. In this case the total energy is deposited in at least two locations by the $e^- - e^+$ pair and by the 511 keV γ. All the SEP events are therefore MSE for which about a quarter of the total energy has been carried away from the primary interaction by a 511 keV photon.

The signal of a bulk-SSE starts with the low current generated by the charges moving through the region with a quasi-null weighting field (this part of the signal is often covered by electronic noise) and then a single current peak when the cluster of holes approach the cathode. The ratio

between the peak amplitude of the current signal (A) and the amplitude of the charge signal (E, energy of the event) is constant for all the SSE generated far enough from the electrodes, see Figure 4.2. In relation to the energy of the event, the A/E ratio is in first approximation constant. Second order differences, on the 0.1% level, are due to the larger cluster size of high energy events and to the impact of the electronic noise on lower energetic ones.

Figure 4.4 shows the distribution of the A/E parameter for the spectrum of a ^{228}Th calibration source. This is the reference spectrum used to calibrate the A/E PSD since three ^{228}Th sources are installed in the GERDA cryostat for energy calibration. The SSE band is the region that contains all SSE and therefore all $\beta\beta$ signals but in the case of a ^{228}Th spectrum, like the one depicted in Figure 4.4, it is mostly populated by single Compton scattering events. The single Compton scattering events extend up to the Compton shoulder of the 2.6 MeV line. The main features of the SSE band are a small downward slope and the increased width at low energies (below 1 MeV). The width of the band represents the A/E resolution of the set-up and for optimal data from vacuum cryostats it can be as good as 1% FWHM at the energy of the DEP (1592 keV). The level of electronic noise, especially at high frequencies, can disturb the measurement of A, reducing the A/E resolution. For this reason the A/E analysis is usually applied only above 1 MeV, where the resolution is similar to the one of the DEP energy. It can provide useful information even at lower energies but in this case the widening of the band at lower energies must be taken into account [103].

The events connected to interaction in the region of the p+ electrode can be found above the SSE band. This region includes about 5% of the volume of a BEGE, depending on the size and the geometry of the crystals. Pairs of charge carriers produced in this region do not comply with the signal formation model of the bulk volume. In these cases also the e^- contribute significantly to the signal formation, since they start their trajectory in the proximity of the readout electrode. The superposition of the mirror charges induced by the e^- and by the h^+, moving simultaneously in the region with strong weighting potential, produces signals faster than the SSE. The amplitude of the current pulse can be up to twice as high as the one of a SSE, if the interaction occurred in the middle of the high weighting potential region. In this case, the charge carriers moving in opposite directions will cross this region in half the time it takes the holes that originated in the bulk to cross it moving towards the cathode. The discrimination of the p+ Contact Pulses (PCP) removes the surface events from the p+ region (readout contact and groove), which is the only

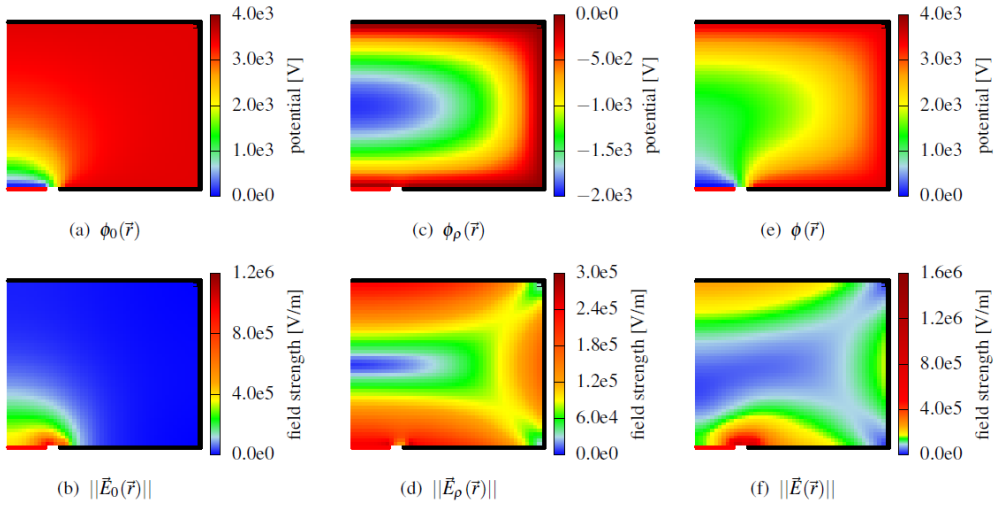

Figure 4.3: Electric potential of a BEGE detector as the sum of the components induced by the bias voltage (top left) and the intrinsic component due to the net impurity charges (top centre) and their sum (top right). The bottom row shows the field strength of the two components and their sum. Figure from [102].

part of the detector sensitive to external α decays. This possibility has been studied with the use of a collimated ^{241}Am placed inside the detector vacuum cryostat, see Chapter 6 of [81].

The MSE have lower A/E values than SSE and populate the lower region of the plot in Figure 4.4. The Full Energy Peaks (FEP) signals are distributed in the region below the SSE band. A tilted band of events connects the DEP at 1592 keV with the SEP at 2103 keV. This band is populated by events in which one of the 551 keV photons escape the detectors after having released part of its energy, while the second does not interact in the detector at all. The DEP counts are concentrated in the SSE band due to its high fraction of SSE.

Part of the events right below the SSE band is constituted by n+ Surface Events (NSP) and, especially at high energy, by soft bremsstrahlung events. In the first case, the signal is slowed down by the less efficient charge collection from the detector surface region. This reduces the amplitude of the current signal and therefore the A/E value. The bremsstrahlung radiation reduces the A/E by carrying part of the energy farther from the primary interaction location.

4.2 Pulse shape analysis for BEGe in Gerda Phase I

The calibration procedure was first described in [100] and later improved for the needs of GERDA Phase I [67] and Phase II [99]. Working on Phase I BEGE dataset as part of the analysis team, I contributed to the application of the PSD to the first BEGE string and in particular to the implementation of the Compton continuum A/E fit.

The A/E PSD is calibrated on the emission of the ^{228}Th. The DEP at 1.592 MeV/ is used as a substitute for the $\beta\beta$-decay. To account for the energy difference between the $0\nu\beta\beta$ and its proxy, the energy dependence of the A/E value for SSE is estimated using the A/E distribution of Compton continuum events from the 2.6 MeV ^{208}Tl line.

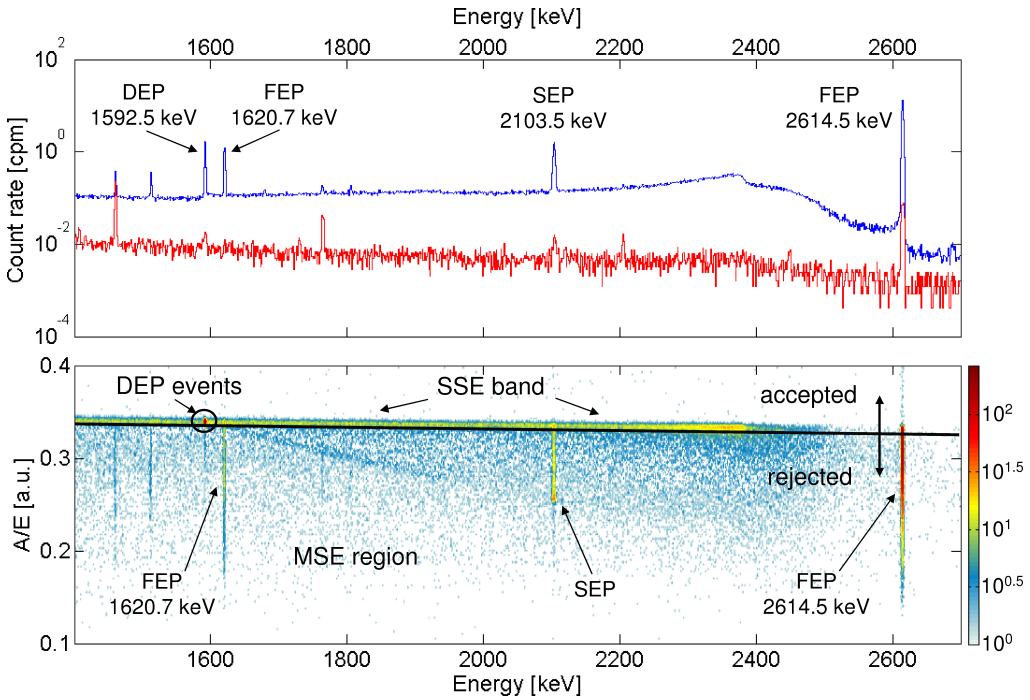

Figure 4.4: Distribution of the A/E parameter for a ^{228}Th spectrum acquired by a BEGE detector in a vacuum cryostat. The top panel shows the ^{228}Th energy spectrum compared with a background measurement, the bottom panel shows the distribution of the A/E parameter and its main features. Figure from [100].

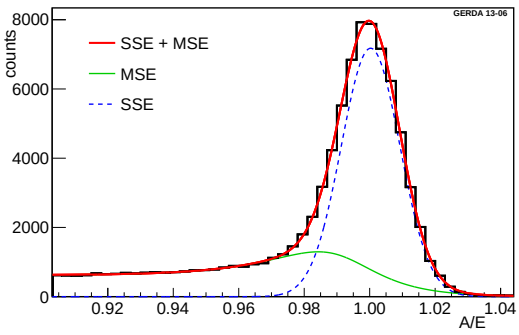

Figure 4.5: Fit of the A/E distribution for a Compton continuum interval. Figure from [67].

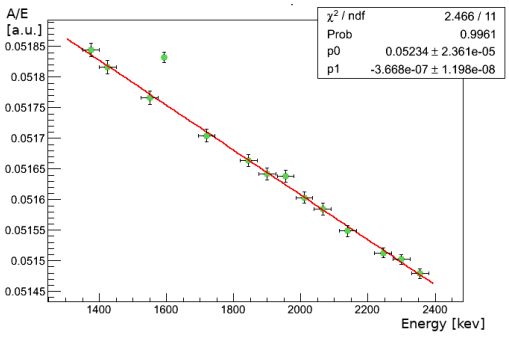

Figure 4.6: Linear regression of the SSE position at different energies for GD32C (Channel 10) in GERDA Phase I relative to the data from September 3 to October 11, 2012.

Events from the Compton continuum can be SSE if the γ escape the detector after a Single Compton Scattering (SCS), or MSE in case of multiple Compton scatterings. The ratio between these two classes depends on the geometry of the detector and the deposit energy but for BEGE detectors the SSE are between 30% and 50%. Figure 4.5 shows the A/E distribution for a 50 keV energy interval populated by Compton continuum events. The SSE are distributed in a narrow Gaussian (around 0.051) while the MSE have a much broader distribution on the left of the SSE band. The distribution of the MSE can be fitted with an exponential tail. An additional MSE component is associated to SCS events whereby the secondary electron produces bremsstrahlung, that can carry part of the deposited energy a few millimetres away from the location of the primary interaction. These events have slightly lower A/E values, thus they deform the left side of the SSE Gauss distribution. Moreover, the bremsstrahlung probability varies with the energy of the electron and therefore the deformation of the Compton continuum distribution is stronger at higher energies.

The position of the SSE band is extracted from the fit of the Compton continuum distribution performed with the following empirical function:

$$f(x) = \frac{n}{\sigma \cdot \sqrt{2\pi}} \cdot e^{\frac{(x-\mu)^2}{2\sigma^2}} + m \cdot \frac{e^{v\cdot(x-l)} + d}{e^{(x-l)/t} + l}; \tag{4.1}$$

where μ, n, and σ are the mean, integral, and standard deviation of the SSE Gaussian term; while m, v, l, d, and t are the parameters of the MSE empirical description. The energy dependence of the SSE band is then computed with a linear regression of the Gaussian positions of the A/E distributions in several Compton continuum intervals, see Figure 4.6.

Once the position of the SSE band has been established, it is possible to select only this type of events by rejecting events with lower A/E (MSE and NSP) or higher A/E (PCP). In GERDA, the threshold of the A/E cut is based on the acceptance of the DEP population. The low A/E cut is set to include a fixed percentage of the DEP, usually 90%. The high A/E cut is defined in relation to the lower one and it is set twice as far from the centre of the SSE band.

Typically, a cut with 90% acceptance of DEP reduces the number of counts in the FEP to about 10–15%, the number of counts in the SEP of the 2.6 MeV line to 5–10%, and the counts in the Compton continuum at 2 MeV to about 40–50%. All the survival probabilities are affected by the electronic noise level which can reduce the A/E resolution, and by the detectors' geometry which can alter the ratio between SSE and MSE.

During the GERDA data-taking, energy calibrations are performed on a bi-weekly basis, with additional calibrations for any hint of instabilities such as energy shifts of the test pulser signals. The fit of the A/E distribution of the Compton continuum regions required more data than the fits of the peak for the energy calibration. Therefore, several consistent calibrations are merged to fit the energy dependence of the SSE and to determine the cut level with the required DEP

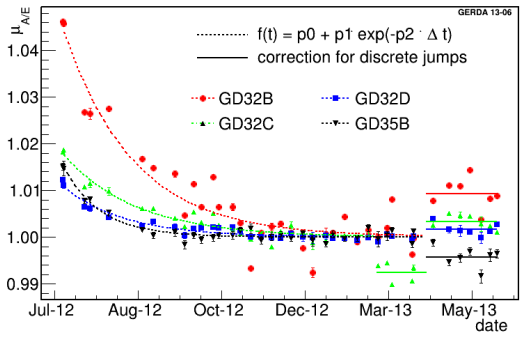

Figure 4.7: Drift of the A/E position over the course of Phase I. The plot shows the mean of the DEP distribution Gaussian fit for different ^{228}Th calibrations. The A/E value is normalized to set $p0 = 1$. Figure from [67].

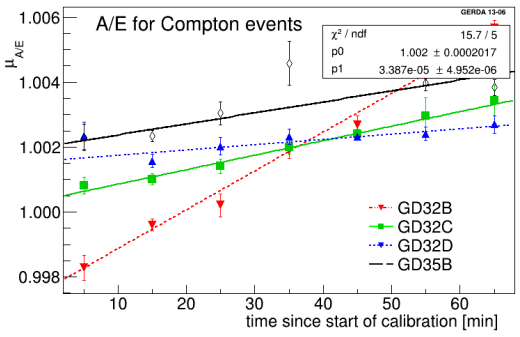

Figure 4.8: Average drift of the DEP A/E value in the first hour of calibration. Data from all Phase I calibrations have been combined after the correction for the long term drift. Figure from [67].

acceptance. The value of the A/E for DEP events and the acceptance of events with a different topology (FEP, SEP, Compton continuum) is monitored for each individual calibration to identify instabilities of the set-up.

During Phase I, two drifts of the A/E value have been observed. One drift towards lower A/E values has been observed over the course of the first months of data-taking. Figure 4.7 shows the positions during the data-taking time. This drift has an effect of 1% to 5% on the A/E value for the DEP. An additional short term drift has been observed during the calibrations with ^{228}Th sources, see Figure 4.8. An increase of about 1% of the A/E mean values was recorded during the first hour of exposition to the sources. The A/E then reverted to the previous values in the 24 hours following the calibration. The recovery was monitored through a comparison between the events in the range 1.0–1.3 MeV in the calibration (Compton continuum) and in the physics data (mostly $2\nu\beta\beta$). These drifts are likely connected to the presence of ions on the surfaces of the groove. Their charge can influence the capacity of the detectors and therefore the value of the A/E.

The short term drift during the calibrations was fitted with a linear regression to extrapolate the A/E position of the SSE band before the irradiation. The long term drift was fitted with an exponential function to interpolate the position of the SSE band in between calibrations. The detector grooves have been reprocessed after the end of Phase I and no drift has been observed in GERDA Phase II.

One of the five BEGE detectors deployed in Phase I was excluded from the analysis due to instabilities. Overall 2.4 kg·yr of exposure were analysed with a signal efficiency of $66\% \pm 2$. The PSD $0\nu\beta\beta$ efficiency was $92\% \pm 2$ and this value was found to be compatible with the acceptance of the $2\nu\beta\beta$ spectrum between 1.0 MeV and 1.45 MeV. Figure 4.9 shows the A/E distribution of the events, the asymmetric cut thresholds were set at 96.5% and 10.7% of the DEP mean A/E value.

Figure 4.10 shows the spectrum of the BEGE dataset. The count rate around the $Q_{\beta\beta}$ is strongly suppressed. In the 400 keV region around the $Q_{\beta\beta}$, 33 events out of 40 are rejected. The background index computed in a 230 keV window, under the assumption of a flat background distribution, is reduced from $42 \cdot 10^{-3}$ cts/(keV · kg · yr) to $5^{+4}_{-3} \cdot 10^{-3}$ cts/(keV · kg · yr).

4.3 Rejection of surface pulses

The A/E pulse shape analysis was developed to reject MSE from γ background. It was then noticed that it is possible to use the same technique to discriminate events generated by energy deposition on the detector surface, for example the ones induced by external β decays. The vast majority (96–98%) of the BEGE surface is covered by the n+ electrode converts. Here, the infused lithium atoms penetrate about 0.5–0.9 mm below the crystal surface [98].

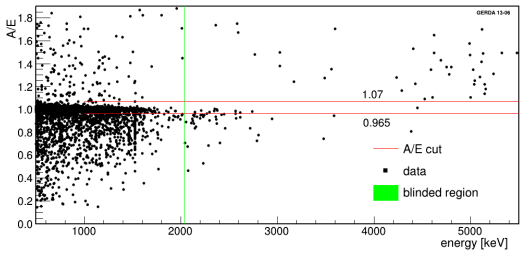

Figure 4.9: Distribution of the A/E parameter in BEGe data of GERDA Phase I. The data from four detectors have been re-scaled to their DEP mean values. The events in the range 0.965–1.07 (red lines) are accepted. The green band covers the region of interest (ROI) for the blinding analysis. Figure from [67].

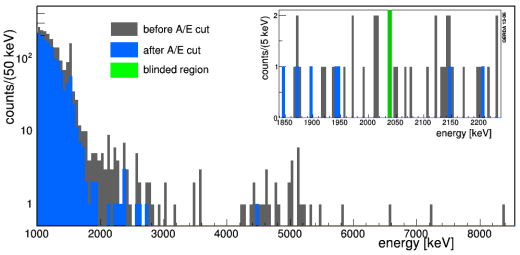

Figure 4.10: Energy spectrum of GERDA Phase I BEGe dataset. The low energy part of the spectrum is compatible with 90% acceptance of the $2\nu\beta\beta$ events. The PSD reduces the background index more than 8 times to the value of $5 \cdot 10^{-3}$ cts/(keV · kg · yr). Figure from [67].

For the purposes of γ-spectroscopy it is often assumed that the diodes are divided in two parts: the active volume and the inactive outer layers. This assumption holds for measurements of γ peaks and for the estimation of their detection efficiency. The investigations of non-discrete features (such as peak to Compton ratio, and the β decay energy spectrum) reveal the presence of a region from where the charges are partially collected. The partial charge collection results in an under-estimation of the energy released in the crystal. An additional transitional volume must therefore be considered between the active bulk and the inactive outer layer.

The empirical model (from Chapter 8 of [98]) that describes the charge collection in the proximity of the n+ surface is shown in Figure 4.11; the crystal volume is divided into the following parts:

- fully active volume (FAV), where the electric field intensity is enough to collect all charges;
- transition layer (TL), where the charges are partially collected;
- dead layer (DL), where the Li doping level is too high to allow for the collection of the holes.

The distance of the FAV from the crystal surface is called full charge collection depth (FCCD). The profile of the charge collection efficiency in the TL is assumed to be linear. This assumption provides a qualitative understanding of the charge collection mechanism. For a quantitative description the profile has to be tailored to the individual detectors, using dedicated measurements of radiations with low penetration power such as the 59 keV ^{241}Am photons.

In the transition layer the electric field is too weak to attract the holes towards the cathode. When a cluster of charge carriers is created in the transition layer, their motion is dictated by diffusion. The holes diffuse until they recombine into the valence band or until they reach the active volume where they are attracted by the cathode. Since the diffusion is isotropic, only a fraction of the holes produced in the transition layer will eventually enter the active volume. Moreover, this fraction is smaller for holes produced farther from the active volume (closer to the crystal surface). Since the holes move faster in the FAV than their diffusion speed in the TL, a cluster of holes crossing from the TL to the FAV stretches along the direction of the field line. This results in slower pulses for which the full charge collection can last up to a few µs. The charge collection can be longer than the integration time of energy filters which are optimised on events of known energy from γ-peaks. In this case, part of the charge that reaches the cathode is not considered in the reconstructed energy. The energy of NSP is therefore a not well defined quantity, since the energy assigned by the signal processing filters is lower than the energy released in the crystal and greater than the energy released in the active volume.

In Chapter 8 of [98] the thickness of the FCCD and of the TL for all GERDA BEGe detectors has been estimated. The measurement is based on the empirical model from Figure 4.11 and the

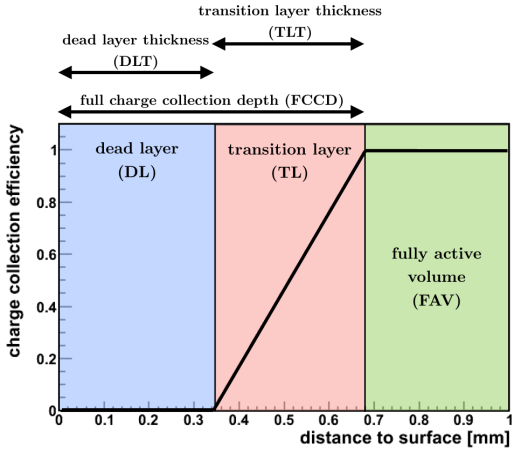

Figure 4.11: Empirical model of the charge collection efficiency in the proximity of the n+ surface. Figure from [98].

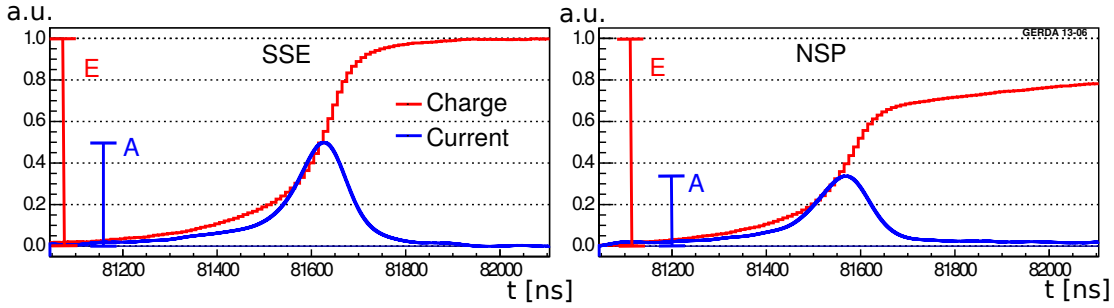

Figure 4.12: Comparison between a n+ surface pulse (on the left) and a single site event pulse (on the right). The blue signals are the charge pulses recorded and current pulses are shown in red.

spectra of the 59 keV peak of ^{241}Am. The TL thickness is about 0.5 ± 0.1 mm and the DL is typically thinner than the TL. The TL accounts for 50–86% of the full charge collection depth.

From the pulse shape point of view, when part of the energy is released in the TL the charge pulse is characterised by a slow charge collection at the end of the leading edge, see Figure 4.12. A long tail is visible on the right side of the peak of the current pulse. If compared with a SSE from the bulk with the same reconstructed energy, the maximum amplitude of the current is lower since the late charges contribute (at least partially) to the value of E but do not contribute to A. It follows that the A/E ratio for slow NSP is lower than for bulk-SSE. It is therefore possible to discriminate with the A/E the events that deposit energy in the proximity of the n+ surface.

The FCCD of the GERDA BEGE detectors is about 0.5–0.9 mm, the FAV accounts therefore only for 91–95% of the total volume. Moreover, the energy depositions are never point-like; the two 1 MeV electrons produced in a $0\nu\beta\beta$ can move about 1 mm in Ge before losing their kinetic energy. Hence, interactions also in the FAV can ionise charge carriers in the transition layer if the secondary particles move towards the surface. A good understanding of the analysis response to the NSP is therefore paramount for the study of continuous features, like the shape of the $2\nu\beta\beta$ spectrum.

4.3.1 Measurements of n+ surface β events in vacuum cryostats

The first investigation of the discrimination power of A/E against n+ surface events is reported in my master thesis [80]. Several BEGE detectors operating in vacuum cryostats have been irradiated

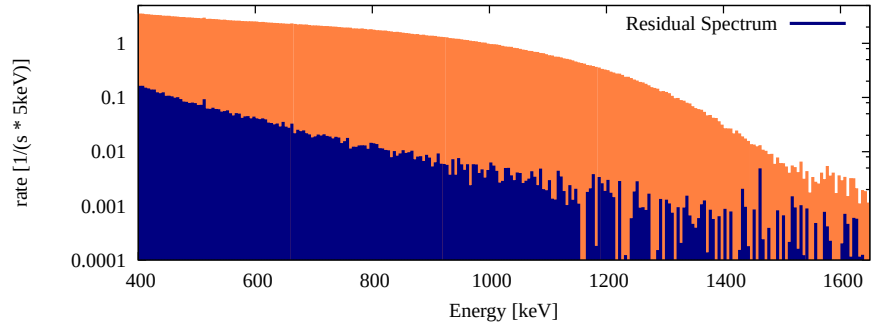

Figure 4.13: Rejection of ^{90}Sr spectrum. The figure shows the spectrum of ^{90}Sr before and after the A/E cut. Figure from [80].

with β sources. The two sources were ^{106}Ru and ^{90}Sr. The ^{90}Sr has a Q-value of 2.3 MeV and provides an almost pure beta spectrum (branching ratio 99.988%). The ^{106}Ru source was chosen for its high energy Q-value (3.5 MeV) to evaluate the rejection at the $Q_{\beta\beta}$ energy of the ^{76}Ge.

The measurement has been repeated on three different BEGe prototypes manufactured with the depleted Ge which was obtained as a by-product of the enrichment process. These detectors have full charge collection depths in the range of 0.45–0.7 mm. These values are slightly smaller than the FFCD of the enriched Gerda BEGe, which are in the range of 0.6–0.9 mm [98]. The detectors were installed in the commercial cryostat provided by Canberra[69] with 1.5 mm aluminium layer entrance window. The 40 µs waveforms were recorded with the same 100 MHz FADC [77] used in Gerda.

The PSD was calibrated on the ^{228}Th spectrum. No high A/E cut was applied in these measurements. All events with A/E below the low A/E cut threshold were rejected by the PSD. The cut threshold was fixed to accept 90% of the DEP events. Also, the $0\nu\beta\beta$ signal acceptance was therefore assumed to be $90\% \pm 5$.

The main systematic of the measurement is coming from the γ contamination of the spectra. The photons can be generated directly by the source (especially by the ^{106}Ru) or be produced by the interaction of the β with the surrounding material (e.g. the aluminium cryostat). For a better understanding of the γ component and to estimate the suppression of the β background, the ^{90}Sr measurement has been reproduced with a Monte Carlo simulation.

Figure 4.13 shows one of the acquired ^{90}Sr spectra and the suppression achieved by the A/E PSD. In the 400 keV around 1 MeV the spectrum is suppressed by about two orders of magnitude (acceptance $0.61\% \pm 0.01$). The residual spectrum does not maintain the same spectral shape of the measured spectrum, revealing that it is mostly composed of interactions of γ radiation.

To test the origin of the residual counts, a Monte Carlo simulation of the measurement has been performed. The locations where the incoming particle interacts with the Ge was recorded along with the amount of energy released in the detector. The simulated events were classified according to the depth of the shallowest interaction: γ-like events, the ones interacting only in the fully active volume; and NSP-like events, the ones releasing energy also in the n+ surface layer (DL+TL). While incoming γ can interact in the transition layer producing a NSP and be classified as NSP-like in the Monte Carlo analysis, the incoming β particles cannot cross the almost 1 mm thick FCCD without losing part of their energy. Figure 4.14 shows the simulated spectrum and its decomposition in the NSP-like and γ-like components. It is possible to reproduce the residual spectrum assuming different suppression factors for NSP-like and γ-like events. The studies on MSE rejection show that the γ background is reduced by a factor that varies between 2 and 10 according to the different topology of the events and detector performance. It will be assumed in this instance that 80% of the γ-like events would be rejected by the PSD. Assuming three orders

of magnitude reduction of the NSP-like events, the residual spectrum is then dominated by the γ-like component, therefore any stronger assumption on the NSP rejection would provide the same results. The second plot in Figure 4.14 shows a comparison between the data and the model. The qualitative agreement between the residual spectra shows how a 99.9% reduction of the NSP spectrum is compatible with the data. The last plot of Figure 4.14 compares the total acceptance of the ^{90}Sr spectrum in the data with the one obtained by the combination of 20% acceptance for γ-like events and 0.01% acceptance for NSP-like events.

The ^{106}Ru decays β^- with a Q-value of 40 keV on ^{106}Rh which then decays on a stable isotope (^{106}Pd) with the Q-value at 3.5 MeV. In 21.4% of the cases, the second β decay is accompanied by photons from several energy levels. To statistically subtract the γ component, this was measured by interposing a 3 mm copper plate between the source and the detector. The copper stops the β particles and alters minimally the γ spectrum. The two spectra have been normalized according to the live-time of the measurements, correcting for the different pile-up rates. An accurate statistical subtraction of the γ component makes it possible to estimate the suppression of the β spectrum. The main systematic uncertainties of this method arise from the fraction of γ that interacts with the copper shield and the additional γ component generated by the electrons' bremsstrahlung.

Figure 4.15 shows the results of the measurement. The first plot reports the spectra acquired with and without copper shield. The β component can be obtained by subtracting the γ component from the total spectrum. The second plot shows this component before and after the A/E discrimination. Some residues of the γ-lines are still visible in these spectra. The last plot of the figure shows the A/E acceptance for ^{106}Ru in 100 keV bins. The suppression of the spectrum is worse at low energies ($E < 1000$ keV) and at high energies ($E > 2000$ keV) where the γ-component is predominant. The region between 1 MeV and 2 MeV shows a substantially constant acceptance. The average acceptance between 1.0–2.2 MeV is $0.82\% \pm 0.06$. This suggests that the results obtained at 1 MeV with the ^{90}Sr measurement can also be applied to the $Q_{\beta\beta}$ energy of 2 MeV.

Both ^{90}Sr and ^{106}Ru spectra could be reduced to less than 1% of their original count rate in the intervals where the spectrum is dominated by β-emissions. The Monte Carlo simulation shows that also in these intervals the residual counts can be associated with the γ components. In particular the ^{90}Sr measurement is compatible with a 1000-fold reduction of the pure β component at 1 MeV and the ^{106}Ru results suggest that this can be assumed also for events with reconstructed energy equal to 2 MeV.

4.3.2 Suppression of β decays on the p+ contact region

Signals produced by surface contamination on the p+ contact and on the groove can be effectively rejected by the high-cut on the A/E parameter. This is important for GERDA because these surfaces are the only region were a BEGE detector is sensitive to external α. The features of the pulses produced by α interaction on the different surfaces of the groove and the p+ surface have been investigated with a ^{241}Am source placed inside the detector's vacuum cryostat [81].

Before the ^{241}Am measurement, the rejection of β radiation on the groove of a BEGE detector had been investigated by Dušan Budjáš and me using a ^{90}Sr source placed in the groove of a bare detector operated in LAr. The measurement was performed in a small LAr cryostat at LNGS used as a test bench for the GERDA detectors. The detector was a BEGE prototype build with depleted Ge.

The cut thresholds were chosen to accept 89% of the DEP, removing the percentile with the highest A/E and the 10% of the events with the lowest A/E. The total $0\nu\beta\beta$ signal acceptance of the double sited A/E cut is a few percentage points lower than the acceptance of the DEP due to the different distribution of the two sample in the detectors. The $0\nu\beta\beta$ is uniformly distributed in the Ge while the DEP events concentrate near the edges where the escape probability of the two 511 keV photons is higher.

The measurement of the background without source was affected by a worse electronic noise than the measurement with the ^{90}Sr source. The electronic noise reduced the A/E resolution of

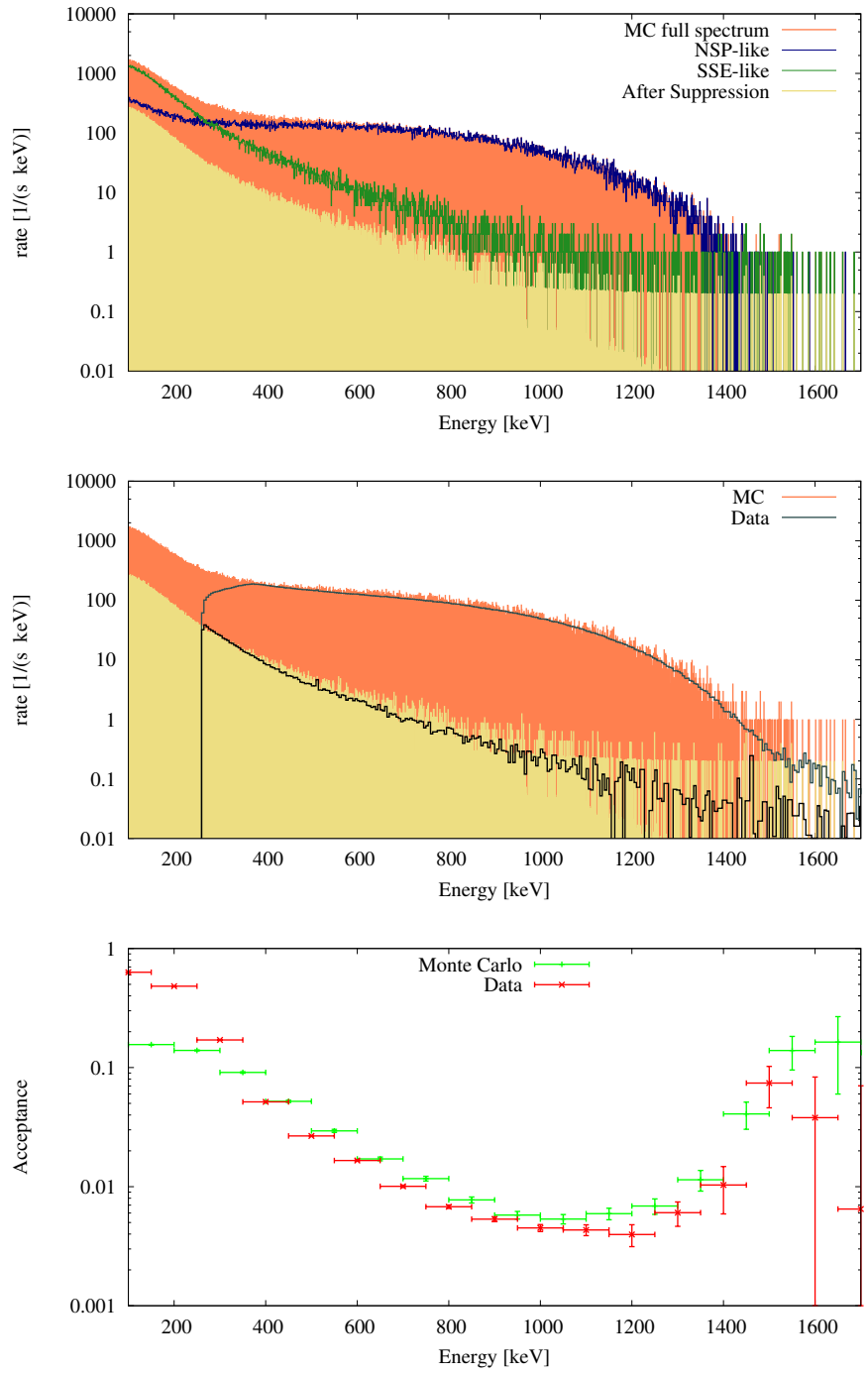

Figure 4.14: Monte Carlo simulation of ^{90}Sr measurement with model. The first panel shows the simulated spectrum, its NSP-like and γ-like components, and their combination assuming 0.01% and 20% acceptance for the NSP-like and γ-like events respectively. The second panel compares the simulated spectra, before and after PSD, with the measured ones. Note that the simulated spectra are re-scaled on the source activity and the measurement time, not on the measured count rate. In the third panel the acceptance of the data is compared with the one obtained for the simulation. Figure from [80].

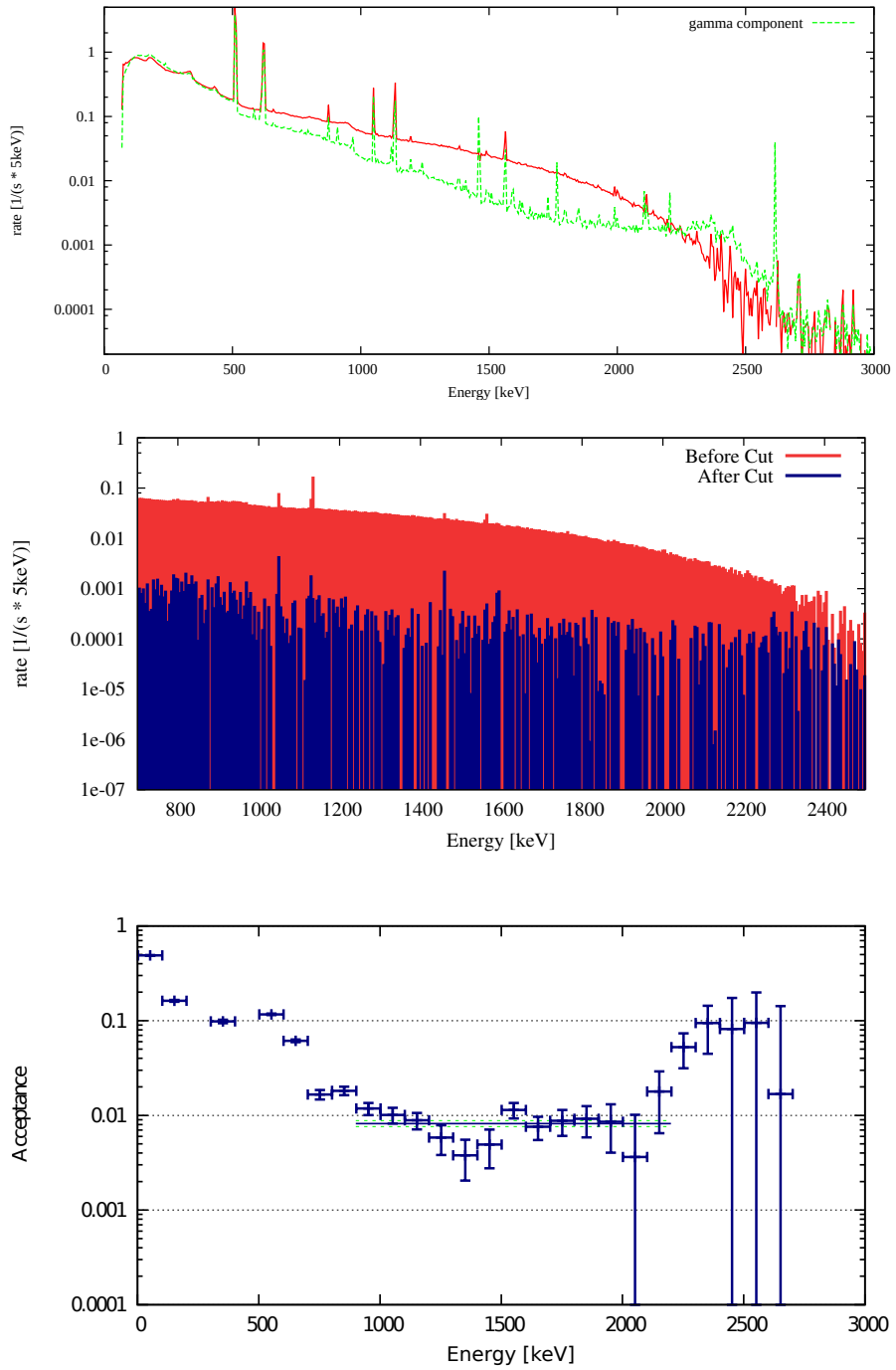

Figure 4.15: Suppression of ^{106}Ru β-spectrum. The first panel shows the total spectrum and the γ-component which is measured interposing a 3 mm Cu shield between the source and the detector. The second panel show the β-component, i.e. the difference between the two histograms of the first panel, before and after PSD. The third panel shows the PSD acceptance of the ^{106}Ru β-component. Figure from [80].

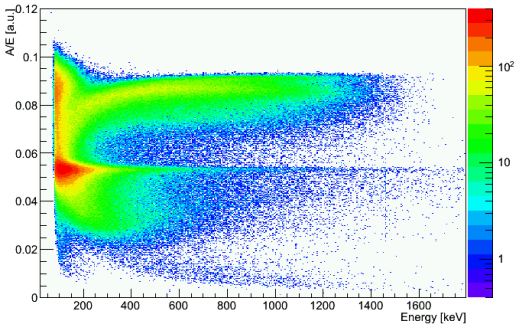

Figure 4.16: Distribution of the A/E parameter for a ^{90}Sr source placed in the groove of a BEGe detector in LAr. The events associated with interaction on the groove surface have higher A/E values than SSE from the bulk.

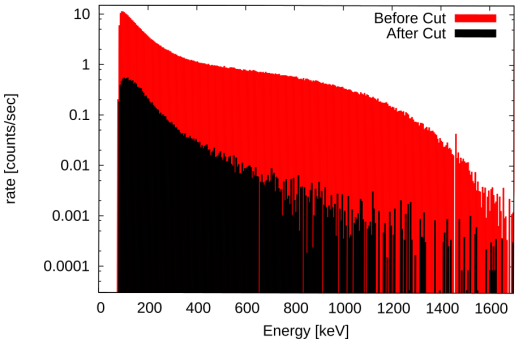

Figure 4.17: Spectrum of a ^{90}Sr source placed in the groove. The double sided A/E cut is set to accept 89% of the DEP events.

the background measurement. The cut on the background was then recalibrated to force the same acceptance of the measurement in the interval 1600–2050 keV, above the ^{90}Sr end-point.

Figure 4.16 shows the distribution of the A/E parameter for the ^{90}Sr measurement. The events from the groove have higher A/E values above the SSE band and are well separated from it. Figure 4.17 shows the measured ^{90}Sr spectrum and the residual spectrum after PSD. The residual counts after PSD have a distribution similar to the one obtained in the vacuum cryostat reported in Figure 4.13. This spectrum shape indicates that the events accepted by the PSD are associated with bremsstrahlung generated in the source holder or in the LAr. The A/E acceptance of the ^{90}Sr was estimated in the interval 1000–1500 keV. The cut set to accept 89% of the DEP reduced the ^{90}Sr count rate in this interval by more than 99.7% (90% C.L.).

4.4 Suppression of ^{42}K

During the commissioning of Phase I a large background induced by ^{42}K, a daughter of ^{42}Ar, was observed. The ^{42}Ar is a cosmogenic isotope with an half-life of 33 yr. It decays β^- on ^{42}K with a Q-value of 600 keV. A simplified decays scheme of ^{42}Ar and ^{42}K is shown in Figure 4.18. While ^{42}Ar has a low Q-value and it is not a direct component of the background in the Region of Interest (ROI), ^{42}K has a Q-value of 3.5 MeV. If the ^{42}K decays directly on the surface of a detector, its β^- emissions can cross the n+ contact and produce events with reconstructed energy above 2 MeV. In 82% of the cases ^{42}K decays on the ground state of ^{42}Ca, in the remaining decays the β^- is accompanied by γ emission. The most prominent γ-line is at 1525 keV with a branching ratio of almost 18%. This is one of the two major γ-lines in the GERDA spectrum together with the line of ^{40}K at 1461 keV. Other γ-emissions with higher energy (3.4 MeV and 2.4 MeV) are also present in the ^{42}K decay scheme. These photons contribute to the background in the ROI even when produced centimetres away from the detectors, however their branching ratios are below the 0.1% level.

Thicker n+ contacts provide better shielding against external β radiation, reducing the e^- energy released in the active volume. Decays of ^{42}K on the detector surfaces are therefore a more prominent background component for BEGe detectors which have a thinner n+ contact (0.5–0.9 mm [98]) than semi-coaxial detectors (1.4–2.6 mm [104]).

If not mitigated, the ^{42}K induced background would have exceeded the background budget of GERDA Phase I, whose goal was 0.01 cts/(keV · kg · yr) in the ROI. The unexpected level of ^{42}K was attributed to a higher concentration of ^{42}Ar with respect to the measurements available at the time (< 41 μBq/kg) [105]. These measurements have later been reconsidered and updated to

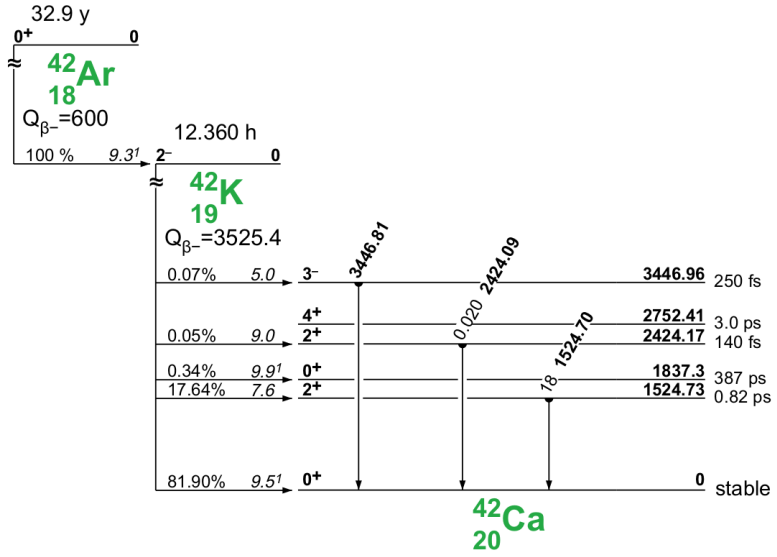

Figure 4.18: Simplified decay scheme for ^{42}Ar and ^{42}K. Figure from [109].

90 µBq/kg [106]. Moreover, it was found that the ^{42}K ions are attracted by the electric field of the germanium detectors and their distribution in the liquid argon is therefore inhomogeneous [107].

After the first commissioning tests, the Ar volume surrounding each detector string was enclosed by a cylinder, called mini-shroud, made from 60 µm copper foil and connected to the ground potential. This solution reduced the ^{42}K decaying on the detector surfaces by limiting the reservoir of LAr from which ^{42}K ions could reach the detectors. For Phase II, the copper mini-shrouds have been substituted by transparent nylon mini-shrouds coated with wavelength shifter to allow the detection of the LAr scintillation light [108].

4.4.1 Monte Carlo simulation of ^{42}K on BEGe detector surfaces

The impact of NSP rejection on the background induced in GERDA by ^{42}K was first estimated with a simple Monte Carlo simulation in my master thesis [80]. The simulation included a single BEGe detector in LAr with uniform distribution of ^{42}K on the n+ surface. The effect of the PSD was estimated with the same model applied to the ^{90}Sr spectrum, see Section 4.3.1. The spectrum was divided into two components: NSP-like and γ-like. The two components were reduced by a factor of 1000 and 5 respectively. The simulation did not include the scintillation light propagation. It was assumed that the LAr veto can detect every event that deposits enough energy in the Ar (100 keV).

Figure 4.19 shows the suppression of the simulated ^{42}K spectrum. The background index in the ROI is reduced by about three orders of magnitudes to 0.12% by the PSD and to 0.08% of its original value by the combination of PSD and LAr anti-coincidence.

A further Monte Carlo simulation including ^{42}K on the p+ contact and on the surfaces of the detector holder was later performed and it is presented here for the first time. Two different FCCD of 1 mm and 0.6 mm were considered. The balance of the three ^{42}K components (n+, p+, and holder) was based on the experimental measurement performed in LArGe [110]. The contributions of the surface components were adjusted to the continuum β spectrum. The contribution from the holder was scaled according to the ratio between the continuum of the spectrum and the intensity of the 1525 keV γ-line. It was found that about one third (32%) of the counts in the peak are due to decays which occurred away from the detector surfaces (on the holder or in the LAr).

The simulated spectrum was scaled to the expected GERDA ^{42}K count rate in the ROI for a BEGe detector with 0.6 mm FCCD operated without mini-shroud. This value was estimated to

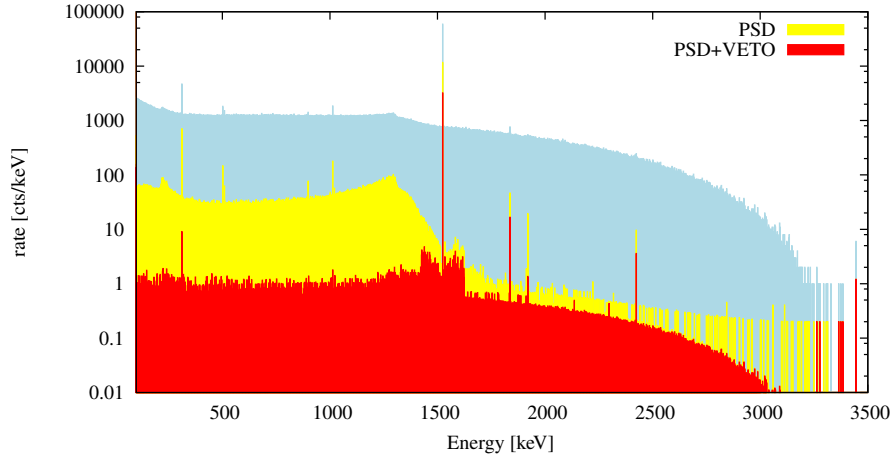

Figure 4.19: Monte Carlo simulation of the ^{42}K spectrum for a single detector in LAr. The effect of the PSD is computed assuming a 99.9% rejection of NSP and 80% rejection of γ. The effect of the LAr anti-coincidence is computed rejecting all the events with more than 100 keV deposited in the LAr. Figure from [80].

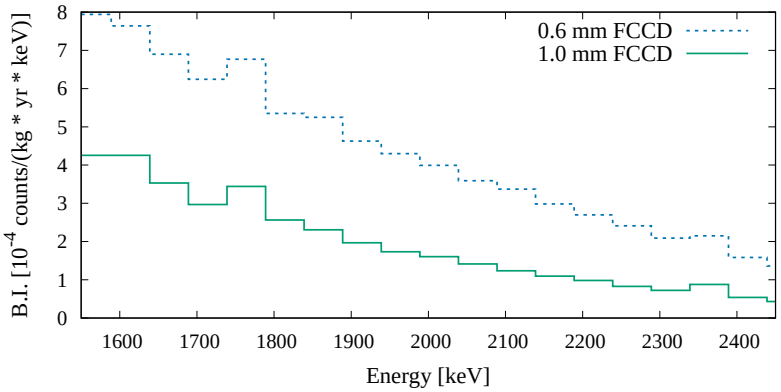

Figure 4.20: Expected ^{42}K spectrum after PSD and LAr veto for two BEGe detectors with FCCD of 0.6 mm and 1.0 mm deployed in GERDA without mini-shroud. The B.I. in the ROI before cuts is assumed to be 0.8 cts/(keV $\cdot$ kg $\cdot$ yr) for the 1.0 mm FCCD detector.

be 0.8(4) cts/(keV $\cdot$ kg $\cdot$ yr). The estimation was based on LArGe measurements scaled to the GERDA set-up according to the intensity of the 1525 keV line.

Assuming this level of ^{42}K, it was possible to estimate the contribution of ^{42}K to the GERDA background level for BEGe detectors with different FCCD. The residual spectrum after PSD and LAr veto expressed in 10^{-4} cts/(keV $\cdot$ kg $\cdot$ yr), is reported in Figure 4.20. The resulting background level in the ROI is $4 \cdot 10^{-4}$ cts/(keV $\cdot$ kg $\cdot$ yr) for the detector with 0.6 mm FCCD and $1.5 \cdot 10^{-4}$ cts/(keV $\cdot$ kg $\cdot$ yr) for the detector with FCCD of 1.0 mm. This simulation shows that with good enough electronic performances (in terms of A/E resolution) it would have been possible to reach Phase II background goal also without mini-shrouds.

4.4.2 Measurements of ^{42}K suppression with enriched Ar

The ^{42}K count-rate in GERDA is too low to test the PSD suppression factor of NSP, especially since all GERDA data are collected with BEGe encapsulated in the mini-shroud. In order to measure

the PSD rejection of ^{42}K, enriched ^{42}Ar sources were produced in Garching using the tandem accelerator of the Maier-Leibnitz Laboratory of the Technische Universität München. A target cell was filled with 500 mbar of ultra pure argon (Ar 6.0). The target was then irradiated with $^{7}Li^{3+}$ ions to produce ^{42}Ar by the reaction ^{40}Ar(^{7}Li,α p) ^{42}Ar.

Two Ar samples were irradiated in July 2011 for 10.17 h and 16.75 h respectively with Li ion at 33 MeV and 24 MeV. The activity of these samples was determined through γ-spectroscopy to be 5.8±1.0 Bq and 5.2±0.9 Bq. The latter has then been dissolved in the LAr of the LArGe [110] test facility at LNGS to test the suppression of PSD without mini-shroud [108].

A second irradiation was performed in October 2012. This time three samples were irradiated for a total of 2.3 days in a larger target cell. The total activity of the new production was 80 ± 10 Bq. The 2012 enriched Ar was used in LArGe to test the design and the impact of the new mini-shroud for Phase II. Part of the Ar has, however, been lost to evaporation during the refill of the cryostat. Despite the original strength of the source, the ^{42}K activity of the mini-shroud run was only about 5 times stronger than in the previous run. Since the mini-shroud further reduces the count-rate, the first run has higher statistics for the measurement of the PSD and the LAr effects.

LArGe is a 1 m^3 LAr cryostat coated with wavelength-shifter reflector foil and equipped with nine photomultiplier tubes to detect the argon scintillation light. It allows for the operation of BEGe detectors with a background level comparable to the one of Gerda Phase I. A p-type BEGe detector of 878 g with 0.6 mm FCCD was used for the measurement with enhanced ^{42}K count-rate.

The m^3 of Ar was spiked with 5.2 ± 0.9 Bq of ^{42}Ar for the measurement without mini-shroud. After the activated ^{42}Ar was dissolved in the cryostat the count rate of the 1525 keV line from ^{42}K increased by a factor 40. The background level was assumed to be equal to the one previously measured in similar conditions, $(0.1 - 4.6) \times 10^{-2}$ cts/(keV $\cdot$ kg $\cdot$ yr) [110]. In the region 1839–2239 keV the expected number counts before LAr veto and PSD was 23. Considering the PSD suppression of γ-emitting calibration sources and Monte Carlo simulation of the light propagation in LArGe [98], 0.6 counts were expected to remain after PSD and LAr veto.

The A/E cut was set to accept 90% of the DEP peak and the LAr veto signal acceptance was 96.5%, estimated by the rate of random coincidences with the test pulser. Figure 4.21 shows the distribution of the A/E parameter for the measurement. Of the 610 counts recorded in the 400 keV ROI only 2 were not rejected by either PSD or LAr veto. It was therefore estimated that the PSD+LAr veto suppression factor of ^{42}K is > 121 (90% C.I.). The limit is weaker than the suppression factor estimated by Monte Carlo analysis but it is limited by the size of the sample.

The new Phase II transparent mini-shroud of wavelength-shifting nylon foil was also tested in LArGe with the same BEGe detector. The Nylon Mini-Shroud (NMS) provides a mechanical barrier, similar to the Cu mini-shroud from Phase I, for the collection of ^{42}K ions on the surface of the detector. The NMS transparency to visible light and its wavelength shifter coating allow for and enhance the detection of scintillation light generated in the proximity of the detectors. A 10–15% improvement of the LAr veto suppression factors for γ-sources (^{228}Th) was measured with the NMS in comparison with the measurement without mini-shroud. The improvement is due to the higher attenuation length of the shifted visible light compared to the 128 nm scintillation light.

The NMS reduced the count-rate of ^{42}K in the 400 keV region of interest by a factor 14(2). The combination of the NMS effect with the limit on the suppression factor (SF> 121) of the active background rejection (PSD+LAr veto) indicates that the ^{42}K count rate can be suppressed by more than three orders of magnitude (SF> 1400). Figure 4.22 shows the measured spectra with and without NMS, re-scaled according to the measurement time, and the effect of the active background suppression.

4.5 Conclusions

The sensitivity of Phase II is driven by the BEGe dataset. Although it represents half of the target mass, the better performances from the point of view of PSD allow for a lower background level while maintaining at the same time a higher signal efficiency. The PSD is based on a single

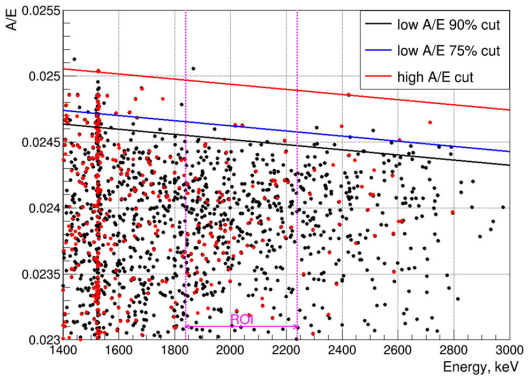

Figure 4.21: Distribution of the A/E parameter in LArGe after increasing the ^{42}Ar concentration. Red dots indicate events removed by coincidence with the LAr veto. In the region 1839–2239 keV, 23 counts are expected from backgrounds not related to ^{42}K decays. Figure from [108].

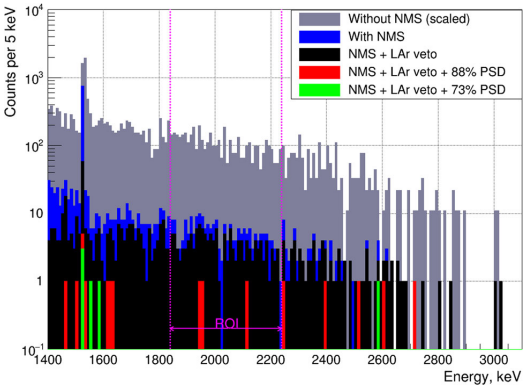

Figure 4.22: Combination of ^{42}K energy spectra measured with and without mini-shroud in LArGe. The two spectra are re-scaled according to their measurement time. Overall, the combination of NMS, PSD and LAr veto shows a 500-fold (90% C.I.) suppression of the ^{42}K spectrum. Figure from [108].

parameter: the ratio of the amplitudes of current and charge signals, A/E. Through this parameter it is possible to select the SSE from the detector bulk and reject MSE and surface events.

The A/E parameter is calibrated on the ^{228}Th spectrum and the background rejection has been successfully tested in Phase I with a first string of five BEGe detectors. These detectors showed some instabilities and drifts of the SSE A/E values in connection with the long operation in LAr and with the exposure to different levels of ionising radiations. Nevertheless, four out of five detectors were included in the final $0\nu\beta\beta$ analysis and contributed to Phase I half-life limit with 2.4 kg·yr, 10% of the total exposure. The first BEGe dataset recorded, without LAr light instrumentation, a background index of 5^{+4}_{-3} kg·yr, only five times higher than the goal for Phase II.

This chapter showed the excellent rejection of external β background that can be achieved with the A/E analysis. Events generated by β decays on the n+ surface produce slower pulses with lower A/E values. Events generated by β decays on the p+ and on the groove surfaces produce faster pulses with higher A/E values. The rejection of these pulses has been tested with a ^{90}Sr sources measured in vacuum cryostats and in LAr respectively. These results indicate the potential for a three orders of magnitude reduction of the β count rate.

The impact of the PSD in combination with Phase II LAr scintillation light veto on Gerda ^{42}K background component has been studied with Monte Carlo simulations and experimental measurements.

The simulations of a BEGe detector show that for detectors with good A/E resolution the residual background, after the PSD and the LAr anti-coincidence veto, is well below the background target of Gerda Phase II. The expected ^{42}K count rate in the ROI is further reduced for detectors with thicker n+ FCCD. This result informed the production of remaining enriched BEGe later deployed in Phase II.

In order to increase the statistics of ^{42}K experimental measurements, samples of enriched Ar were produced by collision with ^{7}Li ions. The activity of the samples was measured with γ-spectroscopy before diluting them in the 1 m^3 cryostat of LArGe. These measurements have been used to develop the design of the transparent nylon mini-shroud of Phase II and to set lower limits to the rejection of ^{42}K events. The combination of PSD and LAr veto reduced the count rate to less than 1%. When the active background reduction is combined with the new transparent mini-shroud, the count rate of ^{42}K events can be reduced to less than 0.1% of its original value.

Chapter 5

Modelling of semi-coaxial detectors signal shapes

This chapter presents a study on the pulse shapes of semi-coaxial detectors. In particular it defines a parametric method to classify α-induced signals according to the position of the energy deposition on the surface of the p+ contanct and groove area. The different pulse shapes have been classified according to their rise times (RT_{10-90} and RT_{2-60}). The choice of the parameters was informed by the visual inspection of α and $2\nu\beta\beta$ signals. A full pulse shape simulation of each detector provides a physical interpretation of the pulse shape features and matches each class to the detector volume where the interaction occurred. This method serves as the basis for the development of the α background pulse shape discrimination described in Chapter 6. Section 5.1 describes the implementation of the pulse shape simulation: the geometry of the detectors, the impurity gradient and the electronic response. The second part, Section 5.2, illustrates the different classes of signals and the parameters of choice for their classification. In Section 5.3 the analysis is applied to the physics data to study the α component of GERDA Phase II spectrum. Finally Section 5.4 summarises the results.

5.1 Simulation of semi-coaxial pulses

5.1.1 Detectors geometry and net impurity concentration

The seven semi-coaxial detectors have different features and histories as they have been previously operated in other experiments: five of them (named ANG1 - ANG5) in the Heidelberg-Moscow experiment (HDM) [63], two of them (RG1 and RG2) in the IGEX experiment [64]. Six detectors were originally produced by ORTEC, while ANG1 was produced by Canberra. They were completely refurbished at Canberra Olen [69] before their deployment in GERDA. The geometry of the electrodes has been modified with a "wraparound" n+ contact, a passivated groove separating the two electrodes and a boron implanted p+ contact covering the full area internal to the inner groove radius [111, 68]. Even though they share a similar electrode configuration (Figure 5.1), each detector must be studied individually to understand the features of their signal shapes.

The semi-coaxials have been characterised in details in the thesis of M. Barnabe Heider [68] and the parameters of each crystal are reported in Table 5.1. Most of the crystals have a radius of about 39 mm, only ANG1 is significantly smaller (29 mm). Four of the five ANG diodes are about 101($\pm$5) mm long, RG1 and RG2 measure 84 mm, and ANG1 only 68 mm. The variety of the dimensions is reflected in the sizes of the read-out contact features: bore-hole radius and depth. The grooves are typically 3 mm wide and 2 mm deep but for ANG1 (6.5 mm width, 4 mm depth) and ANG5 (3 mm width, 8 mm depth).

The signal formation does not depend solely on the geometry but also on the impurity concentration profile. Unfortunately, this can be measured only before the production of the diodes and only limited information is available in [112]. Since the net impurity charge contributes

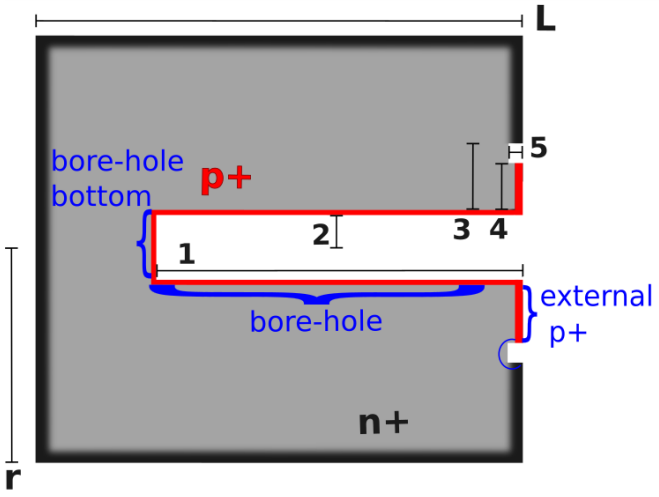

Figure 5.1: Sketch of the semi-coaxial detector geometry. The numbers refer to Table 5.1.

			ANG1	ANG2	ANG3	ANG4	ANG5	RG1	RG2
Radius	(r)	[mm]	29.2	40	39	37.5	39.2	38.7	38.7
Length	(L)	[mm]	68	107	93	100	105	84	84
Bore hole l.	(1)	[mm]	51	94	83	89	94	73	73
Bore hole r.	(2)	[mm]	6.7	7	7.5	7	6.2	6.7	6.5
Groove outer r.	(3)	[mm]	19.5	18	20	18	18	20	20
Groove inner r.	(4)	[mm]	13	15	17	15	15	17	17
Groove depth	(5)	[mm]	4	2	2	2	8	2	2
Dead layer thickness		[mm]	0.7	0.7	0.7	0.7	0.7	0.8	0.8
Depletion voltage		[V]	3000	3000	3000	2800	1000	4200	3800
Impurities from [112]		[10^{10} cm^{-3}]	–	–	0.5-1.3	0.41-0.98	0.14	–	–
Estimated impurities		[10^{10} cm^{-3}]	0.6	0.75	0.52	0.75	0.14	0.65	0.78

Table 5.1: List of parameters from [68] used to define the features of the semi-coaxial detectors in the simulations.

to the electric field, it influences the depletion and the bias voltage required to achieve it. The depletion voltages of the semi-coaxial diodes have been measured before the deployment in GERDA [68].

Using the pulse shape simulation (PSS) package SigGen [113], it is possible to compute the electric field of the diodes. A two dimensional (2D) cross-section of the detectors is sampled with a 0.1 mm step grid and the field is computed for each point of the grid. The total field is the combination of the one induced by the bias voltage and the one due to the net impurity charge. The latter is computed under the assumption of homogeneous impurity distributions with different values for the average net impurity concentration. The values reported in the last row of Table 5.1 provide full depletion at the measured depletion voltages and partial depletion with 100 V less. The assumption of homogeneous impurity distribution is needed because it is not possible to deduce the impurity gradient from the depletion voltage. However, this is an approximation. A gradient of net impurity could have an impact on the accuracy of the pulse shape simulation.

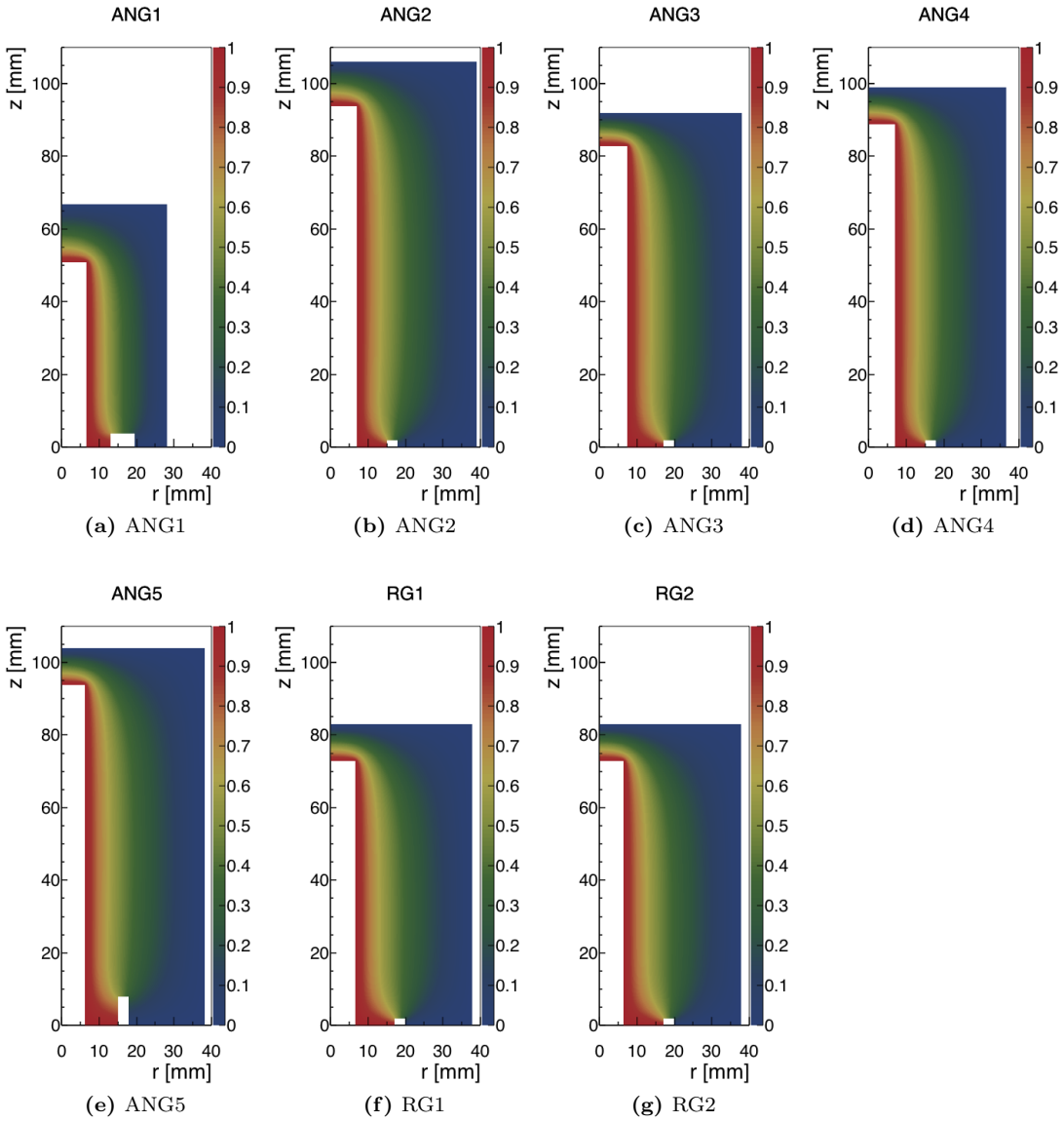

(a) ANG1 **(b)** ANG2 **(c)** ANG3 **(d)** ANG4

(e) ANG5 **(f)** RG1 **(g)** RG2

Figure 5.2: The figure shows the cross-sections of the semi-coaxial detectors deployed in GERDA and their weighting potential ϕ_w. All detectors have similar features, but the differences are such that none can be considered representative for all the others. The weighting potential gradient is greater in the proximity of the read-out electrode, but is not negligible in a considerable fraction of the volume. Therefore, the contribution of the electrons to the signal formation cannot be ignored.

With the estimation of the net impurity concentration and the geometry of the diodes it is possible to compute the electric field and the weighting potential of the diodes (Figure 5.2). Choosing an interaction site the trajectories of the charge carriers are defined by the electric field. The charge signal $Q\left(\overline{r}(t)\right)$ induced on the read-out electrode can be computed according to the Shockley-Ramo theorem [66]:

$$Q\left(\overline{r}(t)\right) = -q_{tot} \cdot \phi_w\left(\overline{r}(t)\right), \tag{5.1}$$

where $\overline{r}(t)$ is the position of the charge q at the time t and $\phi_w(\overline{x})$ is the weighting potential.

5.1.2 Simulated signal shapes

The 2D cross-sections of the detectors modelled by the parameters of Table 5.1 have been sampled with a 1 mm grid. The signals associated with a unitary ionisation in each point of the grid have been generated. A representative sample of pulse shapes produced for ANG2 is shown in Figure 5.3.

For most of the length of a semi-coaxial detector the electric field lines run radially between the bore-hole and the n+ electrode. In this region, the signal shape depends, in first approximation, only on the distance of the interaction location from the detector's axis. This is shown in Figure 5.3 by the three pink signals (r = 30 mm) that are indistinguishable even though they are generated by energy deposition a few centimetres apart. In this region the sum of the charge carrier trajectories length is constant, it is equal to the radius of the crystal minus the radius of the bore-hole. The charge collection time depends then on the velocities of holes (h^+) and electrons (e^-) in the crystal lattice. In the intense field of the diodes the mobility of the e^- is up to two times higher than

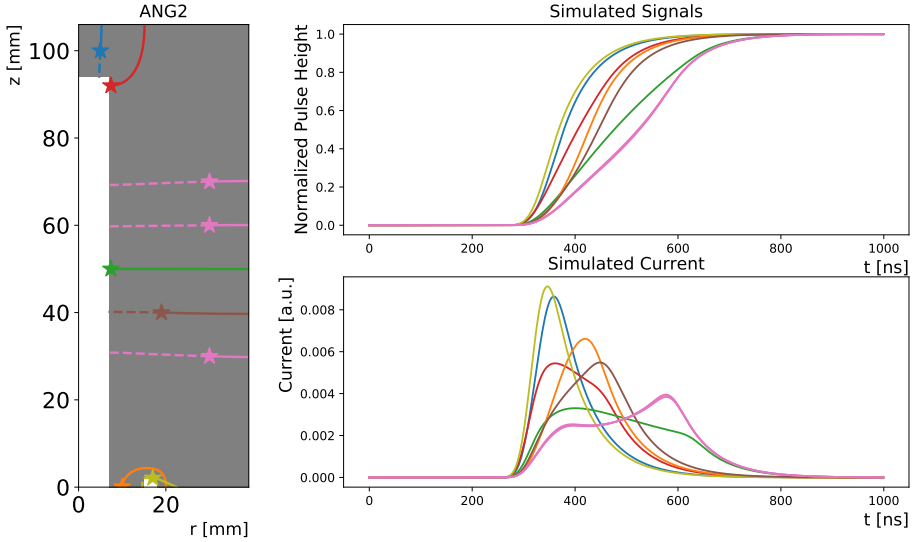

Figure 5.3: Simulated waveforms for different interaction points in the detector volume. The diagram on the left shows the cross-section of one semi-coaxial detector (ANG2), the interaction locations of 9 simulated events (stars) with the trajectories of the holes (dashed lines) and of the electrons (solid lines). The corresponding simulated pulses are presented in plots on the right: charge (current) signals are shown in the top (bottom) panel. The pulse shape of the bulk events depends on the distance from the detector axis (Fig.3 of [67]), as shown by the example of the three indistinguishable pink pulses produced by interactions at $r = 30$ mm. Most of the interactions on the α-sensitive surfaces (p+ electrode and groove) produce faster pulses than the bulk interactions. An interaction along the side of the bore-hole (green) produce a pulse with a fast contribution from the holes (faster than the red and the brown pulses at the start) and a slower electrons contribution (slower than the pink pulses in the final part).

the one of the h^+ (Fig. 11.2 of ref. [65], Fig. 1 of [114], and Fig. 6 of [115]). Since both types of carriers contribute significantly, the fastest signals arise when h^+ and e^- reach the electrodes at the same time. This happens for interactions which are slightly closer to the bore-hole than to the n+ electrode (brown event in Figure 5.3).

Charge carriers generated above the bore-hole are closer to the electrodes and are therefore collected faster. This can be seen in in the blue signal in Figure 5.3. The same is generally true also for energy depositions near the end of the bore-hole (orange in Figure 5.3) where the field lines are not parallel. There is no discontinuity in the signal shape between the end of the bore-hole and its middle section.

At the base of the detector the charge collection is complicated by the presence of the groove. Where the two electrodes are just a few millimetres apart the field is much more intense. A sub-millimetric knowledge of the detectors' geometry would be required to properly reproduce the field around the groove. Moreover, the details of the interface between the Ge crystal structure and the passivation layer, and the mobility of the charges along the crystal surface are largely unknown. The simulation therefore does not take into account the transport of charges along the groove surface. Hence, the simulation does not reproduce the contribution of e^- produced too close to inner edge of the groove or h^+ produced on the outer groove wall (near the n+ electrode). A class of fast rising α-signals with delayed charge collection on the order of tens of µs is present in the data. These signals are probably generated by interactions in the proximity of the groove, e.g. the holes are immediately collected on the p+ electrode while the e^- move with a slower drift velocity along the groove surfaces.

For energy depositions between the groove and the bore-hole (red in Figure 5.3) the h^+ can quickly reach the p+ surface, while the e^- need to move around the groove to reach the n+ region. This results in signals which are faster than the ones produced along the bore-hole (green in Figure 5.3) but slower than the ones generated at the end of the bore-hole (blue in Figure 5.3).

Finally, the simulation geometry does not include the transition layer on the n+ surface. A model for the charge carrier diffusion in the region with weak electric field would be needed to reproduce the slow n+ surface pulses (NSP) which are not relevant for this study since the n+ surface too thick to be crossed by α particles.

5.1.3 Electronic response and pulser signals

The output of SigGen does not consider the effect of the read-out electronics on the signals. Each preamplifier deforms to some degree the detector signals. The model of the electronic response of the GERDA preamplifiers has been implemented by K. Panas (Appendix B of [116]). In this section, his work is summarised and applied to the pulses simulated with SigGen.

The system detector-preamplifier can be described by the equivalent circuit sketched in Figure 5.4. Even though the actual GERDA electronics is more complicated, this model can reproduce the main features that impact the signal:

- The preamplifier has a limited bandwidth;
- The discharge of the feedback capacitor (C_f) through the feedback resistor (R_f) causes an exponential tail;
- The detector has an additional capacitance (C_d) which further limits the bandwidth of the read-out system.

From a Laplace analysis of the circuit, one can find the transfer function of the preamplifier. The response of the preamplifier ($T(s)$) as a function of the complex frequency $s = i \cdot \omega$ is described by the following equation:

$$T(s) = \frac{1}{C_f} \frac{1}{\alpha s^2 + s\left[1 + \alpha\left(\omega_{sum} + \omega_{pre}\right)\right] + \alpha\,\omega_{pre}\omega_{sum} + \omega_f}, \tag{5.2}$$

where

$$C_{sum} = C_f + C_d, \tag{5.3a}$$

$$\omega_{sum} = \frac{1}{R_f \cdot C_{sum}}, \tag{5.3b}$$

$$\alpha = \frac{C_{sum}}{C_f \cdot GBP}, \tag{5.3c}$$

$$\omega_f = \frac{1}{R_f \cdot C_f}, \tag{5.3d}$$

$$\omega_{pre} = \frac{GBP}{K_{pre}}, \tag{5.3e}$$

the K_{pre} is the gain of the preamplifier and the Gain-Bandwidth Product (GBP) is the Gain-Bandwidth Product and expresses the bandwidth of the amplifier at a given amplification level. The following parameters are used here for all the detectors:

- $C_f = 350\,nF$,
- $R_f = 500$ MΩ,
- $K_{pre} = 150 \cdot 10^3$,
- $C_d = 60$ pF.

The GBP parameter can be used to match experimental and simulated waveforms and it is therefore optimised for each detector.

The GBP values were tuned to reproduce the shape of the test pulser and fastest signals, the values obtained are listed in Table 5.2.. The input of the test pulser is recorded alongside the response of the preamplifiers. The transfer function of Equation 5.2 was applied to the input pulser to match the resulting waveform with the output of every detector's preamplifier. The values have been further tuned to reproduce the pulse shapes of a selection of fast signals with the simulated pulses associated to energy depositions near the p+ electrode. Figure 5.5 shows the effect of the electronic response model on an ANG3 simulated pulse arising from the proximity of the p+ electrode and the comparison with an experimental fast rising signal ($RT_{10-90} = 180$ ns).

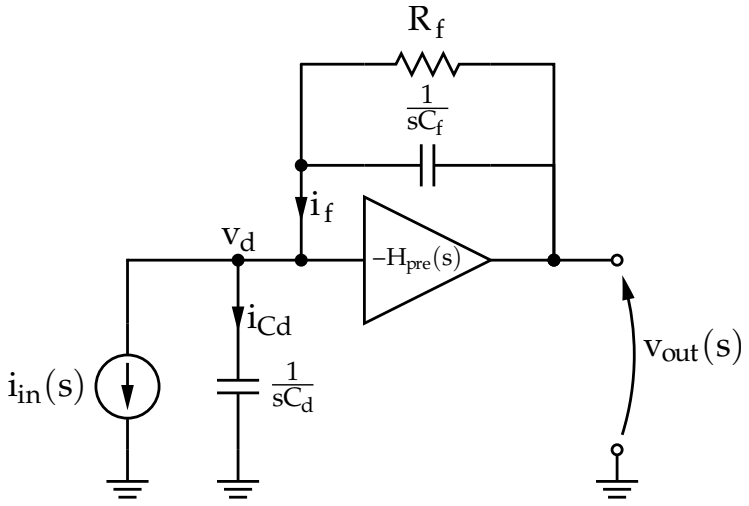

Figure 5.4: Sketch of a generic preamplifier from [116]. The circuit of the GERDA boards can be reduced to this simplified scheme in order to model the electronic response.

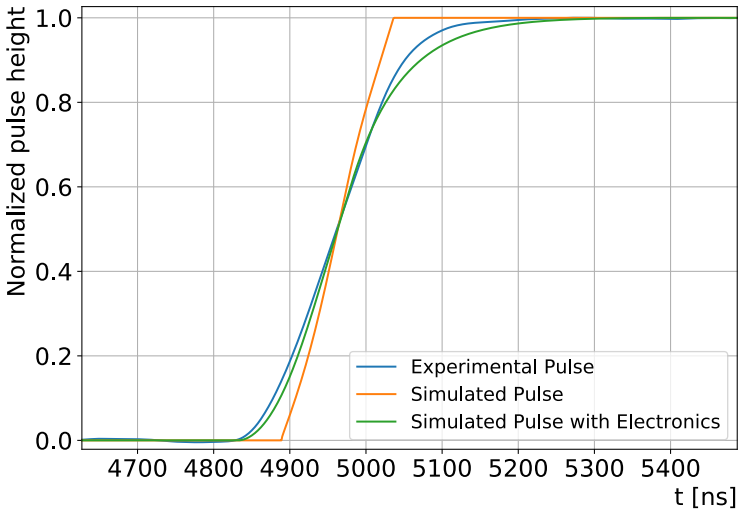

Figure 5.5: Illustration of the impact of the response function on a pulse from ANG3 (r= 12 mm, z= 0.1 mm). The simulated waveform (in orange) is transformed into the green one. The limited bandwidth of the preamplifier removes the high frequency components resulting in a low-pass filter. The exponential tail of the RC feedback is not visible here due to the long time constant, $\tau \sim 50$ µs.

5.2 Pulse shape analysis and modelling

In this section, some GERDA signals from different energy intervals are analysed to search for characteristic features of the α-induced events. Then the recorded shapes are compared to the simulated ones shown in Section 5.1.2. A method to retrieve information about the location of energy deposition from the pulse shape is introduced. It will be shown that with two parameters (RT_{10-90} and RT_{2-60}), it is possible to identify the events associated with interactions on the p+ and groove surfaces.

5.2.1 Visual study of the pulse shapes

The main issue with any pulse shape analysis for the semi-coaxial detectors is that, unlike BEGE, the single site events (SSE) from the bulk of the active volume can produce a wide variety of pulse shapes.

In the top panel of Figure 5.6 a random selection of pulses with energy below 2 MeV is shown. All the pulses are normalised and aligned in time at the 2% quantile of the amplitude. Most of the events with energy between 1.5 MeV and 2 MeV are due to γ and $2\nu\beta\beta$ interactions, i.e. multiple site events (MSE) and SSE from the bulk of the active volume.

In the bottom panels the signals with an energy above 3 MeV (i.e. α decays) are generally faster. The high energy events appear more regular, the pulses tend to cross less. Two groups of pulses can be visually distinguished: within each group the pulses do not cross each other.

The middle panels show the signals with energy between 2 MeV and 3 MeV, here all types of signals can be found. From the composition of the samples in the middle panels it is already

	ANG1	ANG2	ANG3	ANG4	ANG5	RG1	RG2
GBP [MHz]	2500	2700	2550	2900	2450	2900	2700

Table 5.2: Gain-Bandwidth Products adopted for the semi-coaxial detectors.

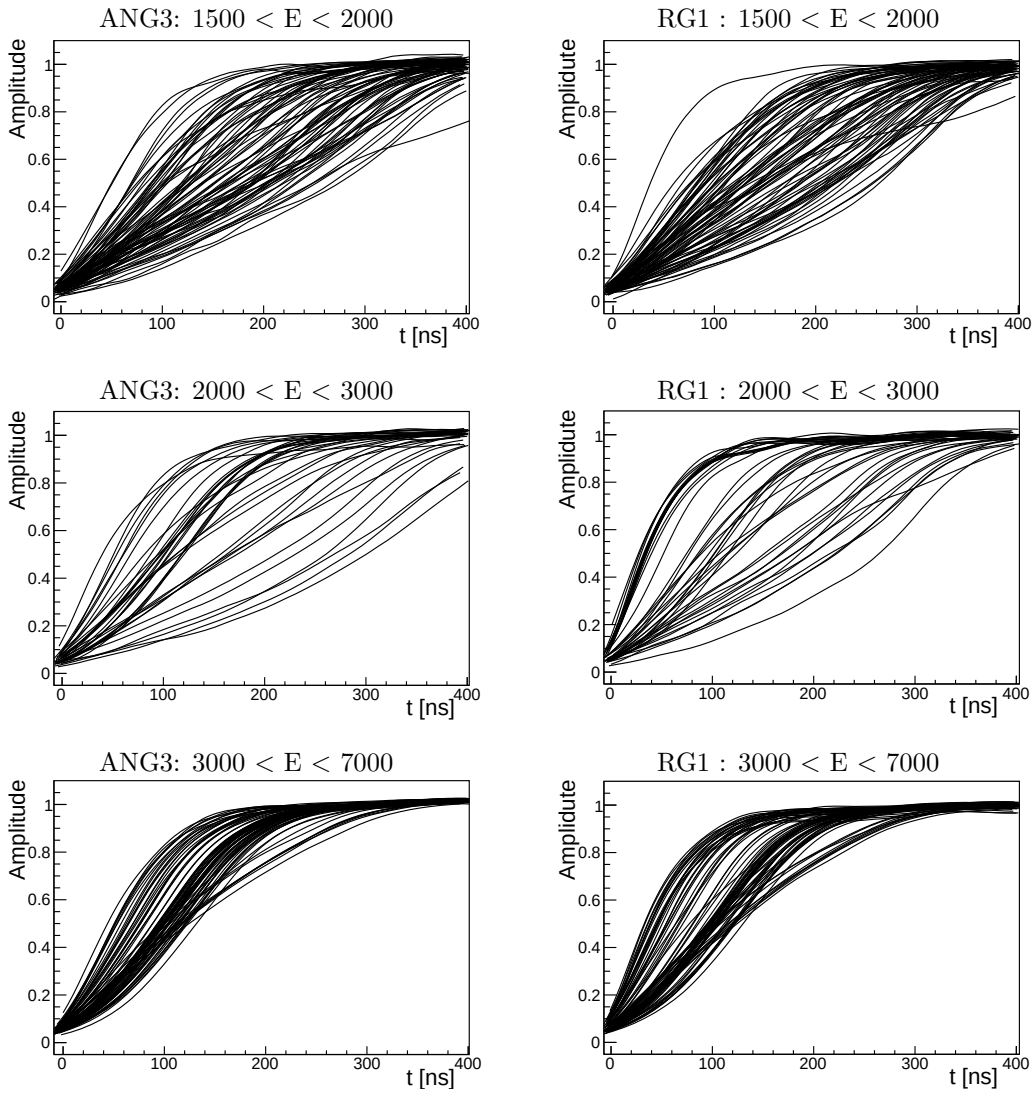

Figure 5.6: Examples of charge signals in semi-coaxial detectors. On the left (right) signals from ANG3 (RG1) are shown. The panels on the top contain events with energy below 2 MeV, where γ background is dominant. The panels in the middle contain all the events with energy between 2 MeV and 3 MeV, i.e. a mix of α and γ induced signals. The bottom panels show the events above 3 MeV, where the γ contribution is negligible. The comparison of the set of waveforms confirms the PSS prediction that α-induced signals (from the surfaces) are generally faster than bulk events. In the bottom panels a slightly slower set of pulses resemble the green signal from Figure 5.3.

possible to deduce that a significant fraction of the background has similar pulse shapes as the high energy α-induced signals. Already from the plot it is possible to distinguish between two or three different characteristic shapes.

The variety of recorded signals of Figure 5.6 can be compared with the simulated pulses of Figure 5.3.

5.2.2 Event classification: Pulse shape analysis parameters

The highest relevant γ line in the GERDA spectrum is the 2.6 MeV peak from ^{208}Tl. The only γ-induced events with higher energy remaining after the muon veto are the γ-coincidences, e.g. from the 2.6 MeV and 580 keV lines of the ^{208}Tl. The population of high energy events (above 3 MeV) provide therefore an almost pure α sample.

Figure 5.6 shows how these events have a faster leading edge (higher current) compared to the other samples. Above 3 MeV the slower pulses are missing. The PSS associates the slower pulses with the bulk volume interaction that occurred far from the bore-hole (pink events in Figure 5.3). The rise time of the leading edge can then discriminate these events from the ones associated to α-sensitive volumes (blue, orange, red, yellow events in Figure 5.3).

The volume next to the bore-hole produces the slowest α signals (green in Figure 5.3) and the fastest bulk signals (brown in Figure 5.3). The electrons produced along the bore-hole need to travel a long way to the outer surface of the detector. The holes contribute only in the very first part of the leading edge while most of the signal is induced by the long path of the electrons. These events (green event in Figure 5.3) are likely to be produced by surface interactions (i.e. α). On the other hand, if the charge carriers are produced farther from the bore-hole both electrons and holes contribute to the mirror-charge on the read-out electrode. In this case fastest signals arise when holes and electrons need the same time to reach the corresponding electrode (brown event in Figure 5.3).

A classification based on a single parameter will most likely identify the fast bulk signals as α-like and misclassify the surface interactions along the bore-hole wall as bulk events. The

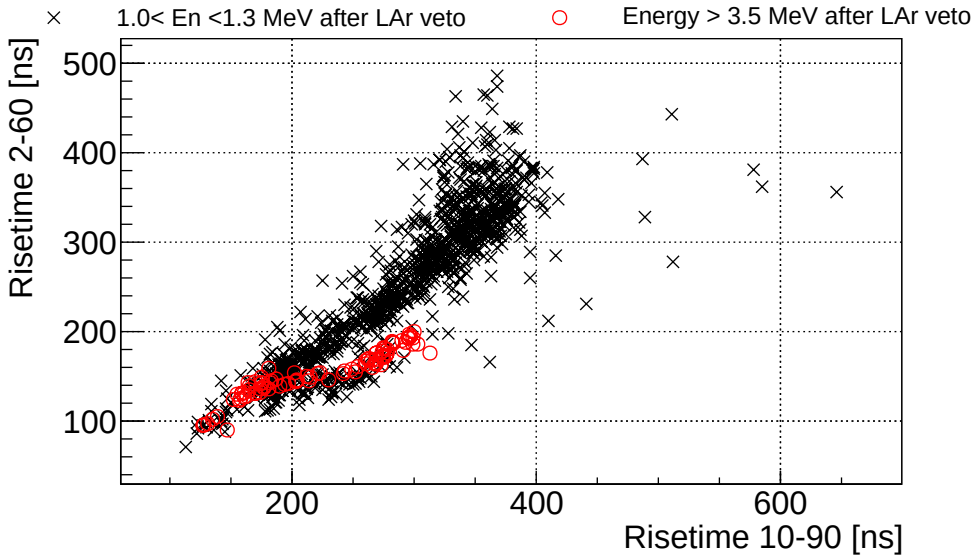

Figure 5.7: Distribution of the rise times parameters for ANG2. The high energy events ($E > 3.5$ MeV) are shown as red circles. The black crosses shows the distribution for events with $1.0 < E < 1.3$ MeV after LAr veto. These are mainly due to $2\nu\beta\beta$ decays and are therefore SSE which are uniformly distributed in the Ge volume. A fraction of $2\nu\beta\beta$ events have similar rise times as the α-induced events but the majority is much slower.

classification must therefore be based on two parameters: one rise time dedicated to the first half of the leading edge and one rise time which is sensitive also to the slower component associated with longer electron paths. For the latter there is a natural candidate: the rise time 10-90% (RT_{10-90}) is already used in GERDA for the quality cuts and other studies and it is known to be a reliable parameter and quite robust against noise. The other parameter should reflect the very first part of the signals which is closer to the amplitude of the baseline and therefore more affected by the electronic noise. After some tests with different rise time thresholds (1-10%, 2-60%, 5-50%), the 2-60% (RT_{2-60}) was chosen. The 2% quantile is shortly after the interaction and just above the amplitude of the noise for high energy signals ($E > 1$ MeV). The position of the 60% quantile can discriminate between energy depositions within the crystal (brown) and on the p+ electrode region outside the bore-hole (red in Figure 5.3).

Figure 5.7 shows the distribution of these two parameters for events due to $2\nu\beta\beta$ and for α-induced events.

5.2.3 Pulse shape simulation and data

PSS validation

In this section the distributions of the rise time parameters for PSS and data are compared. The goal is to understand the limitations of the PSS and to know how far it is a reliable method for the interpretation of the features of the pulses. Besides the electronic response, the effect of the electronic noise must also be taken into account.

The influence of the noise on the estimation of the rise time in the data has been studied by enhancing the noise level of high energy pulses. It was observed that the noise reduces the precision of the RT_{10-90} estimation to ~ 10 ns around 1 MeV. Some detectors, in particular ANG4, show a slightly worse resolution. The RT_{2-60} is more sensitive to the noise level because the 2% quantile amplitude is closer to the baseline level. Overall, for signals with energy above 1 MeV the precision of the rise time estimation is better than 20 ns. More details on the method and on the results are presented in Section 6.1.2.

A 14 ns smearing is applied to the rise time distributions to include the noise in the PSS results. Each point of the PSS grid contributes to the total rise time probability density function with a Gaussian curve with $\sigma = 14$ ns, centred at the rise time value of the point and normalised by the squared distance from the axis. The normalisation takes into account that the PSS samples a 2D cross-section while the $2\nu\beta\beta$ is uniformly distributed in the detector volume.

The resulting distributions are shown together with the experimental ones in Figure 5.8 and Figure 5.9. The simulation can reproduce the main features of the distributions. All distribution show the presence of two peaks at the extremities. The fast rise time peaks can be produced by the limited bandwidth of the read-out electronic, which does not allow to record faster signals. These peaks are described by the simulations after the optimisation of the GBP parameter of the electronic response model, see Section 5.1.3. In the data, the peaks with longer rise time are distorted by the presence of slow NSP. The NSP arise from the outer millimetre of the detectors which account for about 7-10% of the volume. Hence, a similar fraction of the $2\nu\beta\beta$ events are expected to be affected at some level. The discrepancy is bigger for the distributions of the RT_{10-90} because it is more sensitive to the delayed charge collection from the n+ region. Overall, the simulation does reproduce qualitatively the features of the data distributions and describes the differences among the seven detectors. For example, it correctly predicts a wider RT_{2-60} distribution for ANG5, between 100 ns and almost 500 ns.

Rise time maps

The maps in Figure 5.10 and Figure 5.11 report the simulated values of the two rise time parameters for all the points of the 1 mm mesh.

The first clear observation is that the fastest signals are generated between the end of the bore-hole and the top face of the crystals, and in the proximity of the groove. The RT_{2-60} is

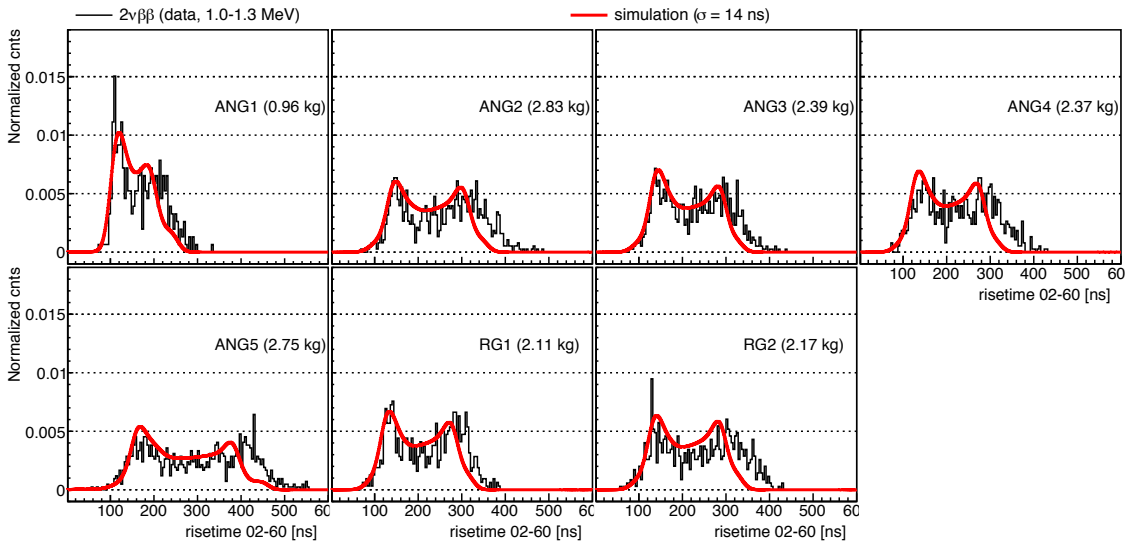

Figure 5.8: Distributions of the RT_{2-60}. In black, the distributions of the rise time parameters for $2\nu\beta\beta$ events are shown. The data selected have energy between 1.0 MeV and 1.3 MeV and survived the LAr veto. The red lines show the distributions of the rise times from the PSS for homogeneously distributed events. The rise time of each point of the 2d 1 mm grid contributes to the distribution proportionally to its squared distance from the vertical axis. The PSS distributions are smeared ($\sigma = 14$ ns) to reproduce the effect of the electronic noise. The discrepancy at the high-end of the distribution is attributed to the contribution of NSP, which are present in the semi-coaxial detector, but not implemented in the PSS model. This difference does not impact the results of this analysis since it is focused on the left side of the distribution which reproduces the data quite well.

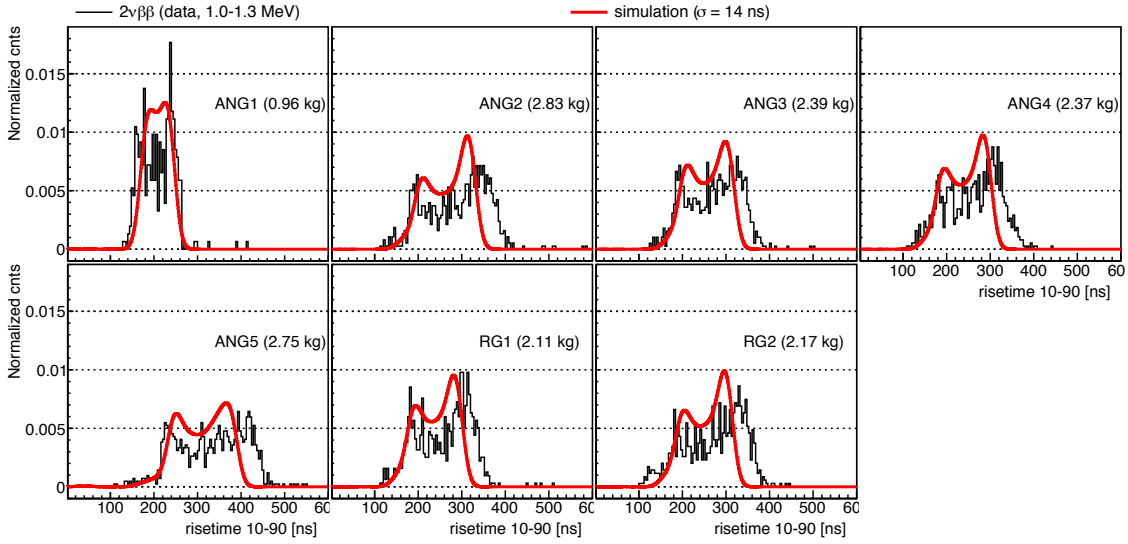

Figure 5.9: Distributions of the RT_{10-90} for $2\nu\beta\beta$ data and PSS (see caption of Figure 5.8).

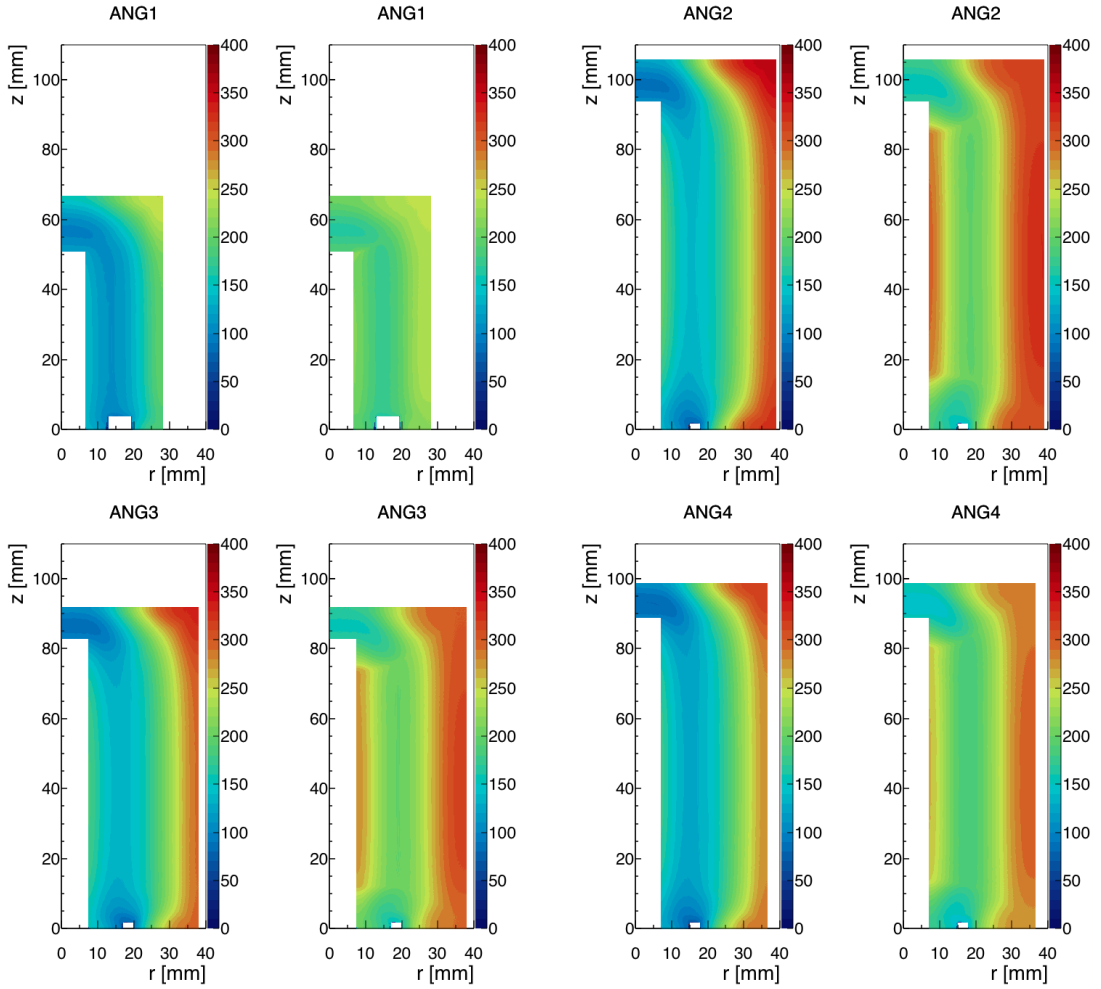

Figure 5.10: PSS rise time maps. The maps of the RT_{2-60} and RT_{10-90} computed from the simulated pulses of the 1 mm grid are shown for the following detectors: ANG1, ANG2, ANG3, ANG4. It can be seen that the fastest signals are associated with the volume surrounding the groove and near the bottom of the bore-hole. The sides of the bore-hole are characterised by higher RT_{10-90} values. It is important to notice that fast pulses arise also from the bulk volume roughly above the groove, events from this region are also classified as potentially α-induced.

more sensitive to the position of the interaction in these two regions. It is also important to notice that the PSS fails to reproduce the charge collection in some portions of the crystals close to the groove. In particular the biggest undefined regions (deep blue colour, RT= 0) occur in ANG1 and ANG4, i.e. the detectors with the biggest grooves. This problem, also present in the other detectors, occurs every time the trajectories of the charge carriers cross the groove surfaces. The trajectory computation accounts only for the internal electric field and the model does not include a description of the charge transportation along the surface.

For all the detectors the two maps have similar features, i.e. in general the RT_{10-90} and the RT_{2-60} are correlated. Slower pulses have higher values for both parameters. The exception is the side of the bore-hole, here the first part of the pulse is relatively fast compared to the last part as seen in Figure 5.3.

These maps show the limits of the rise time parameters. The selection of pulses generated on the α sensitive surfaces may also include pulses from a fraction of the bulk volume. This is also

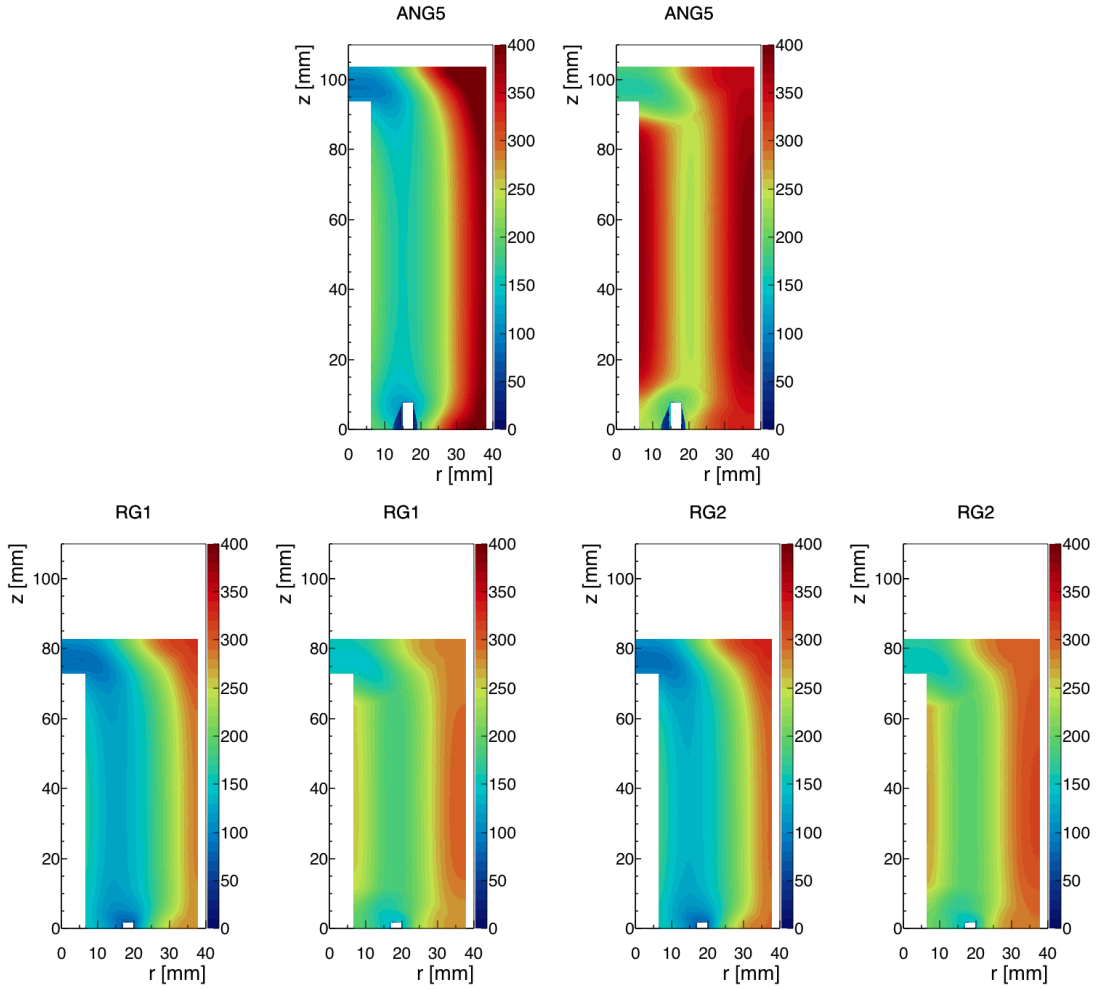

Figure 5.11: PSS Rise time maps. The maps of the RT_{2-60} and RT_{10-90} computed from the simulated pulses of the 1 mm grid are shown for the following detectors: ANG5, RG1, RG2. Also these detectors show the features described in Figure 5.10

evident from Figure 5.3: the red and the brown pulses have similar features, hence any simple analysis will struggle to separate them properly.

Pulse shape analysis

The comparison of the global rise time distributions of data and simulation (Figure 5.8 and Figure 5.9) showed that the PSS can reproduce qualitatively the features of the $2\nu\beta\beta$ distributions. The comparison of the rise time for the events generated along the α sensitive surfaces is shown in Figure 5.12. It must be taken into consideration that the simulated pulses are uniformly distributed along the edges of the 2D crystal section, not on the surfaces. The distribution of the contamination on the GERDA detectors is unknown and there is no reason to assume that it is uniform.

In the PSS scatter plots (central column of Figure 5.12), the points from the lower part of the bore-holes are distributed between the cluster of points from the middle of the bore-hole and those from its brink. This distribution is often not visible in the data or not distinguishable from the higher part of the bore-hole (near its end). In the simulations the waveforms from the end of the bore-hole form a dense cluster of points (blue), which is also usually not visible in the data. These

missing features may be due to the lack of resolution in the measurement of the rise time or to the lack of α contamination on the inner surfaces of the bore-hole.

The left part of the distributions in the data seems often denser than in the simulations (red points). This could indicate a relatively high contamination on the p+ flat surface outside the bore-hole. This effect is emphasised by a geometrical artefact: the simulation samples only one line along the sensitive surface that scales as the square of the distance from the axis and the external part of the p+ contact is the farthest from the axis.

The semi-coaxial signals can be separated into broad classes according to the value of the two rise times:

- **Bore-hole side** with events from the curved side of the bore-hole. These events are described by the green trace of Figure 5.3, the electron-hole pairs are generated in the proximity of the p+ electrode but far from the anode. The leading edge is fast in the first part (small RT_{2-60}) but it slows down due to the long path of the e^-. The points simulated along the side of the bore-hole are shown in green on the left side of Figure 5.12. About 80% of the points are concentrated in the top left of the distribution while the line connecting with the other events are associated with a few millimetres on the top and the bottom of the bore-hole. This class is contained in the **green boxes** in the right side of Figure 5.12 and it is associated with the color **green** in all following plots of the chapter.

- **External p+**, from interactions in the proximity of the horizontal p+ surface outside of the bore-hole. The charge carriers that generate this signals do not need to cross the full thickness of the detector because the electrons are collected next to the groove (n+ wrap around). These events are described by the red trace of Figure 5.3. The points simulated along this section of the p+ electrodes are shown in red in the left side of Figure 5.12. This class is contained in the **red boxes** in the right side of Figure 5.12 and it is associated with the color **red** in all following plots of the chapter.

- **Groove** events, with very fast rise time. If the charge carriers are released in the portion of volume where the electrodes are separated only by the groove their paths are really short. Figure 5.3 shows in yellow a signal of this kind. The inner, top, and outer surfaces of the groove are coloured in orange, violet, and brown respectively on the left side of Figure 5.12. The signals arising from these regions cannot be simulated by SigGen. The trajectories computed according to the electric fields often cross the groove surfaces and SigGen does not include a model for the charge diffusion along the surfaces. This class is contained in the **blue boxes** in Figure 5.12 and it is associated with the color **blue** in all following plots of the chapter.

- **Bore-hole bottom**, in the simulations, interactions on the bottom of the bore-hole produce a cluster of events located in the middle of the other classes. The e^- released in this area move vertically towards the anode and their path have very similar lengths, hence the dense cluster produced by the PSS. These events, described by the blue trace of Figure 5.3, are difficult to distinguish from the other classes of α-induced events. The plots on the left side of Figure 5.12 show the simulated events of this kind in blue. This class is located on the edge between the **blue boxes** and the **red boxes** on the right side of Figure 5.12 .

- **Bulk**, as shown in Figure 5.7 most of the double beta events have longer rise times than all the previous classes. Since the goal of this chapter is to study the α-contamination, all other events will be treated as bulk events not associated with α decay on the surface. Figure 5.3 shows examples of these signals in pink and brown. These events populate the **white region** above the three boxes on the right side of Figure 5.12 and it is associated with the color **black** in all following plots of the chapter.

The thresholds used to distinguish the classes of α-like events are reported in Table 5.3. The values were chosen by observing the distributions of the high energy data and comparing them with the results of the simulation.

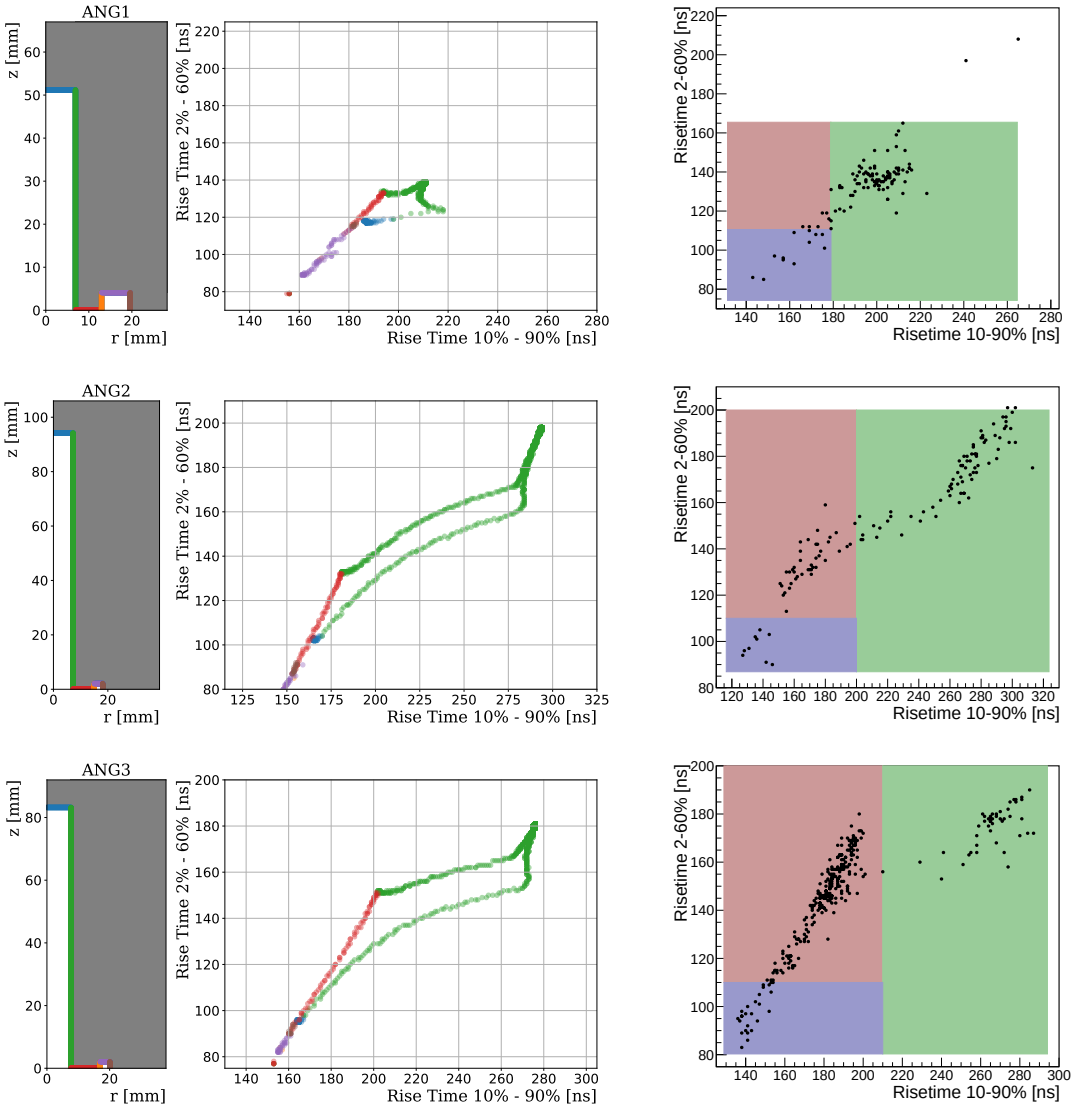

Figure 5.12: Comparison of PSS surface events and high energy events from data. On the left the diagrams show the origin of the simulated signals. The colour code represents the different α-sensitive surfaces: blue for the bottom of the bore-hole, green for the side, red for the external p+ electrode, and orange, purple and brown for the three sides of the groove. The central plots show the rise time values for the simulated pulses. Some of the points from the sides of the groove (orange for the inner side and brown for the outer side) are not properly simulated due to the influence of surface effects. The plots on the right show the rise times' distribution and the classification of the events above 3.5 MeV. The detectors shown here are: ANG1, ANG2, ANG3; on the next page: ANG4, ANG5, RG1, and RG2. The simulation reproduces the features of the distributions and the differences among the detectors. Since the simulation distributions are not affected by the electronic noise, their structures are better defined than in the data (i.e. clusters and bands). Most of the length of the bore-hole sides are associated with dense clusters at the top-right of the green distributions. In the data, these clusters are often visible as main structure on the right side (but the data point are more spread out). The higher edge of the blue region (of the right plots) is approximately set below the green and red points of the simulation.

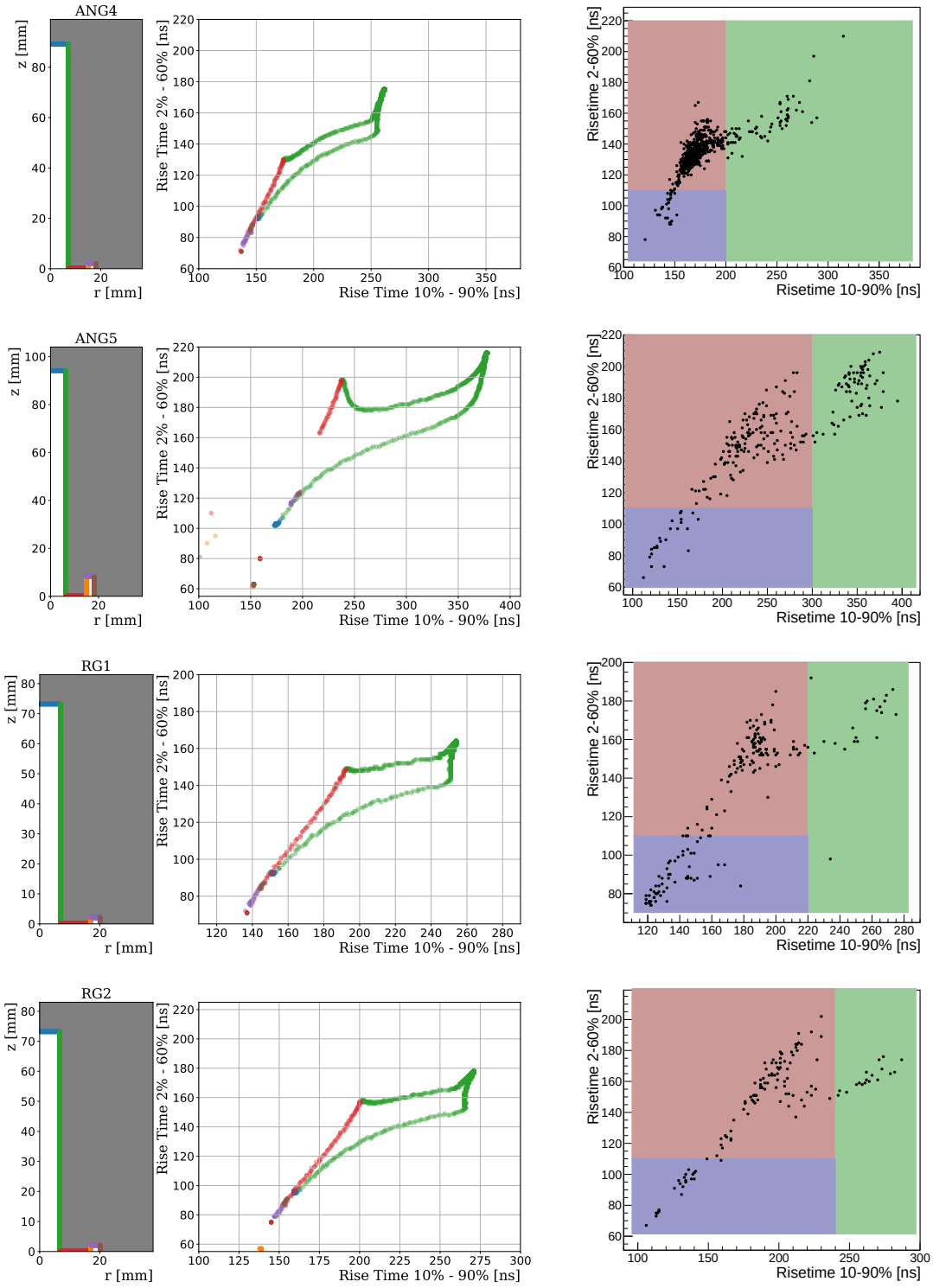

Comparison of PSS surface events and high energy events from data for ANG4, ANG5, RG1, and RG2.

Det.		RT_{2-60}	RT_{2-60}	RT_{10-90}
ANG1	[ns]	110	165	180
ANG2	[ns]	110	200	200
ANG3	[ns]	110	200	210
ANG4	[ns]	110	220	200
ANG5	[ns]	110	220	300
RG1	[ns]	110	200	220
RG2	[ns]	110	220	240

Table 5.3: Thresholds for classification of semi-coaxial signals. The first column reports the RT_{2-60} value that divides groove and flat-p+ events. The second column reports the RT_{2-60} that divides α-induced and bulk events. The third column reports the RT_{10-90} threshold for round-p+ events.

5.3 Application to physics data

The analysis can now be applied to the GERDA spectrum to study the α contaminations of the semi-coaxial detectors. The grey spectrum in Figure 5.13 contains all the events not vetoed by anti-coincidence (with other HPGe, with LAr scintillation or cosmic muons). The events associated with α-sensitive surfaces according to the classification of Table 5.3 produce the three components drawn in red, green, and blue. A significant fraction of the background above 2 MeV can be attributed to α decays. The high energy tail of the $2\nu\beta\beta$ is visible between the ^{42}K line at 1.525 MeV and the $Q_{\beta\beta}$ (2.039 MeV). The $2\nu\beta\beta$ decays are uniformly distributed in the detector and the share associated with each class is proportional to the fraction of the volume associated with the class. The higher count rate of the three coloured spectra below 2 MeV is therefore not associated with α-decays but $2\nu\beta\beta$-decays in the proximity of the p+ contact.

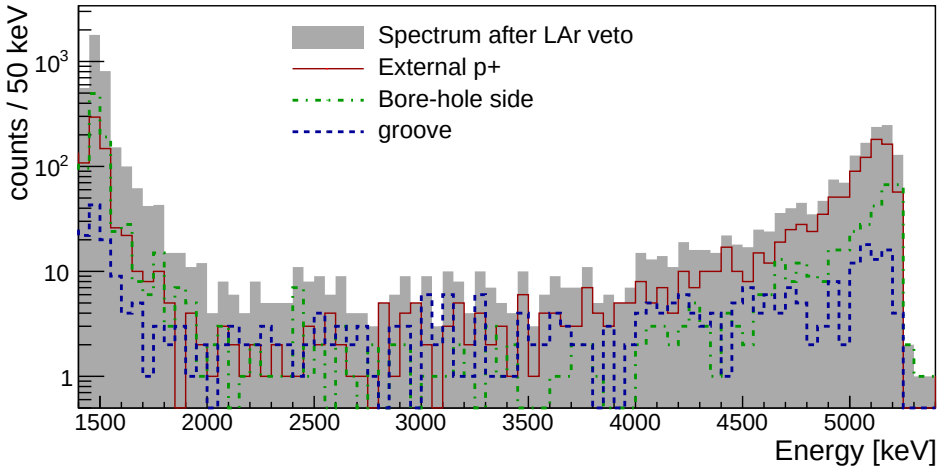

Figure 5.13: Spectrum of semi-coaxial detectors in GERDA Phase II. The grey histograms show the counts after LAr veto and without any PSD cut and the three coloured histograms show the contribution of the α-sensitive surfaces classified according to Table 5.3. The fast pulses are a major fraction of the spectrum at 2 MeV but the shares of the three classes vary in each energy interval. At lower energy (around 1.5 MeV) the green histogram has the highest count rate because it is associated with a larger volume. At higher energy (above 4.0 MeV) the red histogram dominates the α peaks region, this is mostly due to the high count rate of ANG4 and ANG3. The blue component is the flattest one associated with the surfaces with more energy degradation.

The three spectra of the three classes of α events show different features. The red spectrum, associated with the flat p+ surfaces, accounts for the majority of the counts in the α peaks region. Its count-rate dramatically decreases at lower energy where it represents about one third of the total α rate. On the other hand, the blue spectrum of the groove region is in comparison almost constant going from less than 10 counts per bin (50 keV) at 5 MeV to 1 or 2 counts per bin at 2 MeV.

This feature can be explained by the energy degradation of surface α signals. Most α signals are generated by ^{210}Po decays at 5.3 MeV, and some ^{226}Ra at 4.8 MeV. Part of the energy is lost through the thin layer of non-active material, e.g. p+ doped or passivation layer. If the α particle direction is perpendicular to the surface, the energy loss is minimal, thus the energy is reconstructed in the peak a few hundreds keV below the decay Q value. If the particle momentum is parallel to the detector surface, all the energy will be lost in the dead layer. The degradation of the reconstructed energy depends on the incoming angle of the particle and on the thickness of the dead material. A disuniformity of the boron implantation could explain the difference between spectra of α decaying on the external detector surface (red) and on the side of the bore-hole (green). The boron atoms for the p+ doping are shot into the bore-hole at an angle while the crystal is rotating around its axis. The thickness of the p+ dead layer is then most likely different for the horizontal surfaces (i.e. outside the bore-hole) and for the vertical surface (i.e. side of the bore-hole) due to the difference in the incoming angle of the ions. With a thicker dead layer the probability that particles with shallow angles share the Bragg-peak energy between the active and the inactive material decreases. Therefore surfaces with thicker dead layers will have less degraded signals relative to the count rate in the peaks.

There are also indications of a second energy degradation mechanism. Some of the signals with a very fast leading edge ($RT_{2-60} < 110$ ns) are followed by a slow charge collection that continues for tens of µs. Similar signals have been observed by the Majorana collaboration [117] for detectors with a more expansive surface between the detector's electrodes. Our interpretation is that in these cases part of the charge carriers are promptly and properly collected while the rest move much slower on the surfaces that separate the two electrodes. In this case, the energy is further degraded by the missing electrons' contribution. This mechanism deforms the groove region spectrum (blue) shifting some counts to lower energies.

As a result, the relative contribution of the α contamination in the groove is higher at lower energies and the contamination from the surface between the groove and the bore-hole is the dominant one only above 3.5 MeV. Figure 5.14 shows the composition of the spectrum in 500 keV regions, before and after LAr veto. The total contribution from α sensitive volumes constitutes about half of the semi-coaxial counts between 2.0 and 2.5 MeV.

An additional component is present in the interval between 1.4 MeV and 3 MeV compared to the samples considered in the previous sections. The classification is based on samples of SSE, while in this case γ-rays (from ^{42}K, ^{40}K, and ^{208}Tl) produce mainly multiple site events (MSE). The analysis of pulse shapes of MSE in semi-coaxial detectors goes beyond the aims of this work. Nevertheless, since MSE signals consist of two or more single site signals superimposed on each other, the rise time of a MSE is typically larger than the one of SSE. In our classification therefore most of the MSE are identified as bulk events from surfaces not sensitive to α.

5.3.1 Alpha background removed by ANN_MSE

Since the α component is so important in the semi-coaxial background of the ROI, it is natural to evaluate whether it is possible to reduce the background and improve the sensitivity with a rise time based pulse shape discrimination. A well established semi-coaxial PSD technique has already been in use since Phase I, the Artificial Neural Network for MSE (ANN_MSE) [104, 67]. A further PSD technique would be more effective if it were anti-correlated with the ANN_MSE. In other words, removing a class of events already cut by another technique could potentially reduce the $0\nu\beta\beta$ efficiency without an effective reduction of the background. The ANN_MSE is designed to remove MSE which have typically a longer rise time compared to SSE, hence any cut base on the

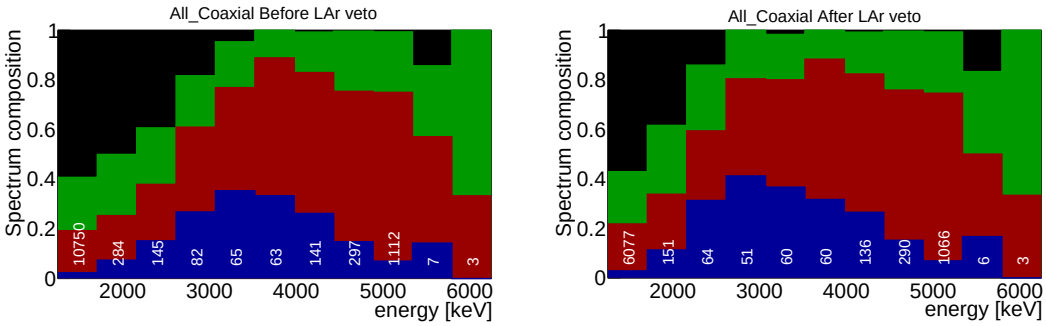

Figure 5.14: Composition of the GERDA spectrum in 500 keV binning, before (after) LAr veto on the left (right). The colour represents the four classes defined by the rise time parameters. The black bars indicate the fraction of events from the bulk volume, below 2 MeV these are mostly due to $2\nu\beta\beta$ decay. The blue ones refer to the events from the groove region. The red ones refer to the flat-p+ events. The green ones refer to the round-p+ events. On the bottom of each bin the total number of counts is reported.

rise time that targets fast α events should be indeed anti-correlated to a certain degree with the ANN_MSE. It has also been shown through Monte Carlo and PSS studies that the ANN_MSE is also sensitive to the location of the interaction and rejects about 20% of the $2\nu\beta\beta$ spectrum [104].

The synergy between the rise time of the signals and the ANN_MSE classification is shown in Figure 5.15. It reports all events above 1.6 MeV with their classification based on the rise times and on the ANN_MSE. It is clear that almost all the green dots, α-like signals from the side of the bore-hole, above 1.8 MeV are rejected by the ANN_MSE. The ANN_MSE tags also some red dots, from the p+ surface outside the bore-hole. These are probably events with interactions near the edge of the bore-hole, which populate the horizontal bands of the RT_{10-90}–RT_{2-60} distribution (Figure 5.12). It can be concluded that the ANN_MSE is rejecting with a good efficiency the α signals with a RT_{10-90} greater than ~ 200 ns.

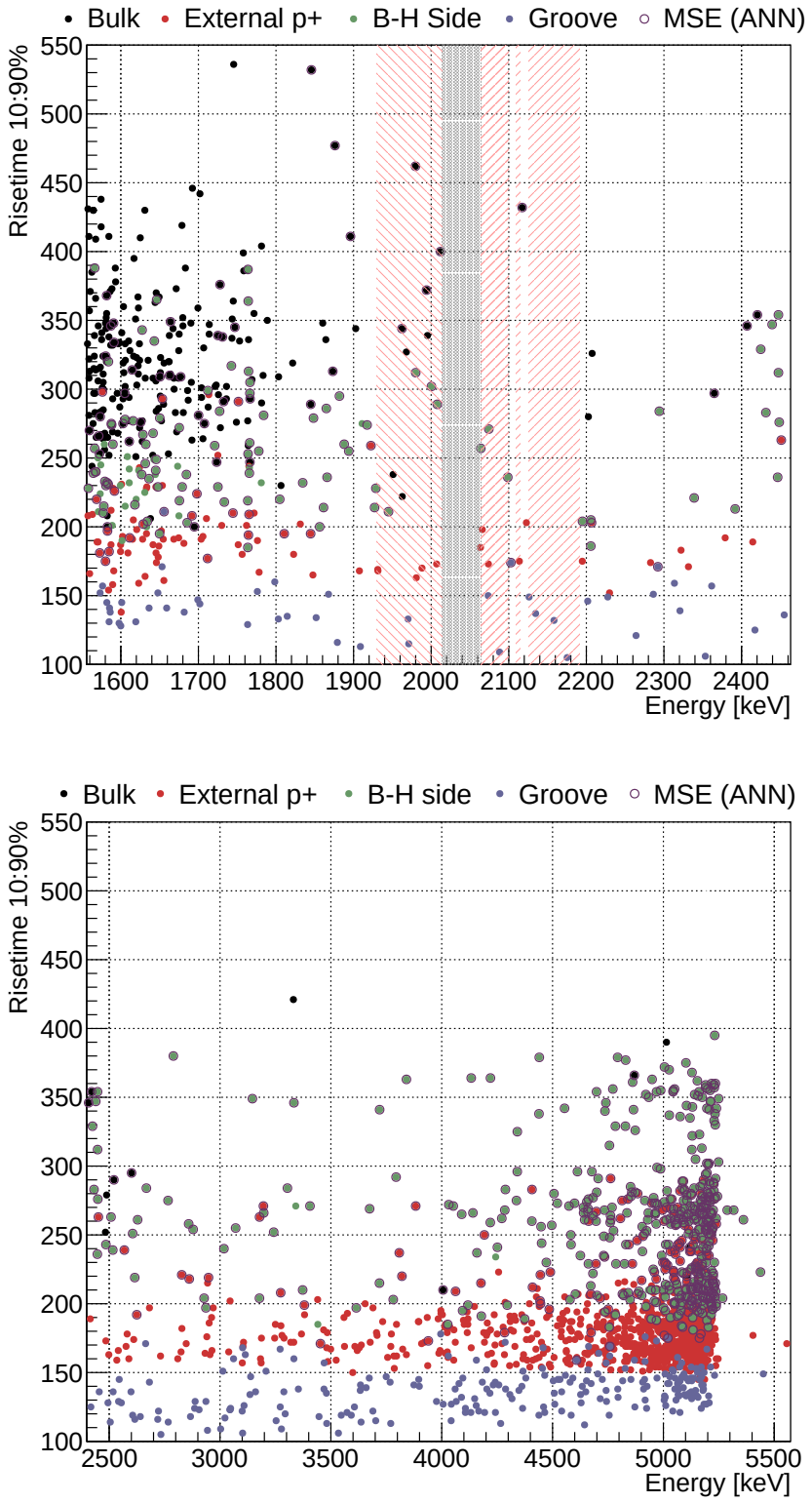

Figure 5.15: Selection of ANN_MSE with respect to the event classes. The plots show the semi-coaxial events above 1.6 MeV, their RT_{10-90}, and their classification. Most of the α from the side of the p+ (green) are rejected by the ANN_MSE. The counts in the interval around the ROI, marked in grey, were removed from the dataset for the blind analysis. The background index is computed in the red side-bands.

5.4 Conclusions

This chapter presented a study of the pulse shape of the GERDA semi-coaxial detectors with focus on the signals produced in the α sensitive part of the volume. The analysis is based on the observation that α signals have fast leading edges. A pulse shape simulation was used to improve the understanding of signal formation and to associate the different signal shapes with the location of the α decay. The high energy events have been classified into three types of signals according to the value of two rise time parameters. The first parameter RT_{10-90} is proportional to the average current induced on the read-out contact. The second parameter RT_{2-60} is sensitive to the first part of the leading edge and to the collection time of the holes.

The PSS can reproduce with good accuracy the features of the rise time parameters in the inner part of the detectors, i.e. around the bore-hole and in the crystal's bulk. Through analysis of the rise times it is possible to study the location of the α contamination. It is clear that the α sources are not uniformly distributed on the surface of the detectors. The critical surface is the external part of the p+ contact which in some detectors seems contaminated. The contamination could be attributed to the handling of the detectors during production. In particular during the production of the electrodes a protective mask is stuck to the base of the detectors to protect the p+ region. Some residue material from the mask may be the possible source of contamination of the external surface of ANG3 and ANG4.

This analysis provides also a better understanding of the source of α signals with delay charge collection. These signals were the reason for postponing the unblinding of the semi-coaxial dataset in the summer of 2017. The signals are due to α decays in the proximity of the groove and they are characterised by very fast leading edges.

The α decays contribute significantly to the background in the ROI. The ANN_MSE developed against γ-induced MSE already removes a fraction of these decays. In the next chapter it will be shown that the residual components can be rejected with a single parametric cut on the RT_{10-90}.

Chapter 6

Pulse shape discrimination for semi-coaxial detectors

This chapter discusses a method based on rise time parameter to reject the α-induced background from the enriched semi-coaxial dataset. The pulse shapes of α events have been described in the previous chapter. It was also shown that a fraction of these events are rejected by the volume cut of the artificial neural network discrimination for multiple site events. The remaining fraction can be removed with a mono parametric (RT_{10-90}) pulse shape discrimination (PSD) method. The design and the performance of the algorithm used to extract the parameter are discussed in Section 6.1. Section 6.2 defines the figure of merit used to set the threshold between $0\nu\beta\beta$-like and α-like pulses. The cut stability and its effects on calibration (Section 6.3) and physics (Section 6.4) data are discussed next. The signal efficiency and its systematic uncertainties are considered in Section 6.5. The background index achieved for the semi-coaxial dataset is reported in Section 6.6 with a summary of the results of this chapter.

6.1 Extraction of the PSD estimator

In order to develop a PSD, the assessment of the reliability of the classifier is paramount. The algorithm used to estimate the rise time parameter is described in detail in this section. Its performances are then tested using four simulated pulses superimposed with experimental electronic noise to mimic the response to pulses with different energies. The goal is to estimate the precision and the accuracy of the rise time estimation.

6.1.1 Design of the algorithm

The first step to compute the rise time between 10% and 90% of the leading edge is to assess the total amplitude of the pulse. Since the amplitude is proportional to the energy of the recorded events, many filters have been developed for this purpose. Among the ones used by the GERDA collaboration (pseudo-Gaussian, ZAC, Gast-trapezoidal), the Gast filter is the only one to provide a direct measurement of the amplitude. The pseudo-Gaussian filter deforms the signals with a series of moving window averages before measuring the amplitude. Its output is proportional to the energy of the event, but different from the amplitude of the original signal. The standard GERDA ZAC filter was also considered, but the reconstructed amplitude varies up to a few percent according to the different filter settings (τ and σ) which are optimised against the energy resolution with every calibration. The Gast filter produces by construction a trapezoidal signal with the same amplitude of the input pulse.

The amplitude of the pulse is measured from the low frequency waveform (LF). The Gast trapezoidal filter consists of: a deconvolution of the exponentially decaying tail of the charge sensitive amplifiers with the characteristic times reported in Table 6.1, a differentiation of the

	ANG1	ANG2	ANG3	ANG4	ANG5	RG1	RG2
τ [μs]	123.6	144.8	124.1	130.4	135.7	158.4	161.9

Table 6.1: Set of time constant for Gast filter deconvolution.

samples 10 μs apart, and an 8 μs wide integration. The amplitude is finally read in the middle of the 2 μs long flat-top of the resulting trapezoidal waveform. Since each sample of the low frequency waveforms is the sum of four 100 MHz samples, the amplitude of the LF waveform is four times larger than the one of the high frequency (HF) waveform.

The rise time is then extracted from the HF trace with the following steps:

1. Baseline restoration, computing the average value between 76.6–78.6 μs
2. Moving Window Average (3x30 ns)
3. Linear interpolation (down to 1 ns)
4. Determination of 10% and 90% quantile positions

The rise time is computed by the GELATIO module GEMDRiseTime, which searches for the first sample above the higher threshold (i.e. 90% of the amplitude) and the last sample below the lower threshold (i.e. 10%).

All the digital filters were already implemented in GELATIO, only a small modification of the GEMDRiseTime module was required to retrieve the amplitude from a filter running on a trace with a different sampling frequency. All modules are documented in the appendix B of Ref. [81] and in the software readme files [118].

6.1.2 Bias, resolution and robustness of the algorithm

The PSD method is based on the comparison of the rise time distributions for the $0\nu\beta\beta$ events and high energy α events. The rise time parameter must therefore be consistent in the energy interval between 1 MeV and 4 MeV. The study of possible energy dependencies will also allow for the evaluation of the $0\nu\beta\beta$ survival probability on the basis of the performance on the $2\nu\beta\beta$ sample (1-1.3 MeV). This section focuses on the stability of the algorithm against electronic noise, Section 6.3 discusses the stability of the survival probabilities for different samples of events.

r [mm]	z [mm]	RT [ns]
5	100	198
25	5	286
8	50	310
35	50	344

Table 6.2: Position and rise times of the simulated waveforms.

Four simulated pulses were used to study the stability of the algorithm. The pulses, shown in Figure 6.1 and in Table 6.2, arise from different positions of the ANG2 detector: the bottom of the bore-hole (r5-z100), the side of the bore-hole (r8-z50), the bulk of the active volume (r35-z50) and the bottom of the detector close to the n+ contact (r25-z5).

The simulated waveforms have been superimposed on baseline events taken from the physics data. The HF and the LF traces have been superimposed on the corresponding baseline using the GEMDAddTemplatePulse GELATIO module. The amplitude of the 2.6 MeV line for each detector is computed as average of all the calibration events in a range of 0.5 keV around 2614.5 keV. Each simulated pulse has been re-scaled using a different baseline to 1%,2%,...,99% and 100% of the 2.6 MeV amplitude. The simulated pulses have been re-scaled in steps of 26 keV of the 2.6 MeV amplitude. The module GEMDAddTemplatePulse also simulates the exponential decay tail from the preamplifier with τ set to 150 ns.

The waveforms produced by GEMDAddTemplatePulse have been analysed with the same chain of modules used for the physics data, with τ fixed at 150 ns instead of the values of Table 6.1.

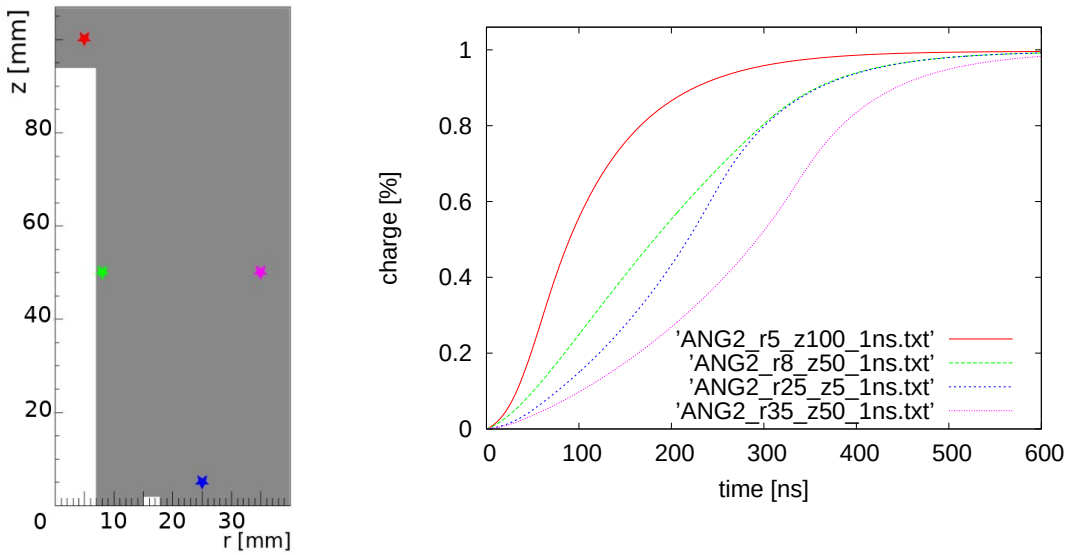

Figure 6.1: The detector sketch on the left shows the position associated with the four waveforms used in Section 6.1.2; the waveforms are shown in the plot on the right. These four pulses are a sampling of the types of SSE found in a semi-coaxial, see Chapter 5. The blue and the green pulses originated in the bulk volume, the red pulse is much faster due to the short distance of the interaction from both electrodes, and the green pulse is similar to the slowest p+ surface events that are selected by ANN_MSE.

The rise time value is then computed as difference between the time position of the 10% and the 90% quantile of the pulse. The amplitude of the pulse, i.e. the value of the maximum, and the position of the baseline are needed to the find position of the quantiles. There are therefore four contributions to the final uncertainty on the rise time estimator: the baseline, the amplitude, and the low and high edge times.

- **The baseline** can be computed both on the HF and LF traces. For the LF trace, several μs of baseline before the trigger are available, the position is computed by averaging about 2000 points relative to $\sim$ 80 μs. For the HF trace, only 2 μs (200 points) of baseline are considered and the estimation of the position is more sensitive to low frequency noise. To control the quality of the baseline position estimation for the HF trace, its value is compared with the one obtained from the LF trace, see Figure 6.2.

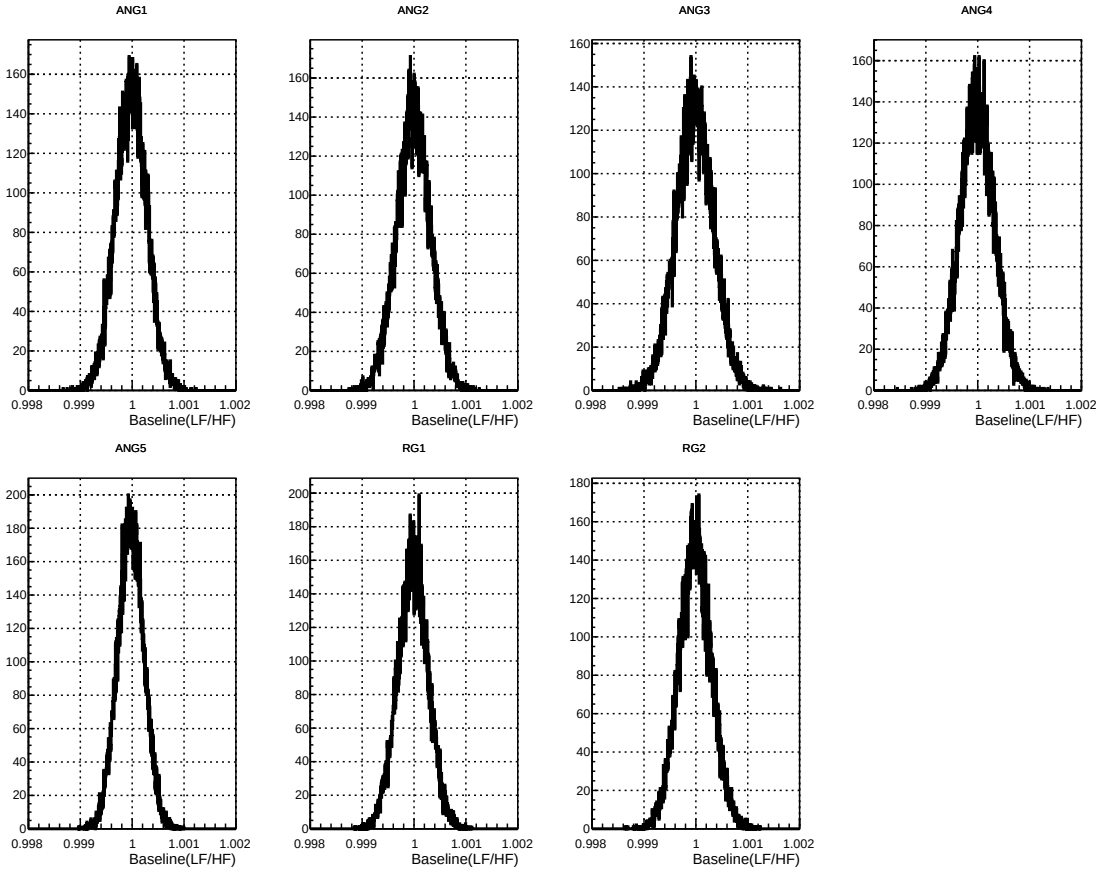

Figure 6.2: Spread of the baseline position measured on the short (HF) trace in comparison with the position measured on the longer baseline of the LF trace. The latter has an higher precision due to the higher number of points available: about 2000 against the 200 points available in the HF baseline. The two values are in better than 0.1% agreement.

- **The amplitude** is computed from the Gast trapezoidal filter. Since the amplitude of the simulated pulses is known, the Gast filter performance can be observed through the ratio between the reconstructed amplitude and its true value. Figure 6.3 shows how the estimation of the amplitude of a pulse is affected by the increase of noise. As expected, the energy filter has a resolution on the per mill level and the centroid of the distribution is not affected by the noise.

- **The low and high edges.** The precision and accuracy of the quantile position are shown in Figure 6.4. The panels on the left show the residuals of the measured rise time compared to the true values (reported in Table 6.2). The resolution is not correlated to the true value, i.e. the first row (rise time$\sim$ 200ns) has a similar spread as the bottom one (rise time $\sim$ 350ns). In particular, above 1 MeV the standard deviation (σ) of the rise time is better than 15 ns. The comparison between the reconstructed positions of the 10% and 90% quantiles are shown in the central and right panels. Is it clear that the main contribution to the spread of the rise time values is coming from the estimation of the 90% quantile position.

In conclusion, the analysis of simulated pulses with different signal-to-noise ratios shows that the estimator of the rise time is reliable above 1 MeV. The distributions of the reconstructed parameters are symmetric, thus indicating the absence of biases or classes of mis-reconstructed events. The resolution is at the level of 14 ns and biases are smaller than 1 ns.

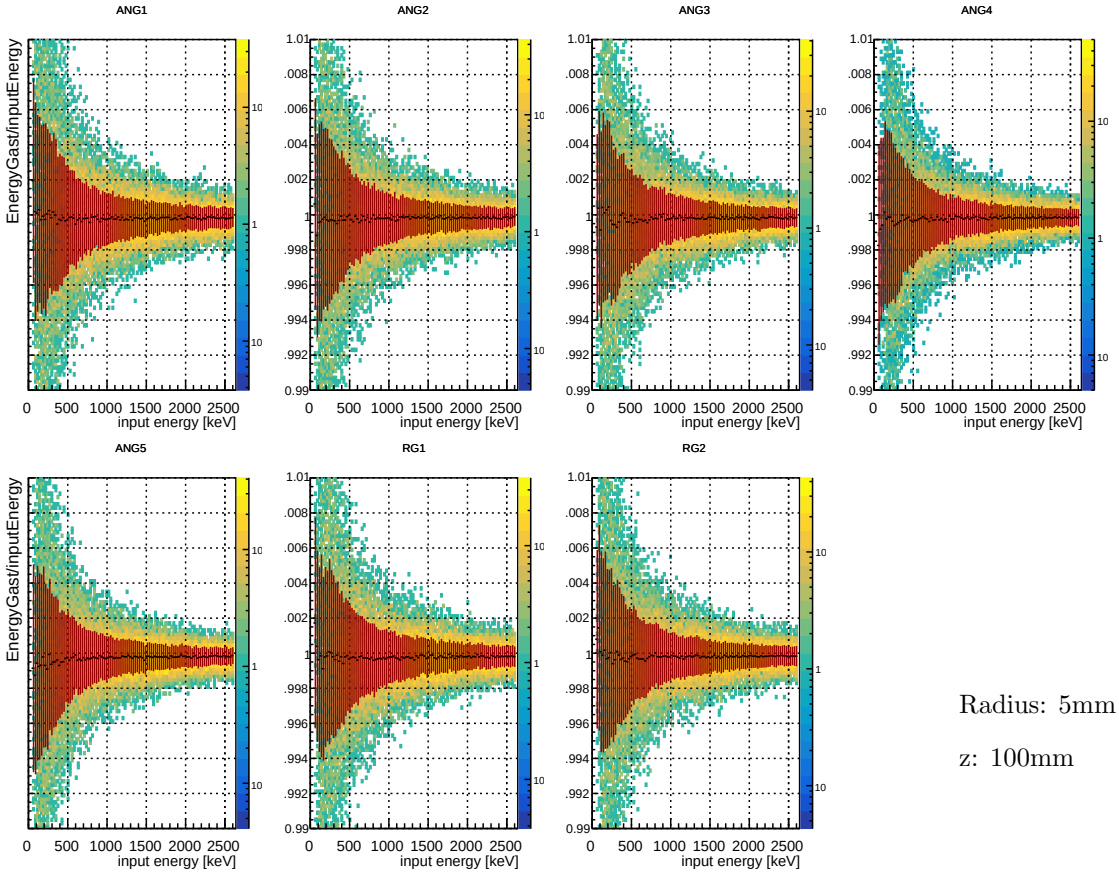

Figure 6.3: Stability of the pulse amplitude extracted by the Gast filter in relation to the noise. The original waveform is simulated for a point like energy deposition above the bore-hole, 5 mm away from the detector axis. The amplitude of the signal is proportional to the desired "input energy" calibrated in relation to the average amplitude of calibration pulses with energy 2614.5 ± 0.5 keV. The noise is obtained from the baseline waveforms of runs 60-88 which passed the baseline quality cuts. Superimposed in red are the centroid values and the spread (std. dev.) of each energy bin. The amplitude measured by the Gast filter is overall reliable. The centroids of the distributions are always within 0.1% of the real value. The resolution of the amplitude is better than 0.1% above 1 MeV.

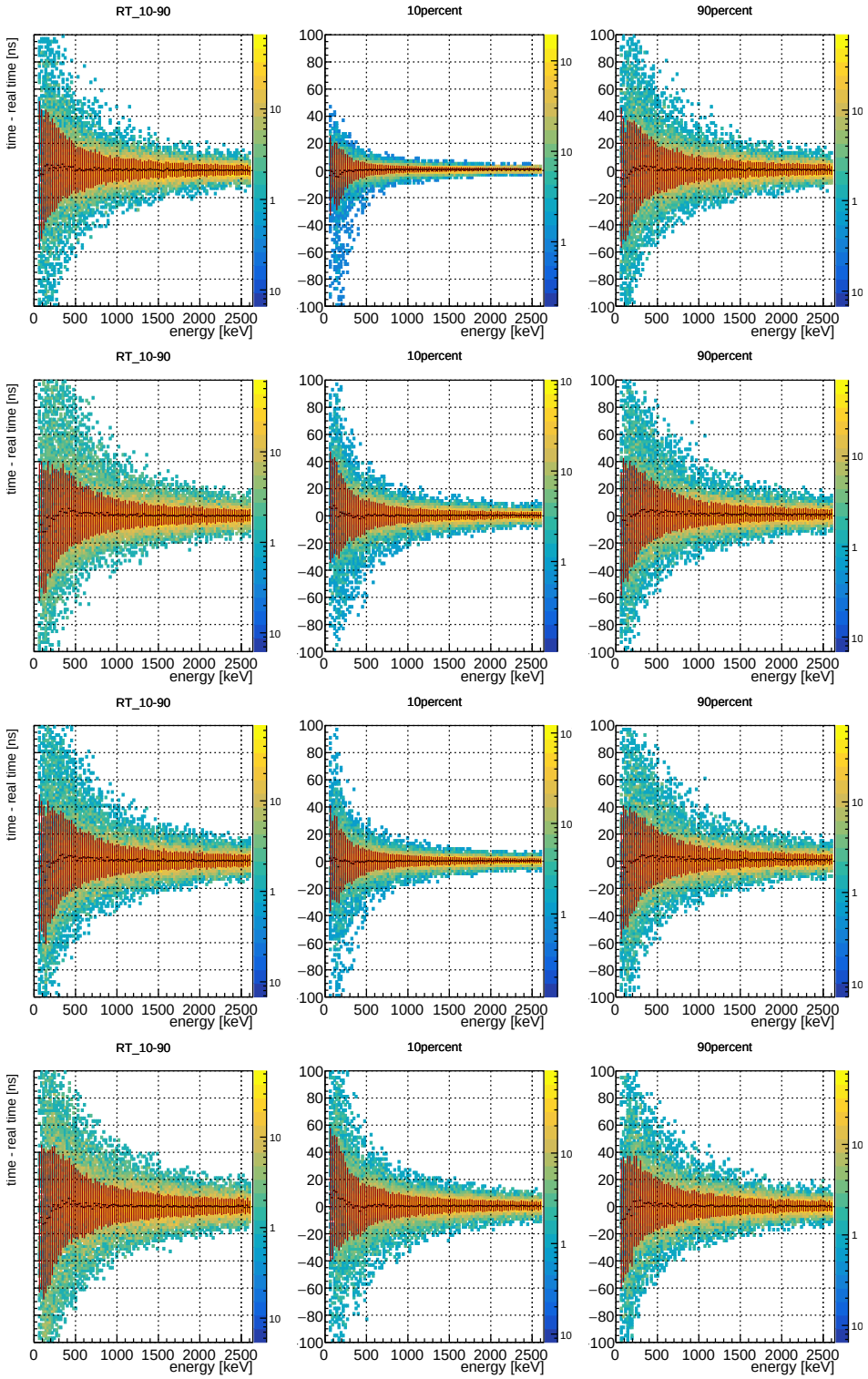

Figure 6.4: The plots show the accuracy and the precision of the rise time 10-90 for the four simulated pulses (from the top r5-z100, r25-z5, r8-z50, r35-z50) injected into a sample of baseline events from physics data. For this figure the pulses have been superimposed to the noise of ANG2. The similar plots for the other detectors are reported from Figure 6.16 to Figure 6.21. The y axis shows the residuals compared to the true value which is computed on the waveform reconstructed at 26 MeV. Superimposed in red are the centroid values and the spread (std. dev.) of each energy bin.

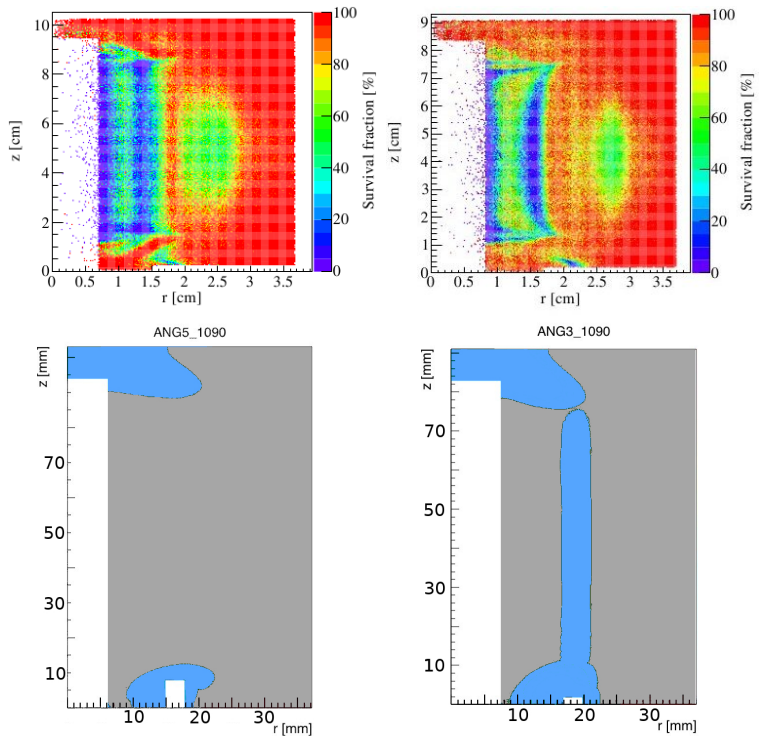

Figure 6.5: Maps of rejected volumes generated with Pulse Shape Simulation (PSS). The top plots (from [104]) show the volume cut of the ANN_MSE for a homogeneously simulated $0\nu\beta\beta$-signal. The bottom plots show in light blue the volume associated with signals with a rise time faster than 215 ns (for ANG5 on the left) and 184 ns (for ANG3 on the right). The maps have been produced by Tommaso Commelato with the PSS described in Chapter 5. In the bottom maps, the fractions of active volume cut are 5.6% and 15.7% respectively. The combination of the two methods removes most of the α-sensitive surfaces. From the maps of ANG5 it is visible that surviving α may come from the corner at the bottom left (around r10 z5). From the maps of ANG3 it is clear than when the Rise Time cut removes more than 10% of the volume (see $2\nu\beta\beta$ acceptance in Table 6.4), it is removing also a fraction of the bulk volume.

6.2 Definition of the cut threshold

This section introduces the method used to determine the cut thresholds below which an event is rejected. The goal is to remove the α events surviving the neural network technique used to discriminate multiple site events (ANN_MSE). The Monte Carlo study in Ref. [104] shows that the ANN_MSE cuts the signals originating in the innermost volume around the bore-hole. A single parametric cut on the rise time 10-90 can remove the remaining α sensitive surfaces (the bottom of the bore-hole and the region of the groove). As Figure 6.5 shows, the volume removed can change significantly according to the performance of the ANN_MSE and it is not possible to define a priori what is the optimal cut threshold.

The thresholds are derived directly from physics data through the comparison of the acceptances for a $2\nu\beta\beta$ and an α. Events between 1 MeV and 1.3 MeV after LAr veto are used as proxy for the $0\nu\beta\beta$ signal. The LAr veto effectively removes the γ-induced events, the remaining spectrum is dominated by $2\nu\beta\beta$ decays. The proxy for the background are the high energy events above 3.5 MeV that constitute a pure α sample. Note that the composition of the background sample is different from the actual background at $Q_{\beta\beta}$, as discussed in Section 5.3, some α components (i.e. groove α) are more affected by energy degradation.

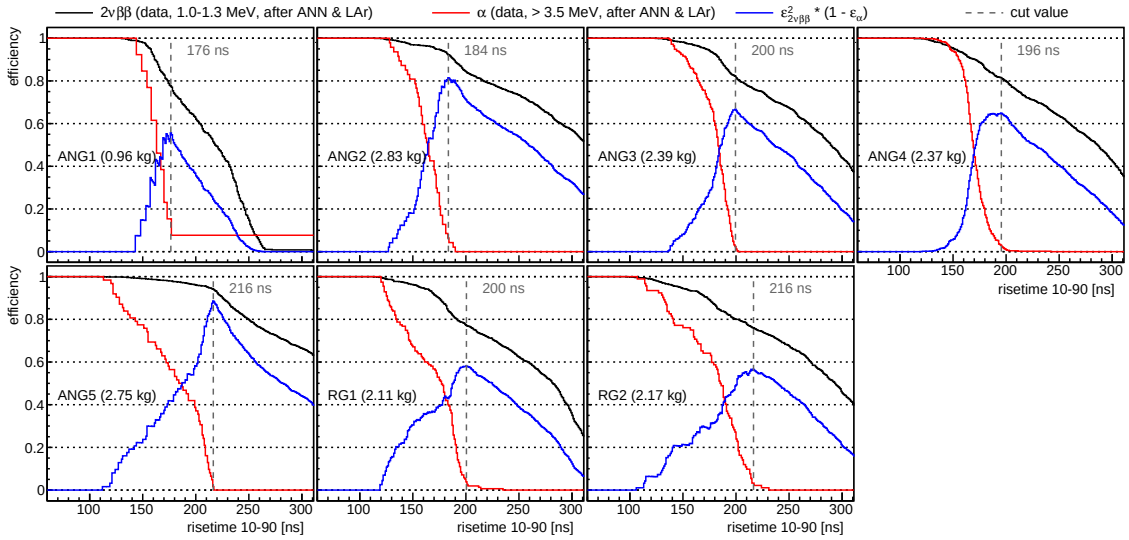

Figure 6.6: Cumulative distribution of the rise time 10-90 parameter for $2\nu\beta\beta$ and high energy events in each detector. In blue the value of the figure of merit is shown. Since the distribution of the high energy events surviving LAr veto and ANN_MSE is quite peaked, the optimal cut removes most of the α contamination. In some detectors (especially ANG1) the limited statistics influence the choice of the threshold. The energy interval on which the background index is computed is not used to determine the cut values to avoid bias in the analysis.

The cut threshold is defined by maximising the signal acceptance and minimising at the same time the signal to noise ratio according to a simple figure of merit:

$$f(x) = \varepsilon^2_{2\nu\beta\beta}(x) \cdot \big(1 - \varepsilon_\alpha(x)\big)\,, \tag{6.1}$$

where $\varepsilon_{2\nu\beta\beta}(x)$ is the signal acceptance of a cut set at x and $\varepsilon_\alpha(x)$ is the corresponding acceptance for α signals. The dependence on the signal acceptance is quadratic because it influences both the exposure and the signal to noise ratio. Moreover, once the expected number of background counts in the ROI is close or below 1 a reduction in exposure can have a bigger (negative) impact on the sensitivity than the background reduction. The cumulative distribution of the rise time for the two samples and the figures of merit for each detector are shown in Figure 6.6.

The robustness of the cut threshold values has been tested against other possible formulations of the figure of merit. The results are shown in Table 6.3. The cut levels are extremely stable, indicating that there is a "natural" threshold strongly defined by two cumulative distributions.

The combined acceptances of the Rise Time and ANN_MSE analysis are reported in Table 6.4. If the Rise Time cut and the ANN_MSE would be independent, their combined acceptance should be equal to the product of their acceptances. Indeed, the product of 84% for the Rise Time cut and 77% for the ANN_MSE is compatible with the acceptance of the combined cut. The value

Figure of Merit	ANG1	ANG2	ANG3	ANG4	ANG5	RG1	RG2
$\varepsilon^3_{2\nu\beta\beta} * (1 - \varepsilon_\alpha)$	170ns	180 ns	198 ns	178 ns	216 ns	196 ns	202 ns
$\varepsilon^2_{2\nu\beta\beta} * (1 - \varepsilon_\alpha)$	**176 ns**	**184 ns**	**200 ns**	**196 ns**	**216 ns**	**200 ns**	**216 ns**
$\varepsilon_{2\nu\beta\beta} * (1 - \varepsilon_\alpha)$	176 ns	190 ns	200 ns	196 ns	216 ns	202 ns	216 ns
$\big(\varepsilon_{2\nu\beta\beta} + (1 - \varepsilon_\alpha)\big)/2$	176 ns	190 ns	200 ns	200 ns	216 ns	202 ns	216 ns

Table 6.3: Cut values extracted from different figures of merit. It is clear that all the figures of merit tested produce similar results. The agreement is due to the slope of the α cumulative distributions and (for some detectors) the limited statistics available in the α sample.

det	Rise Time		Rise Time + ANN_MSE	
	$\varepsilon_{2\nu\beta\beta}$	$\varepsilon_{E>3MeV}$	$\varepsilon_{2\nu\beta\beta}$	$\varepsilon_{E>3MeV}$
ANG1	76.8%±2.0	93%±3	62.4%±2.2	2.7%±1.9
ANG2	92.4%±0.8	63%±5	69.8%±1.3	1.1%±1.1
ANG3	81.8%±1.2	21%±3	64.0%±1.4	0
ANG4	83.1%±1.1	13%±2	58.4%±1.5	3.6%±1.2
ANG5	95.6%±0.6	75%±3	74.3%±1.2	0.6%±0.6
RG1	77.2%±1.4	23%±4	61.3%±1.6	3.0%±1.8
RG2	74.2%±1.4	32%±6	57.7%±1.6	4.0%±2.2
total	84.3%±0.4	39.7%±1.6	64.6%±0.5	2.0%±0.5

$2\nu\beta\beta$:= $1000 < E < 1300$ && $!LArVetoed$

Table 6.4: Survival fraction of $2\nu\beta\beta$ and high energy events ($E > 3$ MeV) for Rise Time cut alone and in combination with the ANN_MSE. The uncertainties are the binomial statistical errors, $\sigma = \sqrt{\varepsilon \cdot (1-\varepsilon)/N}$.

obtained directly from the fraction of events surviving both cuts is however more reliable because it accounts for small correlations, i.e. the two volumes cut may partially overlap.

The third column of the table shows the fraction of high energy events removed by the Rise Time cut, and the last column shows the fraction of high energy events remaining in the spectrum after both. It is clear that the ANN_MSE is more effective in rejecting the α contamination for some detectors than for others. The Rise Time method is then tuned to be complementary and to remove the remaining contamination.

6.3 Stability of the Rise Time PSD

The stability of a PSD based on the rise time estimator and the cut threshold is investigated in this Section. In Section 6.3.1 the cut is applied to calibration and background waveforms with known properties, artificially re-scaled at different energies. The waveform belongs to five dataset: the highly multiple site 2.6 MeV full energy peak, the Compton shoulder with a relatively high single site component, the DEP dominated by SSE close to the external surfaces and edges, the Compton continuum at the $Q_{\beta\beta}$ energy, and the high energy signals from the background spectrum. The energy dependence of the Rise Time cut for different kinds of events is studied with these datasets. The stability in time of the PSD is discussed in Section 6.3.2. Finally, the results are checked on the rise time distribution of the Compton continuum from the ^{208}Tl line at 2.6 MeV (Section 6.3.3) and on the $2\nu\beta\beta$ spectrum (Section 6.3.4).

6.3.1 Impact of the event type and energy on the PSD

The Table 6.5 summarises the selection of the five control samples used to study the Rise Time cut energy dependence. The calibration data are relative to all the calibration runs between December 2015 and April 2017. The events in each sample are artificially normalised at the same energy and then re-scaled at lower energies in steps of 25 keV. In this way, the PSD acceptance can be evaluated for the same set of pulses at different energies.

dataset		energy Min [keV]
cal	DEP	1591.0 – 1594.0
cal	FEP	2614.0 – 2615.0
cal	CmpEdge	2340.0 – 2360.0
cal	$Q_{\beta\beta}$	2019.0 – 2049.0
phy	α	3500.0 – 6000.0

Table 6.5: Summary of the datasets used for energy dependence study.

The waveform ω' at energy E', is produced by re-scaling the waveform ω and superimposing it to a baseline waveform b:

$$\omega'[k] = \omega[k] \cdot \frac{E'}{E} + b[k] \cdot \left(\sqrt{1 - \left(\frac{E'}{E} \right)^2} \right), \tag{6.2}$$

where k is the index running from 0 µs to 160 µs for the LF traces and from 0 µs to 10 µs for the HF traces. All traces, both signals and baselines, are first off-set at zero with the baseline restoration GELATIO module. For each event, the corresponding baselines from the same channel are used to build the low and high frequency traces.

In the assumption of white electronic noise Equation 6.2 provides a waveform with a reduced signal and the same noise RMS (Γ):

$$\Gamma^2(\omega') = \Gamma^2(\omega) \cdot \left(\frac{E'}{E} \right)^2 + \Gamma^2(b) \cdot \left(1 - \left(\frac{E'}{E} \right)^2 \right) \tag{6.3}$$

$$\Gamma^2(\omega') = \Gamma^2(\omega) \cdot \left(\frac{E'}{E} \right)^2 + \Gamma^2(b) - \Gamma^2(b) \cdot \left(\frac{E'}{E} \right)^2, \tag{6.4}$$

$$\text{since } \Gamma^2(b) = \Gamma^2(\omega), \tag{6.5}$$

$$\text{it follows that } \Gamma^2(\omega') = \Gamma^2(\omega). \tag{6.6}$$

Figure 6.7 shows how the rise time is stable for the re-scaled sample of the Compton Edge and does not shift with the energy.

The effect of the noise on the rise time resolution can be seen only on the peak of the distribution which is sharper at 2.2 MeV than at 1.1 MeV. This distortion is compatible with the decrease of resolution from ~ 5 ns to ~ 10 ns visible in Figure 6.4. The change of rise time estimator resolution affects only marginally the distribution which spreads over a large range of rise time values.

The acceptance of the re-scaled samples is shown in Figure 6.8 for ANG2 (for the other detectors see Figure 6.22). All samples have a similar acceptance and no energy dependence is visible above 1 MeV. To search for energy dependencies, a fit with a linear function has been performed for each sample in each detector. All fits are compatible with a flat distribution. Note that in all detectors the acceptance of the samples is always above the acceptance measured for $2\nu\beta\beta$ because of the not uniform spatial distribution of gamma-induced events.

The Compton Edge and the α samples are particularly relevant for the evaluation of the energy stability. The Compton Edge has a large fraction of SSE and can be used as a proxy for the energy dependence of SSE. Figure 6.9 shows the energy stability of these samples for each detector. An upper limit on the energy dependence of the PSD technique can be derived by the analysis of these two samples to be $< 1\%$.

This implies that the $2\nu\beta\beta$ survival probability can be assumed to be the same of the $0\nu\beta\beta$ and no energy correction is needed.

6.3.2 Stability of the PSD in time

Time variations of the detector response or of the read-out electronic performance can affect two aspects relevant for the estimation of the $0\nu\beta\beta$ acceptance:

- the survival probability for the $2\nu\beta\beta$ sample
- the lack of energy dependence that is needed to extrapolate the survival probability for $0\nu\beta\beta$ events from the value measure for the $2\nu\beta\beta$ sample.

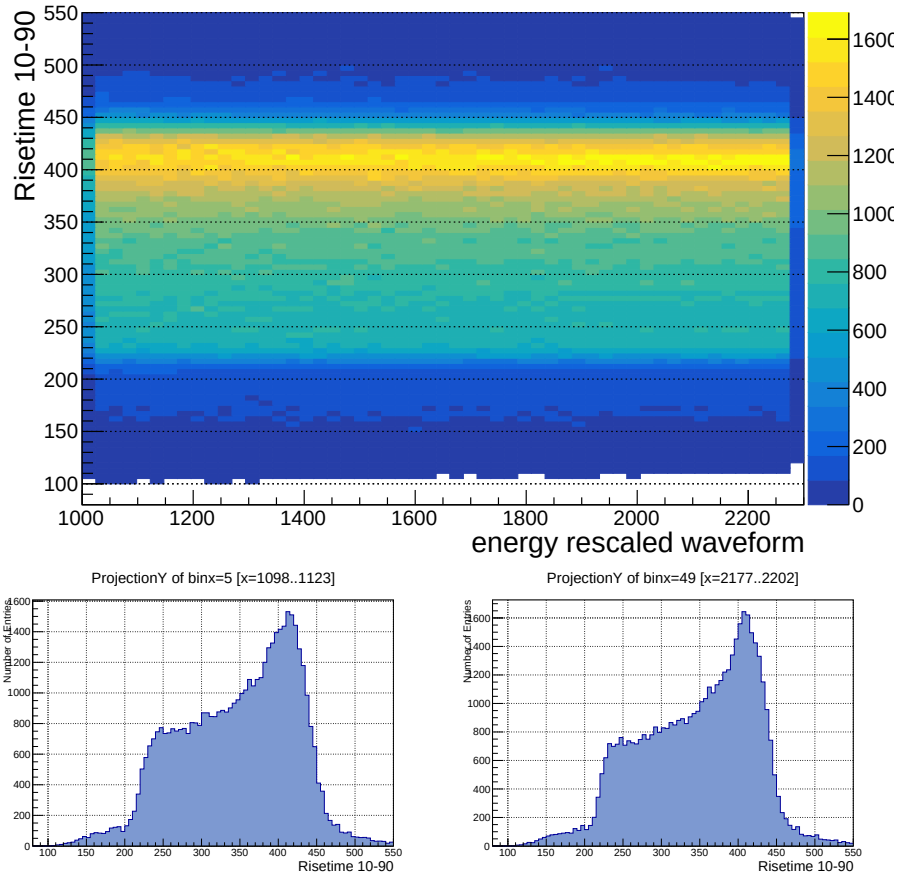

Figure 6.7: The upper plot shows the distribution of the rise time for Compton shoulder events with enhanced noise levels for ANG5. The bottom plots show the distribution of the rise time for one bin at 1100 keV (left) and 2200 keV (right).

Variations of the $2\nu\beta\beta$ survival probability do not represent a problem because they are automatically taken into account as the survival probability is measured directly from data. Splitting the data when a large change is observed can however improve the performance because the cut threshold can be optimised for each sub-set. On the other hand, time variations of the energy dependence impact directly on the systematic uncertainties associated with the extrapolation of the $2\nu\beta\beta$ survival probability.

To monitor the aforementioned quantities of interest, the time dependence has been studied using the rise time distribution of the Compton continuum events from the calibration runs. In particular, the stability of the $2\nu\beta\beta$ survival probability was monitored with the mean value and the 10% quantile of the distribution at 1 MeV. The energy dependence was associated with the difference between the survival probability of the Rise Time cut at 1 MeV (the energy of the $2\nu\beta\beta$ sample) and at 2 MeV (the energy of the $0\nu\beta\beta$ signal).

Figure 6.11 shows the monitoring parameters for ANG4 which is the only detector that shows a jump of the parameters at the time of the HV filter exchange. The plots for all other detectors are shown in Figure 6.28 to Figure 6.25. The jump observed for ANG4 can motivate the separation of the data in two sets. This option has been explored, the definition of the cut threshold for the two sub sets is shown in Figure 6.10. The cut would change from 196 ns to 199.5 (187.5) in the first (second) dataset. The second dataset, however, contains a limited number of α events and the figure of merit of the first dataset is flat between 180 ns and 200 ns. It has been decided, therefore, to use only one cut threshold (196 ns) for both periods. This choice it not optimal in terms of

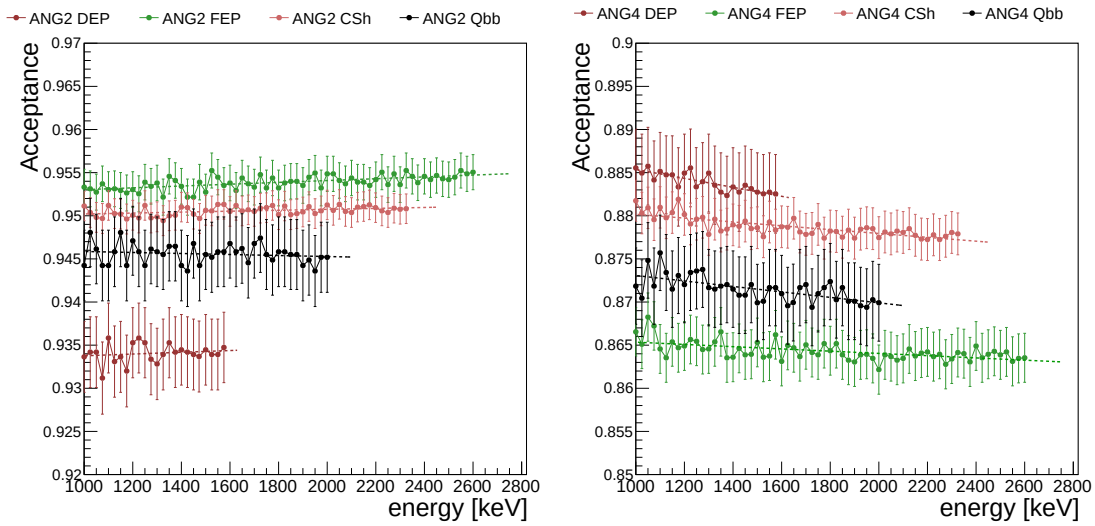

Figure 6.8: Stability of the cut acceptance for different sets of γ induced signals (DEP, FEP, Compton shoulder and Compton Continuum around $Q_{\beta\beta}$). The signals have been extracted from calibrations with Th sources and the noise has been enhanced according to Equation 6.2 with baseline waveforms from the physics dataset. The left plot refers to ANG2, the right plot to ANG4, and similar plots for the other detectors are in Figure 6.22.

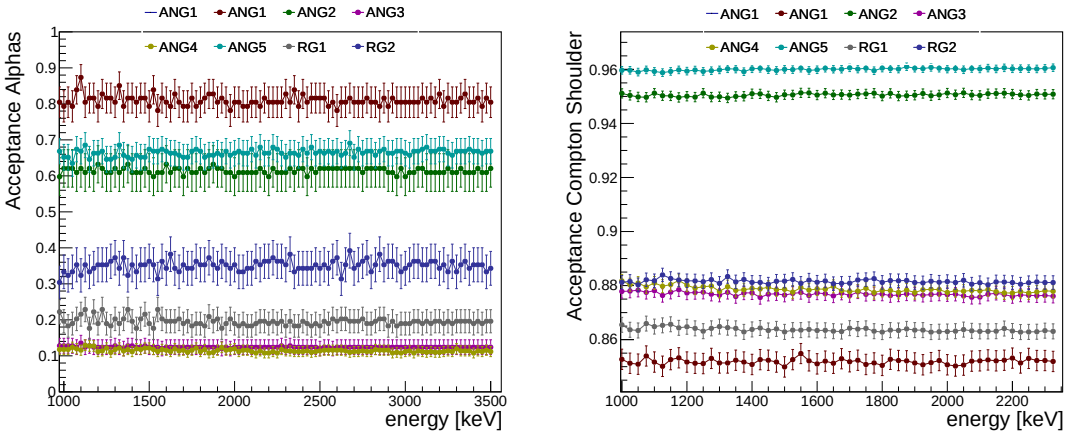

Figure 6.9: Stability of acceptance for a signal proxy (Compton shoulder) and the background proxy (events with $E > 3.5$ MeV in physics runs) with enhanced noise.

efficiency but avoid additional systematic uncertainty. The classification of the events in the ROI side-bands would not be affected by the change of the cut as all the events are very far from the threshold.

6.3.3 Application to calibration data

The data from 12 different calibration runs taken between January 2016 and March 2017 have been analysed. Figure 6.12 shows the energy spectrum before and after the cut. The acceptance of the Compton continuum is constant and no indication of any energy dependence is observed. The spectra of the individual detectors are reported in Figure 6.22.

The Rise Time cut is a volume cut that, according to Table 6.4, excludes about 15% of the innermost volume. A higher acceptance (90%) is then to be expected for γ induced signals which are more likely to be generated in the proximity of the outer surfaces of the crystals (n+ electrode) rather than in the volume around the α sensitive surfaces.

6.3.4 Two-neutrino double beta survival probability

As a final cross check, the survival probability of the $2\nu\beta\beta$ events has been studied dividing the statistics available in different energy bins of 25 keV. The survival probability is shown in Figure 6.13. The survival probability in the different bins is fitted with a constant and the χ^2 test shows that in both cases the data are compatible with the hypothesis of no energy dependence. The fits provide slightly different values in relation to the one reported in Table 6.4 (84.3%) because of the different energy range that here extends till 1450 keV. This is a further strong confirmation that the energy dependence for this analysis is negligible.

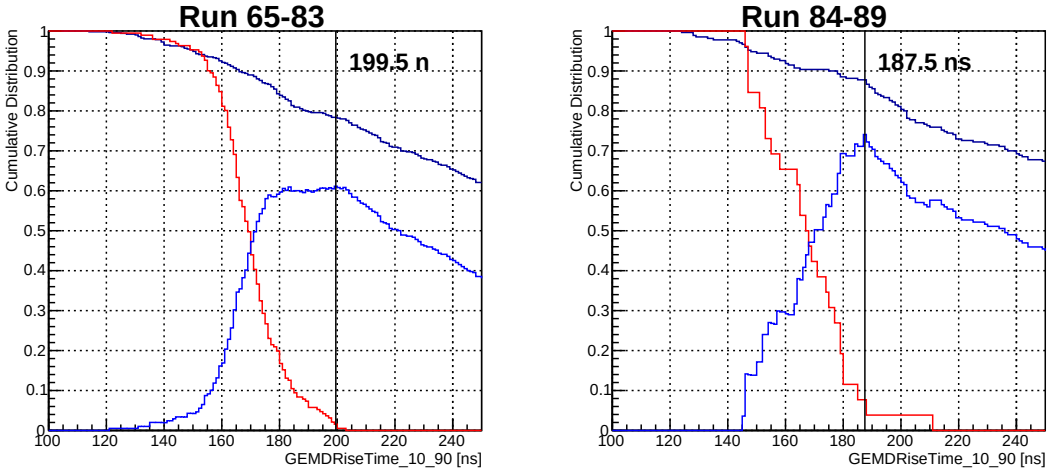

Figure 6.10: Cumulative distributions of the rise time 10-90 parameter for the $2\nu\beta\beta$ and the high energy events in ANG4 before (left) and after (right) the exchange of the HV filters.

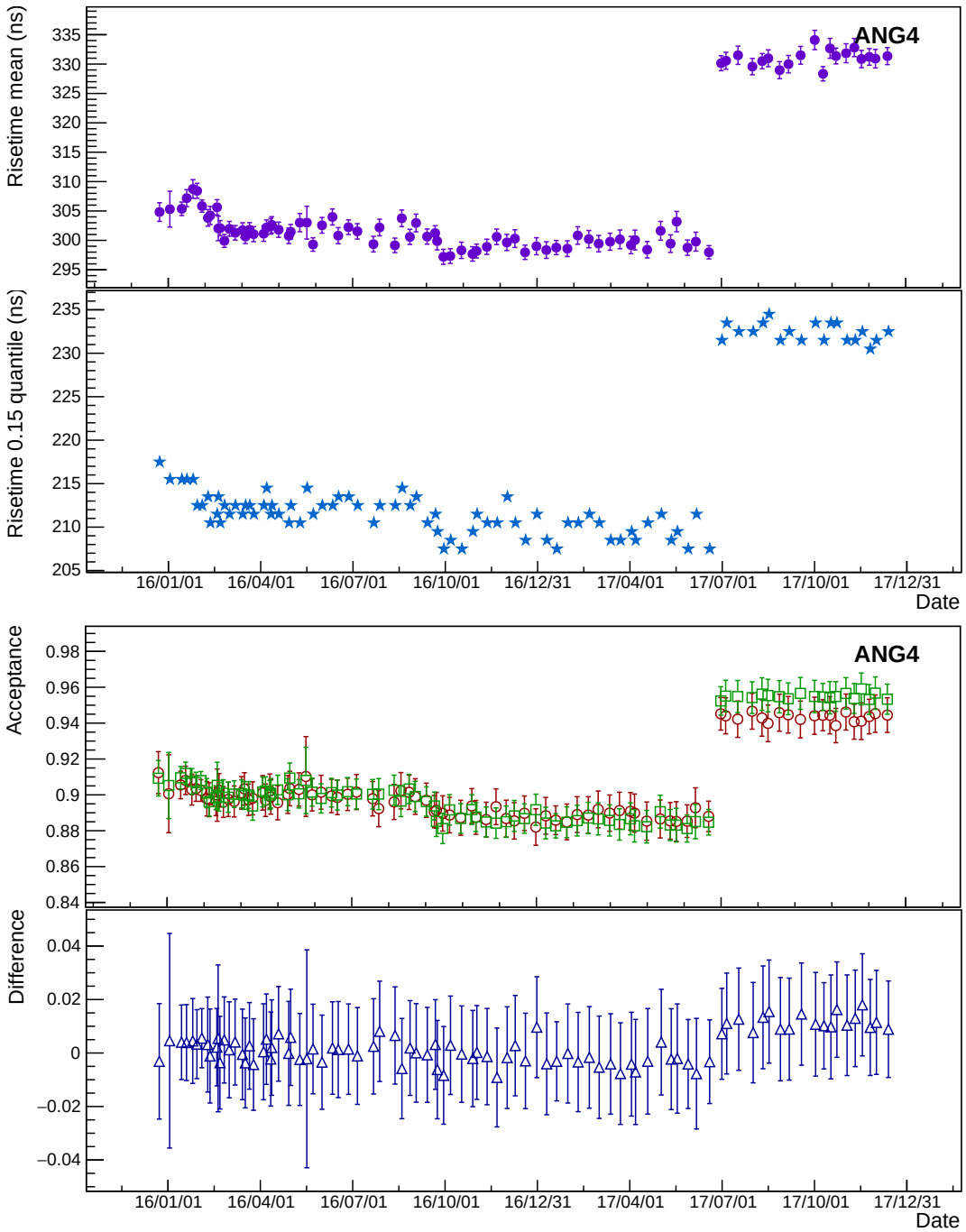

Figure 6.11: The top two panels show the variation in time of the mean value and the 15% quantile of the distribution of the Compton continuum events from calibration data at 1 MeV. The two panels on the bottom report the time variation of the survival probability of the Rise Time cut at 1 MeV (red), at 2 MeV (green) and their difference (blue).

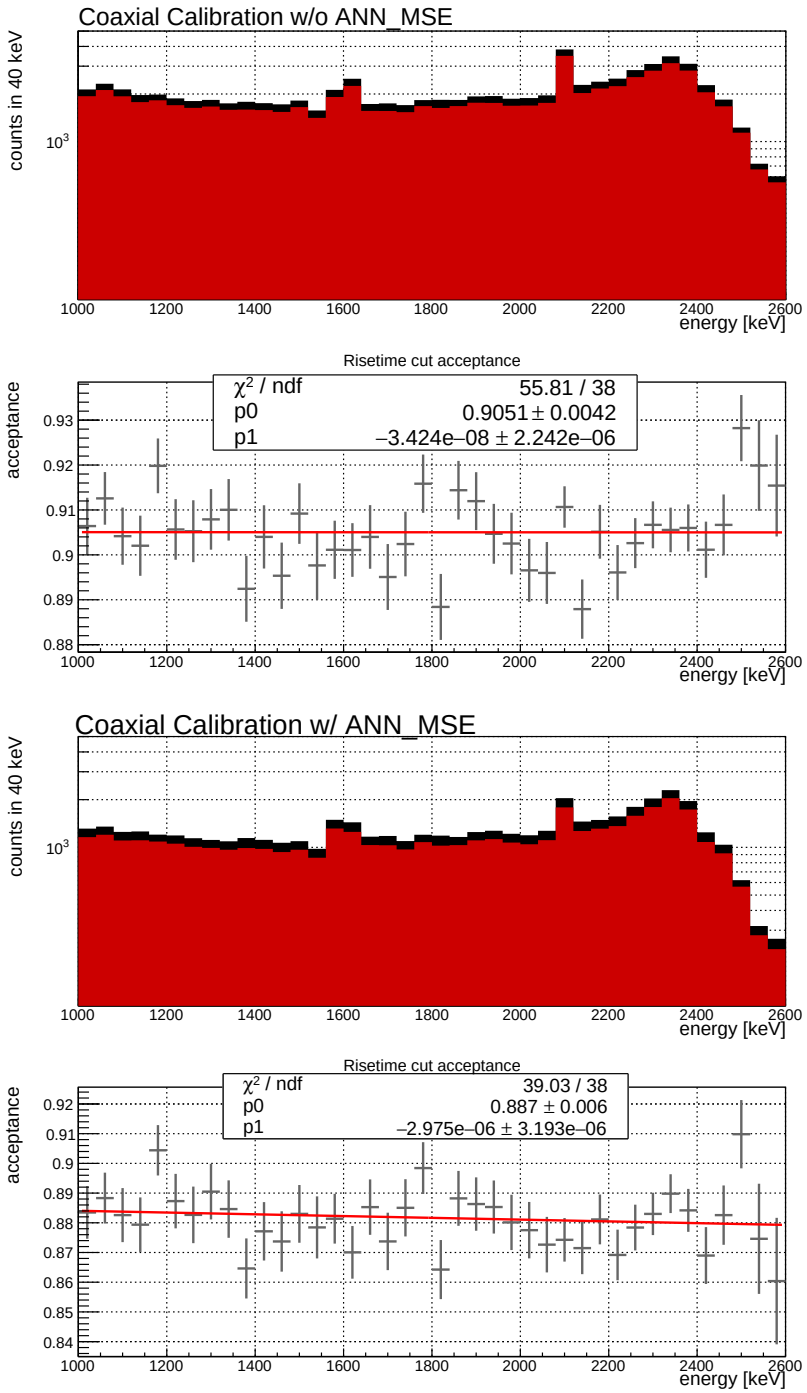

Figure 6.12: Rise Time cut acceptance of Compton continuum spectrum from calibration sources. The black histograms show the ^{228}Th calibration spectra before the Rise Time cut, in red the spectra after the Rise Time cut are shown. In the first panel only the Rise Time PSD is applied, while the bottom part shows the effect of the Rise Time PSD on the events that survive the MSE artificial neural network. Below the spectra the acceptance of the Rise Time cut is fitted with a linear regression. It is compatible with a constant value of 0.90 and 0.89 respectively. The spectrum is taken from a selection of 12 different calibrations between January 2016 and March 2017.

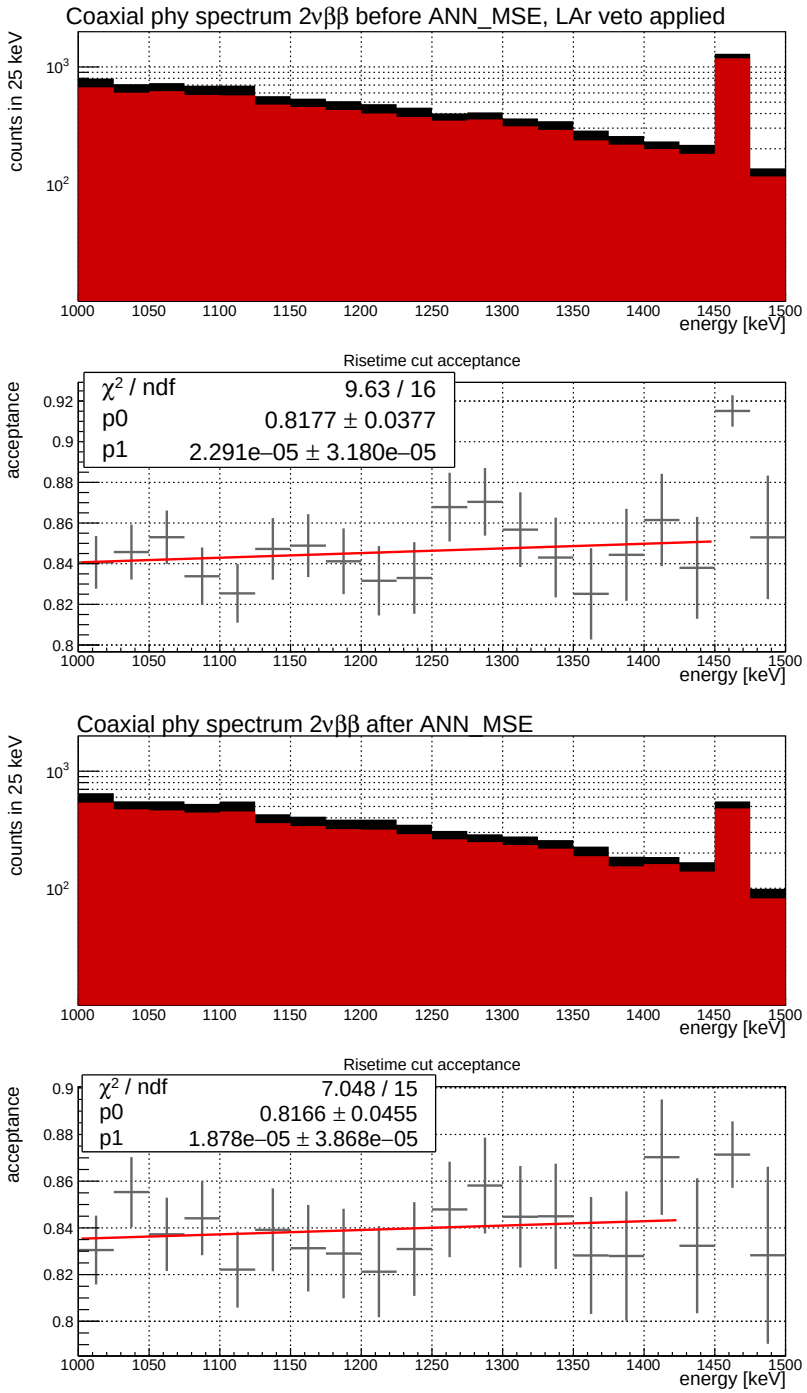

Figure 6.13: Acceptance of the Rise Time cut on the $2\nu\beta\beta$ spectrum before (top) and after (bottom) the application of the ANN_MSE cut. The black histograms show the GERDA spectrum before the Rise Time cut and the red ones after the cut. The fits in the bottom panels show that the acceptance in the energy range 1.00–1.45 MeV is compatible with a constant. The average value of the acceptance in this region is 0.845 ± 0.004 and 0.838 ± 0.005, without and with ANN_MSE respectively.

6.4 Application to physics data

The distribution of the rise time is shown in Figure 6.14 as a function of energy for all coaxial detectors combined, after LAr veto and ANN_MSE. Plots for each single detector are included in Figure 6.23. All events above 3.5 MeV can be only due to α decays and are all clearly concentrated at low rise time values. Most of the events are at the energy of the Po-210 Q-value (5.3 MeV) but a tail of degraded α events extends to lower energies and represents the main background component (after LAr veto and ANN_MSE) in the ROI. Most of the events in the proximity of the ROI are therefore removed by the combination of LAr veto, neural network for MSE and Rise Time cut.

The correlations among these background rejection methods in the ROI side-bands are shown in Table 6.6. The table shows the classification of the 54 counts found in the energy range 1930–2190 keV, excluding 2104 ± 5 keV, 2119 ± 5 keV and of course the blinding window 2039 ± 25 keV. The numbers on the diagonal are the number of events rejected by a single cut and the off-diagonal entries show the numbers of events rejected by two cuts. The only obvious correlation is between LAr veto and ANN_MSE. The last column shows the rejection of $2\nu\beta\beta$ for the PSD techniques, which is computed after LAr veto (see Section 6.2); for the LAr veto the assumption is that the $2\nu\beta\beta$ rejection is dominated by random coincidences. It is clear that the LAr veto is the most efficient background rejection, it removes 32 events (17 of which pass both PSD) while losing only 3% of the signal.

	LAr	ANN	RT	$2\nu\beta\beta$
LAr	17	12	2	3%
ANN_MSE		9	0	23%
RT1090			11	16%

Events cut by all: 1
Events cut by none: 2
Total: 54

Table 6.6: Number of events in the ROI side-bands (runs 65–89) tagged by LAr veto, ANN_MSE and RT1090.

The comparison of the spectrum of the semi-coaxials with the one of the BEGEs in Figure 6.15 shows that with the Rise Time cut the background levels are similar.

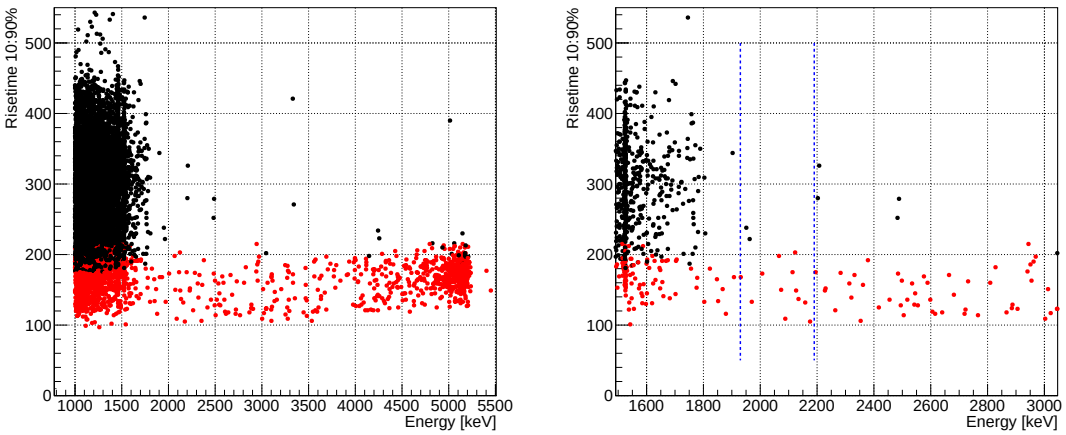

Figure 6.14: Distribution of the rise time 10–90 for events with energy greater than 1 MeV. The plot shows all the events in the coaxial detectors from runs 65–89, after data selection, quality cuts, multiplicity cut, LAr veto and MSE neural network. Below 1.5 MeV it is clear that the $2\nu\beta\beta$ events are distributed between 100 ns and 500 ns, while the α contamination surviving the neural network is concentrated below 200 ns. The red dots are the events removed by the Rise Time cut and the black ones are the events surviving all cuts. Figure 6.23 and Figure 6.24 show the distributions for the individual channels for the runs 65–89 and for the complete Phase II dataset respectively.

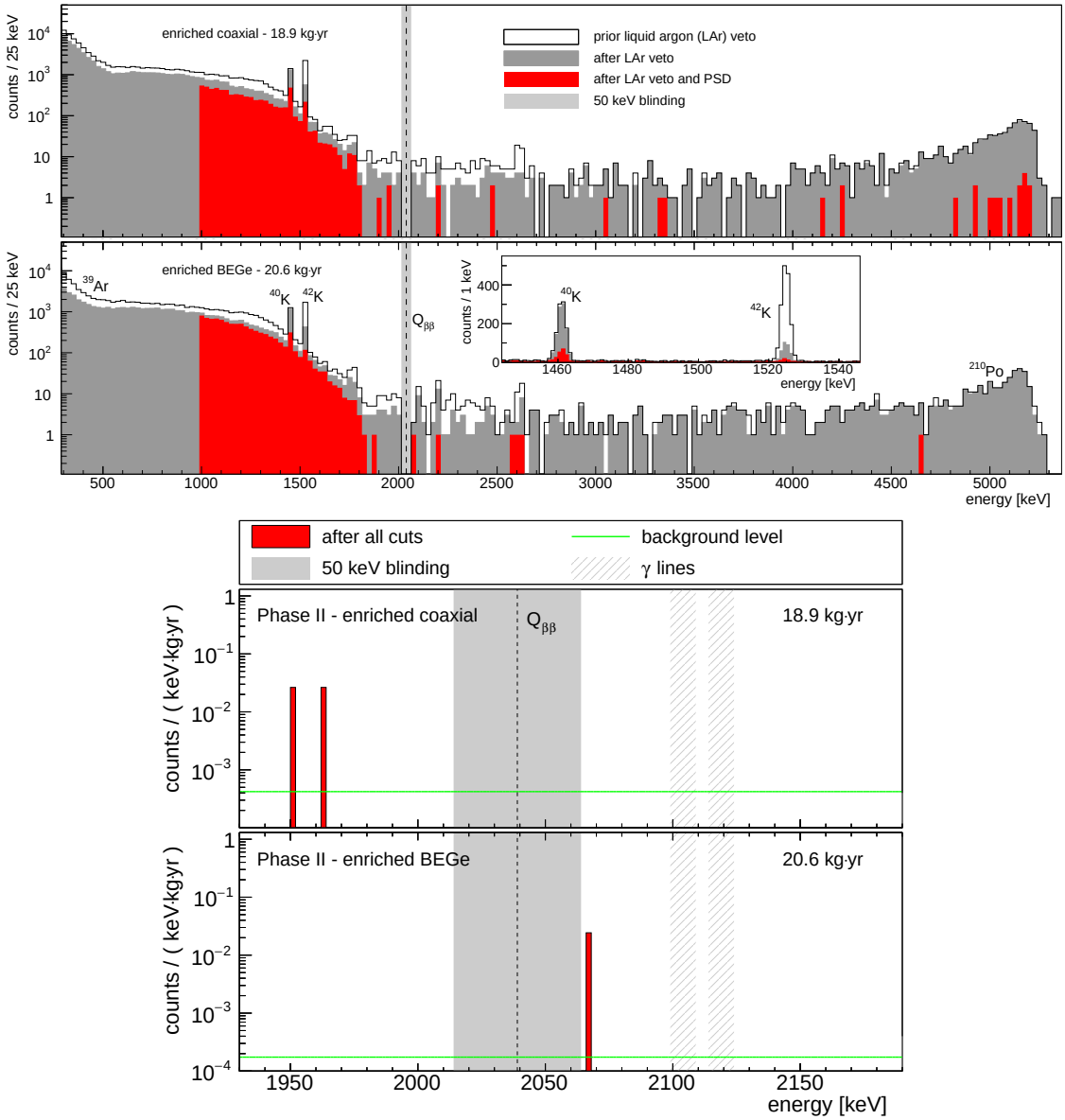

Figure 6.15: Spectra for runs 65-89. The red spectrum shows the events surviving PSD (ANN_MSE and RT1090) and LAr veto. The coaxial spectrum (top) is shown in comparison with the one of the BEGe dataset (bottom). On the second panel a zoom in on the ROI.

6.5 Signal efficiency

Table 6.7 summarises all the parameters of interest for the estimation of the $0\nu\beta\beta$ efficiency and its uncertainty.

The previous sections investigated how the rise time estimator is affected by the noise. The algorithm is unbiased and the rise time of a waveform with different noise levels is always reconstructed around its true value. The maximum deviation of the centroid distribution at 1 MeV is found to be 2.5 ns (ANG4, r25,z5), but the deviation is generally below 1 ns.

The resolution of the rise time estimator increases with the signal-to-noise ratio: the worst detector is ANG4 for which the resolution is 9.2 ns at 2 MeV and 18.5 ns at 1 MeV. For all the other detectors, the resolution is 5 ± 1 ns at 2 MeV and 11 ± 2 ns at 1 MeV. This should be compared with the spread of rise time values for normal samples that range between 100 and 400 ns.

No energy dependence was observed in the analysis with energy re-scaled samples. A linear fit has been performed for each detector and sample to set an upper limit on the dependence. ANG4 is the detector with the worst noise and for it the fit provides a slope between (-0.13 ± 0.07)%/MeV for the FEP and (-0.5 ± 0.5)%/MeV for the DEP. For all the detectors the best fit is always compatible with a flat distribution within two sigmas. The upper limits for the energy dependence are conservatively computed from the ANG4 dataset. The upper limits are given for 95% C.L. and refer to the maximum difference (absolute value) expected between 1 and 2 MeV.

The stability has been also cross checked using the Compton continuum of ^{208}Tl 2.6 MeV line in calibration data and the $2\nu\beta\beta$ distribution. Given that these additional tests also give fully consistent results it can be concluded that the efficiency measured for the $2\nu\beta\beta$ is equal to the efficiency expected for the $0\nu\beta\beta$ signal within a conservative 1% systematic uncertainty.

6.6 Conclusions

A new PSD technique based on the rise time of the charge signals of coaxial detectors has been developed and characterised. A cut based on the rise time corresponds to a pure volume cut. This interpretation is supported by extensive pulse shape simulations and previous works.

The algorithm developed to extract the rise time estimator was found to be unbiased and precise within 14 ns (9 ns) for events at 1 MeV (2 MeV). The estimator was found to be very effective

Table 6.7: Summary of all observed differences between $2\nu\beta\beta$ and $0\nu\beta\beta$.

parameter	maximum value (worst case)	recommended value
bias at 1 MeV	2.5 ns (ANG4)	<1 ns
bias at 2 MeV	0.4 ns (ANG5)	<0.5 ns
estimator resolution at 1 MeV	19 ns(ANG4)	14 ns
estimator resolution at 2 MeV	9 ns(ANG4)	7 ns
energy dependence ($\varepsilon_{2\ \mathrm{MeV}} - \varepsilon_{1\ \mathrm{MeV}}$):		
re-scaled DEP	$(-5 \pm 5) \cdot 10^{-3}$ (ANG4)	$< 1.5 \cdot 10^{-2}$ (95% CL)
re-scaled FEP	$(-1.3 \pm 0.7) \cdot 10^{-3}$ (ANG4)	$< 2.7 \cdot 10^{-3}$ (95% CL)
re-scaled Compton shoulder	$(-2.2 \pm 0.8) \cdot 10^{-3}$ (ANG4)	$< 3.8 \cdot 10^{-3}$ (95% CL)
re-scaled Compton continuum @ $Q_{\beta\beta}$	$(-3 \pm 2) \cdot 10^{-3}$ (ANG4)	$< 7.0 \cdot 10^{-3}$ (95% CL)
maximum time variation $\Delta(\varepsilon_{2\ \mathrm{MeV}} - \varepsilon_{1\ \mathrm{MeV}})$	1% (ANG4)	< 1%

in removing the α-induced events surviving ANN_MSE. A method to define the cut thresholds using a figure of merit has been proposed and applied, the levels are consistent among the seven detectors and robust in comparison to the particular figure of merit chosen.

The technique has been tested with calibration and physics data as well as control samples artificially re-scaled at different energies. No energy dependence has been found and a conservative upper limit between the efficiency measured for $2\nu\beta\beta$ and the one expected for $0\nu\beta\beta$ could be set at 1%. The acceptance of Compton Edge events in the calibration runs has been studied and in general found to be stable.

The technique is already fully integrated in the data-production and the classifiers are available for the complete Phase `II` dataset. In spite of the simplicity of the proposed method, its combination with the MSE/SSE neural network provides a final background index of $0.6^{+0.5}_{-0.3} \cdot 10^{-3}$ cts/(keV $\cdot$ kg $\cdot$ yr) with an overall efficiency for the $0\nu\beta\beta$ of $0.843 \pm 0.004(\text{stat}) \pm 0.01(\text{syst})$ to be combined with the other efficiencies including ANN_MSE. Compared to other techniques it provides a sound and robust estimation of the $0\nu\beta\beta$ efficiency. The GERDA collaboration adopted the Rise Time PSD in combination with the ANN_MSE for the analysis of the semi-coaxial data of the 2018 unblinding (23.1 kg·yr).

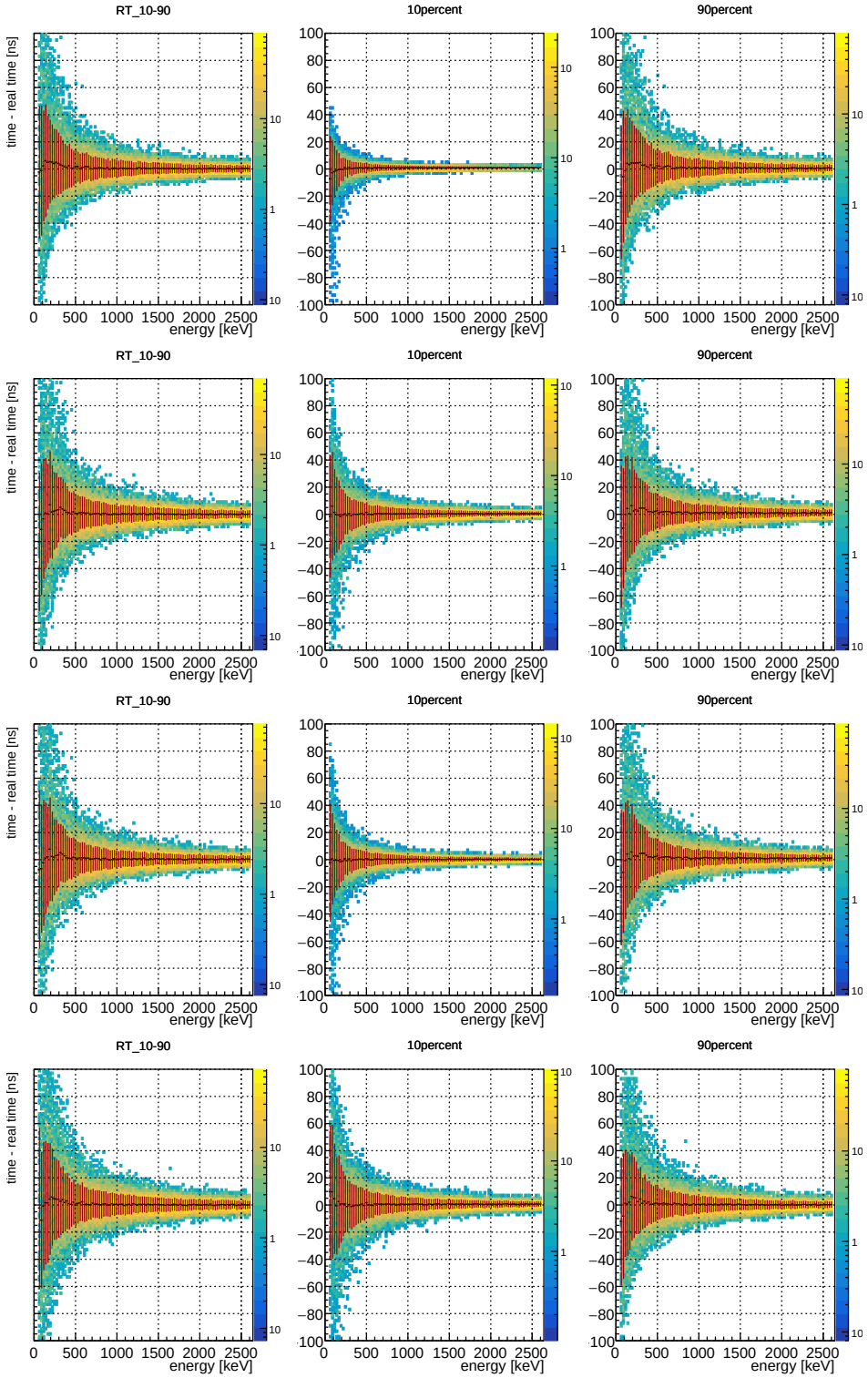

Figure 6.16: The plots show the accuracy and the precision of the rise time 10-90 algorithm for the four pulses, from the top r5-z100, r25-z5, r8-z50, r35-z50 in ANG1. In red are superimposed to the distribution the centroid values and the spread (1σ) for each energy bin.

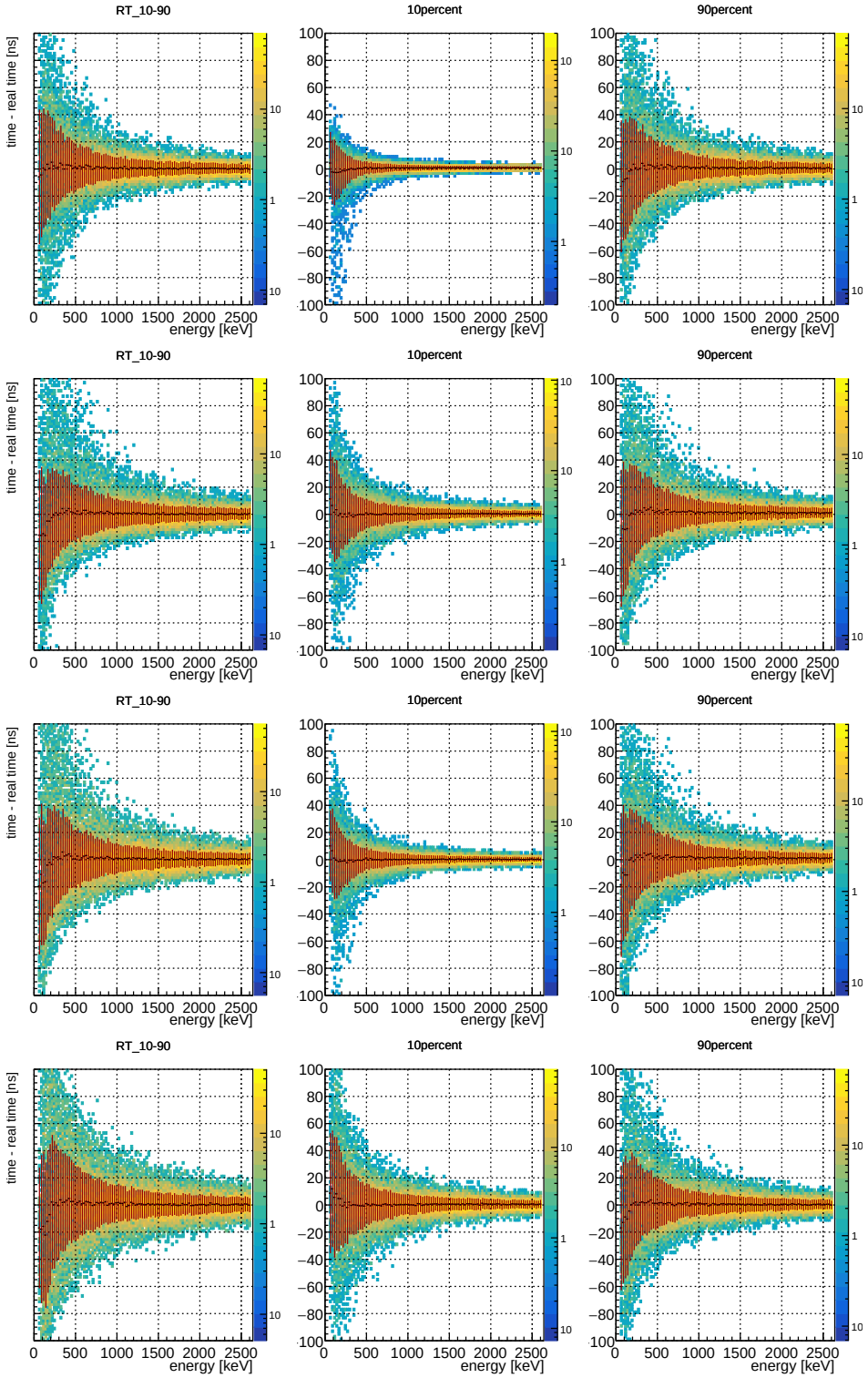

Figure 6.17: The plots show the accuracy and the precision of the rise time 10-90 algorithm for the four pulses, from the top r5-z100, r25-z5, r8-z50, r35-z50 in ANG3. In red are superimposed to the distribution the centroid values and the spread (1σ) for each energy bin.

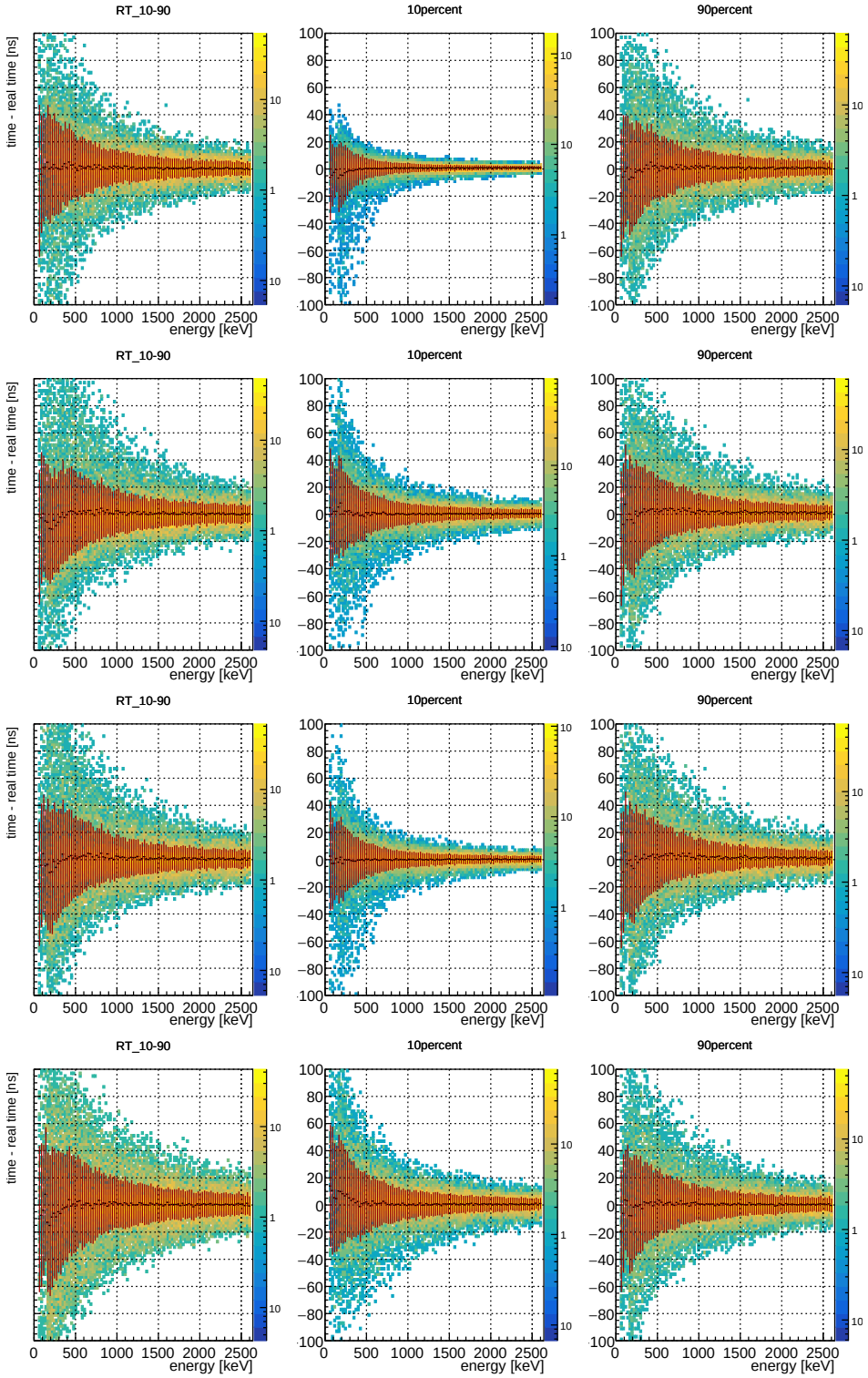

Figure 6.18: The plots show the accuracy and the precision of the rise time 10-90 algorithm for the four pulses, from the top r5-z100, r25-z5, r8-z50, r35-z50 in ANG4. In red are superimposed to the distribution the centroid values and the spread (1σ) for each energy bin.

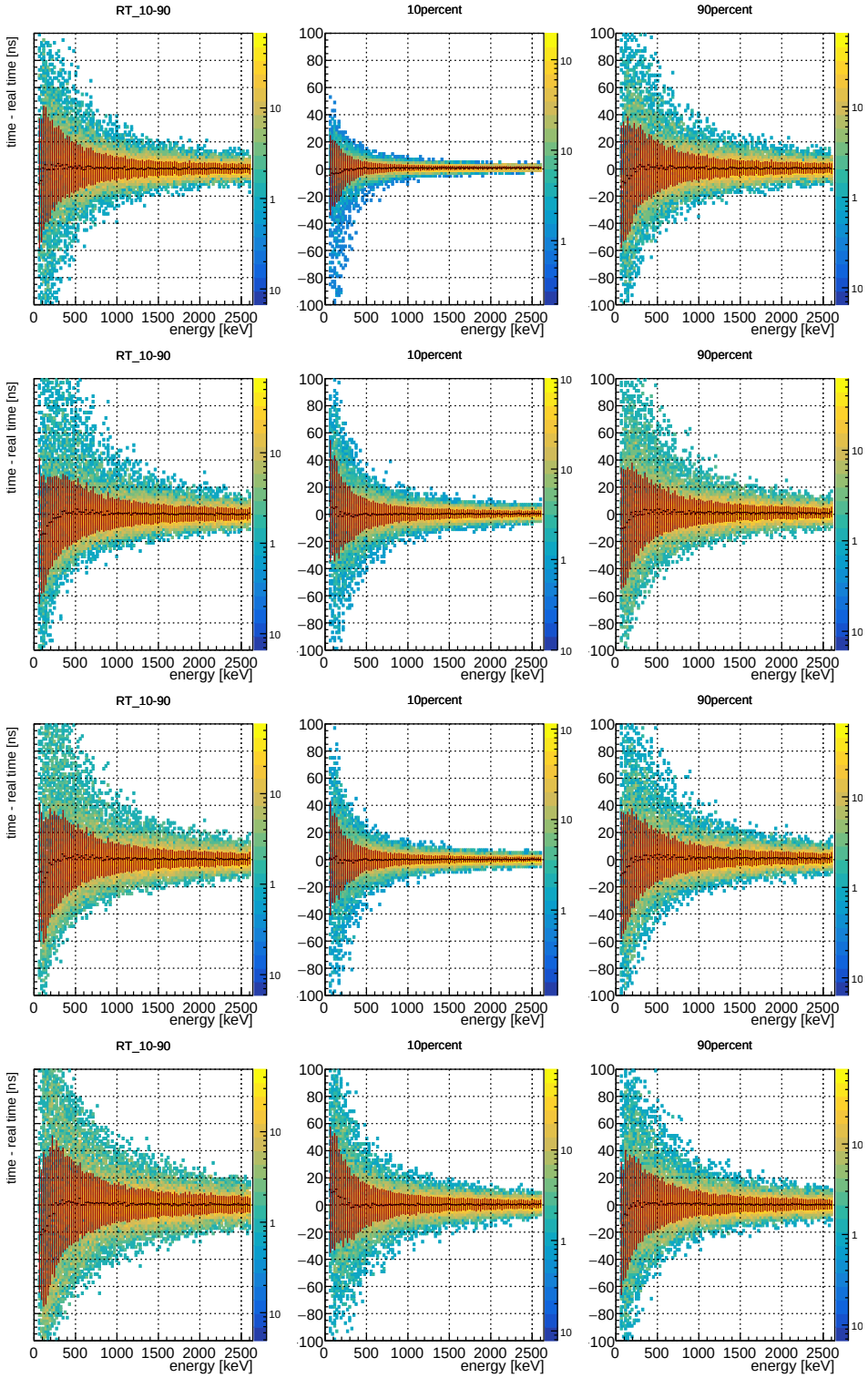

Figure 6.19: The plots show the accuracy and the precision of the rise time 10-90 algorithm for the four pulses, from the top r5-z100, r25-z5, r8-z50, r35-z50 in ANG5. In red are superimposed to the distribution the centroid values and the spread (1σ) for each energy bin.

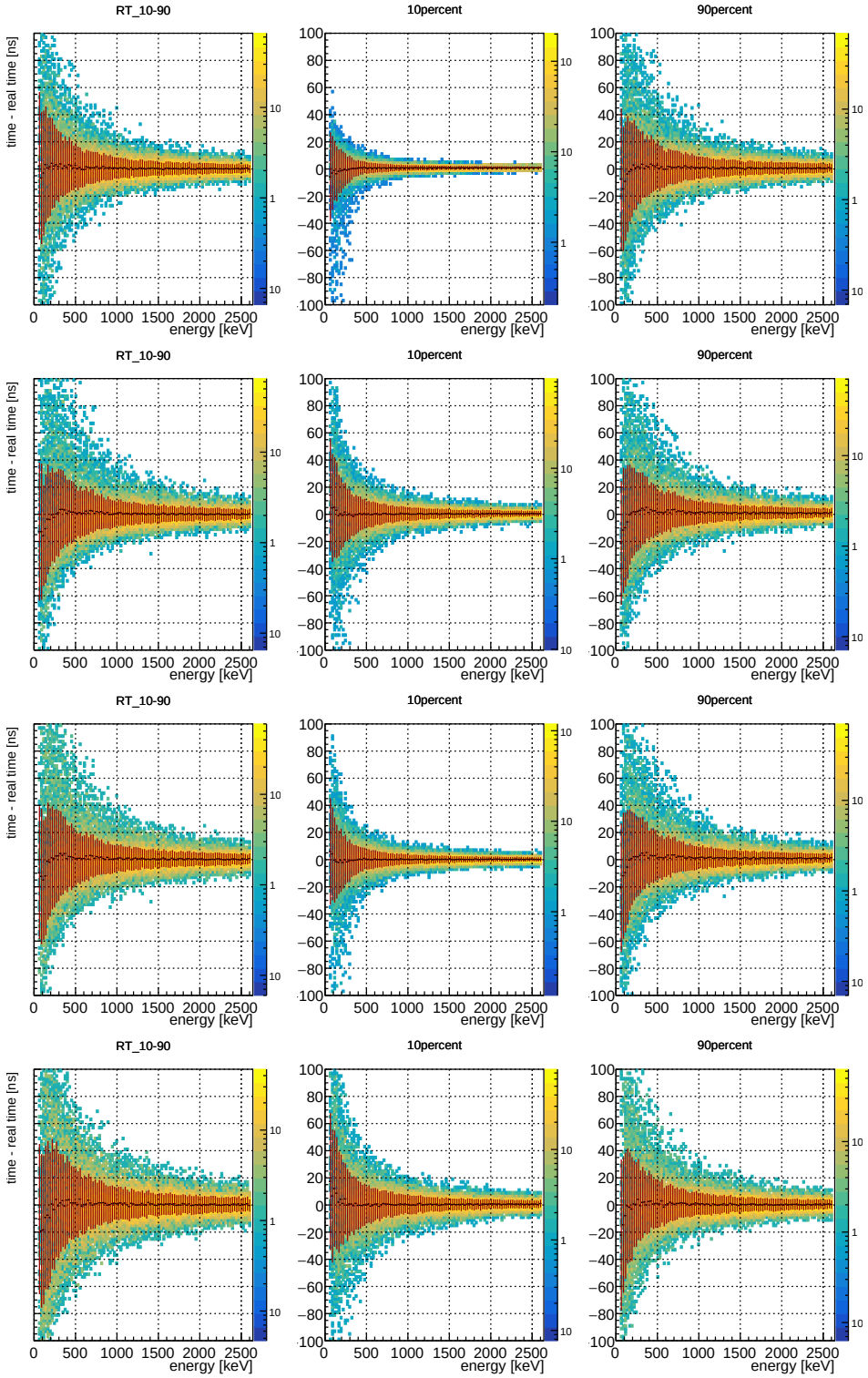

Figure 6.20: The plots show the accuracy and the precision of the rise time 10-90 algorithm for the four pulses, from the top r5-z100, r25-z5, r8-z50, r35-z50 in RG1. In red are superimposed to the distribution the centroid values and the spread (1σ) for each energy bin.

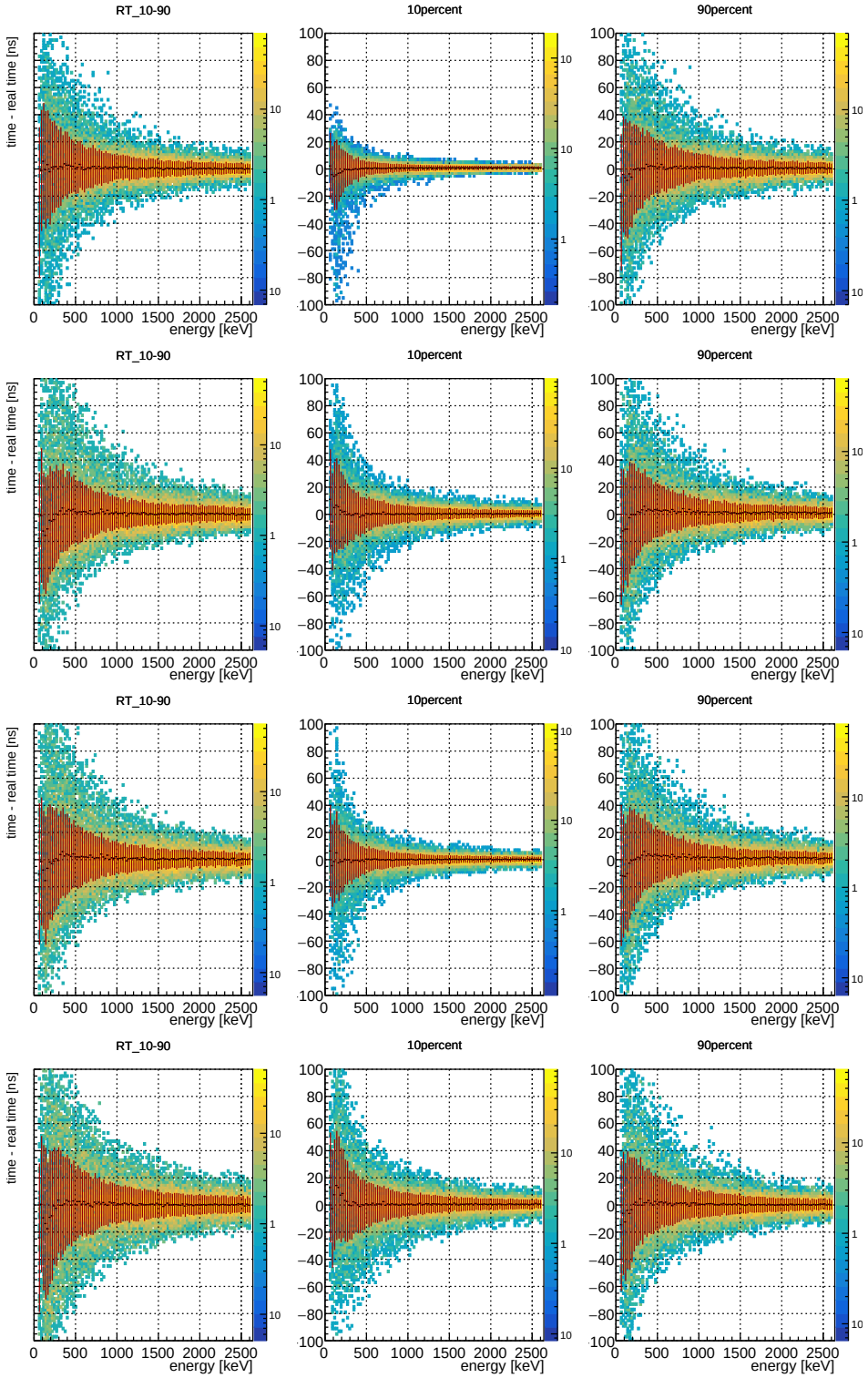

Figure 6.21: The plots show the accuracy and the precision of the rise time 10-90 algorithm for the four pulses, from the top r5-z100, r25-z5, r8-z50, r35-z50 in RG2. In red are superimposed to the distribution the centroid values and the spread (1σ) for each energy bin.

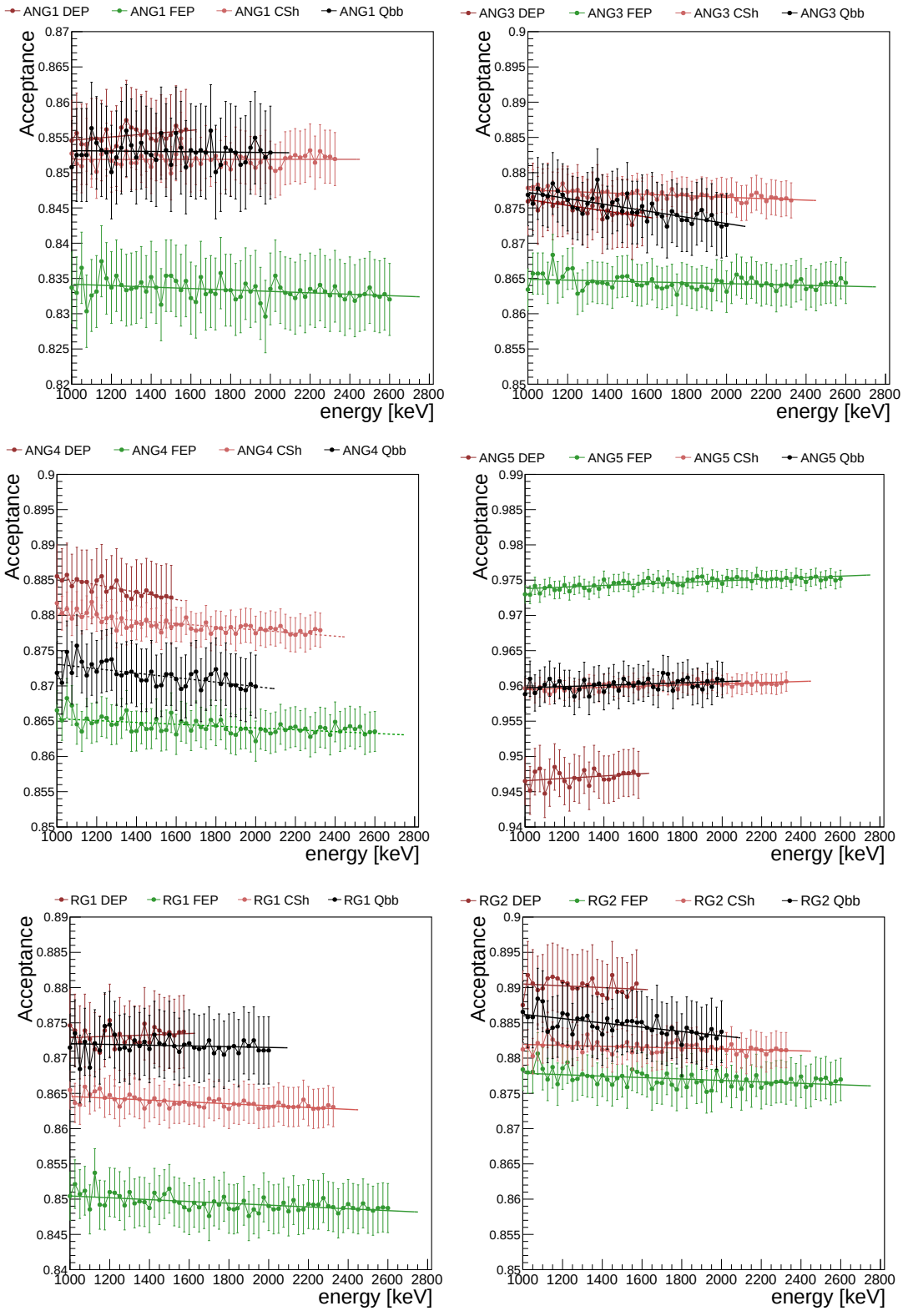

Figure 6.22: Stability of the acceptance for different γ datasets from the calibration with Th sources and enhanced noise.

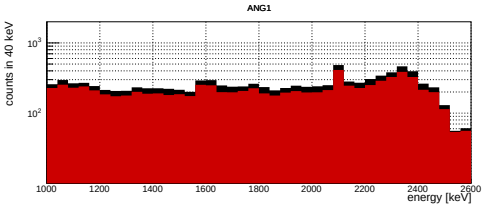
ANG1
counts in 40 keV
energy [keV]

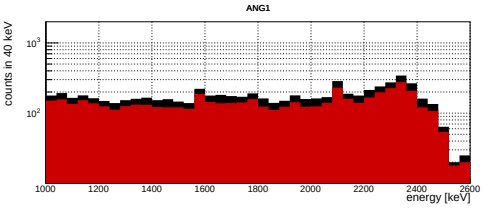
ANG1
counts in 40 keV
energy [keV]

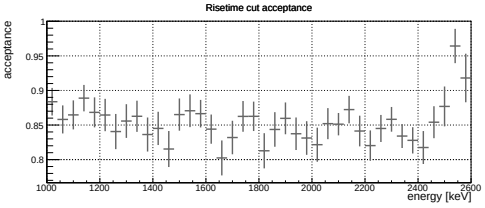
Risetime cut acceptance
acceptance
energy [keV]

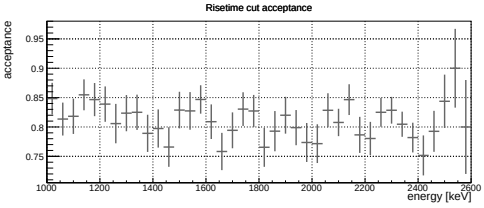
Risetime cut acceptance
acceptance
energy [keV]

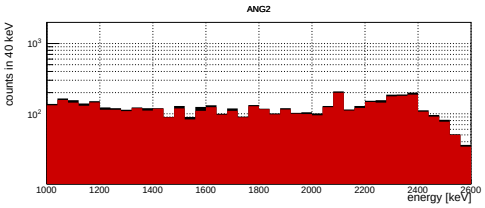
ANG2
counts in 40 keV
energy [keV]

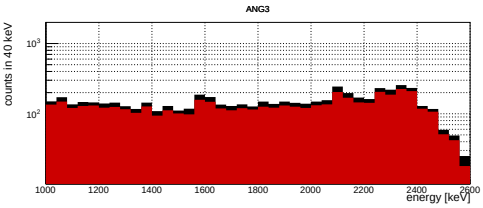
ANG3
counts in 40 keV
energy [keV]

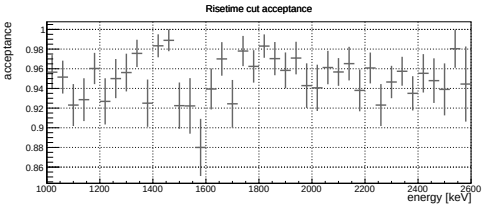
Risetime cut acceptance
acceptance
energy [keV]

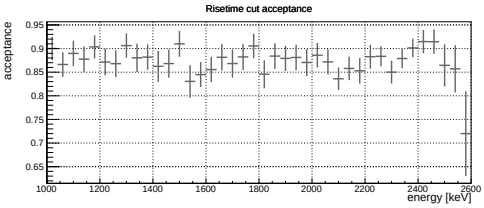
Risetime cut acceptance
acceptance
energy [keV]

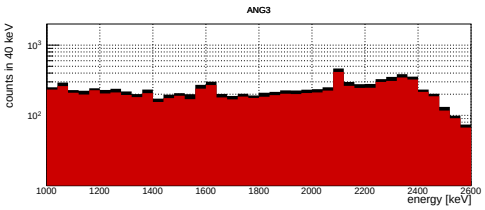
ANG3
counts in 40 keV
energy [keV]

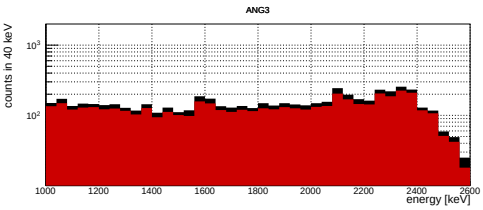
ANG3
counts in 40 keV
energy [keV]

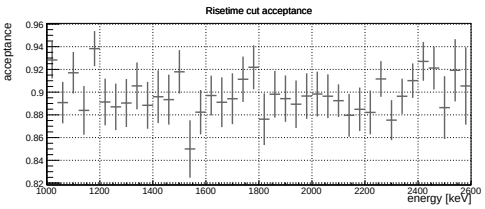
Risetime cut acceptance
acceptance
energy [keV]

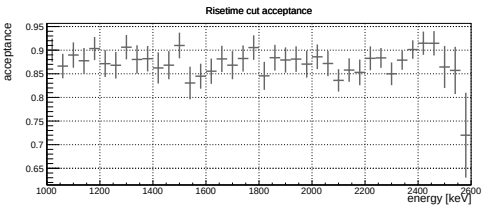
Risetime cut acceptance
acceptance
energy [keV]

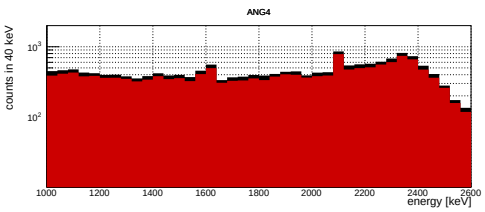
ANG4
counts in 40 keV
energy [keV]

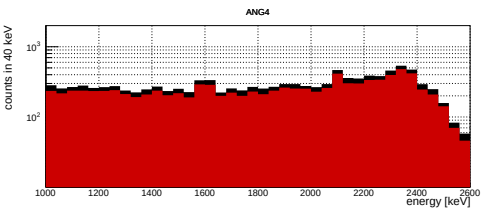
ANG4
counts in 40 keV
energy [keV]

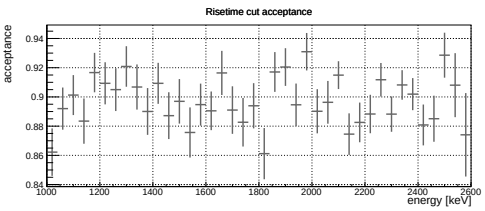
Risetime cut acceptance
acceptance
energy [keV]

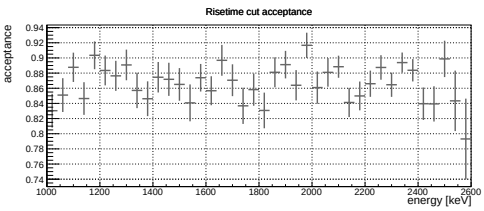
Risetime cut acceptance
acceptance
energy [keV]

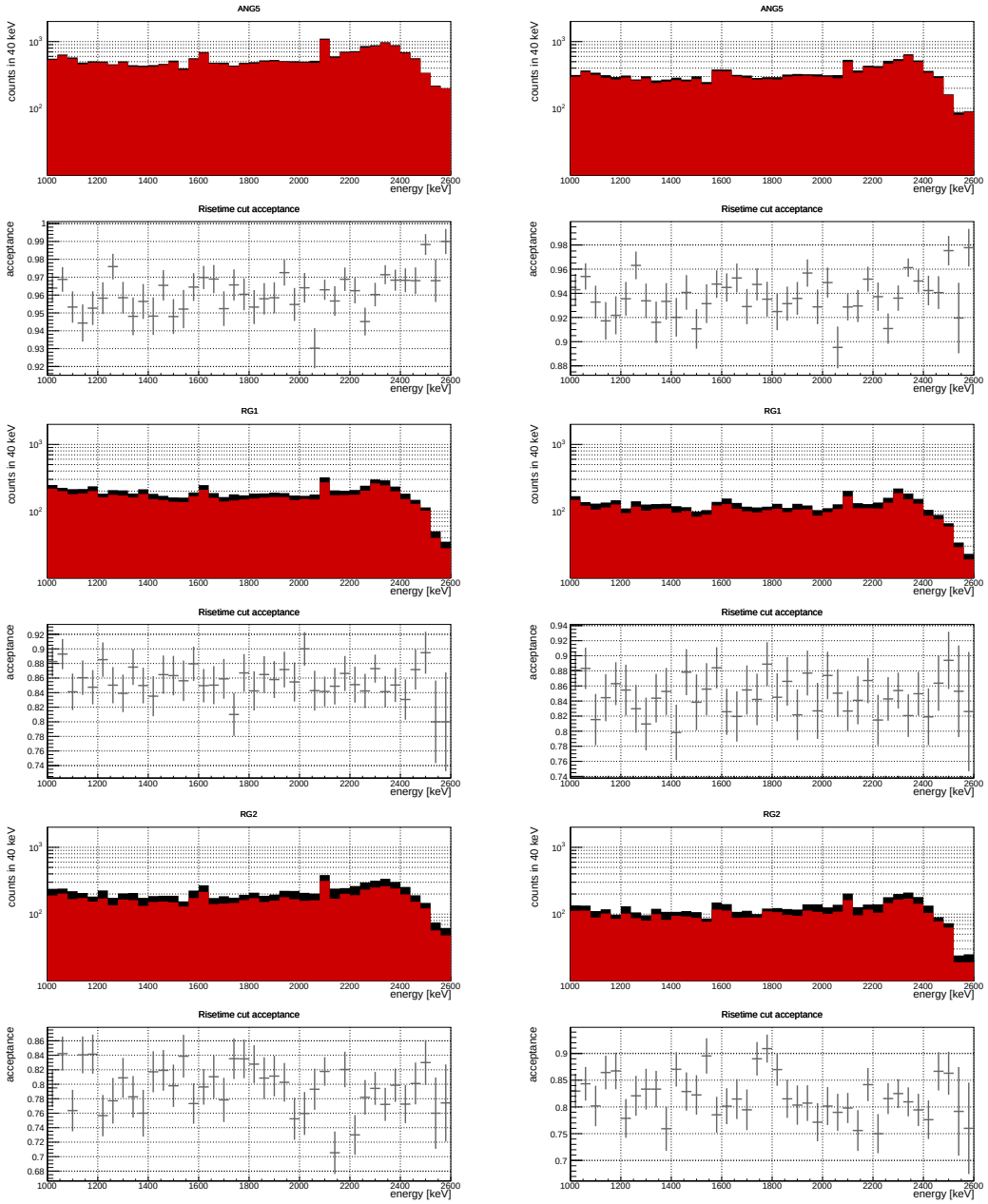

Figure 6.22: Rise Time cut acceptance of Compton continuum spectrum from calibration sources. The black histograms show the ^{228}Th calibration spectra before the Rise Time cut, in red the spectra after the Rise Time cut are shown. For each detector, the left panels show he effect of the Rise Time PSD, while the right side shows the effect of the Rise Time PSD on the events that survive the ANN_MSE. Below each spectrum the acceptance of the Rise Time cut is shown. The data is taken from a selection of 12 different calibrations between January 2016 and March 2017.

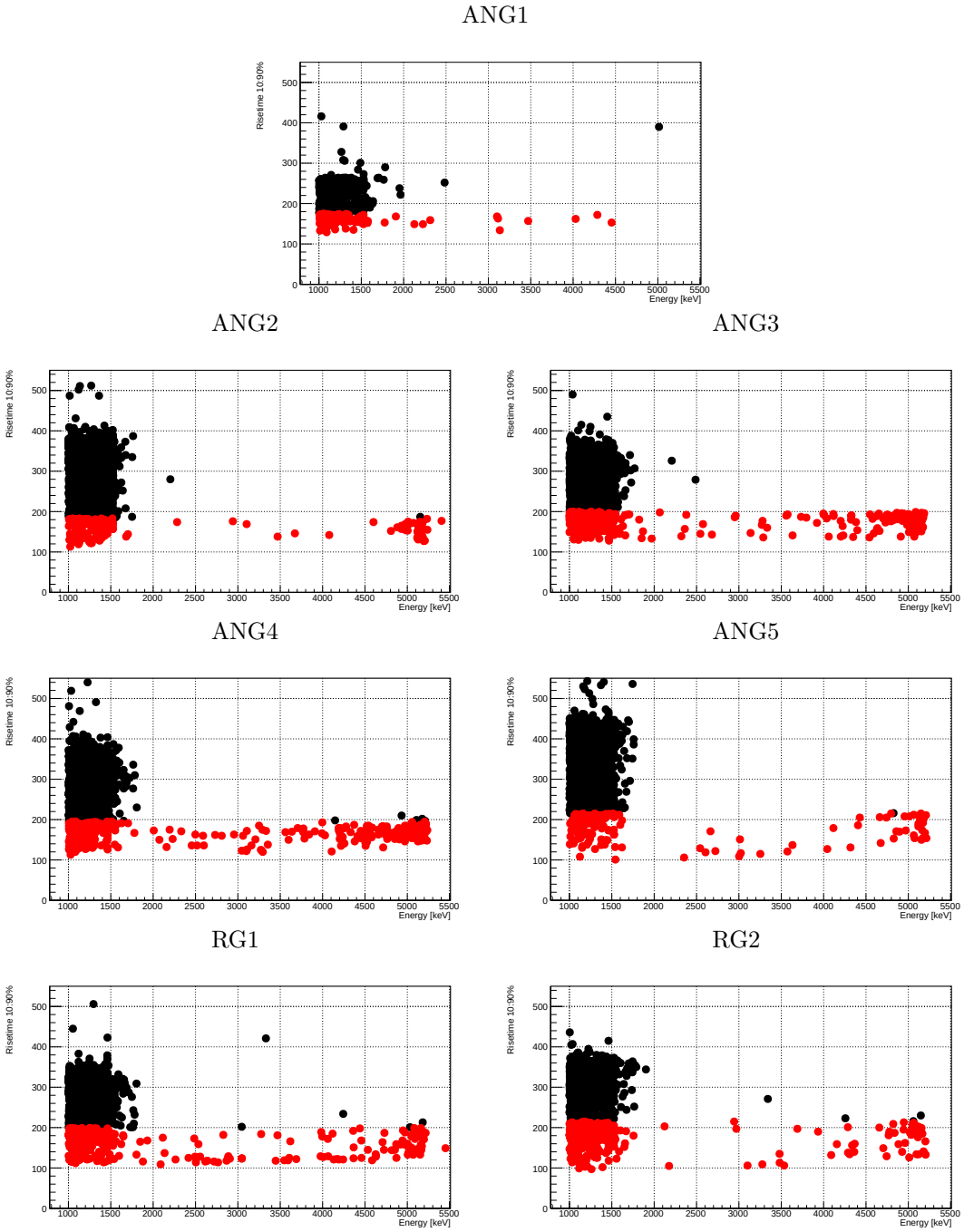

Figure 6.23: Distribution of rise time versus energy for each coaxial detector. The plots show all the events in the coaxial detectors from runs 65–89, after data selection, quality cuts, multiplicity cut, LAr veto and MSE neural network. The red points are for the events cut by Rise Time cut and the black points are for the events surving all cuts.

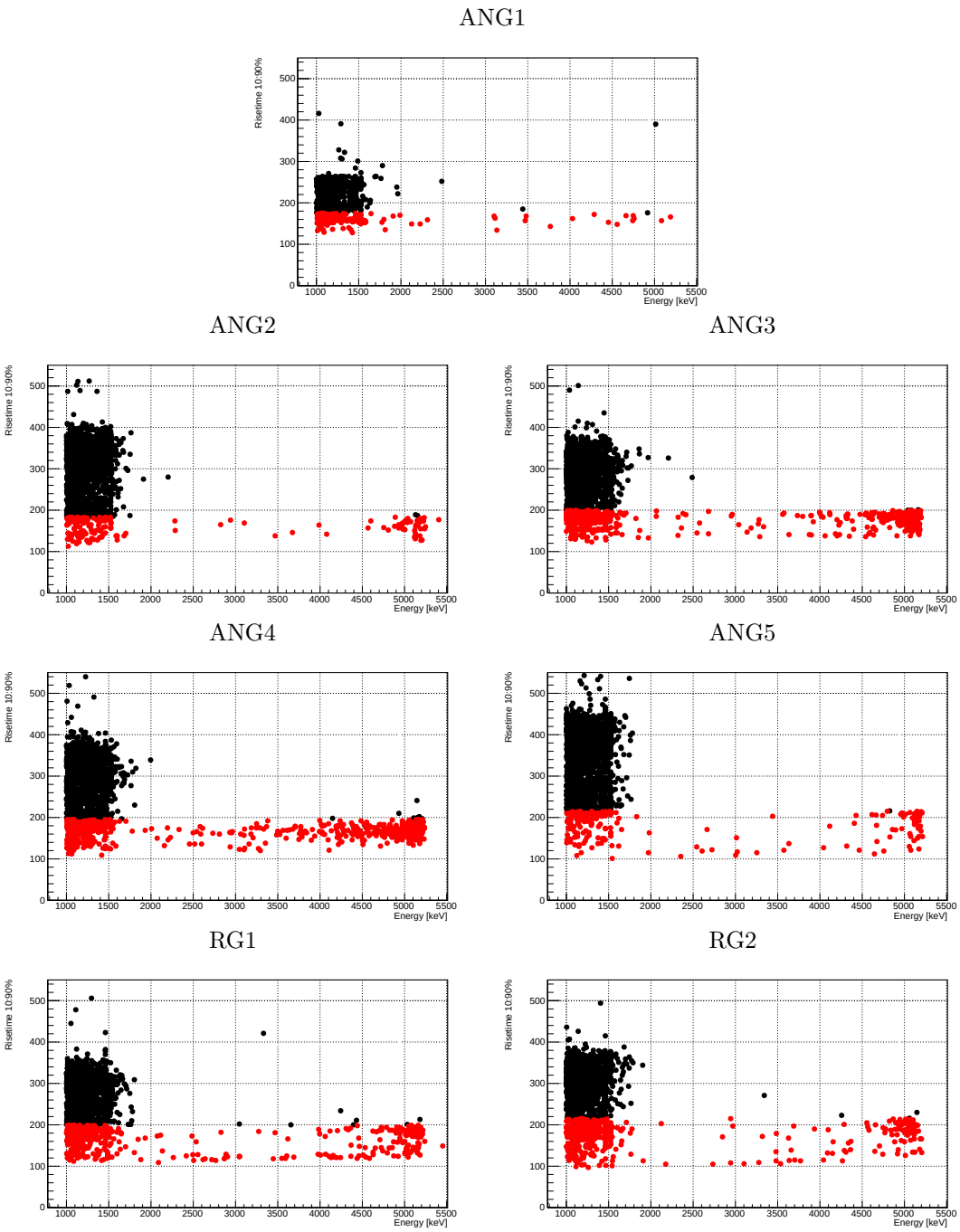

Figure 6.24: Distribution of rise time versus energy for each coaxial detector. The plots show all the events in the coaxial detectors from run 53 to run 89, after data selection, quality cuts, multiplicity cut, LAr veto and MSE neural network. The red points are for the events cut by Rise Time cut and the black points are for the events surving all cuts.

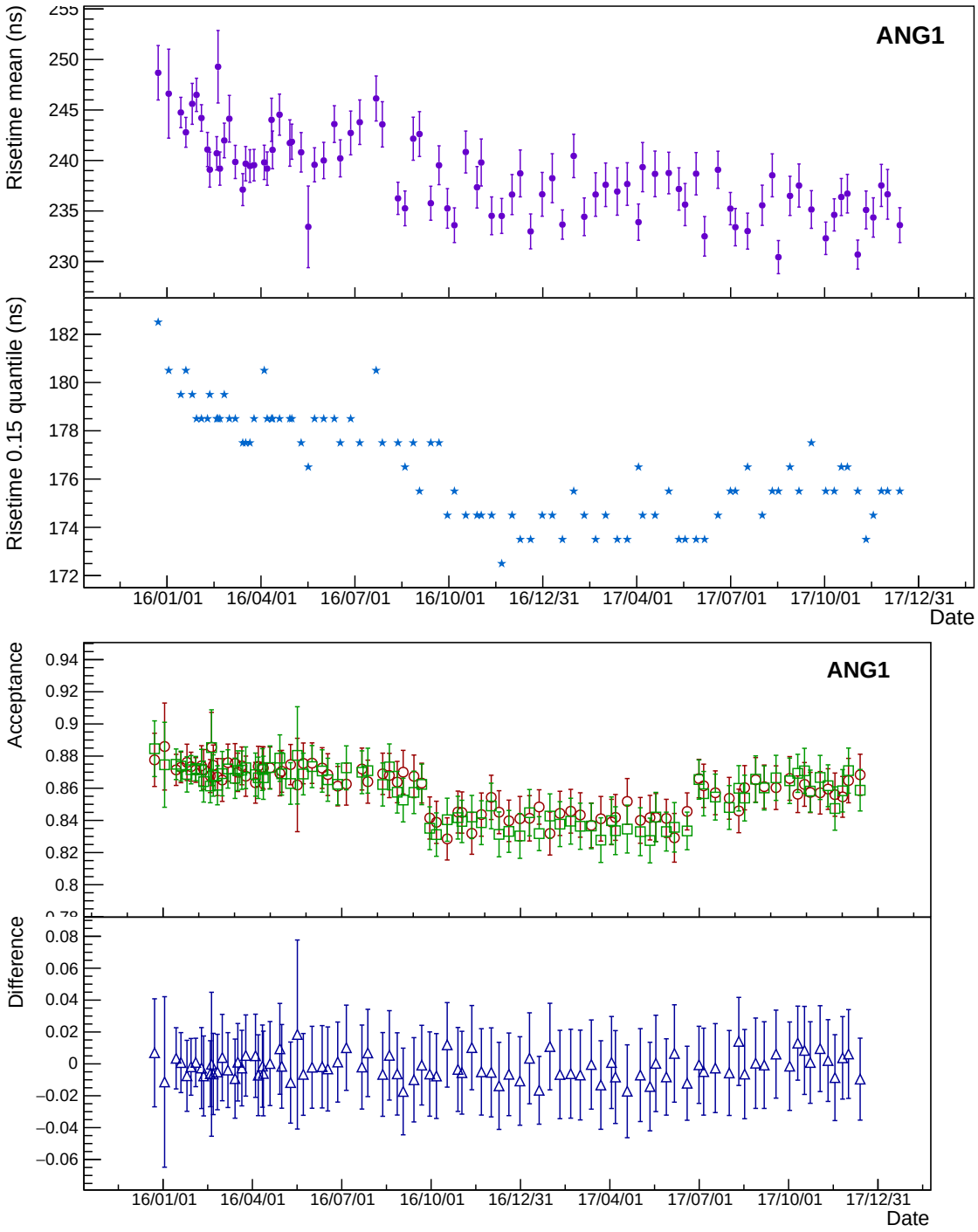

Figure 6.25: Top: variation in time of the mean value and the 10% quantile of the distribution of the Compton continuum events from calibration data at 1 MeV. Bottom: time variation of the survival probability of the Rise Time cut at 1 MeV (red), at 2 MeV (green) and their difference (blue).

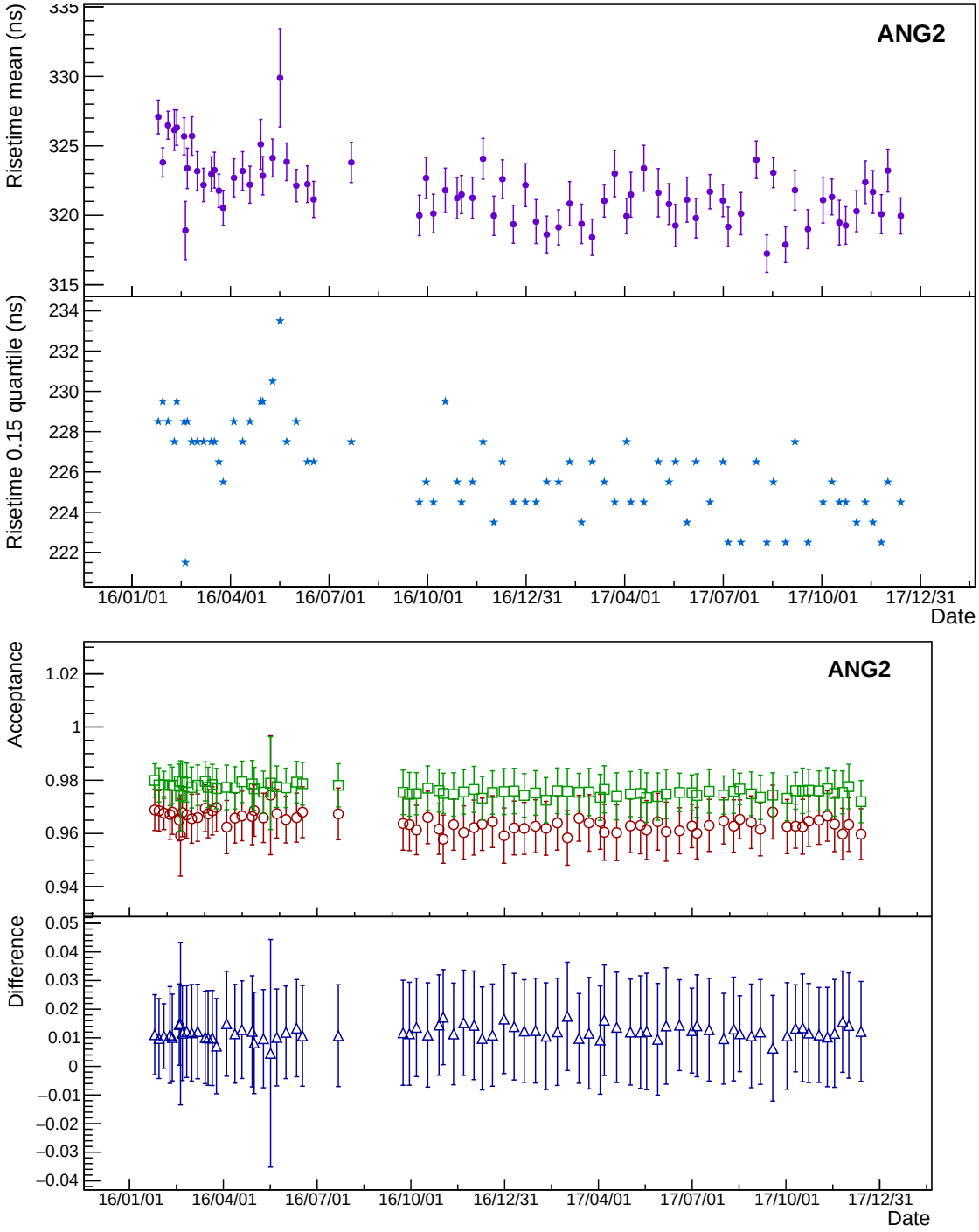

Figure 6.26: Top: variation in time of the mean value and the 10% quantile of the distribution of the Compton continuum events from calibration data at 1 MeV. Bottom: time variation of the survival probability of the Rise Time cut at 1 MeV (red), at 2 MeV (green) and their difference (blue).

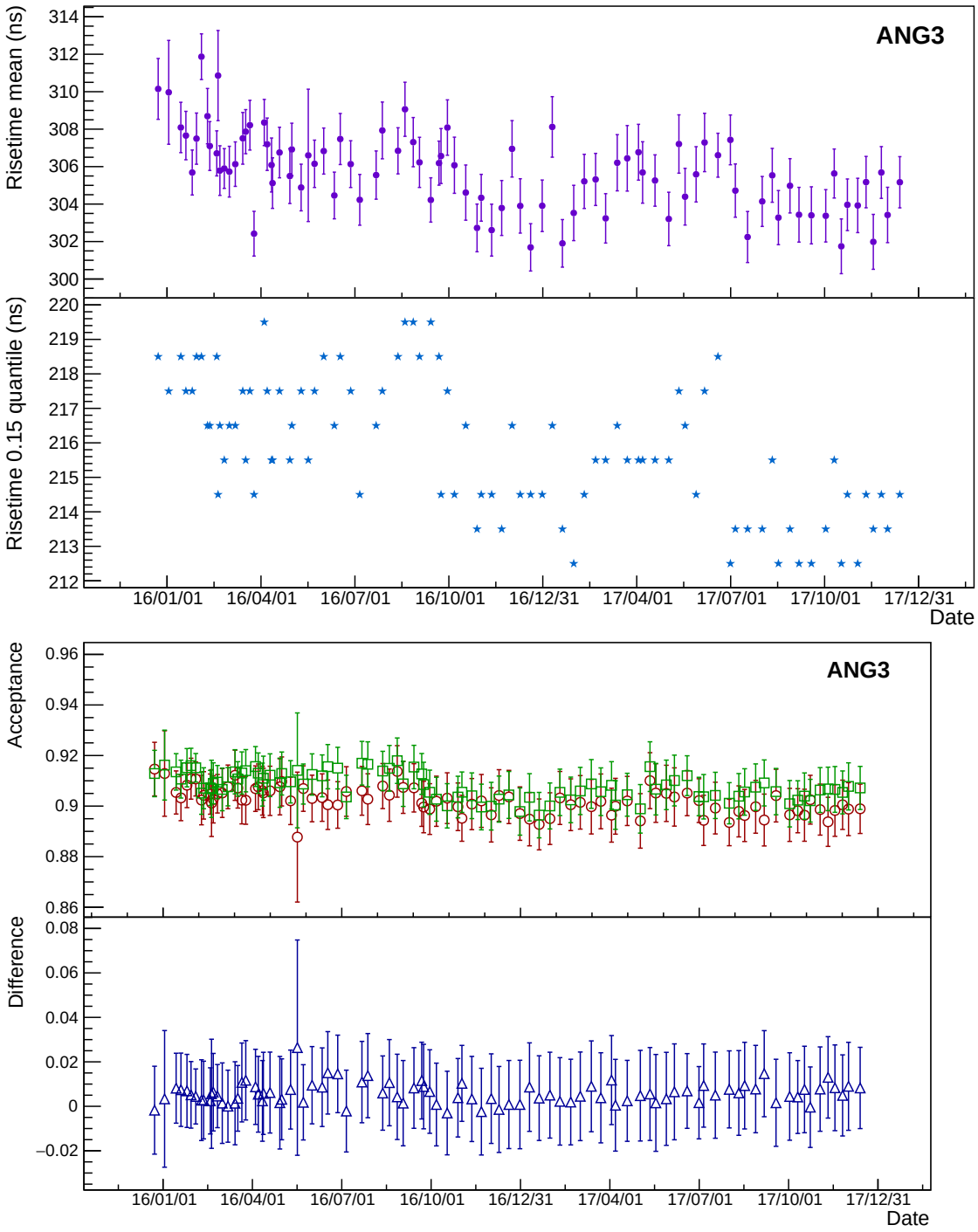

Figure 6.27: Top: variation in time of the mean value and the 10% quantile of the distribution of the Compton continuum events from calibration data at 1 MeV. Bottom: time variation of the survival probability of the Rise Time cut at 1 MeV (red), at 2 MeV (green) and their difference (blue).

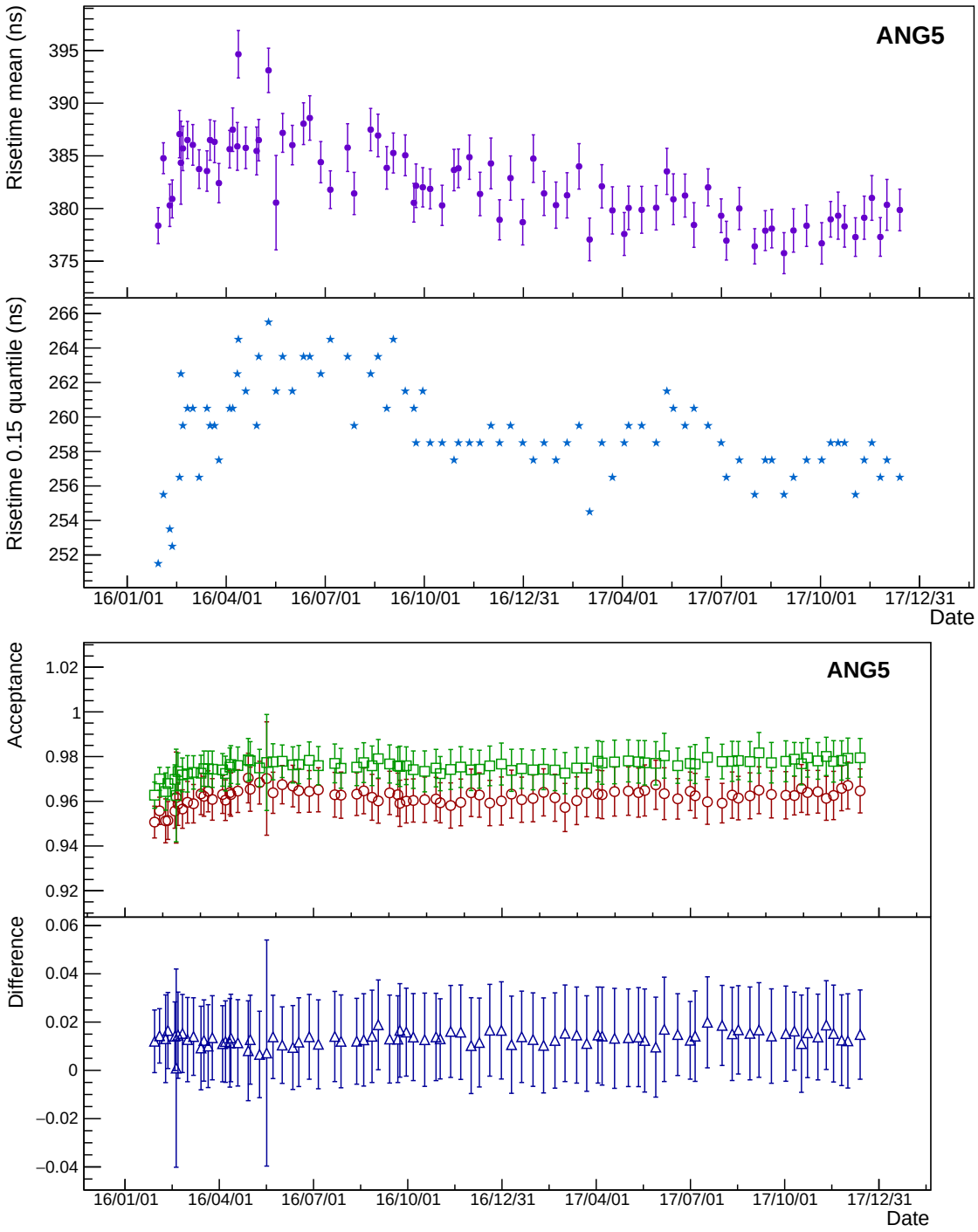

Figure 6.28: Top: variation in time of the mean value and the 10% quantile of the distribution of the Compton continuum events from calibration data at 1 MeV. Bottom: time variation of the survival probability of the Rise Time cut at 1 MeV (red), at 2 MeV (green) and their difference (blue).

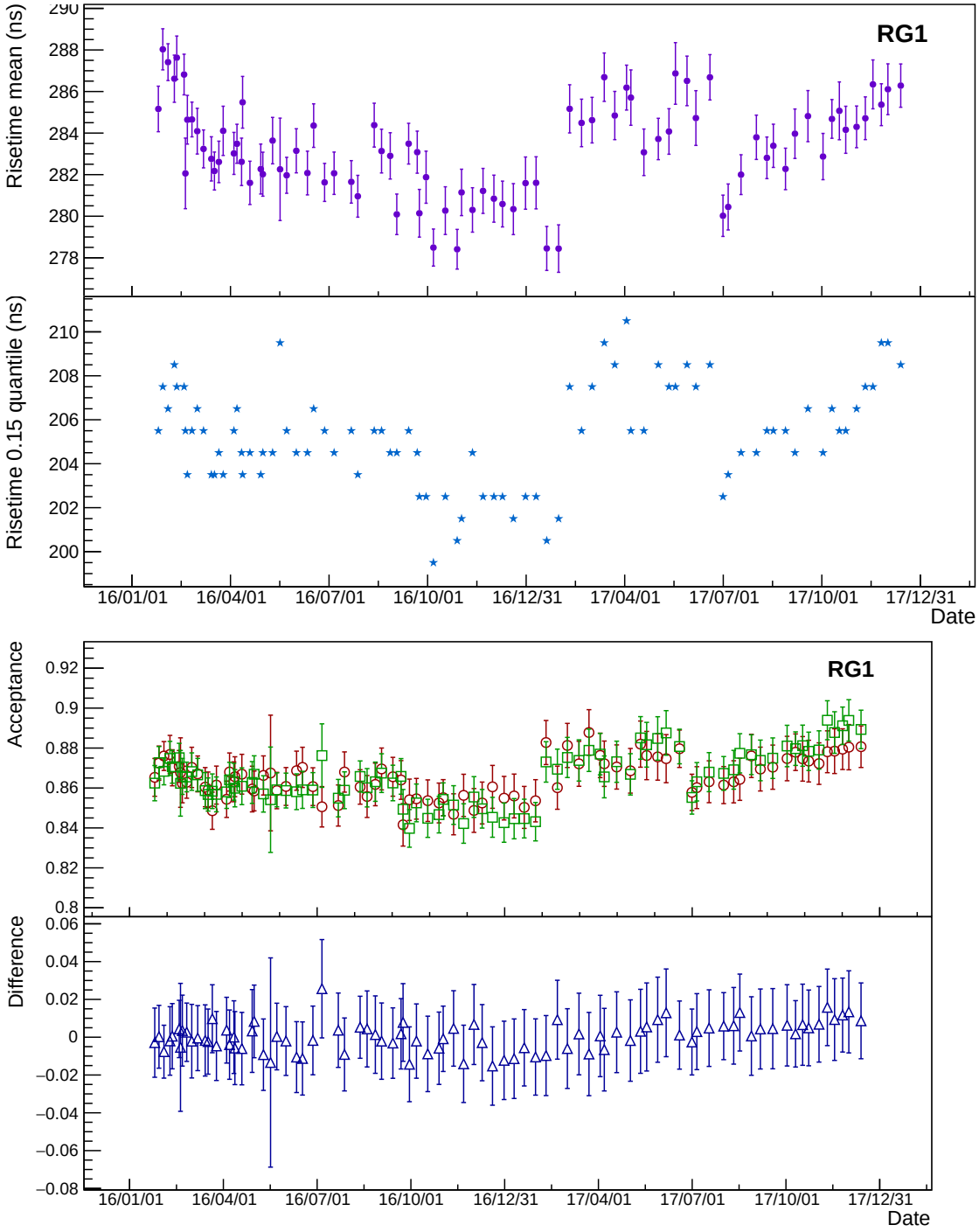

Figure 6.29: Top: variation in time of the mean value and the 10% quantile of the distribution of the Compton continuum events from calibration data at 1 MeV. Bottom: time variation of the survival probability of the Rise Time cut at 1 MeV (red), at 2 MeV (green) and their difference (blue).

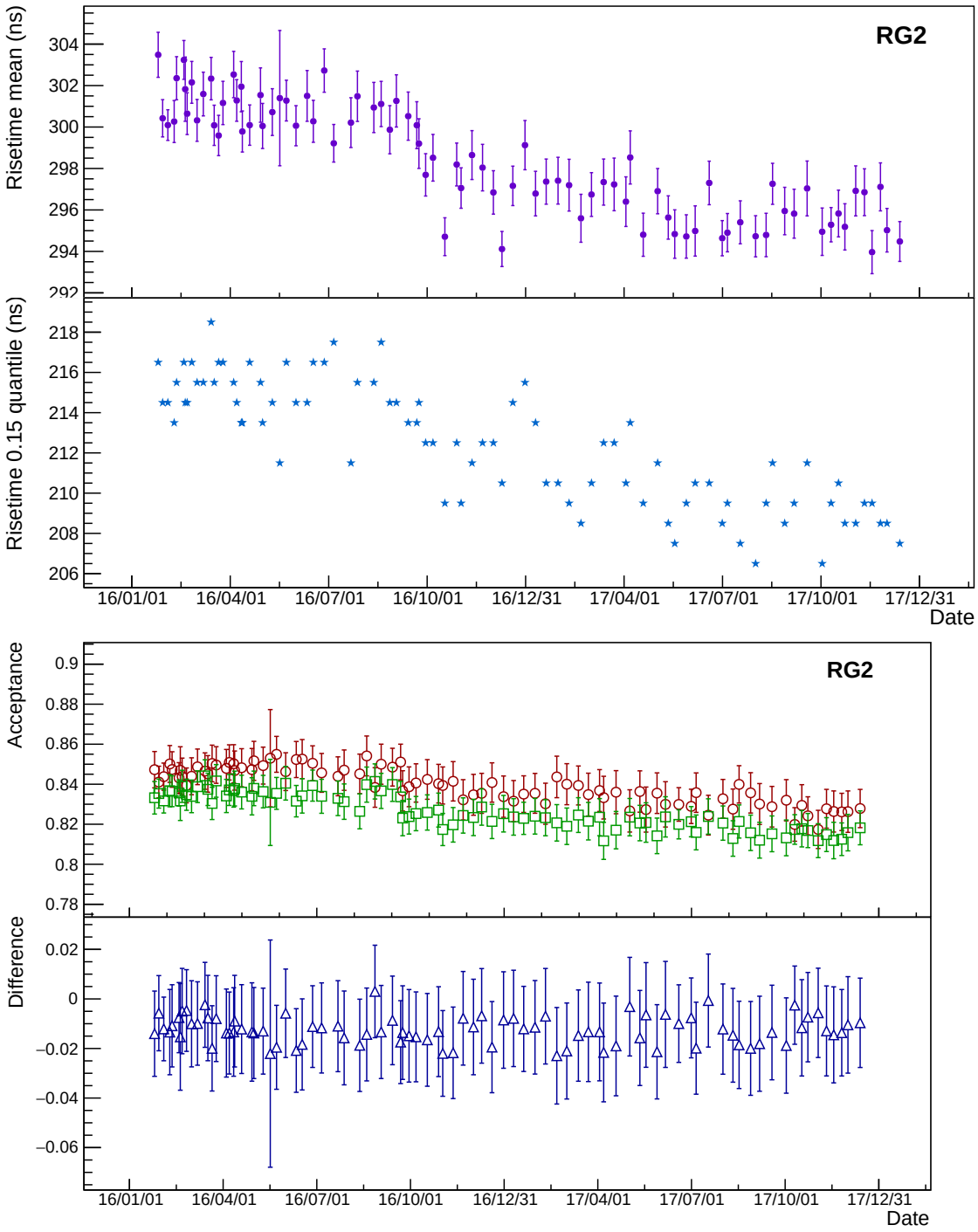

Figure 6.30: Top: variation in time of the mean value and the 10% quantile of the distribution of the Compton continuum events from calibration data at 1 MeV. Bottom: time variation of the survival probability of the Rise Time cut at 1 MeV (red), at 2 MeV (green) and their difference (blue).

Chapter 7

Constraints on the $0\nu\beta\beta$ decay signal

In summer 2018 the GERDA collaboration released 35.7 kg·yr of exposure from the Phase II data. Most of it (23.1 kg·yr) belongs to the semi-coaxial dataset. Part of this data was not included in the previous release due to the evidence of α contaminations surviving the dedicated PSD. The analyses presented in this thesis contributed significantly to the reduction of the BEGE and the semi-coaxial backgrounds. In particular, thanks to the Rise Time PSD, the background of the semi-coaxial detectors is now at the same level as the one of the BEGE dataset and both are better than the design goal of GERDA Phase II. This chapter presents the results of GERDA Phase II. It describes the data-taking (Section 7.1) and the performances of the detectors (Section 7.2 and Section 7.3). The application of the PSD methods and the signal efficiencies are discussed in Section 7.4, followed by Section 7.5 presenting the acquired spectra and the impact of the active background rejection. The $0\nu\beta\beta$ analysis with the computation of the sensitivity and the limits set for $T_{1/2}$ and $m_{\beta\beta}$ are summarised in Section 7.6. Finally, Section 7.7 analyses the relevance of the surface background rejection for the next stages of the LEGEND experiment.

7.1 Gerda Phase II data-taking

Between December 2015 and April 2018 (835 days) GERDA Phase II collected 58.9 kg·yr of exposure, more than twice the 23.5 kg·yr of exposure collected by Phase I in 691 days. The newly acquired exposure is divided in BEGE data (30.8 kg·yr) and semi-coaxial data (28.1 kg·yr).

Just as for GERDA Phase I, a blind analysis was performed. The energy of each event is reconstructed on-line by a digital filter installed in the FADC. All events whose energy falls in the neighbourhood of the $Q_{\beta\beta}$ ($\pm$25 keV) have been stored in a protected disk area not available to the analysis team. These events are processed, as described in Section 3.1, only after the unblinding. Even after the unblinding only the energy of the events and their classification is released to the collaboration. The waveforms and other features of the events from the blinding windows are not made available to avoid biases in the development of new or the improvement of existing active background rejection methods. The blinding window is much larger than the detector energy resolution to account for differences between the energy reconstructed by the on-line filter and by the ZAC filter, and for possible fluctuations of the energy calibration.

The Phase II data have been released three times so far: 5 kg·yr of BEGE data and 5 kg·yr of semi-coaxial data in the summer of 2016 [119]; about 12 kg·yr of BEGE data one year later [120], and 23 kg·yr of semi-coaxial data plus 13 kg·yr of BEGE data in 2018 [51].

The last data release includes one year of BEGE data (353 days) and almost two years of semi-coaxial data (671 days). The semi-coaxial data were not released in 2017 because the higher statistics available revealed the presence of an α contamination which was not rejected by the dedicated Artificial Neural Network analysis. In the following months, the pulse shape analysis based on the Rise Time, described in Chapter 6, was developed and applied to the 28.1 kg·yr of

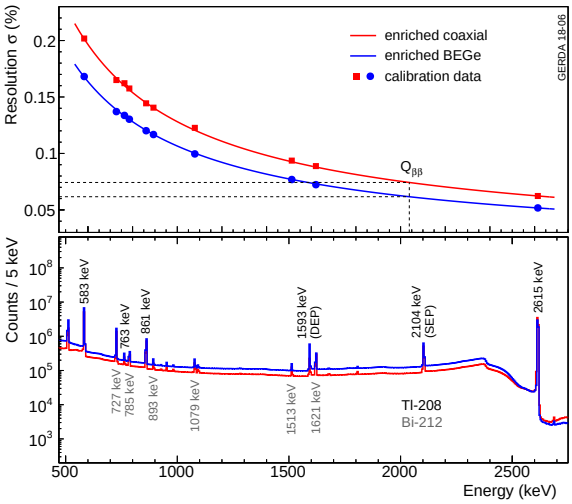

Figure 7.1: Combined spectra of the Phase II ^{228}Th calibrations. The top panel shows the fit of the γ-lines relative resolution (σ/E). For energies above $\sim$ 1.5 MeV the resolution (σ) is better than 1‰ for both datasets. Figure from [51].

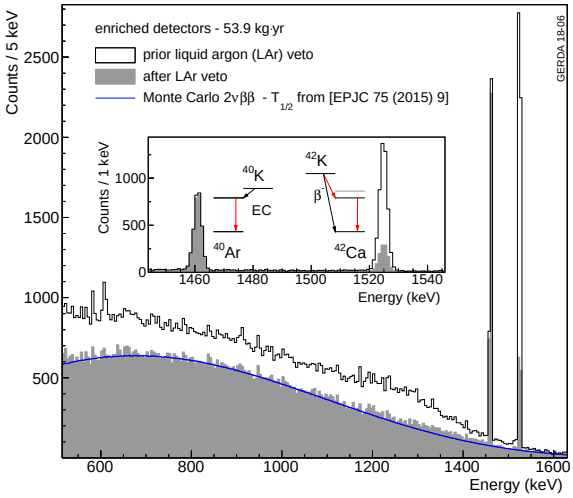

Figure 7.2: Spectrum of the $2\nu\beta\beta$ region. After LAr veto the spectrum is in good agreement with the expected spectrum from $2\nu\beta\beta$. The inset shows the effect of the LAr veto on the two most prominent γ-lines of the GERDA spectrum. Figure from [51].

semi-coaxial data not yet released. The new Rise Time cut was not applied to the first 5 kg·yr of semi-coaxial data to maintain the consistency of this dataset with the previous publications.

During Phase II (from December 2015 to April 2018) the system has been taking physical data for 93% of the time (775.7 days out of 835). The main causes of interruptions to the data-taking have been the weekly calibrations and the maintenance of the system. The array operated in the cryostat for more than 2 years (until May 2018) without being lifted out of the cryostat. Some detectors showed instabilities and leakage current but it was possible to use them for anti-coincidence and they were eventually recovered through adjustments of the bias voltage. Only three HPGe channels (out of 40) were lost, due to the breakage of their JFET transistors: one in July 2016 after operations on the HV filters, and two in May 2017 after a power loss in the laboratory. Less than 20% of the collected data from enriched detectors (73.3 kg·yr) was not included in the $0\nu\beta\beta$ analysis due to instabilities of the energy scale or of the PSA classifiers.

GERDA is currently taking more data with the goal of reaching the target of 100 kg·yr exposure while testing the first prototype detectors for the first stage of the LEGEND experiment.

This Chapter is centred on the results from the 2018 data release.

7.2 Energy scale and resolution at $Q_{\beta\beta}$

The energy of each event is assigned according to the most relevant calibration, in absence of known instabilities of the energy scale the previous calibration is applied. The level of control over the energy calibration allows to merge all physics data into a single spectrum without spoiling the energy resolution. This is possible also because all detectors have similar resolutions (within a factor 2) and the shift between the centroids is much smaller than the resolution. The peaks in the combined spectrum appear therefore to be Gaussian, even though they actually are a mixture of many similar Gaussian distributions. See Figure 7.1 for the combined spectrum of all calibrations for the BEGE and for the semi-coaxial datasets.

The energy resolution of each detector is computed through the fit of the peaks in the combined spectrum of all calibration data. The energy resolution of a dataset is computed from the average

of the detector resolutions (σ_i^2) weighted by the exposure ($\mathcal{E}_i$):

$$\sigma = \sqrt{\frac{1}{\mathcal{E}} \sum_i \mathcal{E}_i \cdot \sigma_i^2}. \tag{7.1}$$

The resolution in the ROI is then extracted from the resolution of the calibration peaks fitted with the function:

$$\sigma(E) = \sqrt{a + b\,E}. \tag{7.2}$$

This results in a full width at half maximum (FWHM) of the expected peak at $Q_{\beta\beta}$ of 3.6±0.1 keV for the semi-coaxial and 3.0±0.1 keV for the BEGe detectors, both corresponding to $\sigma/Q_{\beta\beta} < 10^3$.

7.3 LAr veto instrumentation performances

The LAr veto system includes 31 channels: 16 PMTs, 9 above the array and 7 below, and 15 fibre channels with 4 SiPMs each. All channels operated without major interruptions for the whole data-taking time. The fibre system has been later substituted with an upgraded version in May 2018 while the PMTs will be used until the conclusion of Gerda Phase II.

The thresholds and the veto time windows are optimized individually for each channel. All thresholds are below the average signal amplitude of a single detected photon. The veto windows are about 6 µs and were temporarily reduced, when needed, for the channels showing instabilities.

The rate of uncorrelated coincidences is estimated as the rate of rejected external triggers. Every 40 s the DAQ is triggered to monitor the noise level (baseline events), $2.3\% \pm 0.1$ of these events would be vetoed by random coincidences in the LAr. Most of these coincidences are related to ^{39}Ar decays.

The impact of the LAr veto on the data is evident when looking at the rejection of the ^{40}K and ^{42}K background under the $2\nu\beta\beta$ spectrum, see Figure 7.2. The ^{42}K photon emission is in cascade with its β^- decay which releases 2 MeV in the LAr producing scintillation light. The peak in the spectrum is therefore strongly suppressed. The ^{40}K instead undergoes electron capture and the 1461 keV photon is not accompanied by any energy deposition in the LAr. The suppression of this line ($2.5\% \pm 0.5$) is only due to the random coincidence rate ($2.3\% \pm 0.1$). The Compton continuum from the two lines is completely removed from the spectrum, leaving an almost pure (97%) $2\nu\beta\beta$ spectrum.

7.4 Application of the PSD to Gerda Phase II

7.4.1 Stability and cut levels of the A/E for BEGes

The time stability of the A/E parameter in the BEGe channels has been monitored with the position of the ^{208}Tl DEP and Compton continuum of the ^{228}Th calibrations in the interval 1.0–1.3 MeV. A few finite jumps of the A/E positions were found in correspondence with hardware operations: works on the HV lines, routine maintenance of the clean room above the cryostat, and the temporary installation of a Ra calibration source in February 2017. Only two detectors showed a drift on the level of 5% during the course of Phase II: towards higher A/E values for GD89D and downward for GD91D. The position of the DEP was stable (constant within a sub-percent level) in between hardware operations for all other detectors. The position of the SSE-band in time is approximated with a step function that changes value after each calibration with a greater than 0.5% variation of the DEP position.

The A/E resolution of the 30 BEGe detectors varies between 1.5% and 3.5% ($\mathrm{FWHM}_{\mathrm{A/E}}$). For comparison, the detectors operated in a commercial vacuum cryostat usually have a resolution of 1% or better and the results of Chapter 4 were obtained under the assumption of similar performances. The main reason for the lower A/E resolution of Gerda is the distance between the detectors and their pre-amplifiers (about 30–80 cm). Figure 7.3 shows clearly how the top detectors of each

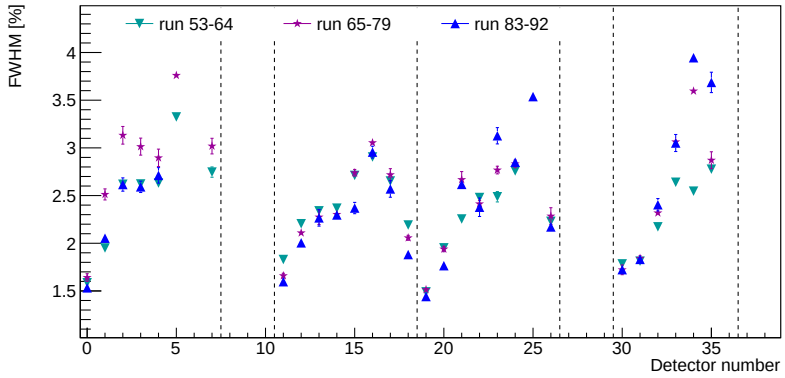

Figure 7.3: Resolution of the A/E parameter for the BEGe detectors of Phase II. The dashed lines represent the division of the detectors in the 7 strings (4 for BEGe and 3 for semi-coaxial detectors). The three periods correspond to the three data releases: Summer 2016 (runs 53–64), Summer 2017 (runs 65–79) and Summer 2018 (runs 83–92). The three series show a clear dependence of the resolution on the detector position within its string. In general, the detectors farther from the preamplifiers (placed above the strings) have a lower resolution, with the exception of the detectors at the very bottom of the strings. The bottom detectors benefit from having only one neighbour. The last detector of the sixth string (channel 36) is a semi-coaxial detector (ANG1) and is therefore not shown.

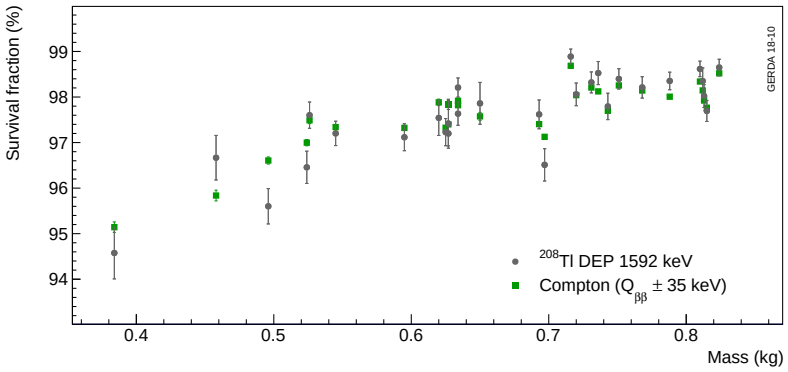

Figure 7.4: Signal acceptance of the high A/E cut. The acceptance of ^{208}Tl DEP and Compton continuum (from calibrations) for each detector is shown in relation to the mass of the detector. Since the dimensions of p+ electrodes do not increase for larger diodes, the size of volume rejected by the high A/E cut is roughly the same for all detectors. Therefore, the relative signal acceptance of the cut increases with the mass of the detector. Figure from [121].

string (channels 0, 11, 19, 30) have a better resolution than the ones that are farther from the preamplifiers near the bottom of the strings (channels 7, 18, 26, 35).

The low cut of the A/E was fixed at 90% acceptance of the ^{208}Tl DEP, which corresponded to 1.2–1.9 $\sigma_{A/E}$ below the mean values of the DEP distributions. This cut is significantly stronger than the one applied in GERDA Phase I, which was 2.6 $\sigma_{A/E}$ below the DEP distribution centroid. This results in a ∼5% reduction of the signal acceptance.

The high cut of the A/E was fixed at 4 $\sigma_{A/E}$ above the mean values of the DEP distributions, this corresponded to 97.3% acceptance of the DEP. For the first data release (Summer 2016), the high cut was placed twice as far from the SSE band centroid as the low cut. This would correspond, according to the different detectors, to values in the range of 2.4–3.8 $\sigma_{A/E}$. Given the big distance between the SSE band and the p+ contact events, the cut was relaxed without an observable increase of the residual α background. Figure 7.4 shows how the signal acceptance of the high A/E cut is correlated with the total volume (mass) of the diodes. This confirms that the high A/E

cut is a volume cut that removes events generated in the proximity of the p+ contact, which has roughly the same size in all BEGe detectors.

The overall PSD acceptance of the ^{208}Tl DEP is $87.6\% \pm 2.5$. The SSE acceptance has been cross checked with an almost pure (97%) sample of $2\nu\beta\beta$ events, i.e. events with energy in the interval 1.0–1.3 MeV after LAr veto. The PSD accepted $84.2\% \pm 0.8$ of these events. Monte Carlo simulations have shown that the different distributions of $0\nu\beta\beta$ and DEP events inside the detector volume result in a $\sim 1\%$ lower acceptance of the high A/E cut for $0\nu\beta\beta$. This is caused by the lower probability that both 511 keV photons generated by pair production in the p+ contact region escape the detector, producing a DEP event. Furthermore, the $0\nu\beta\beta$ events have a higher energy (2039 keV) than the DEP events (1592 keV). The energy difference increases the bremsstrahlung cross-section, this is partially compensated by the probability of γ Compton scattering prior to the pair production in the DEP events. Overall, the MSE fraction of the $0\nu\beta\beta$ events is about 2% higher than for DEP.

7.4.2 Combination of ANN_MSE and Rise Time for semi-coaxials

For the semi-coaxial dataset two pulse shape analyses are sequentially applied: the Artificial Neural Network for MSE identification and the Rise Time analysis described in Chapter 6. The ANN_MSE is an supervised classification network with 50 input parameters and two hidden layers with 50 and 51 nodes. The input parameters describe the shape of the leading edge of the normalized charge pulse. The network is trained with data from the ^{228}Th calibrations: the DEP events at 1592 keV provide a proxy for the SSE signals and the FEP of ^{212}Bi at 1620 keV provide a sample of background events. Two proxies with a larger energy difference could have induced an energy bias into the ANN_MSE. Nevertheless, an energy dependence of the ANN_MSE was found by a study with simulated pulse shapes of Monte Carlo generated events. Correcting the $2\nu\beta\beta$ acceptance for this effect, the $0\nu\beta\beta$ signal efficiency was estimated to be $85\% \pm 5$. From calibration data, it is possible to assert the rejection of the Compton continuum in the ROI. The ANN_MSE rejects 37% of the ^{208}Tl events at $Q_{\beta\beta} \pm 25$ keV. The α background is also reduced by about 40% with large variations among the seven semi-coaxial detectors. The energy dependence and time stability of the ANN_MSE was tested with the same datasets used to test the Rise Time cut (see Section 6.3) and the results are reported in [121]. The combination of the ANN_MSE with the Rise Time cut results in a $0\nu\beta\beta$ signal acceptance of $71.2\% \pm 4.3$. It removes 96% of the signals with energy above 3.5 MeV (i.e. α signals) and reduces the background index of the semi-coaxial dataset to $0.6^{+0.5}_{-0.3} \cdot 10^{-3}$ cts/(keV $\cdot$ kg $\cdot$ yr).

Table 7.1: Summary of main contributions to the $0\nu\beta\beta$ efficiencies in GERDA. The main datasets of Phase I are reported in the first two rows. The ^{76}Ge enrichment fraction is reported as f_{76}. The active volume fraction (AV) has been measured during the characterisation of the detectors before their deployment. The probability to record the full energy of the event is ε_{FEP}. The exposure $\mathcal{E}$ is computed using the total mass of each detector and their live time used for the analysis. Other terms included in the total efficiency (ε) are the efficiency of the quality cuts ($> 99.9\%$) and of the LAr veto (97.4%).

dataset	PSD	f_{76}	AV	ε_{FEP}	ε	B.I.[1]	$\mathcal{E}$ [kg·yr]
I Coax G.	83(3)%	87(2)%	87(2)%	91(1)%	57(3)%	11(2)	17.9
I BEGe	92(2)%	88(1)%	91(1)%	90(1)%	66(2)%	5(4)	2.4
II Coax 1	77(5)%	87(2)%	86(2)%	91.4(8)%	52(4)%	3(2)	5.0
II Coax 2	71(4)%	87(2)%	86(2)%	91.4(8)%	48(4)%	0.6(4)	23.1
II BEGe	87(3)%	88(1)%	88.5(3)%	89.7(1)%	60(2)%	0.6(4)	30.8

[1] In units of 10^{-3} cts/(keV $\cdot$ kg $\cdot$ yr)

7.4.3 Signal efficiency

The overall efficiency of the datasets includes the efficiency of the PSD analyses, the efficiency of the Quality Cut (see Section 3.3), the abundance of ^{76}Ge in the enriched detector and the fraction of active volume (because the exposure is computed on the total mass), and the probability to detect the full energy of the $0\nu\beta\beta$ events. For the main datasets of GERDA, these values are reported in Table 7.1. The stronger PSD cuts that have been applied to the Phase II data to reduce the background level, lower the overall efficiency of about 5–10% with respect to Phase I.

7.5 Spectra and background composition

Figure 7.5 shows the spectra of the main datasets. The grey histograms with PSD and without LAr veto, show that the γ background is better removed by the veto and that the residual Compton continuum from the three γ-lines (1460 keV; 1525 keV; 2614 keV) is still visible after the PSD cuts. For comparison with the effect of LAr veto on γ background, see Figure 7.2. On the other hand, the α background is completely removed by the PSD, with only one event above 2.6 MeV rejected only by the LAr veto.

A Bayesian study of the different components of the spectra (before active background suppression) has been performed to get a better understanding of the GERDA background [122]. A full set of Probability Density Functions (PDFs) for each known background source has been extracted from Monte Carlo simulations of the array. Information on the possible level of contaminations is derived from extensive screening measurements of the materials and the components placed in the proximity of the detectors. Radon emanation measurements, γ-ray spectroscopy with HPGe detectors and Mass spectrometry with Inductively Coupled Plasma Mass Spectrometers (ICP-MS) provided estimates for the contaminations from the ^{228}Th and ^{238}U chains, as well as ^{60}Co and ^{40}K.

The fit has been performed on three spectra: single BEGE detectors, single semi-coaxial detectors, and two-detectors coincidences. The latter provides constrains of the locations of γ-emitters, i.e. ^{42}K and ^{42}K. Distinctive features such as the γ-lines and the high energy spectrum

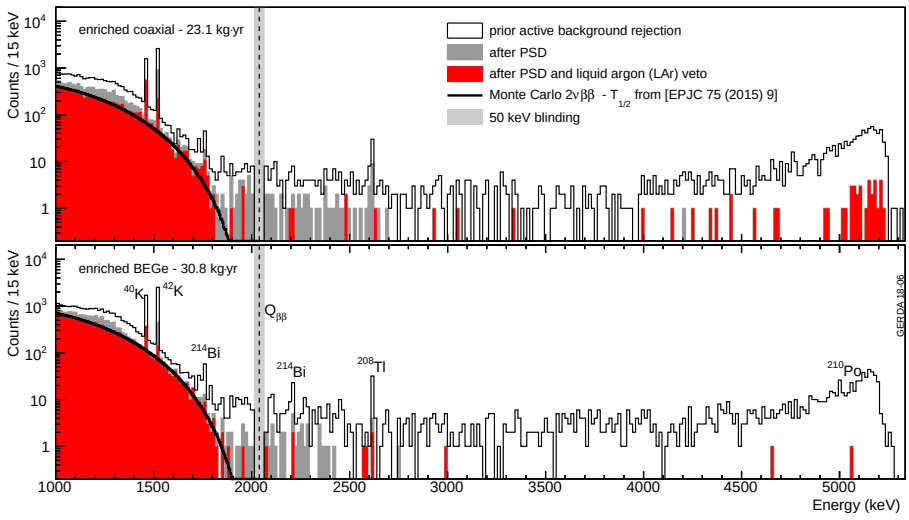

Figure 7.5: Spectra of GERDA Phase II 2018 data release [51]. The top (bottom) panel shows the combined energy spectrum of the semi-coaxial (BEGE) detectors. The first spectrum includes all the single HPGe detector events not rejected by the muon veto. The gray spectrum shows the events accepted by PSD: the A/E cut is applied to the BEGE data; the Rise Time cut and MSE artificial neural network are applied to the semi-coaxial data. The red spectrum includes only the events accepted by PSD and LAr veto.

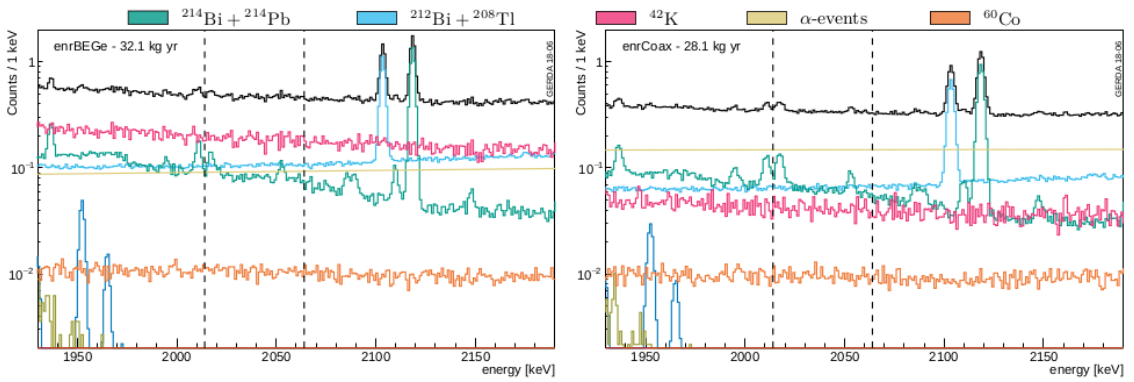

Figure 7.6: Fit of the analysis window before active background suppression [122]. The left panel shows the BEGe dataset(32 kg·yr), the right one shows the semi-coaxial dataset(28 kg·yr). In both cases about half of the background is connected to surface events (^{42}K and α).

of the α events provide clear inputs to the fit. The simultaneous fit of the three spectra describes the composition and the shape of the background around the ROI.

The model describes only the spectra before active background rejection (PSD and LAr veto). The fit of the spectra after all the background rejection is not yet feasible because of the lack of statistics and the lower accuracy of the PDFs for the residual components.

Figure 7.6 shows the background model for BEGe and semi-coaxial datasets in the ROI. In both cases, the most important components are γ- from ^{238}U and ^{228}Th, ^{42}K, and α decays. The main difference between the two datasets is the impact of ^{42}K β decays, which are suppressed by the thicker n+ contact of the semi-coaxial detectors. On the other hand, the α component is about two times more relevant for the semi-coaxial detectors. For both datasets about half of the background is induced by decays on the detector surfaces (α and β) and half is connected to photons produced farther from the detectors.

Figure 7.6 also shows how the overall background in the ROI is in first approximation flat. A minor descending slope is induced by the shape of the ^{42}K beta spectrum and by the Compton continuum produced by the ^{238}U daughters, while the emissions of the ^{228}Th chain have a small positive slope. Only minor distortions of this shape can arise from the active background rejection. Chapter 4 and Chapter 6 showed that the discrimination methods for surface events have no relevant energy dependence. The application of the A/E MSE rejection to the ^{228}Th calibration data also does not show any energy dependence. The LAr veto has a small dependence on the amount of energy, and therefore light, released in the Ar. Thanks to the low veto threshold (below a single photon electron) and the high light yield, this effect is relevant only in the proximity of full energy peaks, i.e. when the 2.6 MeV photons from ^{208}Tl decays release $>$ 2.2 MeV in the germanium. The main known energy dependence from the ANN_MSE is at the level of 1–2% within the 260 keV analysis window.

With the assumption of a flat background distribution, supported by the fit of the spectra before active background suppression, it is possible to extract the expected number of background counts in the ROI for each dataset from the count rates in the neighbouring regions. The analysis window considered for the calculation of the background index (B.I.) is the interval between 1930 keV and 2190 keV with the exclusion of two regions at 2104 ± 5 keV and 2119 ± 5 keV where γ-lines are expected. Figure 7.7 shows the spectra in the analysis window for the data released in 2018. In the last data release, 3 counts were found within the blinding window of the BEGe dataset. The B.I. of the two datasets are reported in Table 7.1. The additional PSD for the semi-coaxial dataset described in Chapter 6 lowered the B.I. from $3 \cdot 10^{-3}$ cts/(keV $\cdot$ kg $\cdot$ yr) to $0.6 \cdot 10^{-3}$ cts/(keV $\cdot$ kg $\cdot$ yr) , the same value registered for the BEGe dataset.

One count is only 2.4 σ away from the $Q_{\beta\beta}$. Given the background rates of the three Phase II datasets, the probability of one or more background counts in a 3 σ interval around the $Q_{\beta\beta}$ is 40%.

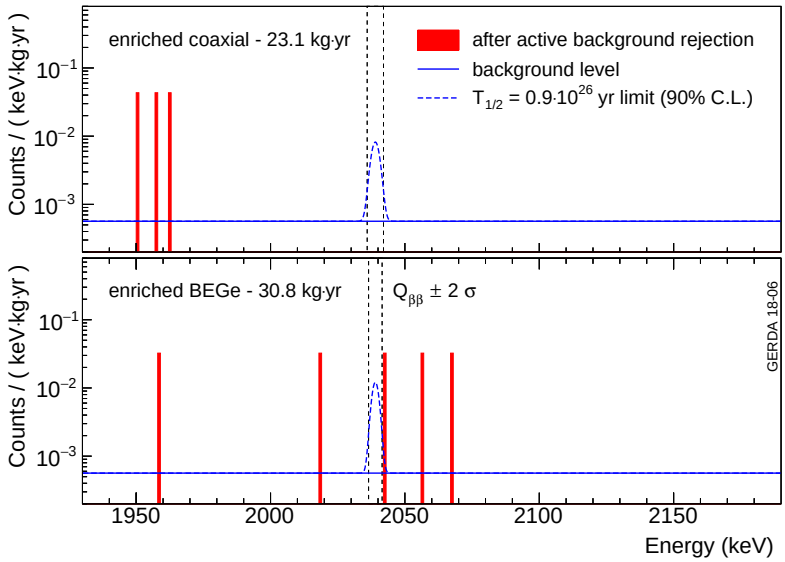

Figure 7.7: Analysis windows after the unblinding. The BEGe dataset contains 3 counts in the blinding windows ($Q_{\beta\beta} \pm 25$ keV), one of which is only 2.4 σ away from the $Q_{\beta\beta}$.

7.6 Sensitivity, limits and their impact

The data of Gerda are grouped into datasets with a coherent energy resolution and background index. The Phase I data is divided into 4 datasets: golden (low background data from semi-coaxials), silver (small dataset of semi-coaxial data with higher background), extra (semi-coaxial data collected in the summer of 2013 after the Phase I data release), and BEGe collected by BEGe detectors. The Phase II data is divided into 3 datasets: coax1 with the first 5 kg·yr of semi-coaxial data released without Rise Time PSD, coax2 with the rest of the semi-coaxial data with better α rejection, and BEGe data.

The $0\nu\beta\beta$ result is extracted by an unbinned maximum likelihood fit of the energy spectra of the 240 keV around the region of interest (ROI). The energy resolution of each dataset is fixed while the background rates are free parameters. The signal strength ($S = 1/T^{0\nu}_{1/2}$) is extracted by the simultaneous fit of all spectra. The likelihood function for each dataset is composed by a Gaussian term centred at $Q_{\beta\beta}$ for the signal and a flat distribution for the background that is assumed flat around the ROI. The signal strength that maximizes the likelihood of the data is $S = 0$, which corresponds to zero signal counts.

The limit and the sensitivity are extracted both with a frequentist and a Bayesian analysis with the same methods adopted for the previous data releases [119]. The limit of the half-life provided by the frequentist analysis is:

$$T^{0\nu}_{1/2} > 0.9 \cdot 10^{26} \text{ yr (90\% C.L.)}.$$

The limit is slightly below the median sensitivity of the experiment, computed through a set of Monte Carlo generated datasets with the same parameters and no $0\nu\beta\beta$ signal. The median sensitivity for limit setting is $1.1 \cdot 10^{26}$ yr. The simulated datasets with no signal provide a stronger limit than $0.9 \cdot 10^{26}$ yr in 63% of the realisations.

The Bayesian analysis assumes flat prior distribution for the background (0–0.1 cts/(keV·kg·yr)) and for the signal strength (S) in the interval (0–10^{-24}) yr^{-1}. The 90% credible interval (C.I.) for the half-life extracted from the posterior distribution for S is:

$$T^{0\nu}_{1/2} > 0.8 \cdot 10^{26} \text{ yr (90\% C.I.)}.$$

Table 7.2: Results from a selection of the running $0\nu\beta\beta$ experiments. The limits and the sensitivity are expressed with 90% C.L. .

	Experiment	Isotope	Sensitivity		Limits	
			[10^{25} yr]	meV	[10^{25} yr]	meV
[51]	GERDA	^{76}Ge	11	104–228	9.0	110–250
[52]	Majorana	^{76}Ge	4.7	157–346	2.7	200–433
[53]	CUPID-0	^{82}Se	0.23	394–810	0.24	376–770
[55]	CUORE	^{130}Te	0.7	162–757	1.5	110–520
[57]	EXO-200	^{136}Xe	3.7	93–287	1.8	147–398
[56]	KamLAND-Zen	^{136}Xe	5.6	76–234	10.7	61–165

The median sensitivity of the Bayesian analysis is $0.8 \cdot 10^{26}$ yr, close to but higher than the limit. The probability to obtain a stronger limit was 59%.

The limit depends, of course, on the assumption in the prior distribution $\mathrm{P}_0(S)$. For example, assuming that all values of effective neutrino masses have the same probability to produce a 50% higher limit:

$$T^{0\nu}_{1/2} > 1.2 \cdot 10^{26} \text{ yr (90\% C.I.)} \qquad \text{with} \qquad \mathrm{P}_0(S) \propto \frac{1}{\sqrt{S}}.$$

Assuming exclusively light Majorana neutrino exchange, the limit on the decay rate of $0\nu\beta\beta$ can be converted into an upper limit on the effective Majorana mass, $m_{\beta\beta} = |\sum_{i=1}^{3} U_{ei}^2 m_i|$. This requires the knowledge of the nuclear matrix element of the decay; for the time being, different values are available in the literature and they differ by factors up to 2–3 according to the nuclear model used for the computation. This uncertainty on the nuclear structure results in a range of possible $m_{\beta\beta}$ values for a given $T^{0\nu}_{1/2}$. The GERDA limit on $T^{0\nu}_{1/2}$ can the thus translated to:

$$m_{\beta\beta} < 0.11 - 0.25 \text{ eV} \qquad (90\% \text{ C.L.}).$$

The limit on the effective Majorana mass can be compared with the ones obtained by other $0\nu\beta\beta$ experiments, also the ones using different isotopes. In particular, the comparison of the sensitivities is not affected by the statistical fluctuation of the background. Table 7.2 reports the sensitivities and the limits of some of the experiments currently running. GERDA has the highest sensitivity for the half-life of the decay and is the first experiment to breach above 10^{26} yr.

Choosing one of the many scenarios for the number of existing (sterile) neutrinos and the hierarchy of their masses, it is possible to constrain the different observables connected to their masses:

- $m_{\beta\beta} = \left|\sum_i U_{ei}^2 m_i\right|$, the effective Majorana mass;
- m_{light}, the mass of the lightest neutrino;
- $\sum m_i$, the sum of the masses of different neutrinos;
- $m_\beta = \sqrt{\sum_{i=1} \left|U_{ei}^2\right| m_i^2}$, the mass observable in the single beta decay;
- $\mathrm{sgn}(\Delta m_{31})$, the ordering of the known neutrino mass eigenstates.

Figure 7.8 shows the allowed parameter spaces and the interplay of the different observables in the scenario with only three neutrinos (no steriles) and $0\nu\beta\beta$ mediated only by light Majorana neutrino exchange. For high values of m_{light}, the mass splittings are small compared to the absolute mass scale. This region of the parameter space is referred to as quasi-degenerate because normal

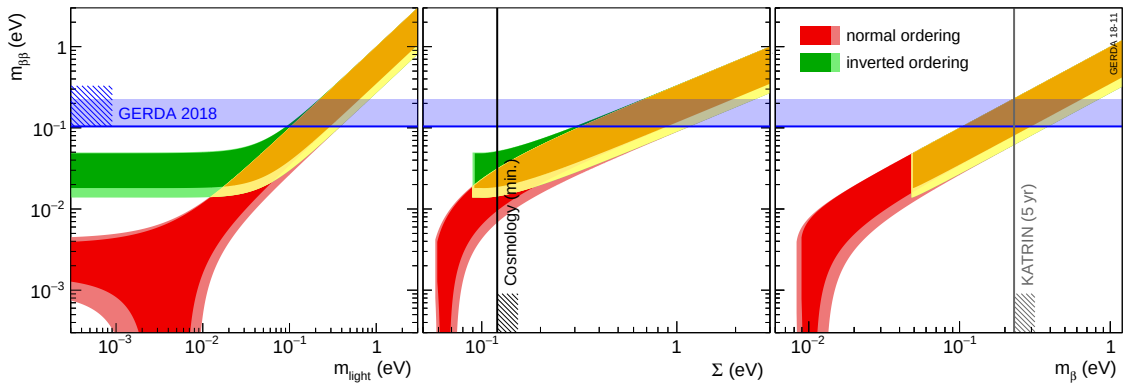

Figure 7.8: Parameter space for the neutrino masses observables ($m_{\beta\beta}$, m_{light}, $\sum m_i$ and m_β) in the scenario with three light Majorana neutrinos. Contours follow from a scan of the Majorana phases (darker region) and the 3σ intervals of the neutrino oscillation data (lighter shades) within NuFIT [124]. The blue horizontal band shows the GERDA limit on $m_{\beta\beta}$, the vertical lines report respectively the limit on $\sum m_i < 0.12$ eV of the Planck collaboration [34] and the m_β sensitivity goal of KATRIN [31]. Figure from [51].

and inverted hierarchy are indistinguishable. The current limits on $\sum$, m_β, and $m_{\beta\beta}$ already exclude a good portion of this space. Besides the $0\nu\beta\beta$ constraints on $m_{\beta\beta}$, the measure of the β spectrum end-point provides a direct measurement of m_β. The current limits on m_β are at 2.2 eV(95% C.L.) [29, 30] but the KATRIN experiment aims to lower it by more than 10 times to about 0.2 eV (90% C.L.) in the next years [31, 32]. The cosmological models describe the impact of the sum of the neutrino masses on the evolution and structure of the universe. Within each cosmological model, the measurements of the anistropy of the cosmic microwave background and of the baryonic acoustic oscillation imply upper limits on $\sum m_i$. The Planck collaboration set a limit of $\sum m_i < 0.12$ eV (95% C.L.) within the framework of the standard spatially-flat 6-parameter ΛCDM cosmology [34]. While the cosmological constraints on the neutrino masses are becoming increasingly robust, they still depend on the choice of model and observation included in the analysis as shown for example in Section 25.3.3 of [123].

7.7 Surface background in Legend

The LEGEND experiment aims to reach a background index in the ROI of about 0.1 cts/(FWHM·t·yr) for its last stage, LEGEND-1000. With the energy resolution of FWHM= 3.0 keV achieved with the BEGE detector in Phase II, the current background level corresponds to about 1.5 cts/(FWHM·t·yr). A further reduction of the background rate by more than one order of magnitude is therefore required.

The first stage of the LEGEND experiment will aim for 1 t·yr of exposure with up to 200 kg of detectors [45]. The allowed background budget to remain near the background free regime with that exposure is about 0.6 cts/(FWHM·t·yr). In order to understand whether the current surface background level would be compatible with the LEGEND-200 goal, it will be assumed here that the entirety of the GERDA Phase II background is caused by decays on the detector surfaces.

The BEGE background index prior to active suppression (PSD & LAr) is 45±3 cts/(FWHM·t·yr). The surface component of the Phase II background must therefore be < 45 cts/(FWHM·t·yr) before cuts. This level has been achieved thanks to the mechanical barrier of the Phase II nylon mini-shroud but it is reasonable to assume that LEGEND will have a passive ^{42}K suppression at least this good. The measurements reported in Chapter 4 showed that, with good A/E resolution, it is possible to reduce these components by at least two orders of magnitude. Such reduction would bring the background rate from ^{42}K and α decays to < 0.45 cts/(FWHM·t·yr) below the goal for LEGEND-200.

Further measures can be taken to reduce these components (for LEGEND-1000) such as the use of Ar depleted in ^{42}Ar. The number of diodes needed for the second stage will also require the collaboration to oversee more closely the production processes; this will most likely result in a lower contamination of the p+ contact region. The α contribution will also be reduced by the combination of the half-life of ^{210}Po (138 d) with the longer run time of the future experiments.

Conclusion

This dissertation reports the results of my work on the HPGe signals for the GERDA experiment: the rejection of spurious events from the GERDA Phase II datasets, the estimation of the potential reduction of external surface backgrounds that can be obtained with the A/E methods for Pulse Shape Discrimination (PSD), and the development of a novel technique to identify the α-induced events in semi-coaxial detectors.

Data selection has been a crucial task for GERDA Phase I because the unphysical events represent a considerable fraction of the recorded data due to the high rate ($\sim$ 10 mHz) of micro-discharges. In order to identify the micro-discharges, a series of digital filters was set up to measure the properties of the recorded waveforms. The events whose properties satisfy all the selection criteria are identified as physical. In contrast to the methods applied in GERDA Phase I, the quality selection implemented for GERDA Phase II is not limited to the analysis of the single waveforms but considers all the HPGe signals of the events. An event is rejected if it contains one or more waveforms not compatible with an energy deposition or an "empty" baseline. All spurious waveforms were removed from the dataset while physical events are accepted with 99.918% probability (i.e. signal acceptance). The computation of the acceptance is based on events with an external trigger (Baseline and Test Pulser events). The visual inspection of the high energy traces (above 1.6 MeV) did not reveal any misclassified unphysical events. On a statistical level, the effectiveness of the quality selection is corroborated by the spectral analysis of the background components which have been fitted according to the GERDA background model and do not show any anomalous structures.

The development of the GERDA PSD methods has been historically focused on the rejection of the γ background events. Their performances have been optimised with the use of distant γ-sources, typically ^{228}Th placed tens of centimetres away from the detectors. The introduction in GERDA Phase II of the liquid argon scintillation veto system, however, drastically reduced this type of background. This thesis showed how the key-role of the PSD for BEGE and semi-coaxial detectors is the rejection of surface backgrounds. These background sources, α and β decays on the detector surfaces, do not produce scintillation light in the LAr and release energy only in a single detector. The PSD is, therefore, the only effective active background rejection. Due to the smaller full charge collection depths of the BEGE detectors, β decays of ^{42}K on the n+ surface are a major component of their background in the Region of Interest (ROI). On the other hand, semi-coaxial detectors are more exposed to α decays due to the relatively larger p+ contact surface.

Thanks to the A/E analysis, in GERDA Phase I the BEGE detectors achieved a background level about two times better than the one of the semi-coaxial dataset, maintaining a higher signal acceptance. As part of the analysis team working on the first BEGE string, I contributed to the calibration algorithms for the A/E parameter and for the determination of the cut levels. With the analysis of β emitters measurements in vacuum cryostats and LAr and through Monte Carlo simulations it was shown that the BEGE PSD could reduce the ^{42}K contribution below GERDA Phase II requirements.

During the course of GERDA Phase II, the semi-coaxial dataset presented an unforeseen class of high-energy events with the characteristic energy distribution of α events. These events had a distinctive shape with the fastest rise times allowed by the bandwidth of the amplifiers. The semi-coaxial dataset was then excluded from the 2017 data release with the goal of developing a dedicated blind analysis to remove this contamination. Here, the pulse shapes of the α-induced

events are described on the basis of the $2\nu\beta\beta$ samples and high-energy α events from the physics runs, and with pulse shape simulations of the seven semi-coaxial detectors. Through the comparison between data and simulations, three classes of α pulses are associated with different interaction locations on the p+ contact area. The analysis of the semi-coaxial spectrum after anti-coincidence cuts shows that more than half of the background in the ROI is induced by α decays. It was also pointed out that the contamination is not uniformly distributed on the sensitive surfaces of the detectors: in particular, it appears to be concentrated on the portion of p+ contact outside of the bore-hole.

A novel single parametric PSD for the residual α background was then developed in the context of this dissertation on the basis of the study of the α-induced events pulse shapes and the analysis of the selection performed by the ANN discrimination of multiple site events. The bias and the precision of the rise time parameter have been evaluated between 1 MeV and 2 MeV, the systematic uncertainty on the signal acceptance was found to be at the percent level. The cut values have been selected through the optimisation of a figure of merit to maximise the experiment sensitivity. The Rise Time PSD applied in the data release of 2018 has a signal acceptance of $84.3\% \pm 0.4(\text{stat}) \pm 1.0(\text{syst})$, and when combined with the ANN the global PSD efficiency is 71(4)%. This value can be compared with the 77(5)% PSD efficiency of the first GERDA Phase II data release. Thanks to the new Rise Time PSD methods developed in the frame of this dissertation, the background index of the semi-coaxial dataset could be reduced from the $3(2) \cdot 10^{-3}$ cts/(keV·kg·yr) of the first release to $0.6(4) \cdot 10^{-3}$ cts/(keV·kg·yr), the same level recorded for the BEGE dataset. The better background level was the prerequisite to increase the median sensitivity to $1.1 \cdot 10^2 6$ yr (in the assumption of no signal) and to set the limits on the half-life: $T^{0\nu}_{1/2} > 0.9 \cdot 10^{26}$ yr (90% C.L.). This results in a median sensitivity for the effective Majorana mass which according to the different calculations of the nuclear matrix element varies in the range $m_{\beta\beta} < 104 - 228$ meV.

The next phase of the ^{76}Ge $0\nu\beta\beta$ search will be the LEGEND experiment. As the currently running experiments (GERDA and MAJORANA) have shown, the reduction of the surface background will be a key element necessary to reach the design goals. The BEGE detectors currently in use in GERDA will be deployed also in the first stage of the next LEGEND experiments, together with bigger detectors designed to provide similar pulse shapes. My studies on the potential ^{42}K reduction achievable with the A/E analysis show that, given a good resolution for the A/E parameter, it is possible to reduce the ^{42}K contribution well below the goal of 0.6 cts/(FWHM · t · yr). Moreover, the discrimination of the surface events will be paramount also for the second stage of LEGEND with 1 t of target mass and the background goal of 0.1 cts/(FWHM · t · yr).

Bibliography

[1] W. Pauli. letter to "radioactive ladies and gentlemen" at the Tübingen conference, 4 Dec. 1930.

[2] C. L. Cowan, F. Reines, F. B. Harrison, H. W. Kruse, and A. D. McGuire. "Detection of the Free Neutrino: a Confirmation". In: *Science* 124.3212 (1956), pp. 103–104. ISSN: 0036-8075. DOI: 10.1126/science.124.3212.103.

[3] Enrico Fermi. "Tentativo di una Teoria Dei Raggi β". In: *Il Nuovo Cimento (1924-1942)* 11.1 (Jan. 1934), p. 1. ISSN: 1827-6121. DOI: 10.1007/BF02959820.

[4] Sheldon L. Glashow. "Partial-symmetries of weak interactions". In: *Nuclear Physics* 22.4 (1961), pp. 579–588. ISSN: 0029-5582. DOI: https://doi.org/10.1016/0029-5582(61)90469-2.

[5] B. Pontecorvo. "Inverse Beta Processes and Nonconservation of Lepton Charge". In: *JETP* 7.1 (1958). [Russian original - ZhETF, Vol. 34, No. 1, p. 247, July 1958]. URL: http://jetp.ac.ru/cgi-bin/e/index/e/7/1/p172?a=list.

[6] G. Danby, J-M. Gaillard, K. Goulianos, L. M. Lederman, N. Mistry, M. Schwartz, and J. Steinberger. "Observation of High-Energy Neutrino Reactions and the Existence of Two Kinds of Neutrinos". In: *Phys. Rev. Lett.* 9 (1 July 1962), pp. 36–44. DOI: 10.1103/PhysRevLett.9.36.

[7] Ziro Maki, Masami Nakagawa, and Shoichi Sakata. "Remarks on the Unified Model of Elementary Particles". In: *Progress of Theoretical Physics* 28 (Nov. 1962). DOI: 10.1143/PTP.28.870.

[8] B. Pontecorvo. "Neutrino Experiments and the Problem of Conservation of Leptonic Charge". In: *JETP* 26.5 (1968). [Russian original - ZhETF, Vol. 53, No. 5, p. 1717, May 1968]. URL: http://jetp.ac.ru/cgi-bin/e/index/e/26/5/p984?a=list.

[9] Raymond Davis, Don S. Harmer, and Kenneth C. Hoffman. "Search for Neutrinos from the Sun". In: *Phys. Rev. Lett.* 20 (21 June 1968), pp. 1205–1209. DOI: 10.1103/PhysRevLett.20.1205.

[10] Bruce T. Cleveland, Timothy Daily, Jr. Raymond Davis, James R. Distel, Kenneth Lande, C. K. Lee, Paul S. Wildenhain, and Jack Ullman. "Measurement of the Solar Electron Neutrino Flux with the Homestake Chlorine Detector". In: *The Astrophysical Journal* 496.1 (Mar. 1998), pp. 505–526. DOI: 10.1086/305343.

[11] V N. Gribov and B M. Pontecorvo. "Neutrino astronomy and lepton charge". In: *Physics Letters B - PHYS LETT B* 28 (Jan. 1969), pp. 493–496. DOI: 10.1016/0370-2693(69)90525-5.

[12] S. Bilenky. "Neutrino oscillations: From a historical perspective to the present status". In: *Nuclear Physics B* 908 (2016). Neutrino Oscillations: Celebrating the Nobel Prize in Physics 2015, pp. 2–13. ISSN: 0550-3213. DOI: 10.1016/j.nuclphysb.2016.01.025.

[13] M. L. Perl, G. S. Abrams, et al. "Evidence for Anomalous Lepton Production in $e^+ - e^-$ Annihilation". In: *Phys. Rev. Lett.* 35 (22 Dec. 1975), pp. 1489–1492. DOI: 10.1103/PhysRevLett.35.1489.

[14] "Precision electroweak measurements on the Z resonance". In: *Physics Reports* 427.5 (2006), pp. 257–454. ISSN: 0370-1573. DOI: https://doi.org/10.1016/j.physrep.2005.12.006.

[15] K. Kodama, N. Ushida, et al. "Observation of tau neutrino interactions". In: *Physics Letters B* 504.3 (2001), pp. 218–224. ISSN: 0370-2693. DOI: 10.1016/S0370-2693(01)00307-0.

[16] L. Wolfenstein. "Neutrino oscillations in matter". In: *Phys. Rev. D* 17 (9 May 1978), pp. 2369–2374. DOI: 10.1103/PhysRevD.17.2369.

[17] T Kirsten. "Retrospect of GALLEX/GNO". In: *Journal of Physics: Conference Series* 120.5 (July 2008), p. 052013. DOI: 10.1088/1742-6596/120/5/052013.

[18] J.N. Abdurashitov, E.L. Faizov, et al. "Results from SAGE (The Russian-American gallium solar neutrino experiment)". In: *Physics Letters B* 328.1 (1994), pp. 234–248. ISSN: 0370-2693. DOI: https://doi.org/10.1016/0370-2693(94)90454-5.

[19] K. S. Hirata, K. Inoue, et al. "Results from one thousand days of real-time, directional solar-neutrino data". In: *Phys. Rev. Lett.* 65 (11 Sept. 1990), pp. 1297–1300. DOI: 10.1103/PhysRevLett.65.1297.

[20] Y. Fukuda, T. Hayakawa, et al. "Evidence for Oscillation of Atmospheric Neutrinos". In: *Phys. Rev. Lett.* 81 (8 Aug. 1998), pp. 1562–1567. DOI: 10.1103/PhysRevLett.81.1562.

[21] Q. R. Ahmad, R. C. Allen, et al. "Direct Evidence for Neutrino Flavor Transformation from Neutral-Current Interactions in the Sudbury Neutrino Observatory". In: *Phys. Rev. Lett.* 89 (1 June 2002), p. 011301. DOI: 10.1103/PhysRevLett.89.011301.

[22] K. Eguchi, S. Enomoto, et al. "First Results from KamLAND: Evidence for Reactor Antineutrino Disappearance". In: *Phys. Rev. Lett.* 90 (2 Jan. 2003), p. 021802. DOI: 10.1103/PhysRevLett.90.021802.

[23] M. H. Ahn, E. Aliu, et al. "Measurement of neutrino oscillation by the K2K experiment". In: *Phys. Rev. D* 74 (7 Oct. 2006), p. 072003. DOI: 10.1103/PhysRevD.74.072003.

[24] P. Adamson, C. Andreopoulos, et al. "Search for Muon-Neutrino to Electron-Neutrino Transitions in MINOS". In: *Phys. Rev. Lett.* 103 (26 Dec. 2009), p. 261802. DOI: 10.1103/PhysRevLett.103.261802.

[25] F. P. An, J. Z. Bai, et al. "Observation of Electron-Antineutrino Disappearance at Daya Bay". In: *Phys. Rev. Lett.* 108 (17 Apr. 2012), p. 171803. DOI: 10.1103/PhysRevLett.108.171803.

[26] J. K. Ahn, S. Chebotaryov, et al. "Observation of Reactor Electron Antineutrinos Disappearance in the RENO Experiment". In: *Phys. Rev. Lett.* 108 (19 May 2012), p. 191802. DOI: 10.1103/PhysRevLett.108.191802.

[27] Y. Abe, C. Aberle, et al. "Indication of Reactor $\overline{\nu}_e$ Disappearance in the Double Chooz Experiment". In: *Phys. Rev. Lett.* 108 (13 Mar. 2012), p. 131801. DOI: 10.1103/PhysRevLett.108.131801.

[28] Ivan Esteban, M. C. Gonzalez-Garcia, Alvaro Hernandez-Cabezudo, Michele Maltoni, and Thomas Schwetz. "Global analysis of three-flavour neutrino oscillations: synergies and tensions in the determination of $\theta 23$, δCP, and the mass ordering". In: *Journal of High Energy Physics* 2019.1 (Jan. 2019), p. 106. ISSN: 1029-8479. DOI: 10.1007/JHEP01(2019)106.

[29] Ch Kraus, B. Bornschein, et al. "Final results from phase II of the Mainz neutrino mass searchin tritium β decay". In: *Eur. Phys. J.* **C** 40.4 (Apr. 2005), pp. 447–468. ISSN: 1434-6052. DOI: 10.1140/epjc/s2005-02139-7.

[30] V. N. Aseev, A. I. Belesev, et al. "Upper limit on the electron antineutrino mass from the Troitsk experiment". In: *Phys. Rev. D* 84 (11 Dec. 2011), p. 112003. DOI: 10.1103/PhysRevD.84.112003.

[31] "KATRIN Design Report 2004". In: *FZKA Scientific Report* 7090 (Jan. 2005). URL: https://www.katrin.kit.edu/publikationen/DesignReport2004-12Jan2005.pdf.

[32] Diana Parno. "KATRIN: Toward a High-Precision Neutrino-Mass Determination with Tritium". In: *XXVIII International Conference on Neutrino Physics and Astrophysics, Heidelberg, Germany* (June 2018). DOI: 10.5281/zenodo.1287933.

[33] Loredana Gastaldo. *Determining the Electron Neutrino Mass with Ho-163*. June 2018. DOI: 10.5281/zenodo.1286950.

[34] N. Aghanim et al. "Planck 2018 results. VI. Cosmological parameters". In: (2018). arXiv: 1807.06209 [astro-ph.CO].

[35] Alessandro Strumia and Francesco Vissani. "Neutrino masses and mixings and..." Version 3. In: (2010). arXiv: hep-ph/0606054 [hep-ph]. URL: www.pi.infn.it/~astrumia/review.html.

[36] J. Schechter and J. W. F. Valle. "Neutrinoless double-β decay in SU(2)×U(1) theories". In: *Phys. Rev. D* 25 (11 June 1982), pp. 2951–2954. DOI: 10.1103/PhysRevD.25.2951.

[37] M. Fukugita and T. Yanagida. "Barygenesis without grand unification". In: *Phys. Lett.* **B** 174(1) (1986), pp. 45–47. DOI: 10.1016/0370-2693(86)91126-3.

[38] Amand Faessler, A. Meroni, S. T. Petcov, F. Šimkovic, and J. Vergados. "Uncovering multiple CP-nonconserving mechanisms of $(\beta\beta)_{0\nu}$ decay". In: *Phys. Rev. D* 83 (11 June 2011), p. 113003. DOI: 10.1103/PhysRevD.83.113003.

[39] Werner Rodejohann. "Neutrinoless double-beta decay and neutrino physics". In: *Journal of Physics G: Nuclear and Particle Physics* 39.12 (Sept. 2012), p. 124008. DOI: 10.1088/0954-3899/39/12/124008.

[40] J. C. Helo, S. G. Kovalenko, M. Hirsch, and H. Päs. "Neutrinoless double beta decay and lepton number violation at the LHC". In: *Phys. Rev. D* 88 (1 July 2013), p. 011901. DOI: 10.1103/PhysRevD.88.011901.

[41] Michael Duerr, Manfred Lindner, and Alexander Merle. "On the Quantitative Impact of the Schechter-Valle Theorem". In: *Journal of High Energy Physics - J HIGH ENERGY PHYS* 2011 (May 2011). DOI: 10.1007/JHEP06(2011)091.

[42] A. Caldwell and K. Kröninger. "Signal discovery in sparse spectra: A Bayesian analysis". In: *Phys. Rev. D* 74 (9 Nov. 2006), p. 092003. DOI: 10.1103/PhysRevD.74.092003.

[43] Steven R. Elliott and Petr Vogel. "DOUBLE BETA DECAY". In: *Annual Review of Nuclear and Particle Science* 52.1 (2002), pp. 115–151. DOI: 10.1146/annurev.nucl.52.050102.090641.

[44] F. T. Avignone III N. Abgrall E. Aguayo. "The MAJORANA DEMONSTRATOR Neutrinoless Double-Beta Decay Experiment". In: *Advances in High Energy Physics* (2014). DOI: 10.1155/2014/365432.

[45] N. Abgrall, A. Abramov, et al. "The large enriched germanium experiment for neutrinoless double beta decay (LEGEND)". In: *AIP Conf. Proc.* 1894.1 (2017), p. 020027. DOI: 10.1063/1.5007652. arXiv: 1709.01980 [physics.ins-det].

[46] V. Alenkov et al. "First Results from the AMoRE-Pilot neutrinoless double beta decay experiment". In: (2019). arXiv: 1903.09483 [hep-ex].

[47] J. W. Beeman, F. Bellini, et al. "Double-beta decay investigation with highly pure enriched ^{82}Se for the LUCIFER experiment". In: *The European Physical Journal C* 75.12 (Dec. 2015), p. 591. ISSN: 1434-6052. DOI: 10.1140/epjc/s10052-015-3822-x.

[48] M Auger, D J Auty, et al. "The EXO-200 detector, part I: detector design and construction". In: *Journal of Instrumentation* 7.05 (May 2012), P05010–P05010. DOI: 10.1088/1748-0221/7/05/p05010.

[49] The NEXT collaboration, J. Martín-Albo, et al. "Sensitivity of NEXT-100 to neutrinoless double beta decay". In: *Journal of High Energy Physics* 2016.5 (May 2016), p. 159. ISSN: 1029-8479. DOI: 10.1007/JHEP05(2016)159.

[50] S. Umehara, T. Kishimoto, et al. "Neutrino-less double-β decay of ^{48}Ca studied by CaF_2(Eu) scintillators". In: *Phys. Rev. C* 78 (5 Oct. 2008), p. 058501. DOI: 10.1103/PhysRevC.78.058501.

[51] GERDA collaboration. "Probing Majorana neutrinos with double beta decay". In: *Sc* (2019).

[52] S. I. Alvis et al. "A Search for Neutrinoless Double-Beta Decay in ^{76}Ge with 26 kg-yr of Exposure from the MAJORANA DEMONSTRATOR". In: (2019). arXiv: 1902.02299 [nucl-ex].

[53] O. Azzolini, M. T. Barrera, et al. "First Result on the Neutrinoless Double-β Decay of ^{82}Se with CUPID-0". In: *Phys. Rev. Lett.* 120 (23 June 2018), p. 232502. DOI: 10.1103/PhysRevLett.120.232502.

[54] R. Arnold, C. Augier, et al. "Results of the search for neutrinoless double-β decay in ^{100}Mo with the NEMO-3 experiment". In: *Phys. Rev. D* 92 (7 Oct. 2015), p. 072011. DOI: 10.1103/PhysRevD.92.072011.

[55] C. Alduino, F. Alessandria, et al. "First Results from CUORE: A Search for Lepton Number Violation via $0\nu\beta\beta$ Decay of ^{130}Te". In: *Phys. Rev. Lett.* 120 (13 Mar. 2018), p. 132501. DOI: 10.1103/PhysRevLett.120.132501.

[56] A. Gando, Y. Gando, et al. "Search for Majorana Neutrinos Near the Inverted Mass Hierarchy Region with KamLAND-Zen". In: *Phys. Rev. Lett.* 117 (8 Aug. 2016), p. 082503. DOI: 10.1103/PhysRevLett.117.082503.

[57] J. B. Albert, G. Anton, et al. "Search for Neutrinoless Double-Beta Decay with the Upgraded EXO-200 Detector". In: *Phys. Rev. Lett.* 120 (7 Feb. 2018), p. 072701. DOI: 10.1103/PhysRevLett.120.072701.

[58] M. Agostini, G. Benato, and J.A. Detwiler. "Discovery probability of next-generation neutrinoless double-β decay experiments". In: *Phys. Rev. D* 96(5) (2017). DOI: 10.1103/PhysRevD.96.053001.

[59] E. Fiorini, A. Pullia, G. Bertolini, F. Cappellani, and G. Restelli. "A search for lepton non-conservation in double beta decay with a germanium detector". In: *Physics Letters B* 25.10 (1967), pp. 602–603. ISSN: 0370-2693. DOI: 10.1016/0370-2693(67)90127-X.

[60] E. Fiorini, A. Pullia, G. Bertolini, F. Cappellani, and G. Restelli. "Neutrinoless double-beta decay of ^{76}Ge". In: *Il Nuovo Cimento A (1965-1970)* 13.3 (Feb. 1973), pp. 747–763. ISSN: 1826-9869. DOI: 10.1007/BF02784100.

[61] D. O. Caldwell, R. M. Eisberg, F. S. Goulding, B. Magnusson, A. R. Smith, and M. S. Witherell. "Recebt results from the UCSB/LBL double beta decay experiment". In: *Nuclear Physics B Proceedings Supplements* 13 (Feb. 1990), pp. 547–550. DOI: 10.1016/0920-5632(90)90123-C.

[62] A.A. Vasenko, I.V. Kirpichnikov, V.A. Kuznetsov, A.S. Starostin, A.G. Djanyan, V.S. Pogosov, S.P. Shachysisyan, and A.G. Tamanyan. "New results in the ITEP/YePI double beta-decay experiment with enriched germanium detectors". In: *Modern Physics Letters A* 5 (1990). DOI: 10.1142/S0217732390001475.

[63] H.V. Klapdor-Kleingrothaus, A. Dietz, et al. "Latest results from the HEIDELBERG-MOSCOW double beta decay experiment". In: *Eur. Phys. J. A* 12.2 (2001), pp. 147–154. DOI: 10.1007/s100500170022.

[64] C. E. Aalseth, F. T. Avignone, et al. "IGEX ^{76}Ge neutrinoless double-beta decay experiment: Prospects for next generation experiments". In: *Phys. Rev. D* 65 (9 May 2002), p. 092007. DOI: 10.1103/PhysRevD.65.092007.

[65] G.F. Knoll. *Radiation of Detection and Measurement.* third ed. New York: John Wiley and Sons, 1999.

[66] Zhong He. "Review of the Shockley–Ramo theorem and its application in semiconductor gamma-ray detectors". In: *Nuclear Instruments and Methods in Physics Research Section A: Accelerators, Spectrometers, Detectors and Associated Equipment* 463.1 (2001), pp. 250–267. ISSN: 0168-9002. DOI: 10.1016/S0168-9002(01)00223-6.

[67] M. Agostini, M. Allardt, et al. "Pulse shape discrimination for GERDA Phase I data". In: *Eur. Phys. J.* **C** 73.10 (Oct. 2013), p. 2583. ISSN: 1434-6052. DOI: 10.1140/epjc/s10052-013-2583-7.

[68] Marik Barnabè Heider. "Performance and stability tests of bare high purity germanium detectors in liquid argon for the GERDA experiment". PhD thesis. Max Planck Institut für Kernphysik, Heidelberg, May 2009. URL: http://www.mpi-hd.mpg.de/ge76/public/2009/phd2009_MarikHeider.pdf.

[69] Canberra Semiconductor, NV, Lammerdries 25, B-2250, Olen, Belgium.

[70] G. Heusser. "Low-Radioactivity Background Techniques". In: *Annu. Rev. Nucl. Part. Sci.* 45 (1995), p. 543. DOI: 10.1146/annurev.ns.45.120195.002551.

[71] H. V. Klapdor-Kleingrothaus, J. Hellmig, and M. Hirsch. "Future perspectives of double beta decay and dark matter search - GENIUS". In: *J. Phys. G: Nucl. Part. Phys.* 24 (1998), pp. 483–516. DOI: 10.1088/0954-3899/24/3/003.

[72] Yu G Zdesenko, O A Ponkratenko, and V I Tretyak. "High sensitivity GEM experiment on 2β decay of ^{76}Ge". In: *Journal of Physics G: Nuclear and Particle Physics* 27.10 (2001), p. 2129. URL: http://stacks.iop.org/0954-3899/27/i=10/a=312.

[73] M. Miyajima, T. Takahashi, S. Konno, T. Hamada, S. Kubota, H. Shibamura, and T. Doke. "Average energy expended per ion pair in liquid argon". In: *Phys. Rev. A* 9 (3 Mar. 1974), pp. 1438–1443. DOI: 10.1103/PhysRevA.9.1438.

[74] I. Abt et al. "A New ^{76}Ge Double Beta Decay Experiment at LNGS: Letter of Intent". In: (2004). arXiv: hep-ex/0404039 [hep-ex].

[75] K.-H. Ackermann, M. Agostini, et al. "The GERDA experiment for the search of $0\nu\beta\beta$ decay in ^{76}Ge". In: *The European Physical Journal C* 73.3 (Mar. 2013), p. 2330. ISSN: 1434-6052. DOI: 10.1140/epjc/s10052-013-2330-0.

[76] S. Riboldi et al. "A low-noise charge sensitive preamplifier for Ge spectroscopy operating at cryogenic temperature in the GERDA experiment". In: *Procs. IEEE Conferences* (Oct. 2010), p. 1386. DOI: 10.1109/NSSMIC.2010.5873998.

[77] SIS 3301, 8 Channel 105 MS/s 14-bit ADC/Digitizer,
STRUCK Innovative Systeme GmbH, 22399 Hamburg, Germany.

[78] D. Gonzalez and others. "Pulse-shape discrimination in the IGEX experiment". In: *Nucl. Instr. Methods* **A** 515 (2003), p. 634.

[79] M. Agostini, M. Allardt, et al. "Results on Neutrinoless Double-β Decay of ^{76}Ge from Phase I of the GERDA Experiment". In: *Phys. Rev. Lett.* 111 (2013), p. 122503. DOI: 10.1103/PhysRevLett.111.122503.

[80] A. Lazzaro. "Studies of high-purity Ge detector signals". M.Sc. thesis. UNIMIB, 2012.

[81] Matteo Agostini. "Signal and background studies for the search of neutrinoless double beta decay in GERDA". PhD thesis. Technische Unversitaet Muenchen, 2013. URL: http://www.mpi-hd.mpg.de/ge76/public/2013/phd2013_matteoAgostini.pdf.

[82] H.V Klapdor-Kleingrothaus, I.V Krivosheina, A Dietz, and O. Chkvorets. "Search for neutrinoless double beta decay with enriched ^{76}Ge in Gran Sasso 1990–2003". In: *Physics Letters B* 586.3 (2004), pp. 198–212. ISSN: 0370-2693. DOI: 10.1016/j.physletb.2004.02.025.

[83] M. Agostini, M. Allardt, et al. "The background in the $0\nu\beta\beta$ experiment GERDA". In: *Eur. Phys. J.* **C** 74 (2014), p. 2764. DOI: 10.1140/epjc/s10052-014-2764-z.

[84] GERDA Collaboration, M. Agostini, et al. "Upgrade for Phase II of the GERDA experiment". In: *The European Physical Journal C* 78.5 (May 2018), p. 388. ISSN: 1434-6052. DOI: 10.1140/epjc/s10052-018-5812-2.

[85] Tobias Bode. "The neutrinoless double beta decay experiment GERDA Phase II: A novel ultra-low background contacting technique for germanium detectors and first background data". PhD thesis. TU Munich, 2016.

[86] N. Abgrall et al. "The Large Enriched Germanium Experiment for Neutrinoless Double Beta Decay (LEGEND)". In: *AIP Conf. Proc.* 1894.1 (2017), p. 020027. DOI: 10.1063/1.5007652. arXiv: 1709.01980 [physics.ins-det].

[87] K. Freund, R. Falkenstein, et al. "The performance of the Muon Veto of the GERDA experiment". In: *The European Physical Journal C* 76.5 (May 2016), p. 298. ISSN: 1434-6052. DOI: 10.1140/epjc/s10052-016-4140-7.

[88] M. Agostini, L. Pandola, P. Zavarise, and O. Volynets. "GELATIO: a general framework for modular digital analysis of high-purity Ge detector signals". In: *J. of Instrumentation* 6 (2011), P08013. DOI: 10.1088/1748-0221/6/08/P08013.

[89] M. Agostini, M. Allardt, et al. "Improvement of the energy resolution via an optimized digital signal processing in GERDA Phase I". In: *Eur. Phys. J.* **C** 75 (2015), p. 255. DOI: 10.1140/epjc/s10052-015-3409-6.

[90] Steven W. Smith. *The Scientist and Engineer's Guide to Digital Signal Processing*. San Diego: California Technical Publishing, 1999. URL: http://dspguide.com/.

[91] H. L. Van Trees. *Detection, Estimation, and Modulation Theory*. New York: John Wiley and Sons, 1986.

[92] J. Stein, F. Scheuer, W. Gast, and others. "X-ray detectors with digitized preamplifiers". In: *Nucl. Instr. Methods* **B** 113 (1996), pp. 141–145. DOI: 10.1016/0168-583X(95)01417-9.

[93] M. Agostini, L. Pandola, and P. Zavarise. "Off-line data processing and analysis for the GERDA experiment". In: *Journal of Physics: Conference Series* 368 (2012), p. 012047. DOI: 10.1088/1742-6596/368/1/01204.

[94] T. Wester. 2018.

[95] to be published.

[96] K. von Sturm. *High energy background modeling - Phase II*. GERDA Scientific / Technical Reports. 2018.

[97] Dušan Budjáš. "Germanium detector studies in the framework of the GERDA experiment". PhD thesis. U. Heidelberg, 2009. URL: https://www.mpi-hd.mpg.de/gerda/public/2009/phd2009_budjas.pdf.

[98] B. Lehnert. "Search for $2\nu\beta\beta$ Excited State Transitions and HPGe Characterization for Surface Events in GERDA Phase II". PhD thesis. U. Dresden, 2016. URL: https://www.mpi-hd.mpg.de/gerda/public/2016/phd2016_bjoernLehnert.pdf.

[99] Victoria Wagner. "Pulse Shape Analysis for the GERDA Experiment to Set a New Limit on the Half-life of $0\nu\beta\beta$ Decay of ^{76}Ge". PhD thesis. U. Heidelberg, 2018. URL: https://www.mpi-hd.mpg.de/gerda/public/2017/phd2017_victoriaWagner.pdf.

[100] D. Budjas, M. Barnabe Heider, O. Chkvorets, N. Khanbekov, and S. Schönert. "Pulse shape discrimination studies with a Broad-Energy Germanium detector for signal identification and background suppression in the GERDA double β decay experiment". In: *J. Instrum.* 4 (2009), p10007. DOI: 10.1088/1748-0221/4/10/P10007.

[101] Raquel Gonzalez de Orduna, Mikael Hult, Erica Andreotti, Dusan Budjas, Stefan Schönert, and Marcin Misiaszek. "Pulse shape analysis to reduce the background of BEGe detectors". In: *J. Radioanal. Nucl. Chem.* 286 (2010), p. 477. DOI: 10.1007/s10967-010-0729-8.

[102] M. Agostini, C. A. Ur, D. Budjas, E. Bellotti, R. Brugnera, C. M. Cattadori, A. di Vacri, A. Garfagnini, L. Pandola, and S. Schönert. "Signal modeling of high-purity Ge detectors with a small read-out electrode and application to neutrinoless double beta decay search in ^{76}Ge". In: *J. Instrum.* 6 (2011), P03005. DOI: 10.1088/1748-0221/6/03/P03005.

[103] Liao Hen-Ye. "Development of Pulse Shape Discrimination Methods for BEGe Detectors". PhD thesis. Max Planck Institute für Physik and LMU, 2016. URL: www.mpi-hd.mpg.de/gerda/public/2016/phd2016-Liao_Heng-Ye.pdf.

[104] Andrea Kirsch. "Search for the neutrinoless double β-decay in GERDA Phase I using a Pulse Shape Discrimination technique". PhD thesis. MPI-K and U. Heidelberg, 2014.

[105] V.D. Ashitkov et al. In: 46 (2003).

[106] A. S. Barabash, R. R. Saakyan, and V. I. Umatov. "On concentration of ^{42}Ar in liquid argon". In: *Journal of Physics: Conference Series* 718 (May 2016), p. 062004. DOI: 10.1088/1742-6596/718/6/062004.

[107] K. Pelczar. "Backgrounds in the GERDA and DarkSide Experiments. Radioactive Ions in Cryogenic Liquids". PhD thesis. Jagiel-lonian University, Kraków, 2016.

[108] A. Lubashevskiy, M. Agostini, et al. "Mitigation of Ar-42/K-42 background for the GERDA Phase II experiment". In: *The European Physical Journal C* 78.1 (Jan. 2018), p. 15. ISSN: 1434-6052. DOI: 10.1140/epjc/s10052-017-5499-9.

[109] Richard B. Firestone, S. Y. Franck Chu, and Coral M. Baglin. *8th edition of the Table of Isotopes: 1998 Update*. John Wiley, New York, Sept. 1997.

[110] M. Agostini, M. Barnabé-Heider, et al. "LArGe: active background suppression using argon scintillation for the GERDA $0\nu\beta\beta$-experiment". In: *The European Physical Journal C* 75.10 (Oct. 2015), p. 506. ISSN: 1434-6052. DOI: 10.1140/epjc/s10052-015-3681-5.

[111] M. Barnabe Heider, C. Cattadori, O. Chkvorets, A. Di Vacri, K. Gusev, S. Schönert, and M. Shirchenko. "Performance of bare high-purity germanium detectors in liquid argon for the GERDA Experiment". In: *2008 IEEE Nuclear Science Symposium Conference Record*. Oct. 2008, pp. 3513–3516. DOI: 10.1109/NSSMIC.2008.4775094.

[112] Oleg Chkvorets. "Search for Double Beta Decay with HPGe Detectors at the Gran Sasso Underground Laboratory". PhD thesis. Max Planck Institut für Kernphysik, Heidelberg, July 2008. URL: http://www.mpi-hd.mpg.de/ge76/public/2008/phd2008_chkvorets.pdf.

[113] Available at https://radware.phy.ornl.gov/MJ/mjd_siggen/ revision 46.

[114] L Mihailescu, W Gast, R.M Lieder, H Brands, and H Jäger. "The influence of anisotropic electron drift velocity on the signal shapes of closed-end HPGe detectors". In: *Nuclear Instruments and Methods in Physics Research Section A: Accelerators, Spectrometers, Detectors and Associated Equipment* 447.3 (2000), pp. 350–360. ISSN: 0168-9002. DOI: 10.1016/S0168-9002(99)01286-3.

[115] Bart Bruyneel, Peter Reiter, and Gheorghe Pascovici. "Characterization of large volume HPGe detectors. Part I: Electron and hole mobility parameterization". In: *Nuclear Instruments and Methods in Physics Research Section A: Accelerators, Spectrometers, Detectors and Associated Equipment* 569.3 (2006), pp. 764–773. ISSN: 0168-9002. DOI: 10.1016/j.nima.2006.08.130.

[116] K.Panas. PhD thesis. 2018. URL: http://www.fais.uj.edu.pl/documents/41628/139367252/KPanas_PhDThesis.pdf.

[117] Julieta Gruszko. "Surface Alpha Interactions in P-Type Point-Contact HPGe Detectors: Maximizing Sensitivity of ^{76}Ge Neutrinoless Double-Beta Decay Searches". PhD thesis. 2017. URL: http://hdl.handle.net/1773/40682.

[118] github.com/mppmu/GELATIO/blob/master/Doc/README/README.MODULES.

[119] M. Agostini et al. "Background free search for neutrinoless double beta decay with GERDA Phase II". In: *Nature* 544 (2017), pp. 47–52. DOI: 10.1038/nature21717. arXiv: 1703.00570 [nucl-ex].

[120] M. Agostini, A. M. Bakalyarov, et al. "Improved Limit on Neutrinoless Double-β Decay of ^{76}Ge from GERDA Phase II". In: *Phys. Rev. Lett.* 120 (13 Mar. 2018), p. 132503. DOI: 10.1103/PhysRevLett.120.132503.

[121] M. Agostini, A. M. Bakalyarov, et al. "Pulse shape analysis in GERDA Phase II". In: (2019). to be published.

[122] The GERDA collaboration. "Background decomposition in GERDA Phase II". In: (2019). to be published.

[123] M. Tanabashi, K. Hagiwara, et al. "Review of Particle Physics". In: *Phys. Rev. D* 98 (3 Aug. 2018), p. 030001. DOI: 10.1103/PhysRevD.98.030001.

[124] Ivan Esteban, M. C. Gonzalez-Garcia, Michele Maltoni, Ivan Martinez-Soler, and Thomas Schwetz. "Updated fit to three neutrino mixing: exploring the accelerator-reactor complementarity". In: *Journal of High Energy Physics* 2017.1 (Jan. 2017), p. 87. ISSN: 1029-8479. DOI: 10.1007/JHEP01(2017)087.

Acknowledgments

First and foremost, I would like to thank you, the readers: the reviewers and my girlfriend. Then I have to acknowledge the contribution of many persons who in one way or another made this work possible.

The results of this thesis have been achieved through a collaborative effort and with the contributions of many members of the GERDA analysis team. Luciano Pandola and Matteo Agostini provided their expert supervision and guidance through all these years. The development of the Quality Cut is based on the digital signal processing software developed by M. Agostini et al. and the GERLA application developed by Jozsef Janicskó was used to visually inspect the waveforms. Most of the merits for the results of the A/E discrimination go of course to Dusan Budjáš who defined and taught me the ways of the A/E and was involved in all the measurements with the BEGE prototypes. My understanding of the BEGE signal formation, in particular for NSP, comes from the many discussions with Matteo and Björn Lehnert. Most of the credit for the measurements in enriched LAr should go to Alexey Lubashevskiy and the LARGE team. The pulse shape simulations of the semi-coaxial detectors were implemented by Tomaso Comellato and Anna Zsigmond analysed the stability in time of the rise time parameter. The collaboration with Andrea Kirsch and Bernard Schwingenheuer has been fundamental for the development and test of the Rise Time discrimination.

Most of the ideas contained in this thesis were conceived during discussions with Matteo but I really want to thank him especially for the pointless debates over every lunch break. For all other, often more productive, discussions I am grateful to Dusan, Christoph, Tobias, and Jozsef. Thanks to my supervisor Stefan Schönert for the trust and support, it has been an honour to work in his group.

One of the biggest contributors to the realization of this document is not a member of GERDA or a physicist: many thanks (and apologies) to Elisabeth who pushed me to conclude this work and endured through the endeavours of translating my drafts into English.

It has been a long journey that brought me to many places and I am glad that I met so many great travellers along the way.

Special thanks go to the sheep and the grapes of Abruzzo.

Grazie soprattutto alla mia famiglia.

List of Abbreviations

$0\nu\beta\beta$	Neutrinoless double beta decay
$2\nu\beta\beta$	Neutrino accompanied double beta decay
ANN_MSE	Artificial Neural Network for Multi-Site Events
B.I.	Background Index
BEGe	Broad Energy Germanium
BL	BaseLine
C.I.	Credibility Interval
C.L.	Confidence Level
CP	Charge Parity
cts	counts
DAQ	Data AQuisition
DEP	Double Escape Peak
DL	Dead Layer
$\mathcal{E}$	Exposure
FADC	Flash ADC (Analog-to-Digital Converter)
FAV	Full Active Volume
FCCD	Full Charge Collection Depth
FEP	Full Energy Peak
FWHM	Full Width Half Maximum
GBP	Gain-Bandwidth Product
GERDA	GERmanium Detector Array
HF	High Frequency
HPGe	High Purity Germanium
HV	High Voltage
LAr	Liquid Argon
LF	Low Frequency
MSE	Multi-Site Event
MSW	Mikheyev-Smirnov-Wolfenstein
NME	Nuclear Matrix Element
NSP	n+ Surface Pulse
PCP	p+ Contact Pulse
PDF	Probability Density Function
PMNS	Pontecorvo-Maki-Nakagawa-Sakata
PMT	Photo-Multiplier Tube
PSA	Pulse Shape Analysis
PSD	Pulse Shape Discrimination
PSS	Pulse Shape Simulation
$Q_{\beta\beta}$	Q-value double beta decay
RMS	Root Mean Squared
ROI	Region of Interest
SEP	Single Escape Peak
SiPM	Silicon Photo-Multiplier
SM	Standard Model
SSE	Single-Site Event
TL	Transition Layer
TP	Test Pulser
ZAC	Zero-Area finite-length Cusp